Spring 1998

Automobile air bag inflation system using pressurized carbon dioxide

Bart Adams
New Jersey Institute of Technology

ABSTRACT

AUTOMOBILE AIR BAG INFLATION SYSTEM USING PRESSURIZED CARBON DIOXIDE

by
Bart Adams

A novel air bag inflator based on the evaporation of liquefied carbon dioxide was developed. A detailed qualitative model was established on the basis of an extensive experimental study. An integrated quantitative model of this inflator was constructed.

The system was studied by discharging the inflator into a tank and measuring pressure and temperature evolution (0-50 ms). The dispersion of the two-phase spray during inflation was investigated by high-speed cinematography.

The optimal storage pressure of the liquid CO_2 was found to be 2000 psig (at 22 °C). Two distinct inflator behaviors were identified. First, at conditions corresponding to an initial entropy below the critical point, a two-phase evaporating spray was ejected from the inflator into the tank. Second, at an initial entropy above the critical point, the inflation sequence constituted the expansion of a real gas without a significant phase transformation. The minimal flow section in the nozzle was found to control the dynamics of this new inflator.

To prevent the formation of solid CO_2 during inflation, small amounts of organic liquids were added to the inflator. A significant increase in tank temperature was observed, resulting in a profound improvement in performance. An explanation for the influence of organic liquids was developed based on a 'layered evaporation model'.

The qualitative model was based on the interaction of the flashing process with the two-phase outflow from the inflator. This interaction was manifested in two different waves, namely a forerunner and an evaporation wave which controlled the evacuation of the two-phase mixture from the inflator. The latter was predominantly dispersed according to classical atomization mechanisms. The generated droplets evaporated partially by consuming their own internal energy and by interacting with tank gases. The characteristics of the condensate were evaluated by a detailed thermodynamic analysis.

The quantitative description of the inflator involved the development of a transient one-dimensional, two-fluid model. Preliminary simulations show excellent agreement with the expected results. The tank model was formulated on the basis of an empirical correlation for the atomization process, coupled with a simple droplet evaporation model, followed by a model for the mixing of real gases.

AUTOMOBILE AIR BAG INFLATION SYSTEM USING PRESSURIZED CARBON DIOXIDE

by
Bart Adams

A Dissertation
Submitted to the Faculty of
New Jersey Institute of Technology
in Partial Fulfillment of the Requirements for the Degree of
Doctor of Philosophy

Department of Mechanical Engineering

May 1998

APPROVAL PAGE

AUTOMOBILE AIR BAG INFLATION SYSTEM USING PRESSURIZED CARBON DIOXIDE

Bart Adams

5/6/98

Dr. Mohamed E. Labib, Dissertation Advisor — Date
Research Professor of Civil and Environmental Engineering,
New Jersey Institute of Technology, Newark, NJ

5/6/98

Dr. Rong Y. Chen, Committee Member — Date
Professor of Mechanical Engineering,
New Jersey Institute of Technology, Newark, NJ

5/6/98

Dr. Pasquale J. Florio, Committee Member — Date
Associate Professor of Mechanical Engineering,
New Jersey Institute of Technology, Newark, NJ

5/6/98

Dr. Ralph Hensler, Committee Member — Date
Director of Engineering Technology, Breed Technologies Inc.,
Boonton, NJ

5-6-98

Dr. Robert P. Kirchner, Committee Member — Date
Professor of Mechanical Engineering,
New Jersey Institute of Technology, Newark, NJ

BIOGRAPHICAL SKETCH

Author: Bart Adams

Degree: Doctor of Philosophy

Date: May 1998

Undergraduate and Graduate Education:

- Doctor of Philosophy in Mechanical Engineering,
  New Jersey Institute of Technology, Newark, New Jersey, 1998
- Master of Science in Mechanical Engineering,
  Free University of Brussels, Brussels, Belgium, 1992
- Bachelor of Science in Electro-Mechanical Engineering,
  Technical College of the City of Antwerp, Antwerp, Belgium, 1989

Major: Mechanical Engineering

Presentations and Publications:

Adams B.,
Thermodynamics and Nature of Particle Formation during Expansion of Liquid CO_2-Organic Solvent Mixtures, Presented at the University of Delaware, June 1997 at the 71st Colloid and Surface Science Symposium

To my parents, my brothers and sister and Marianne

ACKNOWLEDGMENT

I wish to express my sincere thanks to a few of those who assisted me during the course of this work (Spring '95-Spring '98). Most of all, I thank Dr. Mohamed E. Labib for giving me inspiration, guidance and words of encouragement. Also, thanks to Dr. Stanislav S. Dukhin for the hours of stimulating 'small' discussions and to my committee members, Dr. Rong Y. Chen, Dr. Pasquale J. Florio, Dr. Ralph Hensler and Dr. Robert P. Kirchner for their time and comments. I also thank Yacoob Tabani for his help and for starting out as a colleague and ending up as a good friend. The entire staff of Breed Technologies Inc., Boonton, NJ was extremely helpful in providing technical assistance. I would also like to acknowledge Breed Technologies Inc. for their financial support of my project. Furthermore, I thank Dr. R. Dave for allowing me to use the high-speed cinematographic equipment. And last, but certainly not least, I sincerely thank my parents and Marianne for supporting me during the last three years.

TABLE OF CONTENTS

TABLE OF CONTENTS

(Continued)

TABLE OF CONTENTS

(Continued)

TABLE OF CONTENTS

(Continued)

TABLE OF CONTENTS

(Continued)

TABLE OF CONTENTS

(Continued)

TABLE OF CONTENTS

(Continued)

LIST OF TABLES

LIST OF TABLES

(Continued)

LIST OF FIGURES

LIST OF FIGURES

(Continued)

LIST OF FIGURES

(Continued)

Figure **Page**

LIST OF FIGURES

(Continued)

LIST OF SYMBOLS

a	speed of sound	[m/s]
	bubble/droplet radius	[m]
A	area	[m^2]
B	mass transfer number	[/]
c	specific heat	[J/(kg.K)]
	concentration	[/]
C	drag coefficient	[/]
D	molecular diffusion coefficient	[m^2/s]
e	void fraction	[/]
f	force on a bubble	[N]
	fugacity	[/]
h	specific enthalpy	[J/kg], [J/mol]
	heat transfer coefficient	[W/(m^2.K)]
H	enthalpy	[J]
j	evaporation rate	[kg/m^2.s]
k	thermal conductivity	[W/(m.K)]
l	spray peneteration	[m]
L	length of inflator vessel	[m]
	latent heat	[J/kg], [J/mol]
m	mass	[kg]
$\dot{m}$	mass flow rate	[kg/s]
MW	molecular weight	[kg/mol]
n	number of moles	[mol]
	bubble number concentration	[1/m^3]
P	pressure	[Pa], [bar], [atm], [psi g], [psi a]
r	radial droplet coordinate	[m]
R	gas constant	[J/(kg.K)], [J/(mol.K)]
s	specific entropy	[J/(kg.K)], [J/(mol.K)]
t	time	[s]
T	temperature	[K], [°C]
u	specific internal energy	[J/kg], [J/mol]
U	internal energy	[J]
v	specific volume	[m^3/kg], [m^3/mol]
V	volume	[m^3]
w	velocity	[m/s]
	maximum spray width	[m]
Y	mass fraction	[/]
z	coordinate along inflator axis	[m]
Z	compressibility factor	[/]
α	thermal diffusivity	[m^2/s]

LIST OF SYMBOLS

(Continued)

γ	specific heat ratio	[/]
η	mole fraction	[/]
δ	binary interaction coefficient	[/]
μ	dynamic viscosity	[kg/(m.s)]
ν	kinematic viscosity	[m^2/s]
θ	spray angle	[°]
ρ	density	[kg/m^3]
σ	surface tension	[N/m]
τ	characteristic time	[s]
ω	Pitzer acentric factor	[/]
ψ	bubble break-up rate	[$1/m^3.s$]
$\varnothing$	diameter	[m]

Subscripts

A	buoyancy component (force of Archimedes)
amb	ambient
c	property at the critical point
cond	property of the condensate
crit	critical cross section in the flow path
d	droplet property
e	equilibrium value
inflator	property of the inflator
m	virtual mass component
l	liquid phase
P	constant pressure
peak	referring to the peak pressure during a tank test
r	reduced property
ref	property in the reference state
s	solid phase
tank	property of the receiving tank
v	constant volume, vapor phase
vapor	vapor phase
0	initial value
μ	drag component
∞	flat surface value

Superscripts

*	under ideal gas assumption ($P \rightarrow 0$)
cr	critical value
sat	saturation value

CHAPTER 1

INTRODUCTION

1.1 Objective

The objective of this dissertation is to study and develop a new automotive air bag inflator, based on the rapid transformation of liquid carbon dioxide into vapor. This inflator system is simple in principle and basically consists of a pressure vessel, containing the liquefied carbon dioxide, and a release mechanism which can be activated on command. Because of the benign nature of carbon dioxide, the relatively low storage pressure and the simplicity of the system, the novel inflator offers considerable advantages over the existing technology.

The performance of air bag inflators is commonly studied in terms of pressure-time curves, recorded when the generated gas is discharged into a receiving tank. Simultaneous measurement of the average tank temperature allows the calculation of the produced vapor mass and the properties of the condensate that is formed during the inflation. A series of such experiments was performed to study this inflator and to define its design parameters. The latter included: the size of the storage vessel, the optimal initial pressure, the size of the rate determining orifice in the release mechanism, and the effect of small amounts of organic solvents mixed with the liquid carbon dioxide prior to activation. Further understanding of the system was obtained through high-speed cinematographic experimental studies. In addition, an attempt was made to measure the droplet size distribution of the two-phase jet exiting from the nozzle during the inflation sequence.

After identifying the phenomena that determine the performance of the Stored Liquefied Gas Inflator (abbreviated: SLG-Inflator), a comprehensive qualitative model was developed to describe the system. Based on this model, a computer code was written to simulate the behavior of the SLG-Inflator. Preliminary results are included and show excellent agreement with the expected behavior. In addition, quantitative descriptions of the main phenomena in the tank were established.

In this chapter, relevant general information about air bags is summarized. This includes recent safety statistics, the components and types of typical air bag systems and a discussion of the current state of the technology. Next, the novel inflator type is introduced and its potential is illustrated. The choice of carbon dioxide as working fluid is justified and some of its main properties are discussed by means of a simplified phase diagram. All the phenomena relevant to the understanding and modeling of the new system are introduced at the end of the chapter. This discussion demonstrates the strong multi-disciplinary character of this thesis.

1.2 General Information about Air Bags[1]

As of January 1998, nearly 200 million cars and light trucks were traveling on U.S. roads [1]. While they are essential to the modern society, accidents involving these vehicles are the leading cause of death for people between the ages of 5 and 27 [2]. Hence, at present, automobile safety is an issue of paramount importance.

---

[1] Additional information on air bags can be found in [85] or on the Internet at the National Highway Traffic Safety Administration's (NHTSA) web-site (*http://www.nhtsa.dot.gov/airbags/*).

Cars and light trucks are currently equipped with a number of *Passive Safety Systems*. By definition, these systems do not require the intervention of the occupant in order to be activated. Air bags belong to the class of *Passive Restraint Systems*, as is shown Figure 1.1. About 36% of the current vehicles have a driver side air bag. More than 21% of these also have a passenger side air bag. Starting from model year 1998, federal law requires that all passenger cars must carry air bags on both the driver and the passenger sides. A similar ruling holds for light trucks, starting from model year 1999 [1].

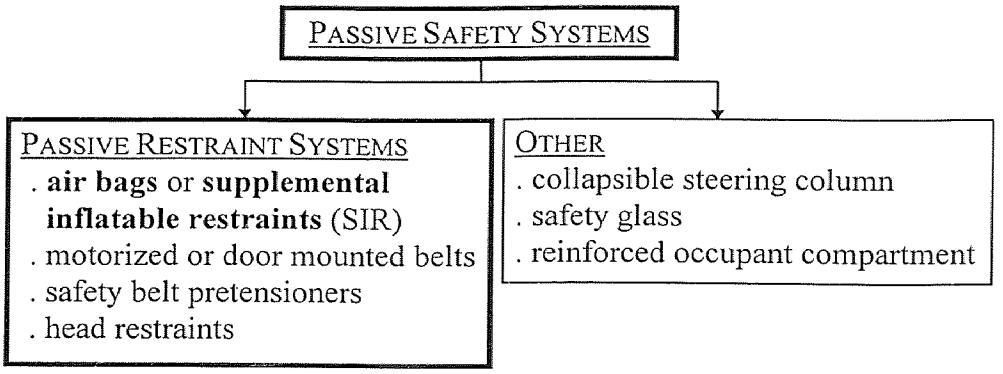

Figure 1.1 Types of Passive Safety Systems

1.2.1 Safety Aspects

Table 1.1 summarizes recent statistical data about the safety aspects of air bags [1]. It indicates that air bags have not only proven to be effective in reducing fatalities, but they also reduce the risk of severe injury to vital body parts considerably.

In a moderate or severe crash, even belted occupants are likely to hit the interior of the car as their belts stretch and pull around their reels. Therefore, safety belts need to be complemented by a secondary restraint system such as air bags. It has to be stressed that air bags are intended to operate as supplemental restraints and should *always* be

accompanied by seat belts. In case no seat belts are worn, the risk of severe injuries, caused by the deployment of the bag itself, increases [94]. Also, seat belts should be worn at all times because they provide protection in non-frontal crashes, unlike most air bags.

Table 1.1 Air Bag Safety Facts [1]

Number of deployments (late 80's - 2/1/1998)	• 2.1 million deployments :
	  • 1.8 million driver side bags
	  • 260,000 passenger side bags

Number of lives saved	• 2474 drivers • 370 passengers • 796 belted and 2048 unbelted
Fatality reduction (head-on crashes)	• 30% reduction for car drivers • 27% reduction for car passengers and light truck drivers
Injury reduction	• 75% effective in preventing serious head injuries • 66% effective in preventing serious chest injuries
Air bag related deaths	• 12 children in rear-facing seats • 39 children not in rear-facing seats • 36 adult drivers • 4 adult passengers

While air bags can drastically reduce the risk of moderate to severe injuries, they can be the cause of minor injuries such as abrasion, laceration and contusion injuries to the face, arms and wrist [94]. Typically, a beneficial shift in injury pattern is observed, with a decrease in severe head and chest injuries and an increase in minor injuries to less vital parts of the body.

Although air bags provide considerable protection in moderate or high-speed crashes, a total of 91 deaths caused by the inflation of air bags in low severity crashes has been reported (Table 1.1). Except for the cases with rear-facing infant seats, almost all of

these fatalities involved unbelted or improperly belted occupants who were too close to the steering wheel or the dashboard when the bag began to inflate. The vast majority of these deaths could have been avoided by buckling up, moving the front seats back as far as possible and seating children under 12 in the back with properly adjusted restraints. According to the NHTSA, the distance between the center of the air bag cover and the center of the driver's breastbone should be at least 10 inches [2]. When these rules are observed, very few people - for example, individuals of extremely short stature - are still at risk for injuries inflicted by the air bag deployment. These people can request a permit from the NHTSA to have an on-off switch installed for their air bags. All other people will be at greater risk if they turn off their air bag.

In response to the fatalities in low-speed crashes, most cars of model year 1998 or later contain *depowered* air bags, which are 20-35% less forceful. This feature should further reduce the need for the on-off switch [2].

The ultimate solution at this point in time seems to be the *advanced* or *smart* air bag. These systems contain additional or more advanced sensors that provide information about the crash severity, the belt usage and the occupant size or position at the time of the crash. Based on this information, the bag deployment is suppressed or tailored such that the risk for injuries is minimized. This technology is expected to be introduced over the next few years and should decrease the risks produced by current air bag designs.

1.2.2 Components of an Air Bag System

Figure 1.2 shows the three typical components of an air bag system. The crash detection hardware consists of multiple acceleration sensors and electronics to interpret the

generated signals. Based on the severity and the direction of the impact, it determines whether the air bag should be activated. If necessary, an electrical signal is sent to the inflator to initiate the gas generation, which, in turn, fills the bag.

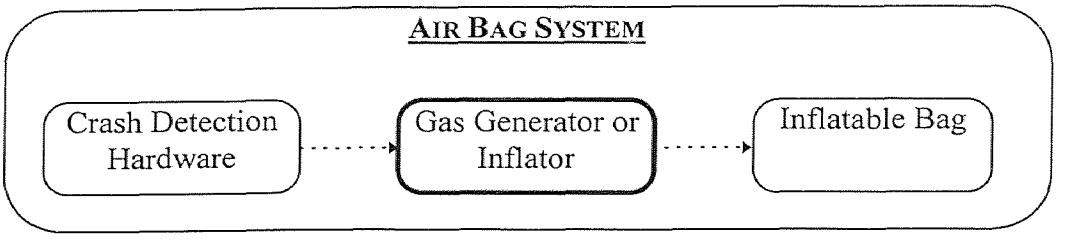

Figure 1.2 Components of an Air Bag System

On average, air bags should deploy in crashes that are equivalent to a vehicle hitting a solid wall head-on at 10-12 mph. The manufacturers Mercedes and BMW adjust this threshold, depending on the belt usage of the occupants.

Ever since it became clear that it was commercially feasible to equip vehicles with air bags, each component of the system has been, and continues to be, the topic of intensive research. Elaborating on the current state of the art of each component is beyond the scope of this dissertation. In the remainder of this text, issues pertaining to the gas generator or *inflator* technology will be considered.

1.2.3 Types of Air Bag Systems

Originally, air bags were intended for use in frontal crashes above a certain severity only. They were not expected to deploy in side, rear, rollover or low speed frontal crashes. Recently, in addition to these frontal air bags, the development of side impact air bags, to be activated in side crashes, has received considerable attention. To date, only a limited

number of commercially available vehicles is equipped with this new type of air bag. Figure 1.3 provides an overview of all air bag types, classified according to the direction of the impact.

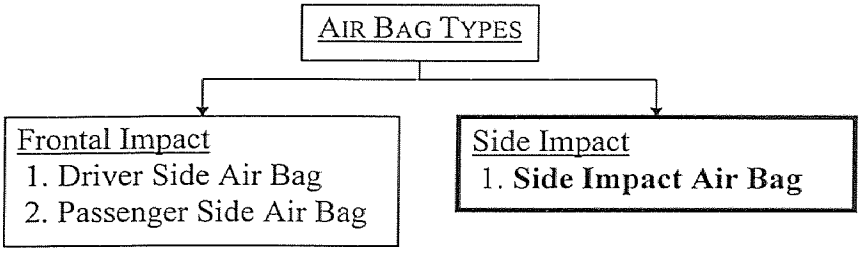

Figure 1.3 Types of Air Bags

The operation principle of a frontal air bag differs significantly from that of a side impact air bag. Frontal air bags are designed as cushions to absorb the kinetic energy of the forward motion of the occupant by deformation and compression of the bag and by forcing out the gas through vent holes. These vents also facilitate the swift deflation of the bag such that it cannot smother or restrict the movements of the occupant after the crash. Typically, frontal air bags are required to deflate in a period of 1-1.5 seconds after the impact. On the other hand, side impact air bags do not rely on energy absorption, but on the generation of sufficient force to move the occupant away from the actual crash location. This way, the risk of injury by the impinging side of the vehicle is reduced. A side impact air bag does not have any vent holes and is expected to maintain pressure. Although side impact bags are primarily designed to protect people's chests, they are also likely to offer some head protection.

1.2.3.1 Driver Side Air Bag: Driver side modules are stored in a compartment inside the steering column of the vehicle. Since the distance between the driver and the steering wheel is considerably smaller than the distance between a passenger and the dashboard, the driver side bag needs to deploy faster than the passenger side bag. The duration of the inflation sequence is about 30 to 45 ms [15]. The nominal volume and the peak pressure of a driver side bag is about 65 liters and 2-3 psig, respectively. Typically, the bag is shaped as a flat spherical disc of about 720 mm in diameter and 150 mm in depth.

1.2.3.2 Passenger Side Air Bag: This air bag module is mounted in the dashboard and contains a bag of about 150 liters. It is quarter-cylindrical in shape and much wider than the driver side air bag. During deployment, a peak pressure of about 1-2 psig is generated inside the bag. The inflation sequence takes 50-65 ms [15] and is more gradual than in the case of a driver side bag. Because of the broad range of human body sizes and the variable position of a passenger on the seat, the design of this air bag is far more difficult than that of the driver side bag.

1.2.3.3 Side Impact Air Bag: Most of the side impact air bags in the early 1990's were door-mounted. Today, the majority of the side impact modules is located in the seat, because this results in a smaller area to be covered and consequently in a smaller bag [9]. Since the space between the vehicle door and the occupant is small, the bag needs to inflate rapidly - typically in about 10-20 ms -. The volume of a side impact bag is about 6-20 liters [9] and, according to an initial study, a peak pressure of 9 psig results in optimal

protection. As stated before, and in contrast to frontal bags, the pressure inside the bag must be maintained over a considerable period of time.

1.2.4 Quantifying the Performance of an Inflator

In the past, it was common to assess the performance of an inflator by looking at the pressure-time curve that was recorded when discharging the device into a rigid tank of a standard size. Especially the peak pressure (P_{peak}) and the time at which it was reached (t_{peak}), were considered important parameters. Clearly, this is a rather crude method and soon the need for a better quantification of the performance was recognized, for example, by simultaneously considering the temperature-time curve [90]. Experiments with actual air bags are expensive and time consuming and are usually not conducted until a later stage in the development cycle of the inflator.

Current specifications of inflators include the size of the module (given by the dimensions of the outer envelope), the number of moles of gas produced and the time it takes to generate 80% of the total mass of gas ($t_{80\%}$). Table 1.2 contains these specifications for the three types of air bags, together with the specifications relating to tank tests.

Table 1.2 Specification of Inflator Performance [5]

	P_{peak} [psig]	t_{peak} [ms]	Envelope Size [mm]	# Moles [/]	$t_{80\%}$ [ms]
Driver Side	17 [(a)]	35	240 x 165 x 80	1.0	40
Passenger Side	35 [(a)]	55	395 x 22 x 125	2.0 - 2.5	60
Side Impact	12 [(b)]	10	--	0.5 - 0.6	10

[(a)] for a 100 liter tank
[(b)] for a 28 liter tank

a) Driver Side Inflator Tank Curve (Receiving Tank volume ≈ 100 liter)

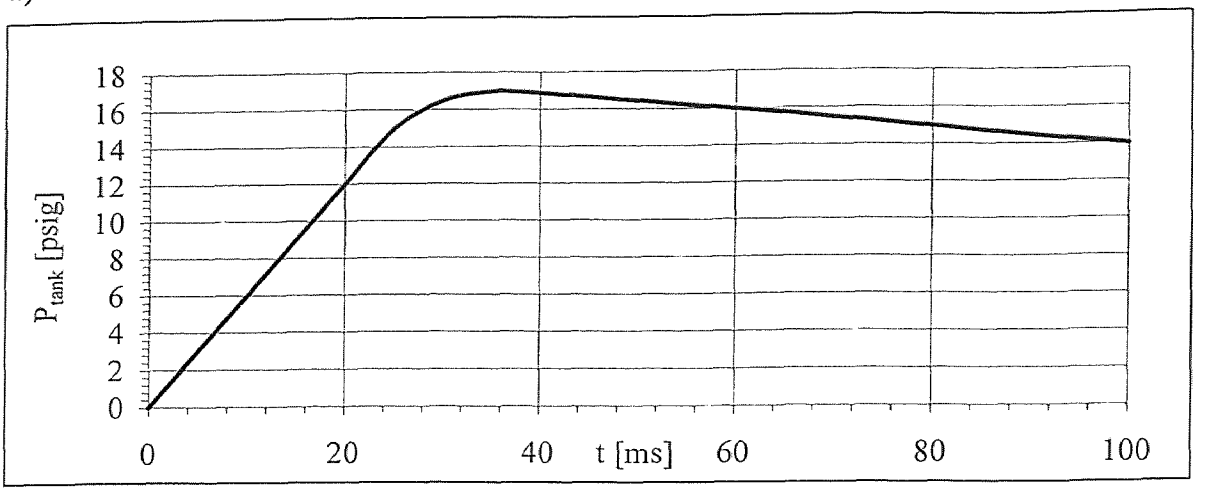

b) Passenger Side Inflator Tank Curve (Receiving Tank volume ≈ 100 liter)

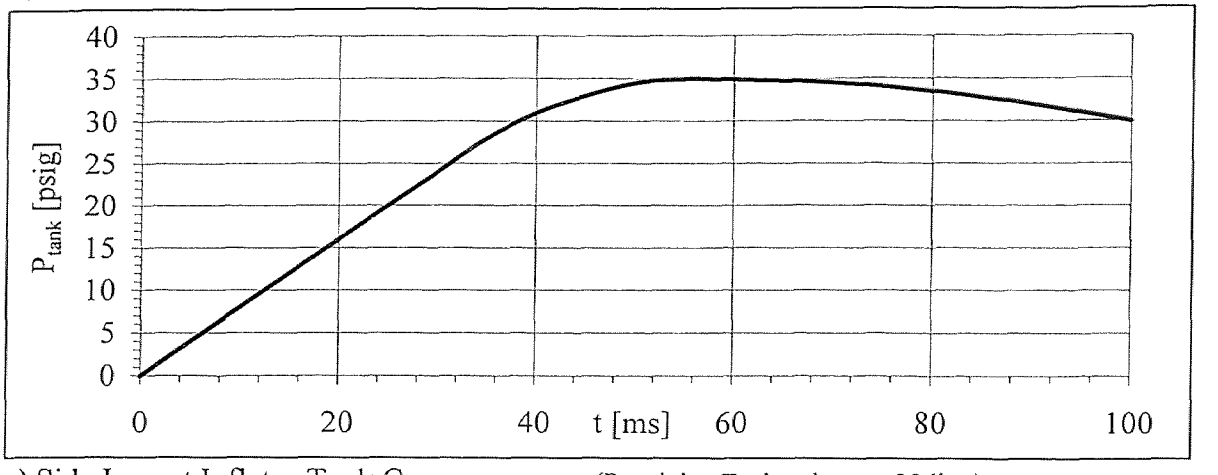

c) Side Impact Inflator Tank Curve (Receiving Tank volume ≈ 28 liter)

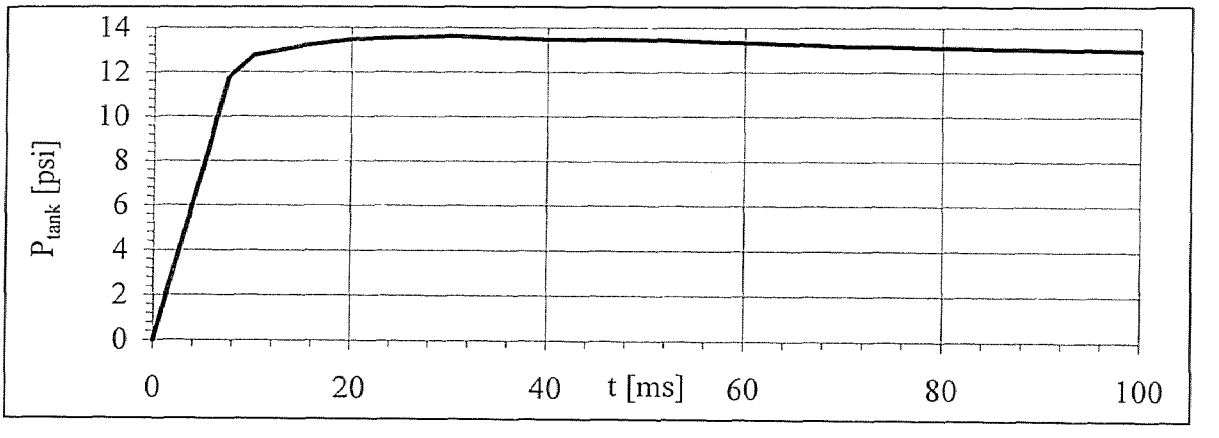

Figure 1.4 Pressure-Time Curves for Different Types of Air Bag Inflators

The values of the peak pressure in the second column of Table 1.2 correspond to tank tests and are considerably higher than the optimal pressure during the actual inflation of an air bag. Typical pressure-time curves of tank tests for the three types of air bags are shown in Figure 1.4(a-c) .

1.2.5 General Design Requirements of an Inflator

In addition to the performance specifications, illustrated in Table 1.2, a number of general demands can be listed:

1. ***Cost:*** The device should be small and simple in design and construction to minimize the raw material, the manufacturing and the assembly costs.
2. ***Power Consumption:*** Only a small fraction of the vehicle power can be used.
3. ***Weight and Dimensions:*** Car manufacturers impose stringent requirements with respect to the size and weight of the air bag module. Since the introduction of air bags, both the size and weight have decreased drastically.
4. ***Safe Deployment:*** To minimize the risk for secondary injuries, the gases and other products in the air bag should be relatively cool and non-toxic.
5. ***Safety in Inactivated State:*** The inflator must be able to withstand large thermal and mechanical stresses and should not pose a safety hazard in emergency situations such as an engine fire.
6. ***Recycling:*** At the end of the lifetime of the car, the inflator module needs to be easy to dismantle and, preferably, at least partially recyclable.

7. ***Influence of Ambient Temperature on the Inflator Performance:*** To assure proper deployment of the bag under all climatic conditions, the inflator performance is required to vary by not more than 10% over the temperature range from -40 to 85 °C.
8. ***Longevity:*** The inflator is expected to be operational for at least 15 years with a minimal change in performance over its lifetime. Especially for devices which rely on chemical reactions this requirement can pose a problem, because of the change in reactivity as the chemical components age.
9. ***Reliability:*** Since the aim of the inflator is to provide life-saving protection, it is required to be extremely reliable.

1.2.6 Current Inflator Technology

Four different types of inflators are either used or under development in current inflator technology.

1.2.6.1 Pyrotechnic Inflator: The majority of commercially available inflators generate gas (at least partially) through the combustion of a pyrotechnic substance. The main advantages of this approach are that it leads to small, light and powerful inflators. Mostly, sodium azide (NaN_3) is used as pyrotechnic substance. An *enhancer*, such as potassium nitrate (KNO_3), is added to speed up the ignition and to assure a high reaction rate during the initial phase of the combustion. Different kinds of oxidizers are used, for example copper oxide (CuO) or silicon dioxide (SiO_2). A typical reaction scheme for this type of inflator is as follows:

$$10\ NaN_3 + 2\ KNO_3 + 5\ SiO_2 \rightarrow 5\ Na_2O.K_2O.5\ SiO_2 + 16\ N_2$$

The reactants are solid pellets and the main combustion products are slag (about 54 mass% [24]) and nitrogen gas (about 99 vol% [26]). Secondary reaction products include CO, CO_2, No_x, NH_3 and SO_2, together with NaOH, Na_2CO_3 and other metal oxide particles. Most of the secondary reaction gases are toxic and hazardous for the environment. Also, a filter needs to be incorporated to remove the airborne particles. The latter not only complicates the system, but also increases the cost and causes a pressure loss. Although the NaOH particles may cause irritation to the skin and the eyes of the occupant, the concentration is such that it does not pose a health hazard. Similarly, the CO concentration remains under the occupational exposure limit at all times [26]. The temperature of the generated gases varies between 260 °C and 650 °C [82]. This necessitates the usage of expensive bag material and increases the risk of facial burns. In addition, heat transfer from the hot gases to the environment causes the bag pressure to drop. Especially for the side impact bag, which needs to sustain pressure for a considerable time, the pressure loss due to heat transfer creates difficulties. However, it is especially the NaN_3 itself that poses a problem [49]. It is toxic when ingested and an azide-water mixture lowers the blood pressure upon contact with the skin. Furthermore, NaN_3 forms primary explosives upon contact with heavy metals such as copper, lead or mercury. This not only generates concerns during the normal lifetime of the inflator, but also complicates the disposal procedure of the car.

1.2.6.2 Stored Gas Inflator: In this type of inflator, the total amount of gas needed to fill the bag is stored under pressure. Usually argon or nitrogen are used at storage pressures

of about 5000 psig (at ambient temperature of 25 °C). This relatively high pressure requires a container with considerable wall thickness and in turn results in a heavy and bulky device. Upon activation, the storage compartment is opened, typically by means of a rupture disk arrangement, and the stored gas expands into the air bag. Because of the short duration of this process, it can be considered adiabatic and all expansion work is compensated for by the internal energy of the gas itself. A number of expressions were developed to describe this expansion under the assumption of ideal gas behavior and a complete discharge of the inflator [60]. Using these relations, typical values for the idealized stored gas inflation sequence were obtained, as shown in Table 1.3. The calculations were done for different working fluids and for the upper and the lower limit of the specified ambient temperatures (requirement 7 of §1.2.5). In reality, the inflator discharge will not be complete (an estimated 3-6% of the initial amount of gas remains inside the inflator) and the final temperatures will be higher than the ones listed in Table 1.3.

Table 1.3 Gas Temperatures for a Stored Gas Inflation Sequence [°C]

	He / Ar		N_2	
Ambient Temperature	-40	85	-40	85
Temperature of Initial Exiting Gas	-40	85	-40	85
Temperature of Final Exiting Gas	≈ -244	≈ -228	≈ -244	≈ -228
Average Temperature Air Bag Gas	-134	-59	-107	-17

Note that the conditions are such that condensation and real gas behavior of the working fluid should be taken into account. During almost the entire inflation sequence, the flow from the inflator is choked and the exit velocity equals the local sound speed of the

working fluid. The evacuation rate is therefore determined by the orifice size, the temperature of the gas and its molecular weight. The difference in average temperature of the gas in the bag (Table 1.3), together with the influence of the temperature on the evacuation rate, explain the strong dependence of the inflator performance on the initial temperature. This is considered to be the main drawback of this inflator type.

In contrast to the pyrotechnic inflator, the generated gases are cold. Besides reducing the risk for facial burns, this eliminates the problem of pressure loss due to cooling. Furthermore, the stored gas inflator is environmentally friendly and easy to recycle. The cost of the stored gas inflator is comparable to that of the pyrotechnic inflator.

At the Breed Technologies Inc., a *Temperature Compensated Stored Gas* Inflator was developed, with a significantly smaller temperature dependence than the traditional stored gas inflator [60]. This is achieved by complementing the traditional inflator with a temperature controlled valving mechanism and a passive temperature reservoir. The valving mechanism is based on the thermal expansion of plastics, while a carefully chosen wire mesh filter functions as heat exchanger. At hot initial conditions, only a very small portion of the expanding gas is lead through the mesh and heat transfer between the gas and the reservoir is limited. The lower the initial temperature, the more the valve directs the gases through the wire mesh and therefore the larger the heat transfer. While the performance of the inflator remains virtually the same, the temperature dependence, and therefore one of the major drawbacks of this type of inflator, is significantly reduced.

It will be shown in the next section that the novel inflator type, which is the subject of this work, is similar to the stored gas inflator in principle and components.

1.2.6.3 Hybrid or Augmented Gas Inflator: This type of inflator combines the previous principles and uses compressed gas and a combustion reaction in a single device. The concept of this inflator is to mix the high-energy reaction products with the stored gas, causing the latter to expand, and to use this mixture to fill the bag. This allows a reduction of the amount of propellant and reduces both the temperature and the particulate content of the generated gas. Early designs contained both the gas and the propellants in one compartment. Production difficulties and undesired autoignition under extreme circumstances lead to designs in which the gas and the reactants are stored in two or more chambers, separated by a burst disc [82]. A wide variety of reactants can be used, including gases, liquids and solids. Versions with three compartments, storing the oxidants and the fuel separately, reduce long term storage problems. The main drawbacks of this inflator type are its complexity, size and high cost.

1.2.6.4 Combustible Gas Mixture Inflator: The combustion of a mixture of gases, for example hydrocarbons and oxygen or hydrogen and air, is used to generate the required amount of gas. A recent project at NJIT, in cooperation with Breed Technology Inc., illustrated the potential of this concept [85]. The main advantages over the NaN_3-system are the lower price, non-toxicity of the reaction products, the environmental friendliness and the fact that the system can be recycled easily. However, due to the high pressures during the reaction, the system tends to be heavy. Work remains to be done to investigate the long-term storage behavior and some other issues such as restricting the reaction to the inflator vessel.

Very recently (October 1997), TRW introduced the *Heated Gas Inflator* [22]. It relies on the combustion of a lean hydrogen/air mixture, stored at 175-310 bar (2500-4500 psig), to generate the required amount of gas. The inflator is claimed to be the cleanest available, since its residue is mere water vapor. The unit is lighter than the pyrotechnic inflator and is easy to recycle. Interestingly, the physical size of the Hearted Gas-Inflator is much larger than any other inflator type. To the best of the author's knowledge, this is the first time since the introduction of commercial air bags that the trend towards ever decreasing inflator sizes has been reversed. This type of inflator is used by some manufacturers in their 1999 model year.

1.3 Novel Approach

The discussion of the inflator technology in the previous section demonstrates that no single type meets all the design requirements in a satisfactory way. The combustion based systems, on the one hand, are small and powerful but invariably raise safety, recycling and health issues. The stored gas inflator, on the other hand, is non-toxic and simple, but needs a relatively complicated mechanism to minimize the temperature dependence of its performance and is large and heavy.

In this research, a novel inflator type, based on the rapid phase transformation of a liquefied gas into vapor, is studied and developed. It will be shown that, if certain problems are overcome, the new type meets more of the design requirements than other inflator types.

The new system consists of a storage compartment, which contains the liquefied gas, and a nozzle with a built-in release mechanism. Like other inflator designs, the latter

is made of a burst disc which can be made to rupture on command. Upon activation, the release mechanism opens the storage chamber, causing a sudden pressure drop and initiating the rapid phase transformation in the fluid. Subsequently, the generated vapor, along with entrained liquid, exits the chamber through the nozzle as a two-phase jet and fills the air bag. Ideally, the total amount of liquid is transformed into vapor within the required time.

Clearly, the system is similar to the stored gas approach, but it involves a phase transformation instead of an expansion and it stores the working fluid as a liquid instead of a gas. Based on this similarity, the novel type is called the *Stored Liquefied Gas Inflator*. Storing the fluid as a liquid is beneficial because of the higher density, i.e. the same amount of fluid fits into a smaller volume. However, in order to store the working fluid in the liquid phase, the pressure inside the vessel must exceed the saturation pressure corresponding to the fluid temperature. For substances with a critical point slightly above ambient conditions, this can be achieved at relatively low storage pressures. Hence, a careful selection of the working fluid leads to the reduction of both the storage volume and pressure and consequently to the elimination of two important disadvantages of the stored gas inflator. At the same time, all the advantages of the stored gas inflator, such as simplicity, low-toxicity and low price, are maintained.

Similar to the stored gas inflator, the heat transfer to the system during the deployment sequence is negligible. Hence, the latent heat of evaporation and the energy for the expansion of the gas is taken from the fluid's internal energy. On the one hand, this leads to the production of cool gas, which is advantageous for the same reasons as mentioned in the case of the stored gas inflator. On the other hand, this may lead to

phenomena that obstruct the filling of the bag, such as freezing of the fluid inside the inflator vessel or solidification of the evaporating liquid in the bag. Both effects result in a loss of part of the working fluid for the purpose of filling the bag. These and all other relevant phenomena are discussed in section §1.3.3.

The previous discussion illustrates that, if one succeeds in transforming the stored liquid into gas such that the air bag is filled in a satisfactory manner, the new inflator type offers more advantages than any other type:

1. simple in principle and construction, therefore inexpensive and reliable
2. no health or environmental risks
3. small and light compared to stored gas inflators
4. easy to dismantle and recycle
5. no long term storage problems since no chemically active substances are involved
6. cool gas is produced, thus minimizing the risk for facial burns and making it easier to maintain pressure over a long time
7. low power consumption

Although the new principle is intended in the first place to be used as an inflator for side impact air bags, it is obviously not limited to this type of air bag or this technology.

1.3.1 Selection of the Working Fluid

Table 1.4 lists some common fluids with a critical point slightly above ambient conditions. Considering issues such as cost and safety, carbon dioxide is clearly the best

choice from this list. Not only do some of the other substances form explosive mixtures upon dilution in air, but all of them are more expensive than CO_2. In addition, CO_2 is virtually nonreactive, readily available and has a well-documented behavior. Some general properties of CO_2 are discussed in the next section.

Table 1.4 Critical Temperature and Pressure of some Common Fluids [45]

Substance	Formula	T_c [°C]	P_c [bar]
acetylene (ethyne)	C_2H_2	35.9	62.5
carbon dioxide	**CO_2**	**31.4**	**73.8**
ethane	C_2H_6	32.1	49.4
ethylene (ethene)	C_2H_4	9.2	51.2
freon 13	$CClF_3$	28.8	38.7
freon 23	CHF_3	26.0	48.4
refrigerant 503	[1]	19.4	43.3
xenon	Xe	16.6	59.0

[1] Azeotrope 40.1% (mass) CHF_3 & 59.9 % $CClF_3$

1.3.2 General Properties of CO_2

The physical properties of CO_2 have been the topic of intense research in the past and are now readily available in the literature. The majority of the CO_2 properties used in this work are based on references [12,30,95].

At ambient conditions, CO_2 is a colorless and almost odorless gas with an acidic taste and a density of about 1.5 times that of air. It is present in the atmosphere in small quantities, about 0.03 vol%, and is fairly inert. Concentrations in air above 5 vol%, are toxic and prolonged exposure causes loss of consciousness and eventually death [4]. Carbon dioxide has a simple, linear molecule with very low polarity and no dipole moment. Its quadrupole moment, however, is strong enough to affect its thermodynamic

properties and to cause a behavior quite different from other gases with nonpolar molecules of similar size and molecular weight.

The pressure - volume - temperature relationship - so called *PvT-information* - for CO_2, is shown in a simplified T-s phase diagram in Figure 1.5 . The critical point (at 304.21 K and 73.825 bar and indicated by *cp*) is located at the top of the vapor-liquid (v+l) coexistence dome. The line *t-t'-t''* (at 216.58 K and 5.185 bar) represents the triple point. This line separates the vapor-liquid and the vapor-solid (v+s) coexistence regions. The other two boundaries of the vapor-liquid region are the saturated liquid - or *boiling* - line to the left and the saturated vapor - or *dew* - line to the right, indicated as *t'-cp* and *t-cp* respectively. Similarly, the two sublimation lines *b'-t''* and *b-t* are the remaining boundaries of the vapor-solid two-phase region.

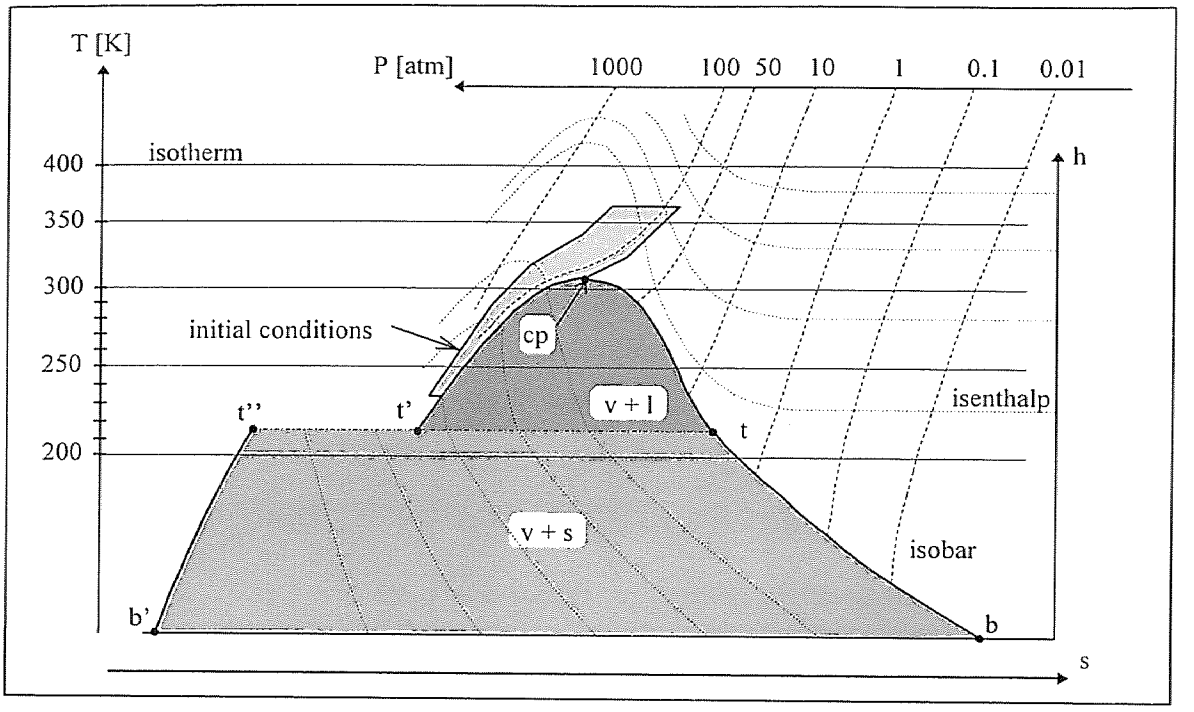

Figure 1.5 Simplified Phase Diagram of CO_2

The negligible compressibility of the solid phase reduces the corresponding region to a line, coinciding with the *b'-t''* sublimation line. The liquid region extends to the left of the boiling line and runs into the supercritical region on top. While not clearly visible on a diagram of this size, it can be shown that the isobars in the liquid region do not coincide. As a result, liquid carbon dioxide cannot be approximated as an incompressible liquid. This does not only mean that the compressibility has to be taken into account when modeling the system, but also that the optimal storage pressure for the inflator is likely to be higher than the saturation pressure. Another indication of the non-ideal liquid behavior is the significant difference between the isobaric and the isochoric specific heat capacity in this region. Strictly speaking, the supercritical region extends from the critical isotherm and the critical isobar upwards. Practically, however, for applications such as supercritical fluid extraction, this area is considered to be outlined by the isotherms corresponding to T_c and 1.1 x T_c and the isobars corresponding to P_c and 1.5 x P_c [53]. The vapor region is located to the right of both the supercritical and the two coexistence regions. At low pressures and elevated temperatures - the upper right corner in Figure 1.5 - the isenthalps run parallel to the isotherms. This indicates the ideal gas behavior of the vapor in this region. Note that the 1 atm isobar intersects the right hand sublimation line rather than the dew line, in accordance with the common knowledge that it is impossible to liquefy CO_2 at ambient pressure.

Only thermodynamic equilibrium states (i.e. states corresponding to slow variations of properties) are represented in Figure 1.5. Rapid changes generate states that deviate from this diagram. This is discussed in greater detail in the next section.

According to the general specifications (§1.2.5), the inflator performance is required to be nearly constant for ambient temperatures ranging from -40 °C to +85 °C. At the same time, the storage pressure should be lower than that of a stored gas inflator (typically about 5000 psig) to avoid a heavy and bulky device. The lower limit on the storage pressure will be determined by the performance of the inflator itself and is not known at this point. These considerations provide the range of initial conditions that need to be investigated. Table 1.5 summarizes the limits of this range, which is also represented in Figure 1.5.

Table 1.5 Initial Conditions of CO_2 in the Inflator

	Lower Limit	Upper Limit
P	--	350 bar ≈ 5000 psi g
T	-40 °C	+85 °C

1.3.3 Relevant Phenomena in the System

Figure 1.6 contains a symbolic representation of the SLG-Inflator, along with a list of physical phenomena that occur in each component of the system. The phenomena marked with an asterisk (*) were not taken into account in the description of the system. This section contains a brief description of the events that take place in each component of the system during a typical inflation sequence. All phenomena which are encountered in the following chapters are introduced during this description. The interaction of these phenomena is discussed and key references are included. Since the inflator drives all effects in the system, this component is considered first, followed by the nozzle with the

built-in release mechanism and, finally, the receiving tank or the air bag. All phenomena are introduced and described in the same order as they appear in the lists of Figure 1.6.

In this section, it will be assumed that the initial entropy of the inflator is below that of the critical point of CO_2. The case with an initial entropy in excess of that of the critical point is discussed in Chapter 4.

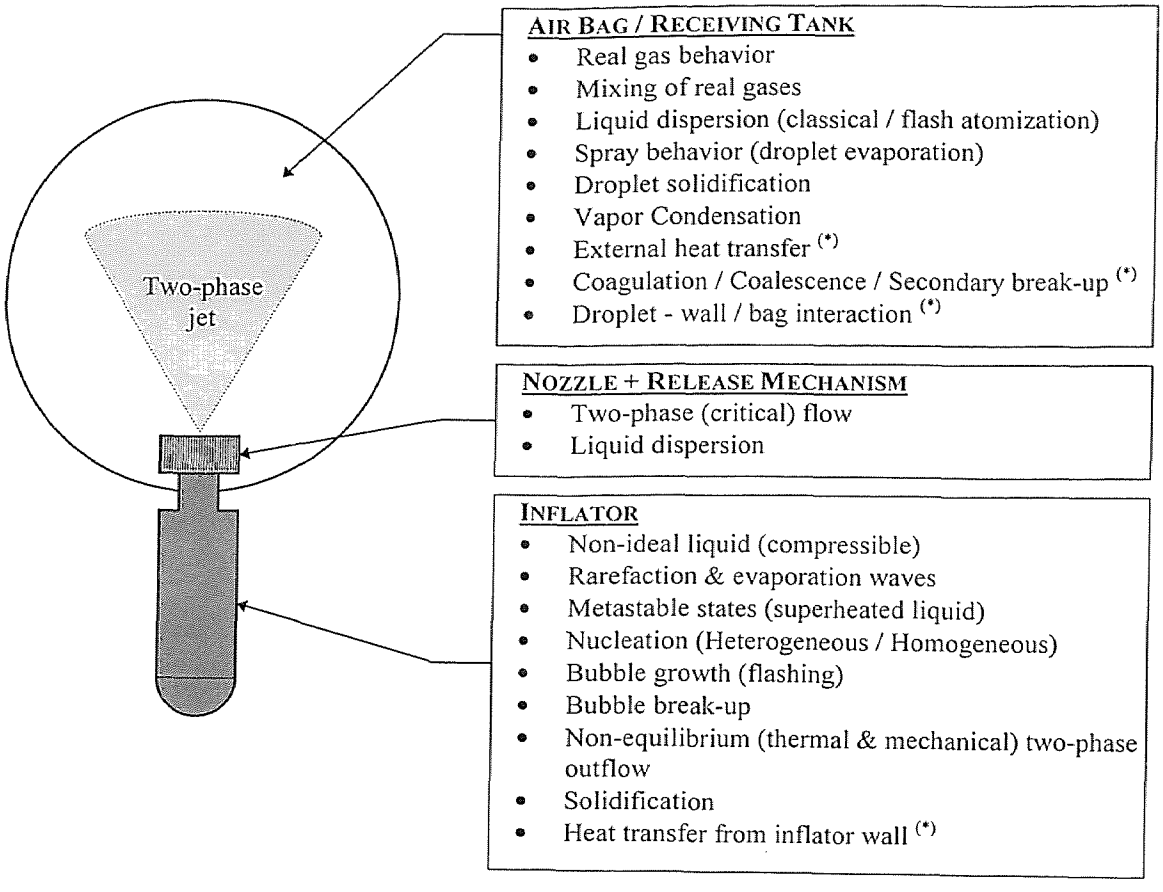

Figure 1.6 Components of the SLG-Inflator with Relevant Physical Phenomena

1.3.3.1 Phenomena in the Inflator Vessel: For this discussion, it is assumed that the vessel is tubular in shape (i.e. a relatively high length to diameter ratio) such that a one-dimensional approximation of the phenomena is justified.

Prior to activation, the inflator vessel is filled with compressed liquid carbon dioxide. In Figure 1.5, this corresponds to a point in the lower part of the shaded region which contains the initial conditions. As shown in the previous section, even at low temperatures, the compressibility of liquid carbon dioxide cannot be neglected. Hence, when modeling the system, it is not justified to approximate the CO_2 in the initial state as an ideal liquid. Instead, a more complicated equation of state needs to be used. Chapter 5 contains a detailed discussion of the selection of the equation of state. In the final model, an equation with 27 constants is used, which is shown to cover the entire fluid region of CO_2 [46].

When the inflator is activated, the release mechanism ruptures the burst disk. In this section, the opening time of the mechanism will be neglected. The destruction of the burst disk initiates a rapid pressure drop in the system under the shape of a steep rarefaction wave, traveling through the liquid at the local speed of sound towards the closed end of the vessel. This wave is referred to in the literature as the *(elastic) forerunner* [47,63,86]. Due to the small dimensions of the inflator vessel, the forerunner reaches the closed end within the first millisecond after the start of the inflation sequence. After hitting the closed end, the forerunner bounces back towards the front of the vessel but is attenuated drastically by localized vapor formation [47,63]. The passage of the forerunner causes a rapid isentropic expansion of the liquid [52]. As is often the case in fast processes, the system's behavior deviates from equilibrium and evaporation does not

start when the pressure downstream of the forerunner attains the local saturation value. Instead, the pressure drops further and the liquid enters a *metastable state* in which it becomes *superheated.* By definition, a liquid is superheated when it exists at a temperature above the boiling point corresponding to the local pressure. It is metastable because its entropy is not maximum for its given energy. The effect of the forerunner in Figure 1.5 corresponds to a vertical drop to a point inside the vapor-liquid coexistence region. In reality, however, no vapor formation has taken place and the actual state of the liquid cannot be represented in the diagram. The region in the phase diagram to the right of the saturated liquid line, containing the superheated liquid states is called the *metastable region.* Metastable liquids are well-behaved and have reproducible properties which can be calculated by extending the chosen equation of state into the metastable region [58]. The departure from equilibrium is usually expressed as the difference between the actual temperature and the boiling point corresponding to the local pressure. This difference is called the *superheat.*

At a certain value of the superheat, depending mainly on the depressurization rate and cleanliness of the liquid and the apparatus, the superheated liquid suddenly starts to evaporate. Since the process is considered adiabatic, part of the internal energy of the liquid is used to supply the latent heat of evaporation. Therefore, the phase transformation results in a drop in temperature. At the same time, the generation of vapor leads to an increase in pressure. Both effects reduce the superheat and push the system towards its new equilibrium state. The phase transformation under consideration differs from boiling by the fact that it is adiabatic and therefore not driven by heat transfer. Instead, it is the pressure drop in the system that causes the evaporation. Such phase transitions are called

flashing or *flash boiling*. Due to the interest of the nuclear power industry in the flashing phenomena to estimate the pressure loss in a cooling circuit caused by a pipe failure, a considerable amount of work has been done on the flashing of water. Studies focus both on the inception of flashing [34,54,77,97] and on the calculation of the maximum - so called *critical* - flow rate [21,28,61,69]. A number of studies have been performed on the flashing of cryogenic liquids - freons in particular - [40,42], and some use CO_2 as working fluid [37,52,54,58]. The initiation of flashing in a superheated liquid is described by nucleation theories [14,20,29,77], which predict the volumetric formation rate of evaporation nuclei. Under extremely clean conditions and for very rapid depressurizations, the initiation of evaporation is driven by density fluctuations. This is described in the *homogeneous nucleation theory*. In most practical situations, however, a significant number of impurities acts as evaporation nuclei and expedites the initiation of flashing. This process is described by the *heterogeneous nucleation theory*. The further the departure from equilibrium (i.e. the larger the superheat) the faster and the more violent the flashing process [29].

There exists an upper limit for the size of the superheat. No matter how high the depressurization rate or how clean the fluid and the vessel, evaporation cannot be delayed past a certain, reproducible limit. This limit is called the *maximum superheat* or *superheat limit*. Extensive work has been performed by Skripov [81] and Lienhard [57] to determine the maximum superheat experimentally. Cases where this limit is reached are often referred to as *vapor* or *thermohydraulic explosions* because of the violent nature of the phase transformation. Experiments prove that the superheat limit for a liquid, where homogeneous nucleation initiates the evaporation, lies very close to the *liquid spinodal*

limit [57]. The spinodal limits, at least the ones that are of interest in the current discussion, are located at the high density inflection points of the subcritical isotherms in a pressure-volume phase diagram. As such, they mark the transition from negative slope of the isotherm to positive slope, or from thermodynamic metastablility to absolute instability. The *liquid spinodal line* is formed by connecting these inflection points. This is illustrated in Figure 1.7, which contains a P-v phase diagram of CO_2. The diagram was generated with the same equation of state which is used in the actual model of the SLG-Inflator [46]. The metastable liquid region is located between the saturated liquid line and the liquid spinodal. Similar to the liquid spinodal, the low density inflection points of the subcritical isotherms mark the *vapor spinodal line*. In contrast to the liquid spinodal, the vapor spinodal does not lie in the vicinity of the limit of maximum supersaturation of the vapor phase (i.e. the onset of homogeneous nucleation in the condensation process). Hence, it is of no importance in the current work and it is not represented in Figure 1.7.

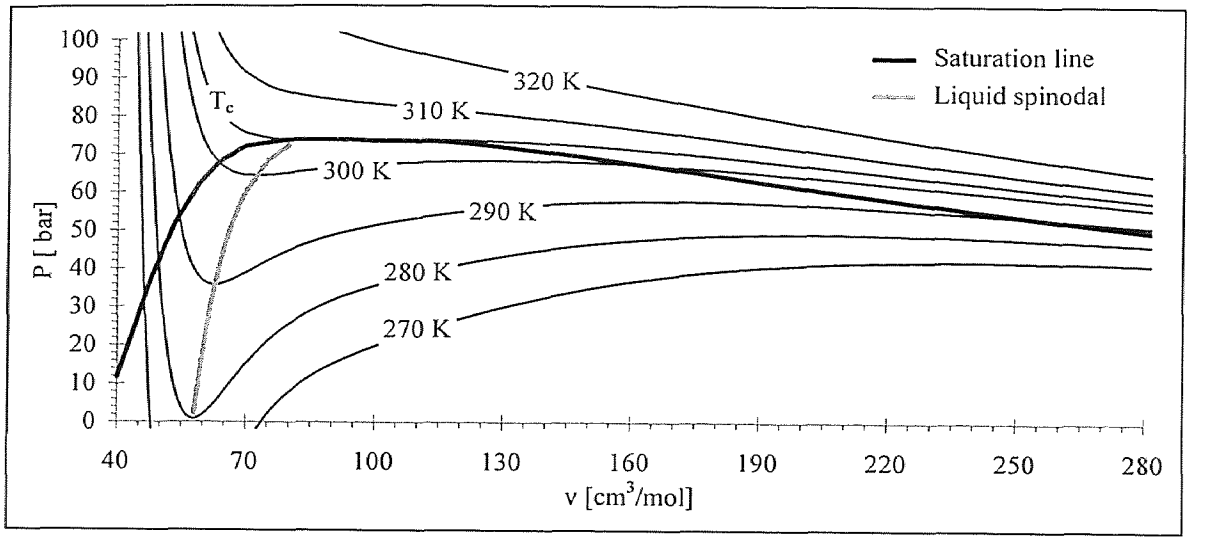

Figure 1.7 P-v Phase Diagram of CO_2

Nucleation theories indicate a very strong dependence of the formation rate of nuclei on the local temperature. Consequently, since the temperature decreases as soon as the flashing commences, nucleation occurs over a very short period. After the formation of the nuclei, the flashing process continues at the interface between the two phases, and it causes the freshly formed bubbles to grow. Bubble growth has been studied extensively in the past [25,48,70]. In applications similar to the current one, it is common to assume thermally controlled bubble growth [21,28,47,63].

Simultaneous to the nucleation and bubble growth phenomena, a two-phase outflow starts to develop under influence of the pressure gradient between the inside and the outside of the inflator. In the early stages, when the vapor fraction is low and most of the fluid is still in the liquid phase, the flow rate is limited by inertia. Due to the difference in density between the liquid and the vapor phase, the latter accelerates faster and a relative velocity between both phases develops. Likewise, the difference in thermal conductivity leads to a difference in temperature. As a result, the flow inside the inflator will be non-equilibrium, both from thermal and from mechanical point of view. The relative velocity between both phases generates hydrodynamic instabilities on the surface of the growing bubbles [47,63]. The amplitude of these disturbances increases with the relative velocity. When the instabilities exceed the consolidating effect of the surface tension, the bubble will break up in smaller bubbles. Note that this process is similar to the atomization of a liquid jet in a gaseous atmosphere, which is considered during the discussion of the phenomena in the receiving tank. The break-up of the bubbles leads to a drastic increase in interfacial area and, therefore, to enhanced mass transfer and evaporation.

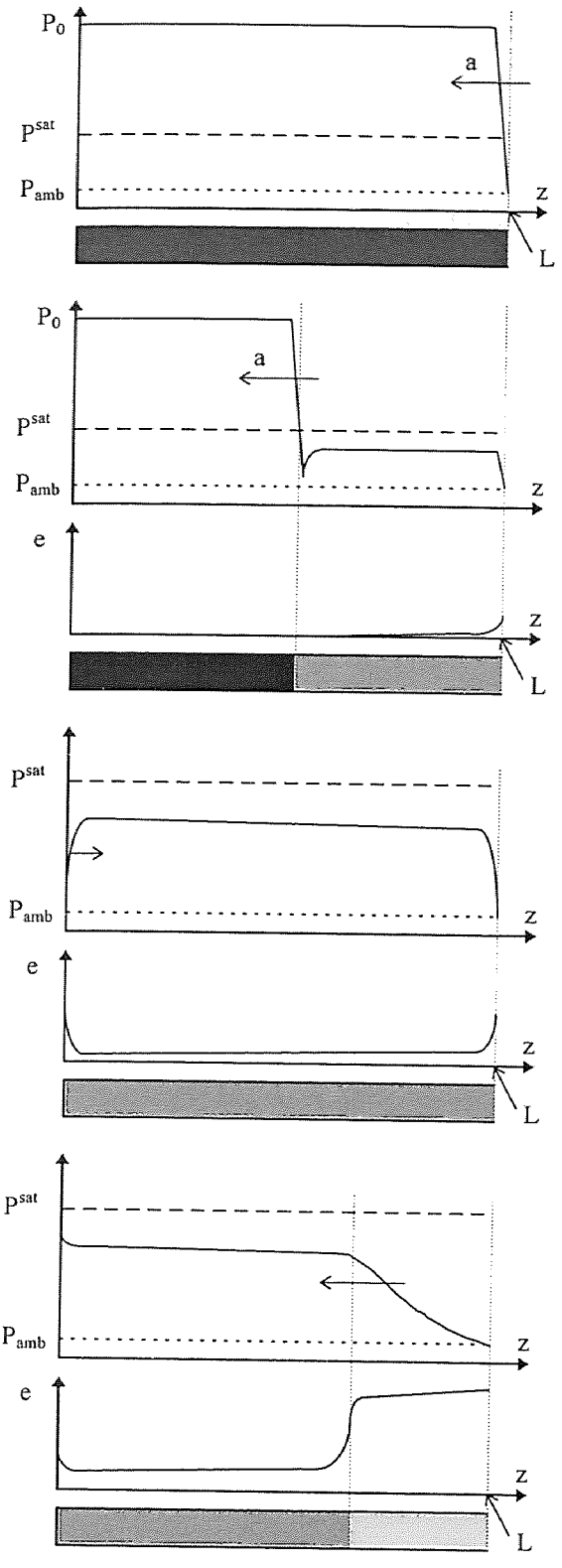

At $t = 0$, the burst disk ruptures instantaneously and the *forerunner* starts to propagate towards the closed end of the inflator at the local speed of sound (a). No vapor has been formed in the inflator and the void fraction is uniformly zero. All liquid is in the subcooled initial state (P_0, T_0).
(P^{sat} : vapor pressure corresponding to T_0)

■ : subcooled liquid

At $0 < t < t_f$ ($t_f = L/a$), the forerunner has propagated through part of the inflator. The liquid upstream of the forerunner is still in the initial state. The liquid downstream enters the metastable state, after which nucleation and evaporation brings it closer towards equilibrium.
The void fraction is very low due to insufficient time for significant bubble growth.
Near the open end of the inflator, the outflow commences and the bubbles break up, which leads to an enhanced evaporation.

▒ : two-phase mixture (e «)

At $t \approx t_f$, the forerunner has traveled through the entire inflator and is reflected from the closed end. This creates a local pressure drop and an increase in nucleation and evaporation. In return, this causes the forerunner to die out shortly afterwards.
Nucleation has occurred over the entire length and bubble growth has progressed further near the open end of the inflator. Enhanced evaporation at both ends causes a slight increase in the void fraction.

At $t \gg t_f$, the *evaporation wave* has propagated through part of the inflator, at much lower speed than the forerunner. The evaporation wave causes bubble break-up, which leads to a drastic increase in interfacial area and hence, in evaporation. In turn, this leads to a two-phase mixture of relatively high void fraction and low temperature downstream of the evaporation wave. Because of the low temperature, the flashing rate is limited and the pressure drop due to outflow can not be compensated. Hence, a gradual decrease in pressure behind the flashing front is observed.

▒ : two-phase mixture (e »)

Figure 1.8 Propagation of the Forerunner and the Evaporation Wave in the Inflator

Since the outflow, and thus the relative velocity, develops first at the open end of the vessel, the coupling between the fluid flow and the flashing process generates a second wave process. The *evaporation wave* (also *flashing front* or *interfacial wave*) similar to the forerunner, travels from the open end towards the closed end of the vessel, but at a much lower speed. It progresses through the vessel with a marked increase in bubble number concentration and void fraction [47,63,75,86]. After the evaporation wave reaches the closed end of the inflator vessel, a gradual pressure decrease occurs until the end of the inflation sequence. Figure 1.8 illustrates the existence of the two wave phenomena in the inflator.

For the evaporation inside the inflator, all latent heat of evaporation is taken from the initial energy of the liquid. As a result, the liquid cools down during the inflation sequence. In the later stages of the process, part of the liquid in the vessel and/or the tank will reach the triple point and solidify. This part of the fluid is considered lost for the inflation.

During the evacuation of the vessel, the void fraction changes from zero to a value close to unity. Correspondingly, the two-phase flow pattern in the vessel evolves from single phase liquid flow to bubbly flow, slug flow, annular flow, mist-annular flow and finally, dispersed droplet flow. As is common practice, the transition between flow patterns is assumed to occur at empirically determined values of the void fraction. The constitutive equations of the model, which describe the interfacial transport processes, are dependent on the flow pattern. In cases with drastic changes in the void fraction, it is necessary to adapt the constitutive equations during the simulation.

As stated before, heat transfer from the vessel walls during the process is neglected. This is justified, based on the very short time of the inflation sequence.

1.3.3.2 Phenomena in the Release Mechanism and the Nozzle: During the inflation sequence, two important phenomena occur inside the nozzle with the built-in release mechanism.

In the initial stages of the process, the mass flow rate of the two-phase mixture through the nozzle is limited by inertial effects of the fluid and by the finite opening time of the mechanism. As the evacuation progresses, the two-phase flow through the nozzle accelerates and the exit velocity increases. The acceleration of the flow is enhanced by the evaporation process, since this reduces the density and therefore the inertia. At some point, shortly after the appearance of the evaporation wave, the mass flow rate reaches its maximum or *critical* value and the flow becomes choked. For single-phase gas flows, the phenomenon of choking is well-understood. It is generally accepted that for a one-dimensional, isentropic gas flow, the maximum flow rate is limited to the local sound speed through the smallest cross section in the flow path. Multi-phase critical flow is nearly always considerably more complicated because of thermal and mechanical non-equilibrium between the phases (i.e. difference in temperature, pressure and velocity). Approaches for the simulation of critical two-phase flow range from mainly theoretical [23,31,38], to semi-empirical [28,69] and highly-empirical [43,51].

The second phenomenon that needs to be addressed in this section, is actually initiated in the nozzle and continues in the receiving tank. It concerns the dispersion of the liquid phase in the two-phase jet from the nozzle. Both the shape and the dimensions

of the nozzle determine the behavior of the two-phase spray inside the tank to a large extent. A considerable number of correlations, for a variety of nozzle types and shapes, has been established [56]. A large part of the work in the past was driven by the strong interest of car manufacturers for evaporating sprays [33,80,84]. For the current model, the two-phase flow is assumed to have an annular structure - i.e. a liquid core surrounded by a vapor layer - and a correlation for a flashing injector is used [84].

1.3.3.3 Phenomena in the Receiving Tank (or Air Bag): In this section, it is assumed that the inflator discharges in a receiving tank which was filled with nitrogen gas prior to the experiment.

The CO_2 vapor in the two-phase jet from the nozzle will expand into the tank and mix with the nitrogen that is already present. The state of the CO_2 vapor is located close to the vapor saturation curve and its behavior deviates from that of an ideal gas. In the current model, the real gas effects during the expansion, such as for example the Joule-Thomson effect, and the mixing with nitrogen is modeled by means of a cubic equation of state and a simple mixing rule [65].

As discussed in the previous section, the dispersion of the liquid phase is initiated in the nozzle and continues in the receiving tank. Elaborate theories exist for the break-up of low and moderate speed, single-phase, subcooled liquid jets [6,56]. A thorough qualitative understanding of the dispersion of liquid jets at higher velocities has not yet been established and intensive research is ongoing. The dispersion of subcooled liquid jets will be referred to as *classical* atomization and relies on hydrodynamic forces. A large number of correlations is available to predict the droplet size distribution and the

shape of the resulting spray [6,56]. When the liquid is not subcooled (i.e. its temperature is such that the corresponding vapor pressure equals or exceeds the pressure of the medium that is surrounding the jet), flash evaporation might enhance the dispersion. This process is called *flash atomization* and has received limited attention in the past [64,71,76]. In contrast to classical atomization, the main driving force for the dispersion of the liquid in this case is the evaporation process. Flash atomization leads to sprays with a large spray angle, so called *feathered* sprays [62]. In this work, the shape of the two-phase jet from the nozzle was studied by means of high-speed cinematography.

The dispersion process transforms the liquid phase of the jet into individual droplets with a certain size distribution. Depending on the internal temperature and the surrounding conditions, these droplets will evaporate and generate additional CO_2 vapor. For the current application, it is of interest that the evaporation proceeds at maximum speed. Since the evaporation rate depends to a large extent on the size distribution of the droplets, accurate modeling of the dispersion process is necessary. The evaporation of sprays has been studied in the past, often with the application of fuel injectors in mind, but still remains an active field of research [6,33,56,80]. During the evaporation of a droplet, the latent heat will be supplied by the internal energy of the liquid or the surroundings, or a combination of both. Two scenarios must be considered. On the one hand, if the latent heat is mainly compensated for by the internal energy of the liquid, the droplet will cool down considerably during the evaporation. This is the case for the evaporation of highly volatile droplets [56]. When the temperature of the liquid reaches the triple point, the droplet will solidify and is lost for the remainder of the inflation sequence. On the other hand, if sufficient energy is supplied by the surroundings, the

droplet will evaporate completely. This is the case for the evaporation of droplets with low volatility [56].

Especially during the first stages of the experiment, the pressure increase in the tank is the result of the generation of CO_2 vapor. During this process, the contents of the tank cools down considerably and a significant temperature gradient between the walls and the CO_2-N_2 mixture is established. The resulting heat transfer from the walls to the gas mixture is expected to interfere with the measurements, since it also leads to an increase of the pressure in the tank. Bearing the limited time of the inflation sequence in mind (typically about 30 ms), heat transfer is neglected during the actual evacuation of the inflator.

The experimental observations indicated that the temperature in the tank, immediately after the end of the inflation sequence, was considerably higher than the saturation temperature corresponding to the local pressure. Therefore, general vapor condensation cannot have occurred during the expansion.

In addition to the effects described above, other phenomena occur in the tank. All of them are assumed to be of secondary importance and will be neglected. During the experiment, the two-phase jet impinges on the walls of the receiving tank. This produces additional break-up of the droplets and establishes heat transfer between the liquid and the wall. Studies on the interaction of fuel jets with the sides of the combustion chamber have been performed [6]. Because of the dense character of the spray, secondary droplet interaction occurs. Depending on the relative velocity, this will lead to coagulation or secondary break-up [6].

1.4 Present Work

A detailed study of the SLG-Inflator is presented in this work. The novel inflator is based on the rapid phase transformation of liquefied CO_2, and offers considerable advantages over the existing technology.

The performance of the inflator was primarily studied by means of tank tests, in which the pressure and temperature were measured as a function of time. In addition, high-speed cinematographic recordings were made to investigate the dispersion characteristics of the two-phase jet from the inflator during the inflation sequence.

Theoretical models have been developed to simulate the phenomena inside the SLG-Inflator and the receiving tank. Because of the complex nature of the process, a large number of phenomena is involved. These phenomena include, among others: vapor nucleation in a metastable liquid; bubble growth by flashing; bubble break-up; two-phase, non-equilibrium, critical outflow; dispersion of a two-phase jet and spray evaporation.

Chapter 2 contains a description of the components of the main experimental set-up and procedures. In addition, a brief discussion of the results of a typical main experiment is included. At the end of the 2nd chapter, the experimental set-up and procedure for the high-speed cinematography study is described.

Prior to the experimental study of the SLG-Inflator, a series of experiments was conducted in which the inflator was filled with pressurized N_2 instead of liquefied CO_2. By comparing the results with the output of a simple theoretical model, the performance of the experimental set-up was assessed. Both the results of the experiments and the description of the theoretical model are presented in Chapter 3.

The first part of Chapter 4 contains a discussion of all results pertaining to the experimental study of the SLG-Inflator. A comprehensive qualitative model of the system is presented in the second part of this chapter. The tank tests are considered first and illustrate the influence of design parameters such as the size of the inflator, the storage pressure, the initial inflator temperature and the area of the critical flow section. In addition, experiments were conducted with varying initial conditions in the receiving tank and with small quantities of organic liquids added to the CO_2. The results of the high-speed cinematography studies are discussed next. After the presentation of the qualitative model, the latter is used to explain the main experimental observations described in the first part of Chapter 4. At the end of the chapter, a qualitative explanation for the effect of the organic liquids on the performance of the system is included.

All modeling aspects are discussed in Chapter 5. First, a general model for the behavior of CO_2 is presented. This is followed by a discussion of the calculation of the generated vapor mass during the inflation sequence. The main model, which consists of two parts, corresponding to the inflator and the tank, is given next. The SLG-Inflator Model constitutes a comprehensive two-fluid model, based on the conservation laws for the liquid and the vapor phase. The main parts of the Tank Model are an empirical description of the dispersion of the two-phase jet from the nozzle and a simplified droplet evaporation model.

Chapter 6 contains the conclusions of this research and a list of the main contributions is included. Also, suggestions for further improvement of the inflator's performance and future work are formulated.

CHAPTER 2

EXPERIMENTAL SET-UP AND PROCEDURES

2.1 Introduction

Two kinds of experiments were performed to study the SLG-Inflator and to assess the effect of the various design parameters on its performance. The principal experiments, referred to as *main* experiments in this text, correspond to tank tests. These experiments are commonly used for inflator development in industry. In these experiments, the device is discharged into a tank of known size and the resulting pressure and temperature change is used to evaluate the inflator performance. Based on these pressure and temperature curves, the performance of the inflator for the actual inflation of an air bag can be predicted to great extent. The experimental set-up and the procedure for the main experiments are described first. A detailed discussion of the results of a typical main experiment are presented next. The initial conditions for this experiment are considered nominal and the results are used as a reference for all other main experiments.

The second kind of experiments concerns a high-speed cinematography study of the system. Both the experimental set-up and procedure are described in the second part of this chapter.

During this research, attempts were made to determine the size distribution of the evaporating CO_2 droplets in the two-phase spray from the inflator. A Malvern Mastersizer, based on small angle light scattering, was used for this purpose. Due to the highly transient character of the spray, its variable orientation and size, and the large

temperature gradients between the center of the spray and the surroundings, no conclusive data could be obtained.

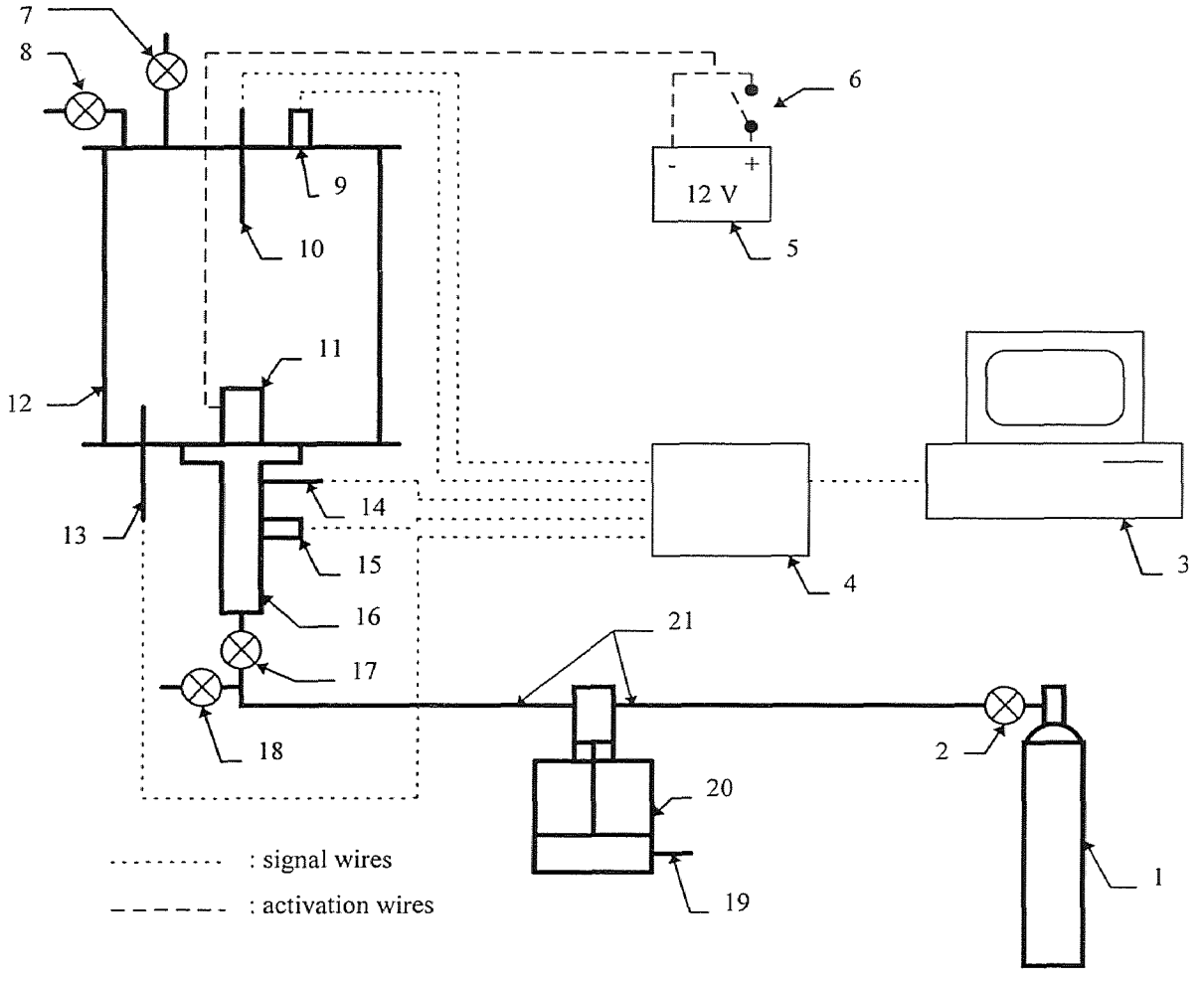

1	CO_2 Cylinder	8	Tank Purging Valve	15	Vessel Pressure Transducer
2	CO_2 Supply Valve	9	Tank Pressure Transducer	16	Inflator Vessel
3	Personal Computer	10	Tank Thermocouple 1	17	Vessel Filling Valve
4	Data Acquisition Box	11	Nozzle + Release Mechanism	18	Vessel Venting Valve
5	12V Battery	12	Receiving Tank	19	Air Supply
6	Activation Switch	13	Tank Thermocouple 2	20	Booster Pump
7	Tank Venting Valve	14	Vessel Thermocouple	21	CO_2 Filling Hose

Figure 2.1 Schematic Layout of the Main Experimental Set-up

2.2 Main Experiments

Figure 2.1 contains a schematic layout of the main experimental set-up. All important components of the set-up are discussed below. The main experiments in this work are similar to *Blowdown Experiments*, as described in the literature [11,18,37,40,42,52]. However, these blowdown experiments are almost exclusively conducted to develop models which predict the behavior of a system in case of an emergency, for example the failure of a chemical reactor or a pipe in the cooling circuit of a nuclear power plant (so called 'LOCA': Loss of Coolant Accidents). In contrast, in the case of the SLG-Inflator, the blowdown process is the desired effect and concerns the normal operation mode rather than an emergency.

2.2.1 Inflator Vessel

Two stainless steel vessels were used during the experiments. Both of the vessels are cylindrical in shape and have a collar fitted to them, such that they can be mounted on the bottom plate of the receiving tank by means of four clamps. The collar contains two O-rings to make a gas-tight seal between the tank and the inflator. When mounted on the bottom plate of the tank, the vessel itself remains outside, while the nozzle and the release mechanism are inside.

The first vessel, shown in Figure 2.2 and referred to as vessel 'A', is a two-ended reactor vessel [(1)]. A hole in the side wall (hole '*3*' in Figure 2.2) was manufactured to allow the connection of a pressure or temperature sensor. The release mechanism is mounted on the vessel in hole '*2*'. The other side, hole '*1*', is connected to the filling

[(1)] Manufactured by Autoclave Engineers Inc., Erie, Pennsylvania 16512, USA

assembly. Part of the original closure design is used, including a hollow conical plug which sits on the tapered part of hole *'2'* in Figure 2.2. The inside diameter of the plug is 7.96 mm.

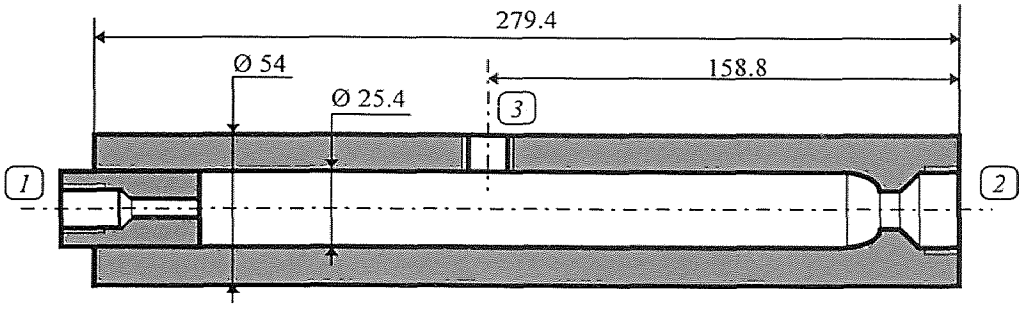

Figure 2.2 Cross Section of Inflator Vessel A [dimensions in mm]

The internal volume of the reactor was measured by filling it with water and recording the weight increase. The result was 113 ± 1 ml, which corresponds well to the 103 ml nominal capacity, as specified by the manufacturer.

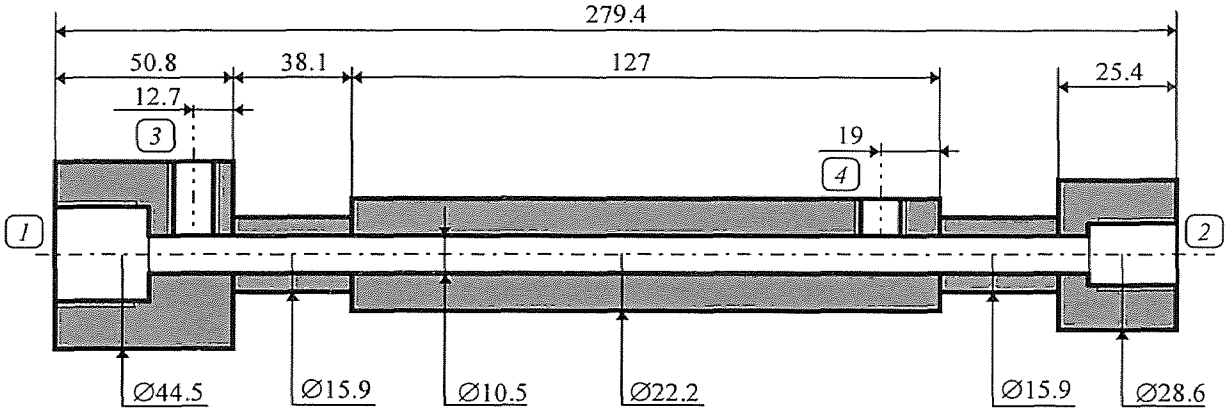

Figure 2.3 Cross Section of Inflator Vessel B [dimensions in mm]

The second vessel, referred to as vessel 'B', was manufactured by Breed Technologies Inc., and consists of pieces of stainless steel pipe which are welded

together. Figure 2.3 is a cross sectional view of this vessel. One end of the vessel - hole '*2*' - is connected to the release mechanism and the other end - hole '*1*' - to the filling assembly. Hole '*4*' in the side wall is used to mount a thermocouple. The other hole in the side wall - hole '*3*' - is used to connect a pressure transducer. Again, the vessel volume was measured by filling it with water and recording the weight increase. The result was 26.0 ± 0.5 ml. For safety reasons, before the experiments started, the vessel was tested by static water pressure up to 15,000 psig at room temperature. Most of the experiments were conducted with this vessel.

2.2.2 Release Mechanism and Nozzle

The release mechanism consists of a burst disk that can be ruptured on command by means of an actuator. The entire mechanism is housed inside the nozzle, which is mounted on the end of the inflator. A different nozzle and release mechanism was used for each inflator vessel. All parts were made of stainless steel.

2.2.2.1 Release Mechanism: Figure 2.4 (a&b) shows the principle of both release mechanisms. The dotted lines near the bottom mark the contours of the inflator vessel to which the nozzle is connected.

Both mechanisms are driven by a piston actuator[(2)]. This cylindrical device (33 mm long and 8 mm in diameter), is activated by applying 12 V from the battery through the activation wires.

[(2)] Manufactured by ICI Explosives, Aerospace and Automotive Business, Nobel's Explosives Co. Ltd., Stevenson Scotland, UK. Part # : Metron DR 2000 Series : DR2006/C1

The electrical signal initiates the explosion of a small pyrotechnic charge at one end of the actuator. The energy of this reaction is used to push a 14 mm long axial rod through the housing and out of the other end of the actuator. The average force with which the rod is pushed from the actuator is about 2300 N.

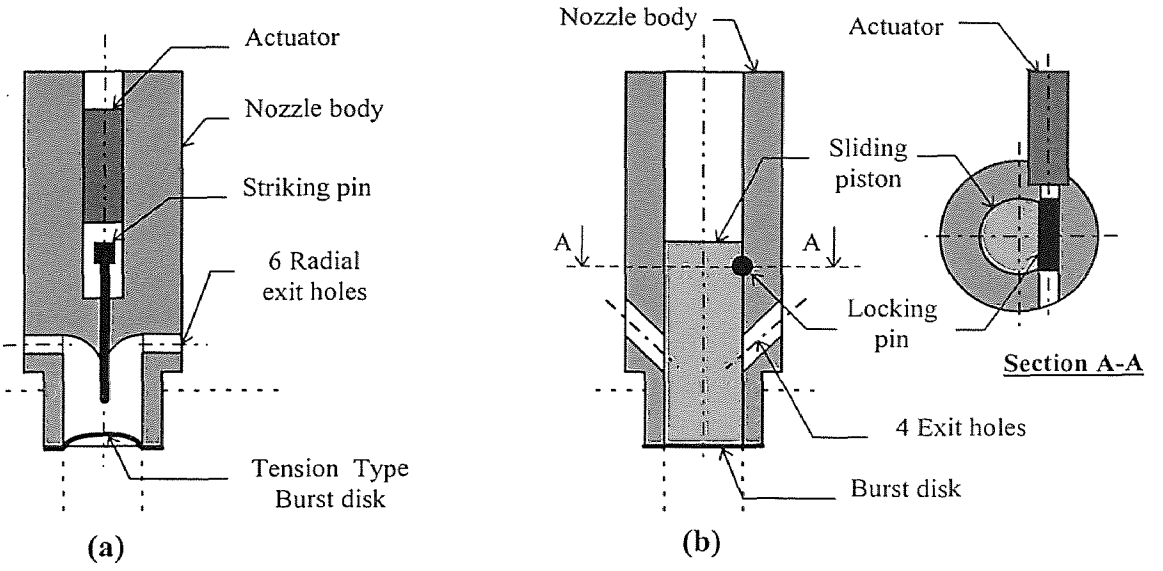

Figure 2.4 Nozzles with Built-in Release Mechanisms

In the first mechanism, Figure 2.4(a), the actuator is mounted such that the actuator rod hits the striking pin and pushes it through the burst disk, which causes it to fail. The rating of the burst disk is critical in this design. On the one hand, it should be strong enough to withstand the stress that is generated by filling the inflator with pressurized liquid. On the other hand, it was observed that burst disks with a rating considerably higher than the storage pressure, do not fail catastrophically when punctured by the striking pin. Instead, only part of the disk tends to be destroyed or only a central hole is made. Therefore, in order to perform the experiments at different initial pressures,

a series of disks with varying rating was used[3]. The usage of a rated burst disk limits the flexibility of the release mechanism. The opening time of the first mechanism is determined by the rupturing of the burst disc and is expected to be negligible.

The actuator in the second mechanism, Figure 2.4(b), is identical to the one used in the first mechanism. Although the second mechanism is slightly more critical in manufacturing precision, it avoids the usage of rated disks and is therefore considerably cheaper and more flexible. Brass shim - thickness 0.0254 mm - is used as a burst disk and is supported by the sliding piston in the inactivated state. The piston is held in place by the tangential locking pin. Upon activation, the actuator rod pushes the locking pin through the tangential channel, allowing the sliding piston to move freely along the axis of the nozzle body. At that point, the shim stock is no longer supported and it is ruptured by the pressure in the vessel. Finally, the piston is pushed upwards and the exit holes of the nozzle are cleared. In practice, additional components are needed to slow down the sliding piston as it reaches the top of the nozzle body and to prevent the locking pin from shooting out sideways. A simplified dynamic analysis of the mechanism was performed. The only forces acting on the sliding piston are assumed to be the inflator pressure, which is taken constant and equal to the storage level, and gravity. Initially, the piston is stationary and positioned such that it supports the burst disk. The calculation of the accelerated motion of the piston yields the time that it takes to reach the lower and the upper edge of the exit holes in the central channel in the nozzle. The results for inflator pressures ranging from 50 - 2000 psig are shown in Figure 2.5. For inflator pressures exceeding 1000 psig, the exit holes are cleared completely in 2 ms or less. The distance

[3] Manufactured by Oklahoma Safety Equipment Co., Broken Arrow, OK, USA, rating : 830 - 1550 psig.

between the curves represents the time for which the nozzle is only partially opened (i.e. the piston is located somewhere between the lower and the upper edge of the exit holes).

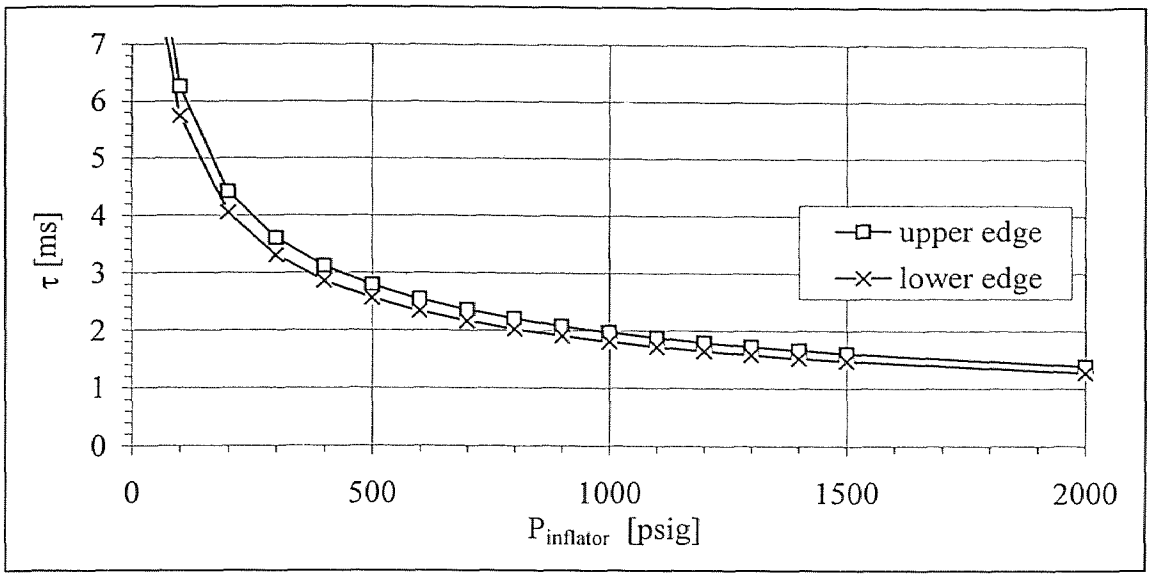

Figure 2.5 Characteristic Times of the Second Release Mechanism

2.2.2.2 Nozzle: The nozzle of Figure 2.4(a) was used in combination with inflator vessel A (Figure 2.2). After rupturing the disk, the fluid flows through the central channel of the nozzle and through six, equally spaced, radial exit holes into the receiving tank. The diameter of the axial channel is 12.7 mm. Each exit hole is 4.8 mm in diameter. Both the cross section of the central channel and the total area of the six holes combined, is larger than the inner diameter of the conical plug in the closure mechanism of the inflator vessel. Therefore, the plug will limit the evacuation rate of the vessel. The radial orientation of the exit holes assures that there is no thrust force on the vessel during the inflation sequence.

The second nozzle, Figure 2.4(b), was used in combination with inflator vessel B (Figure 2.3). Once the sliding piston of the mechanism clears the exit holes, the fluid flows through the central channel in the nozzle and through the four holes into the receiving tank. The diameter of the central channel is 11.2 mm, which is slightly larger than the inner diameter of the inflator vessel (10.5 mm). The four exit holes are at a 45° angle with the nozzle axis and are each 6.35 mm in diameter. Putting the holes at an angle instead of radially facilitates the outflow of the fluid. At the same time, it introduces a thrust force on the device during the inflation sequence. This force is absorbed by the four clamps on the bottom plate of the receiving tank.

Table 2.1 summarizes the most relevant information about the two inflator vessels and their corresponding nozzles and release mechanisms.

Table 2.1 Overview of Inflator and Nozzle Characteristics

	Vessel A	Vessel B
Overall Length [mm]	279.4	279.4
Outside Diameter [mm]	54.0	44.5 ↔ 15.9
Inside Diameter [mm]	25.4	10.5
Volume [ml]	113.0	26.0
Inner Surface [mm^2]	23300(*)	9400(*)
Smallest Area in Flow Path [mm^2]	49.8	86.6
Pressure Measurement	yes	yes
Temperature Measurement	no	yes
Nozzle Arrangement	Figure 2.4(a)	Figure 2.4(b)
Type of Burst Disk	Rated	Brass Shim
# Exit Holes	6	4
Exit Hole Diameter [mm]	4.8	6.4
Combined Area of Exit Holes [mm^2]	108.6	128.7
Exit Hole Direction	Radial	45°

(*) Estimated on the basis of simplified internal dimensions.

2.2.3 Receiving Tank

The receiving tank consists of a Plexiglas tube, pressed between two circular, chromated, steel plates by means of four tie rods. O-rings between the plates and the tube end guarantee a gas-tight seal. Figure 2.6 contains a cross sectional drawing of the receiving tank.

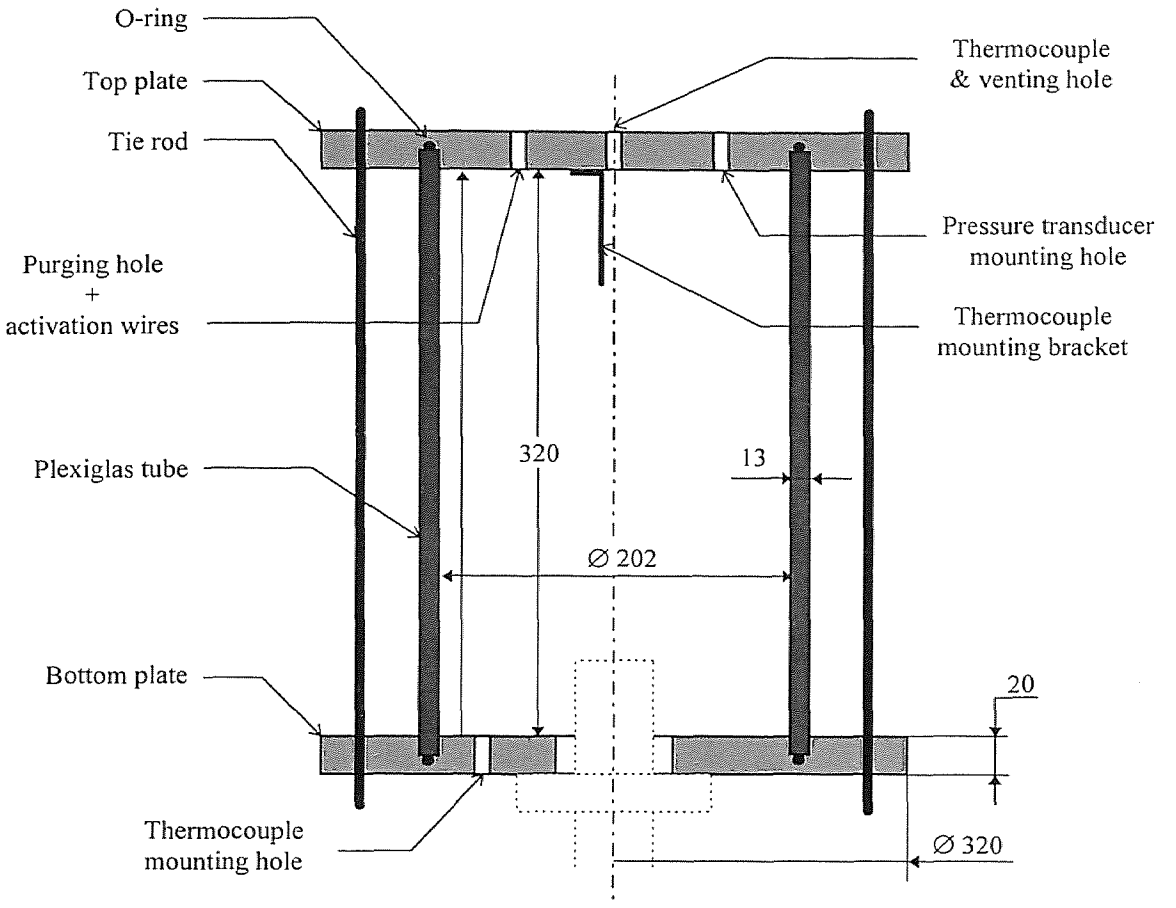

Figure 2.6 Cross Section of the Receiving Tank [dimensions in mm]

The dotted lines at the bottom of Figure 2.6 mark the contours of the inflator vessel when it is mounted on the bottom plate. The volume of the tank was measured by filling it with water and measuring the weight increase. The result was 9.72 ± 0.09 liter. A finite

element analysis was performed on the receiving tank to investigate the stresses in the Plexiglas tube. For the analysis, the maximum pressure inside the tank was taken to be 10 bar. The simulation indicated that this load generates a maximum stress of 16 N/mm^2 at the point where the tube end meets the steel plates. Since this is less than a quarter of the maximum allowable stress - specified by the manufacturer as 66.2 N/mm^2 -, the design was considered to be safe.

2.2.4 Pressure Transducers

Three different strain-gage pressure transducers were used during the main experiments. Table 2.2 summarizes the relevant properties of each sensor. The first two transducers in Table 2.2 were used to measure the inflator pressure. The second one was used only in experiments where the initial inflator pressure exceeded the range of the first transducer.

Table 2.2 Pressure Transducer Specifications

Manufacturer	Type / Model	Range [psig]	Response time [ms]	Output
Omega	PX213-3KG5V	0 - 3000	1 ms	0.5-5.5 V
Barksdale	403-09-0	0 - 10000	> 1 ms (*)	0.5-5.5 V
Data Instruments	XPRO	0 - 100	1 ms	4-20 mA

(*) Observed during simultaneous measurement of the vessel pressure with both the first and the second sensor connected to the inflator.

Because of the larger response time, only static pressure measurements were performed with the second sensor (i.e. measuring the initial inflator pressure). The last transducer in Table 2.2 was used to record the pressure evolution inside the tank. All transducers measure relative pressures.

2.2.5 Thermocouples

Two different kinds of thermocouples were used in the set-up. The thermocouples in the receiving tank, part 10 & 13 in Figure 2.1, are described first. Both are unsheathed, fine gage, E-type thermocouples with a beaded junction and a wire diameter of 0.0005 inch (12.7 μm)[4]. The miniature dimensions of the thermocouple guarantee a fast response. Measurements, provided by the manufacturer [7], indicate a response time[5] of the thermocouples of 4 ms when submerged in air flowing at 20 m/s. Especially in the first stage of the inflation sequence, a rapid response of the sensors is required to accurately record the fast changes in the system. Since the turbulence in the receiving tank is maximal during the first stage, it is estimated that the mixing velocity exceeds 20 m/s and a response time of less than 1 ms is anticipated. In the later stages of the experiment, when the tank gases are fairly stagnant, a larger response time is expected. Since the temperature variations in the tank will be smaller and slower than in the initial stage, this will not pose a problem. The main drawback of this kind of thermocouple is obviously its low mechanical strength. Not only does this complicate the handling procedure, but it also restricts its position in the set-up to regions away from the direct path of the two-phase jet.

The thermocouple inside the inflator - part 14 in Figure 2.1 - is an E-type, pencil probe, eroding thermocouple[6]. Its junction is made by smearing small particles from one metal to another by means of an emery cloth.

---

[4] Purchased from Omega Engineering Inc., Stamford, CT, USA. Part # : CHCO-0005.

[5] The *response time* of a thermocouple is defined as the time required to reach 63.2% of the final value after an instantaneous temperature change.

[6] Manufactured by NANMAC Corporation, Framingham, MA, USA. Part # E12-3-E-U-¼N-SP.

The result is a very thin junction, which, according to the manufacturer [8], allows response times of less than 10 μs. The junction is continually renewed by the eroding effect of the gas stream. While this thermocouple works well in fluid streams with a relatively large heat capacity - either a dense fluid or a high flow rate -, the body of the sensor tends to disturb the temperature field in flows with a small heat capacity. This causes the results of the dynamic inflator temperature measurements to become unreliable after the first few milliseconds.

All thermocouples are used in combination with a miniature full bridge compensator[7] and a signal conditioner[8], which amplifies the thermocouple output to 0-5 V at a sampling rate of 2500 Hz.

The output of the thermocouple circuit was experimentally correlated to temperature over the range of 0-50 °C. This was done by gradually heating an oil bath and recording both the output of the circuit and the temperature indicated by an accurate mercury thermometer. A linear expression was established : $T\ [°C] = a_0 + a_1.v$, with $a_0 = 0.3024919$, $a_1 = 328.30524$ and v the circuit output in volts. This expression was used in all experiments to correlate the measured output of the signal conditioner to the actual value of the temperature.

2.2.6 Data Acquisition System and Computer

The data acquisition box, with four input channels, samples and digitizes the output signals from the sensors before sending the information to the computer.

---

[7] Manufactured by NANMAC Corporation, Framingham, MA, USA. Part # F11-12.
[8] Purchased from Omega Engineering Inc., Stamford, CT, USA. Part # :OM5-WMV-50B-C.

The latter contains software that was developed by Breed Technologies Inc. The program allows the specification of the sampling rate, the storage of the data in a text file and the real time display of all sensor outputs. Most of the experiments were performed with a sampling rate of 1000 Hz. Higher sampling frequencies are not useful since the response time of the sensors is about 1 ms.

2.2.7 Gas Booster Compressor

When CO_2 is ordered from a manufacturer, it is delivered in cylinders at a pressure of about 830 psig. The required inflator pressure in the experimental set-up, typically 2000 psig, was obtained by means of a booster pump[9]. This is a purely mechanical device which consists of a large area, reciprocating, air driven piston, directly coupled by a connecting rod to a small area gas piston which operates in a high pressure gas barrel section. There is no risk of hydrocarbon contamination of the produced gases or liquids as the pistons run without lubrication. Gases such as propane, CO_2, nitrous oxide and others can be pumped either as a gas or a liquid. The pump has a piston area ratio of 62:1 and a maximum outlet pressure of 9000 psig.

2.2.8 Gases

The CO_2 that was used in the experiments was of the quality 'Bone Dry'. In the majority of the cases, nitrogen was used to purge the receiving tank prior to the experiment. The nitrogen that was used was of pre-purified quality with a water content of less than 3 ppm.

---

[9] Manufactured by Haskel International Inc., Burbank, CA, USA. Model AG-62.

2.3 Procedure of Main Experiments

A brief description of the standard experimental procedure is presented in this section. In addition, information is provided about the experiments in which the procedure differed considerably from the standard procedure. These include experiments at low initial tank temperature, high initial inflator temperature and cases where an organic liquid was added to the system.

2.3.1 Standard Experimental Procedure

The following steps were taken during each of the main experiments:

1. Record ambient pressure from a mercury barometer.
2. Power up the data acquisition box and the computer and allow 30 minutes for the sensors to heat up. At this point, two of the data acquisition channels are connected to the pressure transducers, while the other two are connected to the vessel thermocouple and the tank thermocouple in the bottom plate.
3. Assemble the release mechanism and insert a new actuator.
4. Zero all data channels after making sure that the pressure transducers are exposed to ambient pressure and shorting the input of the thermocouple signal conditioners. This is equivalent to submerging the thermocouples in an ice bath, which corresponds to the reference temperature of the cold junction compensator.
5. Purge the inflator with CO_2, insert a burst disk and attach the nozzle to the vessel.
6. Use the booster pump to increase the pressure in the inflator. This has to be done in stages, such that time is allowed for the inflator to cool down after every compression.

7. Close the filling valve of the inflator, bleed off the CO_2 from the filling hose and disconnect the hose from the vessel.
8. Mount the inflator on the bottom plate of the receiving tank.
9. Connect the activation wires to the actuator and assemble the receiving tank.
10. Purge the receiving tank with nitrogen or another dry gas by opening the venting valve while the gas flows in through the purging valve. After purging, both valves are closed. This action removes the moisture from the tank and prevents it from condensating on the cold CO_2 spray.
11. Record the initial vessel temperature and connect the signal wire from the vessel thermocouple to the top tank thermocouple.
12. Initiate the data capturing sequence on the computer by entering a file name, the duration of the experiment and the sampling rate.
13. Close the switch in the activation wires to fire the actuator.
14. After the data capturing sequence has terminated, the system is left to equilibrate until the temperature in the receiving tank becomes uniform and is only slightly below ambient temperature. During this time, the pressure and the temperature in the tank are recorded repeatedly. This allows an accurate calculation of the initial amount of CO_2 that was contained in the inflator prior to activation.
15. Open the venting valve of the tank and the filling valve of the vessel to release the gases from the system.
16. Remove the vessel from the bottom plate.
17. Disassemble and clean all parts of the experimental set-up.

2.3.2 Procedure for Experiments at Low Initial Tank Temperature

Experiments at low initial tank temperature were conducted with both N_2 and CO_2 as purging gas. The case in which N_2 was used, is discussed first.

Cooling was obtained by placing the receiving tank, except for the tank pressure transducer, in a refrigerator at a controlled temperature. After allowing time for the equilibration of the temperature (at least 4 hours), the tank, wrapped in thermal insulation, was removed from the refrigerator. Subsequently, the vessel was mounted on the bottom plate and the tank was opened to connect the activation wires to the actuator. Then, the tank pressure transducer, also wrapped in thermal insulation, was mounted on the top plate of the tank. Further reduction of heat transfer was accomplished by separating the transducer and the cold tank wall by means of a short plastic tube. In a last step prior to the experiment, the tank was purged with cold N_2, which had been stored in the same refrigerator as the tank. Typically initial tank temperatures downto about -40 °C could be attained in this manner.

For experiments at lower initial tank temperature (below -50 °C), CO_2 was used as purging gas. The procedure was similar to the one above, but before the tank was closed, several pieces of dry ice were placed on the bottom plate inside the tank. Time was allowed for the sublimation of the dry ice and the excess CO_2 vapor was bled off through the purging valve of the tank. After complete sublimation of the dry ice, the purging valve was closed and the actuator was activated.

In all experiments, the inflator was connected to the cold tank for about two minutes before the activation of the release mechanism. This time proved sufficient for significant heat transfer between the inflator and the tank to occur. Hence, the inflator

temperature tended to drop below ambient conditions during the preparation of the experiment. To compensate for this cooling, electrical heater tape was wrapped around the inflator and the power was regulated such that the inflator temperature remained close to ambient. Because the inflator temperature is measured at only 1 location and because of the influence of the inflator wall temperature on the nucleation process [52], the heating of the inflator is a source of significant uncertainty.

2.3.3 Procedure for Experiments at High Initial Inflator Temperature

The standard experimental procedure for the main experiments was followed, except that the inflator was heated by means of electrical heater tape. To minimize internal temperature gradients, the heater tape was wrapped over the entire length of the part of the inflator that remains outside the tank during an experiment. In addition, the temperature was maintained at the required level for at least 15 minutes before activating the actuator. The power supply to the heater tape was controlled manually by means of a variable transformer and the inflator thermocouple was used to monitor the temperature.

2.3.4 Procedure for CO_2/Organic Liquid Experiments

The standard experimental set-up was used for all experiments. The organic liquids were added to the CO_2 in the following manner. After purging the inflator with CO_2 for at least 1 minute, the filling valve was closed and the inflator was placed in a vertical position with the mounting hole for the nozzle facing upwards. A plastic cap was placed over the nozzle hole to prevent the surrounding air from entering the inflator. Using a pipette, a specified amount of solvent was metered and injected in the vessel through the nozzle

hole (after removing the plastic cap). In order to minimize the evaporation of the organic liquid, care was taken to mount the nozzle assembly on the inflator immediately after the injection of the solvent. Subsequently, the booster pump was activated for several strokes to build up pressure in the filling hose. Only then, the filling valve was opened and the pressurization of the vessel was completed. This procedure was adapted to prevent the organic liquid from flowing into the filling hose. The remainder of the experimental procedure was identical to the standard procedure.

2.4 Reference Experiment

This section contains the results of a typical main experiment. The initial conditions that were used are considered nominal, and the corresponding results serve as a base of comparison for all other main experiments. Hence, this experiment is referred to as the *Reference Experiment*. The nominal initial value of the inflator pressure is the result of the study of the effect of the initial pressure on the performance of the system. This study is described in Chapter 4, along with the other experimental results and the qualitative model of the system.

Table 2.3 lists the initial conditions for the Reference Experiment, together with the typical amounts of fluid in each compartment. The initial amount of N_2 in the tank was calculated using the ideal gas law and the knowledge of the pressure, temperature and volume. The amount of CO_2 in the inflator was obtained by measurements of the equilibrium pressure and temperature in the system after the experiment. This procedure is described in §2.3.1.

Table 2.3 Nominal Initial Conditions

	Tank	Inflator B
Fluid	N_2	CO_2
Volume [dm^3]	9.72	0.026
P_0 [bar] (psig)	$1^{(*)}$ (14.7)	139 (2000)
T_0 [°C]	$22^{(*)}$	$22^{(*)}$
#moles [/]	0.40	0.55
mass [g]	11.2	24.1

$^{(*)}$ These values depend on the atmospheric conditions and are liable to change. An accurate measurement was made prior to each experiment.

The evolution of the tank pressure, the inflator pressure and the average tank temperature is shown in Figure 2.7(a-c). As stated before, the measured pressures are relative to ambient pressure. Typical for nearly all main experiments are the two distinctive stages in the tank pressure curve (Figure 2.7(a)). In the first stage, the tank pressure increases rapidly at a rate of about 0.2 psi/ms. The maximum pressure at the end of the first stage is 5.3 psig, which is reached at about 33 ms after the first drop in inflator pressure was detected. This maximum pressure corresponds to P_{peak} in the common tank tests. The results of the high-speed cinematography studies, which will be discussed in Chapter 4, indicate that the end of this first stage coincides with the end of the existence of the two-phase jet in the tank. The rapid increase in pressure in this stage is the result of the expansion of the vapor phase of the jet, in combination with the rapid evaporation of small and high-energy liquid droplets. The flat part of the curve during the first 3 ms is due to the finite opening time of the release mechanism and the finite response time of the pressure transducer.

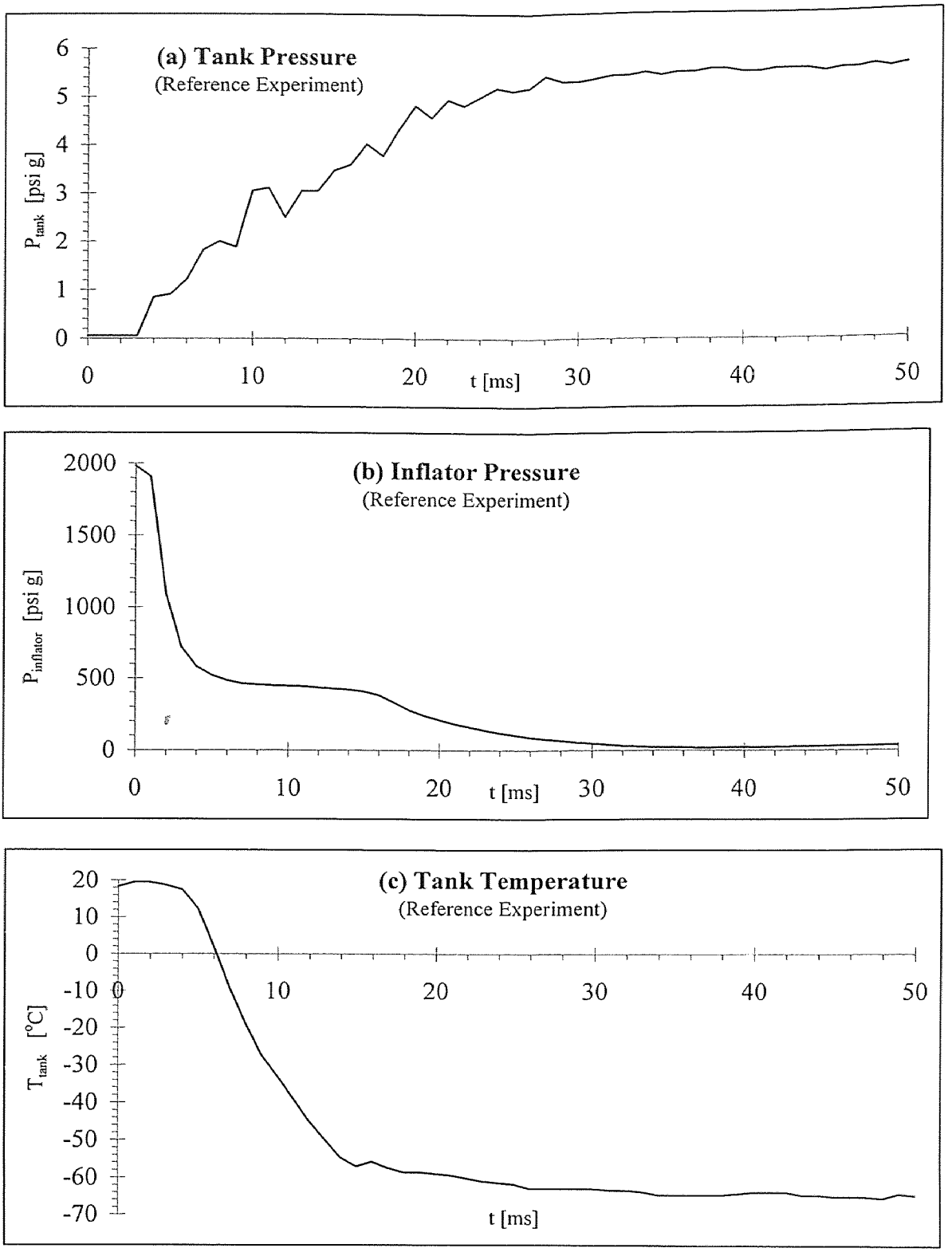

Figure 2.7 Measurements during the Reference Experiment

The increase in pressure in the second stage of the curve is considerably slower. Initially, the pressure rises at a rate of about 0.06 psi/ms, but after 100 ms this rate continually decreases and eventually reaches zero as the system attains equilibrium with the surroundings. The slower increase in pressure is the result of two phenomena. First, heat transfer from the tank walls starts to become important and heats up the gaseous mixture, which leads to an increase in pressure. Second, the same heat transfer causes the solidified droplets to sublimate. The latter generates more CO_2 vapor and also increases the pressure.

The inflator pressure curve is shown in Figure 2.7(b) and typically contains four characteristic stages. The first of these is the relatively slow pressure drop during the initial 2 ms. As shown in Figure 2.5, the duration of this stage corresponds to the time for the sliding piston of the release mechanism to reach to lower edge of the exit holes in the central nozzle channel (see Figure 2.4(b)). The additional volume inside the nozzle, which is created by the movement of the sliding piston, is about 10% of the total inflator volume. During the first 2 ms, the compressed liquid CO_2 expands isentropically into this additional volume. The second characteristic stage in the inflator curve starts at about 2 ms, and consists of a rapid decrease in pressure. During this stage, the forerunner propagates through the vessel at the local speed of sound and bounces back from the closed end. The finite opening time of the mechanism is expected to flatten the forerunner [63]. At the end of the second stage, about 5 ms into the inflation sequence, nucleation has occurred over the entire length of the inflator and the generated bubbles continue to grow by evaporation at the interfacial surface. The maximum depressurization rate is observed during the second stage of the curve and is about 55 bar/ms. The third stage of

the curve corresponds to the flat part extending from about 5 to 15 ms. In this time, the evaporation wave, which was initiated at the end of the second stage, propagates towards the closed end of the inflator. The last stage in the curve, a gradual decrease in pressure, starts when the evaporation wave passes the location of the pressure transducer. Assuming that the evaporation wave started to travel shortly after the steep pressure drop in the second stage of the curve, its average velocity can be calculated as 15-20 m/s. This corresponds well to the values listed in the literature [47,63]. The average depressurization rate during the experiment is about 4.5 bar/ms. Most of the other experimental studies were done at lower depressurization rates [11,18,37,40,42,52]. The end of the 4^{th} stage in the inflator curve coincides with the end of the first stage in the tank pressure curve and the end of the two-phase jet from the nozzle.

The result of the measurement of the average tank temperature is shown in Figure 2.7(c). It is obtained by averaging the signals from the top and bottom thermocouple in the receiving tank and is based on the assumption of good mixing of the gaseous components in the tank. Certainly during the early stages of the experiment ($t < 30 \ldots 40$ ms), the turbulence inside the tank is such that this assumption is justified. A straightforward manner to check this assumption consists of comparing the signals from the top and the bottom thermocouple during the inflation sequence. When good mixing takes place, both thermocouples should generate a similar signal. This procedure was performed for each experiment and in nearly all cases, both thermocouples generated very similar readings throughout the inflation sequence. To the best of the authors knowledge, this is the first time that the measurement of the average temperature in tank tests was performed with high accuracy. Other studies which include the results of tank tests

measure only tank pressure [24] or use an approximate tank temperature measurement [85]. Three distinctive stages in the temperature curve are observed. In the first one, lasting to about 5 ms, the temperature remains virtually constant. Up to that time, most of the phenomena take place inside the inflator and little flow from the nozzle has occurred. The second stage is characterized by a rapid drop of the temperature and lasts to about 33 ms. During this stage, the two-phase jet exits from the nozzle. The vapor component of this jet expands and mixes with the nitrogen. The liquid component is dispersed and evaporates partially. The interaction of the evaporating droplets with the tank gases depends on the initial conditions in both the inflator and the tank. Both the expansion and mixing of the vapor phase and the interaction of the tank gases with the evaporating droplets cause a temperature drop in the tank. The end of the second stage coincides with the end of the evacuation of the inflator. At the onset of the third stage in the temperature curve, at about 33 ms, a minimal temperature of -64 °C is reached. During the third stage, the temperature stays constant at its minimal value, until about 1 s after the start of the experiment. At the onset of the third stage, the conditions in the tank are relatively far from saturation conditions and the constant temperature is caused by the slow sublimation of the generated dry ice and the slow rate of heat transfer to the system.

By combining the tank pressure and the tank temperature curves, together with the knowledge of the initial amount of nitrogen and the dimensions of the tank, the evolution of the generated amount of CO_2 vapor can be calculated. It is assumed that the volume of the liquid and solid CO_2 in the tank is negligible. A detailed description of this calculation is included in Chapter 5. Basically, a mixture of real gases is considered and

modeled by means of the Peng-Robinson equation of state in combination with a van der Waals Mixing Rule. The result is shown in Figure 2.8.

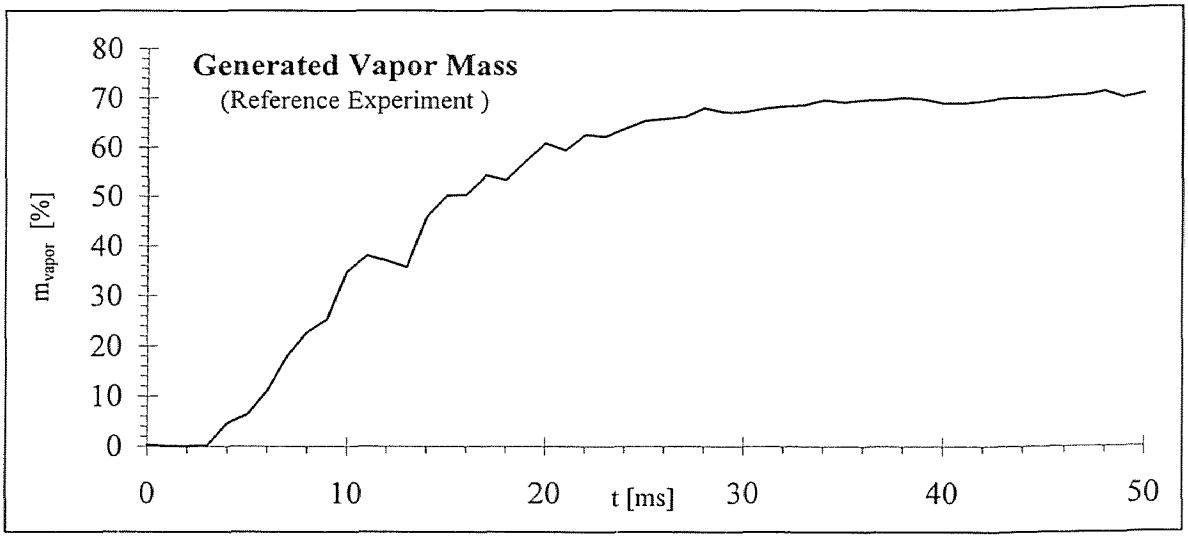

Figure 2.8 Generated Vapor Mass during the Reference Experiment

The generated CO_2 vapor mass is represented relative to the initial amount of CO_2 in the inflator. The mass curves are considered to be the most important output of the main experimental set-up. Similar to the tank pressure curve, two stages can be distinguished. In the first stage, lasting to about 33 ms, a rapid increase in generated vapor mass is observed. For the purpose of the inflation of an air bag, it is mainly this first stage that is of interest. About 68% of the initial inflator mass is transformed into vapor at the end of the inflation sequence. During the second stage, starting at about 33 ms, the generated vapor mass increases slowly, as the dry ice in the tank sublimates. Typically, the curve does not reach 100% transformation into vapor until after 1s. However, at that stage in the experiment, the gases in the tank are stagnant and it is likely that thermal stratification has occurred. As a result, the assumption of good mixing fails and the measured

temperature does no longer represent the average tank temperature. Hence, the generated mass curve contains a high degree of uncertainty in this region. An indication for the thermal stratification is the relatively large difference between the signals from both tank thermocouples which is typically observed at this stage in the experiment.

Using the value of the generated vapor mass, the partial pressure of CO_2 in the tank was determined. Based on this partial pressure, the corresponding saturation temperature was calculated and compared to the measured average tank temperature. Since the latter was at all times considerably higher than the saturation temperature, it was concluded that condensation does not occur in the receiving tank. Like the calculation of the generated vapor mass, this conclusion is based on the assumption of a uniform tank temperature.

During each main experiment, a visual observation of the formation of dry ice in the receiving tank was performed. Although an accurate assessment of the amount is difficult, comparative conclusions could be formulated. In the reference experiment, dry ice was formed in two isolated locations in the receiving tank.

2.5 High-Speed Cinematography Set-up

In order to obtain accurate visual observations of the two-phase spray which exits from the nozzle during the inflation sequence, a high-speed cinematographic study was performed. The spray size, shape and penetration velocity provide valuable information about the phenomena which govern the dispersion and evaporation of the liquid. Depending on the quality of the images, an estimate of the droplet sizes and velocities can be made.

Three different kinds of recordings were made. In all cases, a Kodak EktaPro 1000 Motion Analyzer in combination with a Kodak EktaPro Intensified Imager was used. This is an analog system which stores the recordings on special video tapes. The imaging rate is variable an can be set to 30, 60, 125, 250, 500 or 1000 images per second. After the recording, the tapes can be played back at a reduced rate or frozen on a single frame. Also, the tapes can be copied onto ordinary video cassettes and images can be digitized and stored in a personal computer for further processing.

A series of spray images are included in Chapter 4.

2.5.1 Tank Images

The first recording is an observation of the two-phase spray as it is released in the receiving tank during the main experiments. A halogen spot, reflected from an umbrella located near the upper right corner of the tank, was used as a continuous light source. The camera was fitted with a 50 mm lens with an aperture setting of 8. This provided sufficient focal depth to see both the front and the back of the tank clearly. The diameter of the upper part of the nozzle (31.75 mm) can be used as length scale. During the recording, no information of the other sensors was captured and the thermocouple mounting bracket inside the tank was removed to avoid the obstruction of the view. The tank was purged with nitrogen as in the standard procedure of the main experiments.

2.5.2 Jet Images

The second recording contains images of one of the four jets exiting from the nozzle, as it expands freely in a stagnant nitrogen atmosphere. A special expansion chamber was built

for the experiments. The side walls of the chamber were constructed from Plexiglas, while the top and the bottom was covered with black plastic sheeting. The end wall, opposite to the nozzle hole, was also covered with plastic sheeting, but contained venting holes to relieve the pressure when the jet was released. The objective of the chamber was to surround the spray with dry nitrogen, such that condensation of moisture upon contact with the cold CO_2 vapor was avoided. Prior to the recording, the chamber was thoroughly purged with nitrogen. During the actual experiment, the supply of nitrogen was turned off, such that the spray expanded in a stagnant atmosphere.

A xenon slip-sync strobe[10], with a maximum flashing frequency of 300 Hz, was used as light source. The flashes are synchronized with the imaging system through the external probe trigger. A recording rate of 250 images per second was used. The flash duration is not accurately specified by the strobe manufacturer and lies between 8 - 30 μs when operated in the 131-300 Hz range. Simple ways of measuring the flash duration are known [88], and were considered in case the quality of the images would allow the estimation of the velocity of individual particles by measuring their corresponding blur on a single frame. The actual light emerges from a flexible bundle of fiber optics, connected to the strobe head. Different backgrounds and positions of the light source were tested. A black background with the light source located in the top of the chamber was used. Everything was kept as dark as possible and it was mainly the luminescence of the spray droplets that shows on the images.

[10] Manufactured by Chadwick-Helmuth Company Inc., El Monte, CA, USA. Model : Strobex 8440-3.

The camera was positioned perpendicular to the side wall of the expansion chamber, at the same height as the nozzle exit. It was fitted with a 50 mm lens on aperture setting 2.8. The camera position was about 2 meters away from the expansion chamber.

The distance between the nozzle exit and the light source functioned as a length scale. It was measured in the experimental set-up to be about 560 mm. This length scale was used when determining the dimensions of the spray.

2.5.3 Nozzle Exit Images

The last series of images are detailed observations of a nozzle exit hole. The objective was to closely monitor the type of jet that emerged from the vessel and to determine its lifetime accurately.

The set-up was similar to the one from the jet images, and the same chamber was used to surround the spray with nitrogen. The camera was fitted with a macro lens with an aperture setting of 8. It was positioned perpendicular to the chamber and close to the side wall. The observed area is roughly 8 by 10 mm. The same strobe as in the jet images was used, but it was located at the top of the chamber, directly above the nozzle exit hole. A frame of a collection of beads of 200 and 500 μm was used as length scale.

CHAPTER 3

IDEAL GAS EXPERIMENTS AND VALIDATION OF THE PERFORMANCE OF THE MAIN EXPERIMENTAL SET-UP

3.1 Introduction

Prior to the actual experimental study of the SLG-Inflator, several experiments were conducted in which the inflator was filled with pressurized N_2 instead of CO_2. These preliminary experiments are referred to as the *ideal gas experiments*. The primary objective of the ideal gas experiments was to estimate the reliability and the accuracy of the measurements obtained from the main experimental set-up. The inflator conditions in these experiments were such that the behavior of the N_2 in the system approached that of an ideal gas. Based on this observation, a theoretical model which predicts the measurements in the main experimental set-up during the ideal gas experiments was developed. By comparing these simulations with the actual measurements, the accuracy of the measurements was estimated. A similar procedure to validate the performance of the experimental set-up was followed in [52,85]. The experimental results and the corresponding simulations of the ideal gas experiments are presented in the first part of this chapter. Next, the theoretical model is discussed. Finally, the accuracy of the measurements of the main experimental set-up is assessed.

With respect to the inflator, the expansion of the N_2 in the ideal gas experiments is very similar to that during a typical inflation sequence of the Stored Gas Inflator (§1.2.6.2). In order to assure ideal gas behavior of the N_2, the initial inflator pressure in the ideal gas experiments was lower than the typical storage pressure of the Stored Gas

Inflator (e.g. 5000 psig). However, in both systems, the flow from the inflator is choked for nearly the entire process and a drastic drop in temperature of the inflator gases occurs. Assuming a complete evacuation of the inflator (i.e. expansion into vacuum), the temperature drop in the Stored Gas Inflator was calculated and listed in Table 1.3. Because of the lower initial inflator pressure, and because the inflator is discharged in a receiving tank with initially ambient pressure (i.e. an incomplete evacuation), the temperature drop in the inflator during the ideal gas experiments will be less than in the case of a Stored Gas Inflator.

3.2 Experimental Results

For the ideal gas experiments, the standard experimental procedure was followed (except for filling the inflator with N_2) and the receiving tank was purged with N_2 in all cases. Initial inflator pressures in excess of the pressure of N_2 in the storage cylinders were obtained by means of a booster pump.

Table 3.1 Ideal Gas Experiments

Exp. #	Initial $P_{inflator}$ [bar] (psig)	Initial $T_{inflator}$ [°C]	$Z^{(*)}$ [/]	Inflator Size [ml]	Measurements
1	35 (500)	24	1.00	100	P_{tank}
2	60 (850)	24	1.00	100	P_{tank} , $P_{inflator}$
3	70 (1000)	25	1.00	100	P_{tank} , $P_{inflator}$
4	104 (1500)	26	1.01	100	P_{tank}
5	139 (2000)	25	1.02	100	P_{tank}
6	70 (1000)	25	1.00	26	P_{tank} , $P_{inflator}$
7	139 (2000)	24	1.02	26	P_{tank} , $P_{inflator}$, T_{tank}
8	277 (4000)	25	1.13	26	P_{tank}

(*) Per definition: Z= (P.v)/(R.T). Values that differ from unity indicate non-ideal gas behavior.

Table 3.1 provides an overview of all ideal gas experiments that were conducted. The last column lists the properties that were recorded during each experiment. The ideal gas behavior of N_2 was verified for each set of initial inflator conditions by calculating the corresponding compressibility factors using Lee & Kesler's Tables [16]. The resulting compressibility factors are listed in the 4th column of Table 3.1. For experiments 4, 5, 7 and 8, a deviation from ideal gas behavior is observed. As expected, the non-ideality increases with the initial inflator pressure. The implications of this deviation will be discussed in this section. The experiments with the large inflator vessel (experiments 1-5) will be discussed first.

Figure 3.1 compares the simulated and the measured evolution of the tank pressure for experiments 1 and 3-5 of Table 3.1. The vertical marks on the simulated curves indicate the transition from choked to non-choked flow. Typically, the flow is choked during 75-80% of the expansion. The expanding N_2 in the tank causes considerable pressure fluctuations during the experiment.

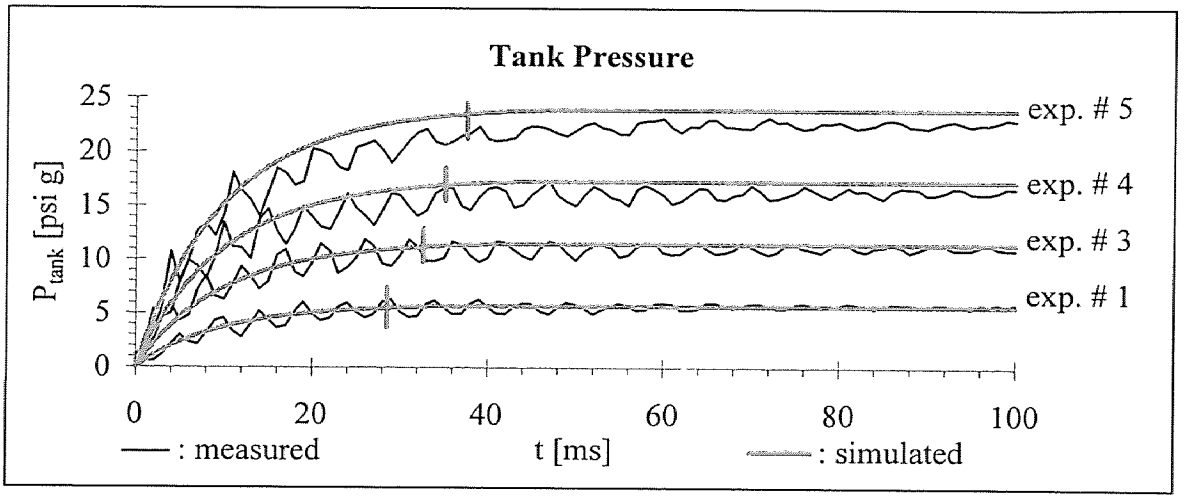

Figure 3.1 Measured and Simulated Tank Pressure for Experiments 1, 3, 4 and 5

These fluctuations disappear after about 200 ms. An attempt was made to relate the period of these pressure fluctuations to the dimensions of the receiving tank and the sonic velocity of N_2. No simple relationship could be established and it is believed that the fluctuations are the result of a complex interaction between shock waves bouncing off the top, bottom and side walls of the tank. For the experiments at low initial inflator pressure (experiments 1&3), excellent agreement is observed. At higher initial inflator pressure (experiments 4&5), a small difference in the magnitude of the tank pressure is shown. The latter is caused by the non-ideal gas behavior of the N_2 in the inflator. As shown in Table 3.1, the compressibility factor of N_2 for experiments 4 and 5 exceeds unity. As a result, the actual initial amount of N_2 in the inflator will be lower than that predicted by the ideal gas law.

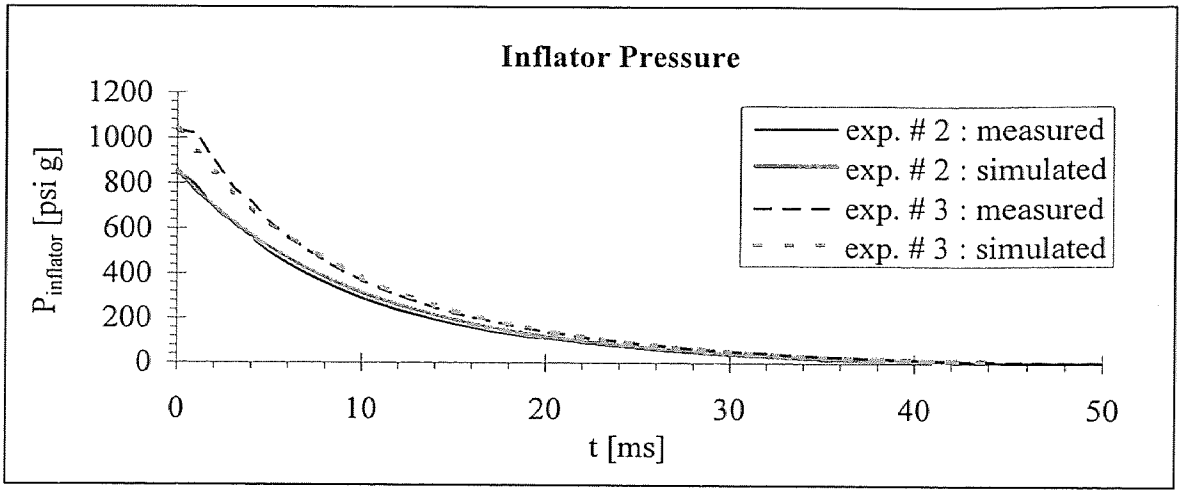

Figure 3.2 Measured and Simulated Inflator Pressure for Experiments 2 and 3

This effect is taken into account by dividing the calculated tank pressure by the compressibility factor corresponding to the initial inflator conditions. This procedure was

performed for the tank pressure curve of experiment 5. Subsequently, the difference between predicted and measured tank pressure was averaged over the time interval from 50 to 100 ms. The result showed an average difference between predictions and measurements of slightly more than 3%. The limited duration of the time interval justifies neglecting the influence of external heat transfer during the calculation.

Figure 3.2 shows the measured and predicted inflator pressure evolution for experiments 2 and 3. Excellent agreement is observed. This concludes the discussion of the results of the N_2 experiments with the large inflator vessel.

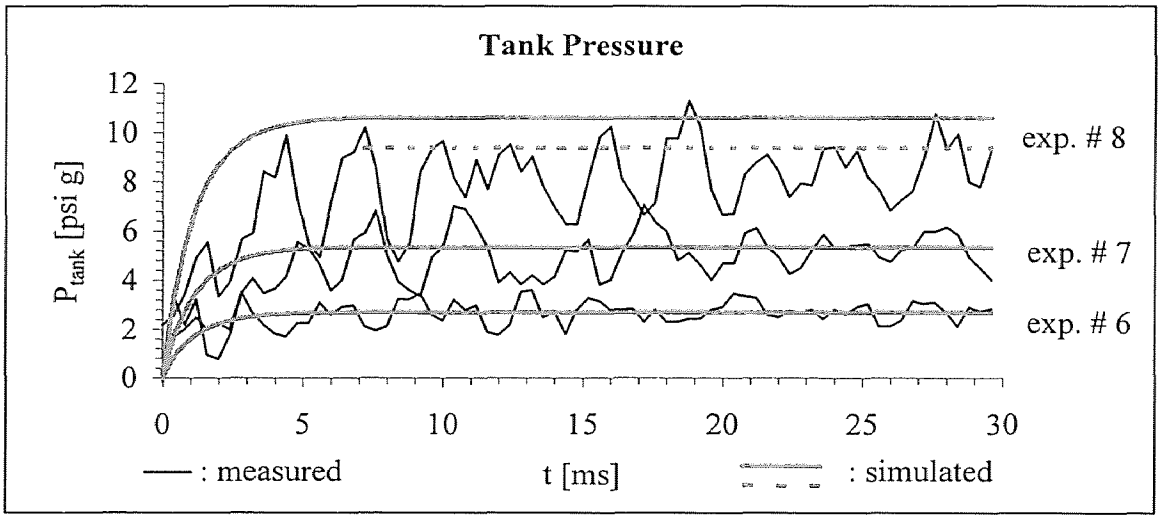

Figure 3.3 Measured and Simulated Tank Pressure for Experiments 6-8

The simulated and measured tank pressure for the last 3 experiments of Table 3.1 (with the small inflator vessel) are compared in Figure 3.3. The absolute magnitude of the pressure fluctuations is the same as before (Figure 3.1). Relative to the average pressure level, the fluctuations have increased in amplitude. For experiment 6, with low initial inflator pressure, the measured and simulated curves correspond very well. The

experiments with high initial inflator pressure (experiments 7&8) show a significant deviation between measurement and simulation. Using the same procedure as before to compensate for the non-ideal gas behavior of N_2 in experiment 8, the dotted line was obtained. The difference between the measured and the predicted tank pressure was averaged over the interval from 50-100 ms. An average deviation of 6.5 % was obtained.

Figure 3.4 contains the measured and simulated inflator pressure for experiments 6 and 7 of Table 3.1. While the evacuation process of the large inflator vessel (volume of 100 ml) lasts about 40 ms, the expansion from the small inflator (volume of 26 ml) is completed in less than 10 ms. The finite opening time of the release mechanism is taken into account by translating the simulated curves parallel to the time-axis over a distance of 2 ms. The latter is approximately equal to the time it takes for the sliding piston in the second release mechanism to clear the exit holes in the central channel of the nozzle. This time was calculated in §2.2.2.1.

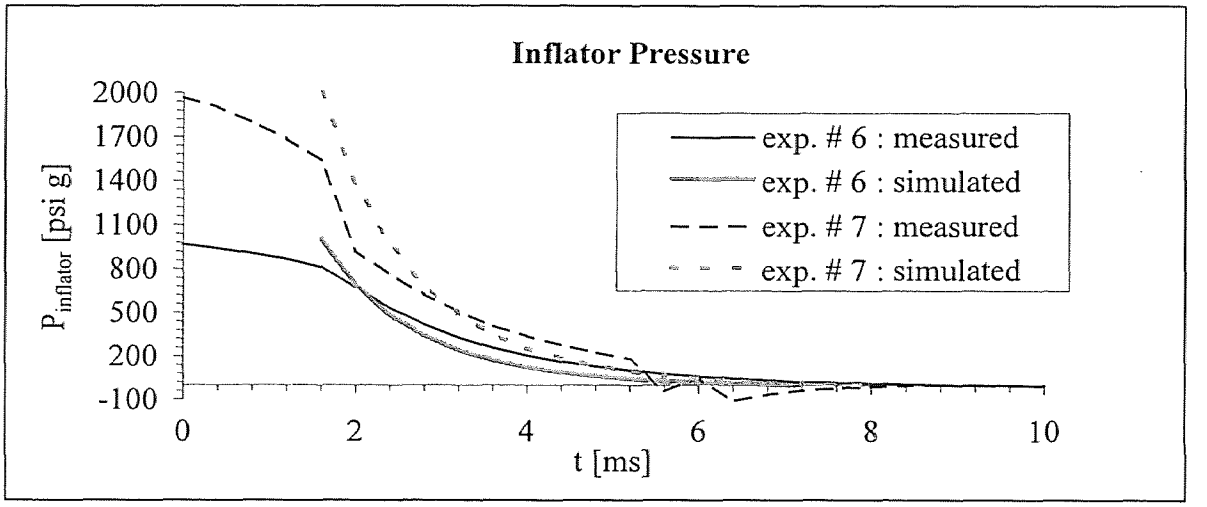

Figure 3.4 Measured and Simulated Inflator Pressure for Experiments 6 and 7

For times larger than 2 ms, both the amplitude and the dynamics of the simulated and the experimental curves agree very well.

During experiment 7 of Table 3.1, the average tank temperature was also recorded. The result is compared with the corresponding simulation in Figure 3.5. Again, the simulated curve is translated to compensate for the opening time of the release mechanism. At first, the discrepancy between the measurement and the simulation seems significant.

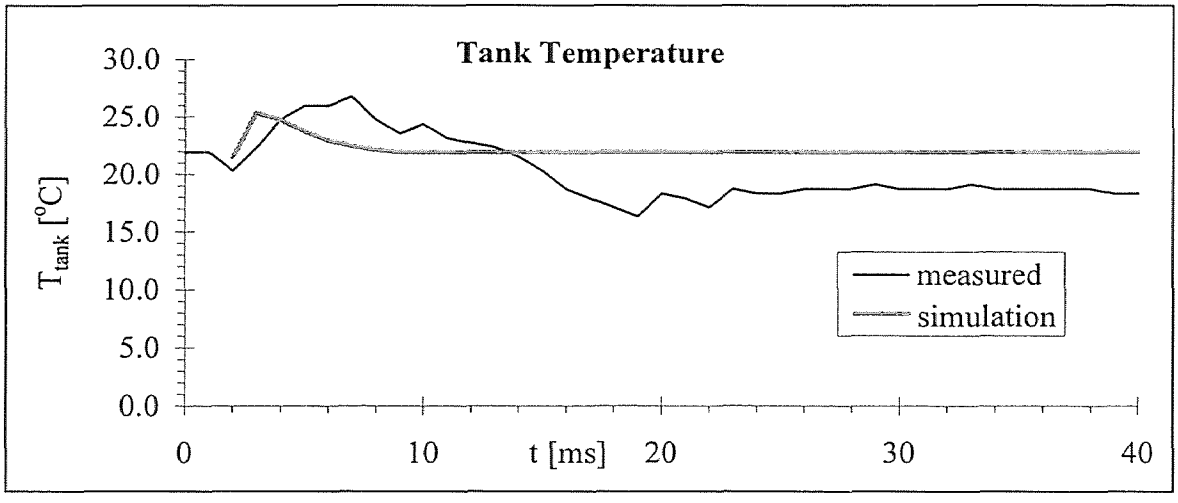

Figure 3.5 Measured and Simulated Tank Temperature for Experiment 7

However, two issues need to be taken into account. First, based on the experimental results in this section and those of the Reference Experiment in §2.4, it is clear that the tank temperature variation for an ideal gas experiment is much smaller than that for an actual inflator experiment in which liquefied CO_2 is used. Hence, assuming that the absolute error on the temperature measurement is the same for both types of experiments, the relative error for the experiments with liquefied CO_2 will be considerably smaller than

in Figure 3.5. The second issue concerns the drop of the measured temperature below the simulated value that occurs at about 14 ms in Figure 3.5. As discussed earlier, the expansion during the N_2 experiments is identical to that during the inflation sequence of a stored gas inflator. Hence, similar to the predictions in Table 1.3, the N_2 that remains inside the inflator after the completion of the expansion is extremely cold. It is believed that the drop in temperature in Figure 3.5 is caused by the mixing of the remaining gas in the inflator and the tank gases. This is not taken into account in the model.

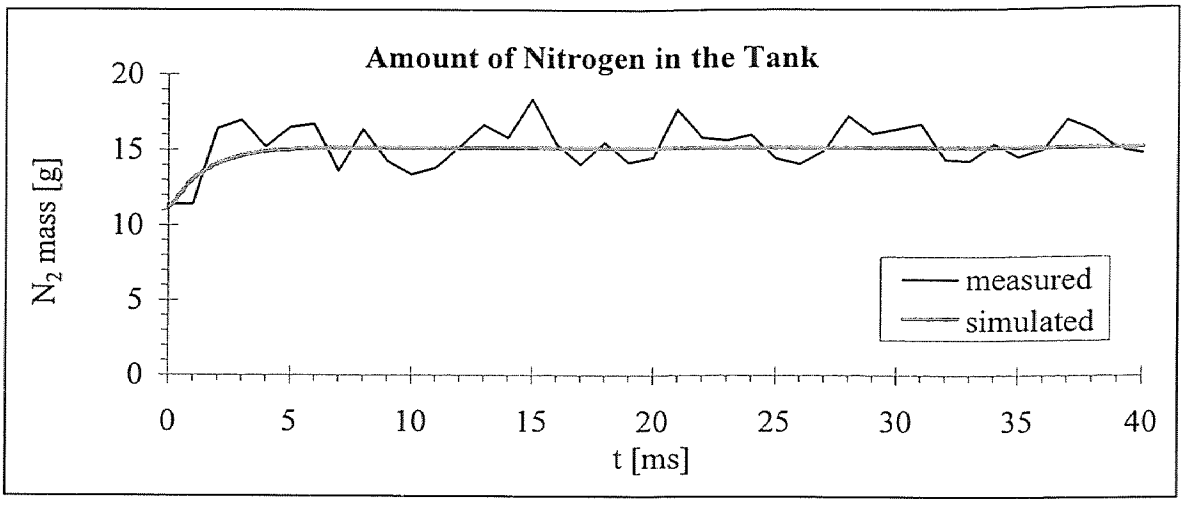

Figure 3.6 Measured and Simulated Mass of Nitrogen in the Tank for Experiment 7

The amount of N_2 in the tank was calculated using the measurement of the tank pressure and the average tank temperature. Conditions are such that ideal gas behavior may be assumed. The initial amount of N_2 in the inflator was calculated from measurements of the pressure and temperature in the system after it equilibrated with the surroundings. Using the ideal gas law, along with the knowledge of the tank volume and the initial amount of N_2 in the tank and the inflator, the increase in mass in the tank could

be calculated. This result is compared with the corresponding simulation in Figure 3.6. Excellent agreement between the simulation and the experiment is observed.

3.3 Theoretical Model

As shown in Table 3.1, at initial inflator pressures below 100 bar, N_2 exhibits ideal gas-behavior. Based on the short duration of the experiment, it is justified to neglect heat transfer from the tank or inflator walls to the expanding gas. In addition, the influence of wall friction and viscosity is assumed to be negligible. Hence, the process can be modeled as an isentropic expansion of an ideal gas. Furthermore, the considerable length to diameter ratio of the inflator suggests a one-dimensional approximation of the flow. The specific heat capacity of N_2 varies very little in the temperature range under consideration and was considered to be constant. Figure 3.7 contains a schematic representation of the main experimental set-up, with an indication of the two control volumes which are considered in the model. The adiabatic walls indicate that no heat transfer is taken into account.

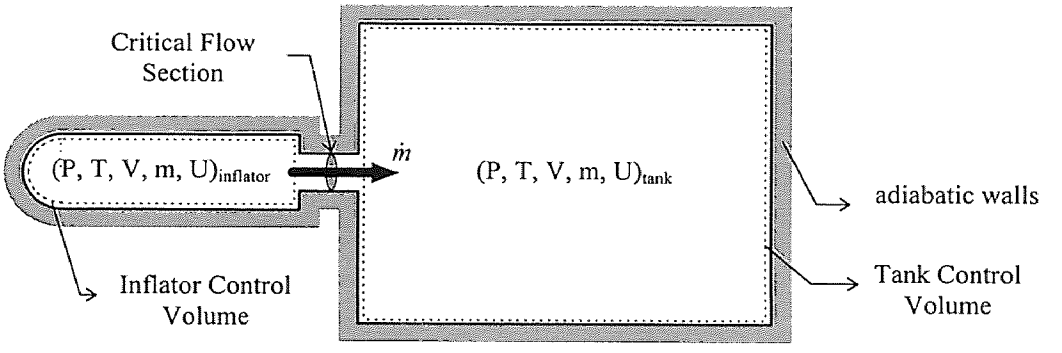

Figure 3.7 Control Volumes in the Ideal Gas Model

The two control volumes are connected through the nozzle, with a known area of the critical flow section (A_{crit}). Throughout the expansion, a relatively powerful N_2-jet exits from the nozzle and causes strong mixing in the tank. Based on this observation and on the relatively small size of the inflator vessel, a uniform temperature in both control volumes is assumed during the expansion process.

The mass flow rate ($\dot{m}$) between the two control volumes was calculated using the well-known one-dimensional laws for the isentropic flow of an ideal gas [74]. Transient effects during the initial stages of the experiment are neglected and the process is assumed to be quasi-steady. If the pressure ratio[1] is smaller than the critical ratio, the flow from the inflator is choked. The critical pressure ratio is determined by:

$$P_{critical} = \left(\frac{2}{\gamma + 1}\right)^{\frac{\gamma}{\gamma - 1}} \tag{3.1}$$

When the flow is choked, the velocity of the gas through the critical section in the nozzle is sonic and the Mach number reaches unity in this section. For this case, the mass flow rate is given by:

$$\dot{m} = A_{crit} \cdot \frac{P_{inflator}}{\sqrt{T_{inflator}}} \cdot \sqrt{\frac{\gamma}{R} \cdot \left(\frac{2}{\gamma + 1}\right)^{\frac{\gamma + 1}{\gamma - 1}}} \tag{3.2}$$

On the other hand, if the pressure ratio is larger than $P_{critical}$, the flow is not choked. This is the case in the last stages of the experiment, and the Mach number at the critical section is smaller than 1:

[1] The *pressure ratio* is defined as the ratio of the pressure inside the tank to the pressure inside the inflator.

$$M = \sqrt{\frac{2}{\gamma - 1} \cdot \left(\left(\frac{P_{tank}}{P_{inflator}} \right)^{\frac{1-\gamma}{\gamma}} - 1 \right)} \tag{3.3}$$

Based on this, the mass flow rate becomes:

$$\dot{m} = A_{crit} \cdot \sqrt{\frac{\gamma}{R}} \cdot \frac{P_{inflator}}{\sqrt{T_{inflator}}} \cdot \frac{M}{\left(1 + \left(\frac{\gamma - 1}{2} \right) \cdot M^2 \right)^{\frac{\gamma+1}{2(\gamma-1)}}} \tag{3.4}$$

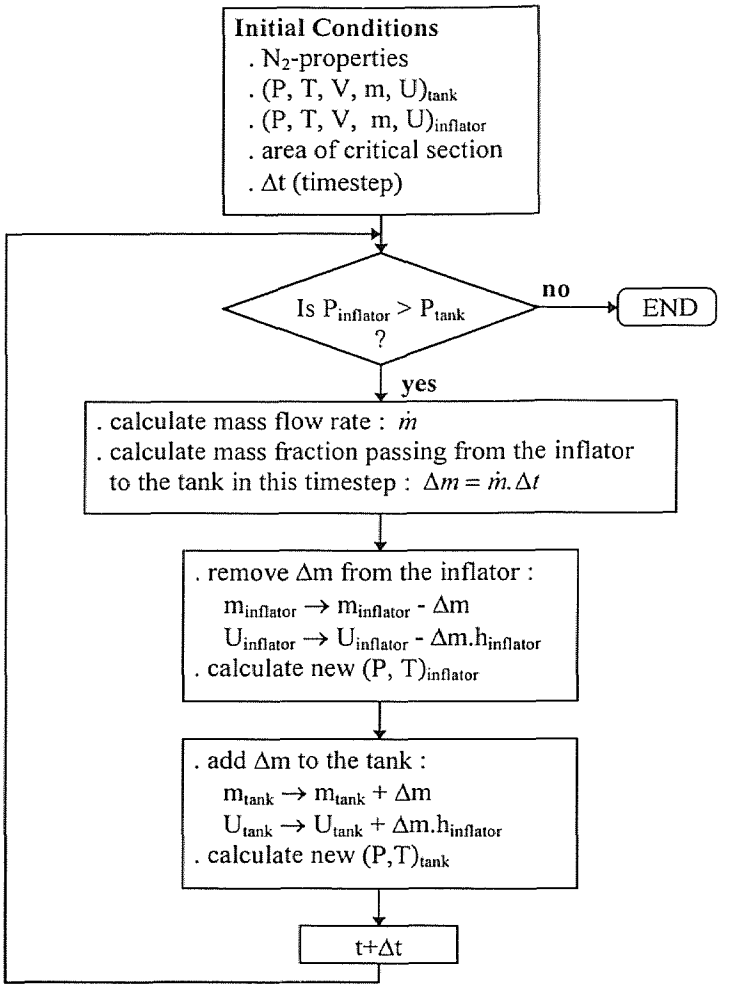

Figure 3.8 Flow-chart of the N_2-model

The concept of the model is similar to that used to simulate the Stored Gas Inflator [60] and basically combines the mass and energy balance for each control volume with the calculation of the mass flow rate between them. A computer program was developed to perform the calculations and a flow-chart of the code is included in Figure 3.8. A typical output of the program is shown in Appendix A.

In addition to this model, a simulation with a professional CFD-code - from *AEA Technology Computational Fluid Dynamics Services, Inc.* - was performed in which the two-dimensional character of the flow was considered. Since this gave no significantly different results for the predicted pressure and temperature evolutions, the simple one-dimensional model was used for all other simulations.

Instead of developing a computer program, analytical expressions for the evolution of the tank and the inflator properties during the experiment could have been derived. For example, the expression for the decrease in the inflator pressure is given in [52]. Similar relations could have been developed for the other properties. However, since this involves a considerable amount of mathematical manipulations, the current approach (i.e. writing a small computer program) was preferred.

3.4 Performance of the Main Experimental Set-up

The results in this Chapter demonstrate that even in the case of the N_2-experiments, in which the expansion process occurs about five times faster than in the actual CO_2 experiments, all sensors react sufficiently fast. In addition, based on the comparison of the experimental results and the theoretical simulations, the pressure and temperature measurements in the main experimental set-up are estimated to have an uncertainty of

approximately 3-5%. Since it is expected that the absolute error of the measurements is the same for both the N_2-experiments and the CO_2- experiments, the larger variations in pressure and temperature during the CO_2-experiments will produce a smaller relative error. Hence, an uncertainty of 3-5% is a conservative estimate.

A more accurate assessment of the uncertainty of the measurements could be obtained by extending the theoretical model to include non-ideal gas behavior and the mixing of the gases in the tank and the inflator (i.e. two-dimensional effects). This lies beyond the scope of this research.

During the experimental study of the stored liquefied gas inflator, several key experiments were repeated to verify the reproducibility of the results. For all cases, the measurements varied less than the above uncertainty.

CHAPTER 4

EXPERIMENTAL STUDY OF THE STORED LIQUEFIED GAS INFLATOR

4.1 Introduction

The objectives of the experimental study were to obtain a thorough phenomenological understanding of the system and to develop a qualitative model of the SLG-Inflator. For this purpose, a systematic study was performed of the influence of the main system parameters on the inflation sequence. The main system parameters include: the initial conditions in the receiving tank, the size of the critical section in the nozzle and the initial inflator conditions. High-speed cinematographic recordings of the tank phenomena during the Reference Experiment and of the two-phase jet from the inflator were made and the observations were correlated with other experimental results. In addition, the effect of adding small amounts of different organic liquids to the CO_2 in the inflator was investigated. Based on the experimental results of this research and with the aid of similar studies in the literature, the dominant phenomena describing the behavior of the SLG-Inflator were identified. This detailed understanding has served as the basis for developing a quantitative model (Chapter 5).

The current chapter consists of two main parts. In the first part, the results of the experimental study of the SLG-Inflator are described. In the second part, the qualitative model of the SLG-Inflator is presented and a detailed discussion of the experimental observations is given. An overview of the experimental data is provided in Figure 4.1.

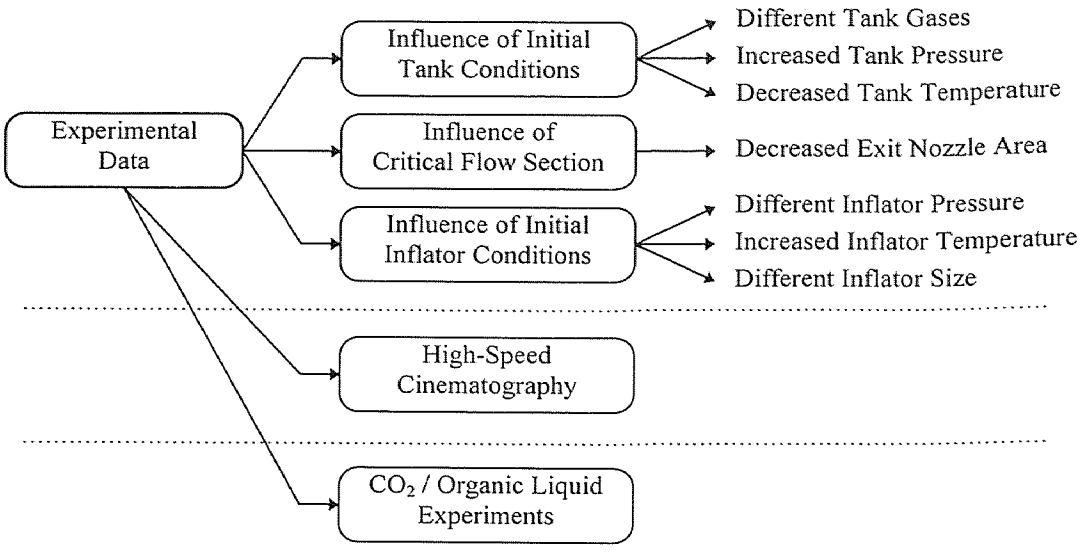

Figure 4.1 Overview of the Experimental Data

As illustrated in Figure 4.1, the presentation of the experimental results is organized in 5 sections, as follows:

1. ***Influence of Initial Tank Conditions:*** The initial tank conditions were varied by using different tank gases, increasing the initial tank pressure and decreasing the initial tank temperature. The objectives of these experiments were to assess the influence of the tank conditions on the performance of the inflator and to obtain understanding of the complex phenomena that occur in the tank during the inflation sequence. The phenomena under consideration include the dispersion of a two-phase jet, the evaporation and solidification of liquid CO_2 droplets, the mixing of non-ideal gases and heat transfer from the tank gases to the evaporating spray. Heat transfer from the tank walls is neglected because of the short duration of the inflation sequence.

2. ***Influence of Critical Nozzle Section:*** To illustrate the influence of the critical flow section in the nozzle, results are presented of an experiment in which the critical section was reduced.
3. ***Influence of Initial Inflator Conditions:*** Experiments were performed at different initial inflator pressures and temperatures. Based on these results, the optimal storage pressure for the SLG-Inflator was determined and the influence of the ambient temperature was assessed. In addition, to illustrate the effect of the inflator volume, results of an experiment with a larger inflator vessel are presented.
4. ***High-Speed Cinematographic Observations:*** Additional information about the tank phenomena and the behavior of the two-phase spray from the nozzle was obtained with the aid of high-speed cinematography.
5. ***Influence of Organic Liquids:*** Organic liquids were added to the system in order to prevent (or delay) the CO_2 from freezing during the last stages of the inflation. These experiments have demonstrated a drastic change in the tank measurements. No references to this effect were found in the literature and it is believed that these results constitute a new phenomenon.

A comprehensive qualitative model of the SLG-Inflator is presented at the beginning of the second part of this chapter. The model was developed by combining the current experimental data, thermodynamic evaluations of the system and results from previous studies. The most important studies with respect to the inflator phenomena were published fairly recently (1992, 1994) [47,63]. They contain a detailed discussion of the interaction between the flashing process and the two-phase outflow of water from a

tubular vessel. This interaction is essential for the understanding of the system. Based on the qualitative model, key observations of the experimental study are explained. Phase diagrams of the critical and metastable liquid region of CO_2 were generated to clarify the effect of the initial inflator conditions. Also, a qualitative explanation for the observations pertaining to the CO_2/Organic Liquid experiments is included.

The experimental set-ups and procedures were described in Chapter 2, together with a detailed discussion of the results of the Reference Experiment (see Table 2.3 for the initial tank and inflator conditions). Since these results serve as the basis for comparison with other experiments, they are repeatedly referred to in this chapter.

In nearly all experiments, condensate (liquid and/or solid CO_2) is formed in the tank and/or inflator during the inflation sequence. For the cases in which both the tank pressure and tank temperature were measured, the amount and average specific internal energy of the condensate at the end of the inflation sequence were determined. The amount of condensate is an important parameter for the assessment of the performance of the SLG-Inflator, since it represents the fraction of the initial liquefied CO_2 that is not transformed into vapor. The calculation of the amount and average specific internal energy is based on a combination of the conservation of mass and the first law of thermodynamics. A discussion of the energy analysis of the system is included in Appendix B. By comparing the average specific internal energy of the condensate to that of saturated solid CO_2, the condensate phase can be estimated. A table with the specific internal energy of saturated solid CO_2 is included in Appendix B.

In addition to evaluating the amount and the properties of the condensate that is being produced, the energy analysis of Appendix B was used to determine the energy

redistribution in the system during the inflation sequence. These results are presented in the second part of this chapter and provide an indication of the energy exchange between the tank gases and the evaporating spray.

4.2 Experimental Results

In this section, the results of the experimental study of the SLG-Inflator are presented.

4.2.1 Influence of Initial Tank Conditions

As shown in Figure 4.1, three different types of experiments were conducted to assess the influence of the initial tank conditions on the behavior of the system. For all cases, nominal inflator conditions were used (i.e. $P_0 = 2000$ psig; $T_0 \approx 22$ °C, see Table 2.3).

In the first type of experiments, three different gases (He, N_2 and CO_2) were used to purge the receiving tank. Because of the difference in density and specific heat capacity of the purging gases, the initial internal energy in the tank is different for the three cases. The standard experimental procedure was followed (§2.3).

In the second type of experiments, the pressure of the purging gases in the tank was increased. Experiments were conducted with two different gases (N_2 and CO_2), each time at a relative initial tank pressure of 3 atm (i.e. an absolute pressure of 4 atm). The higher initial tank pressure led to a significant increase in the initial amount of purging gas and hence, to a considerable increase in the initial internal energy of the tank. The standard experimental procedure was followed, with the exception of filling the tank to a relative pressure of 3 atm. Since the sensors were zeroed prior to the purging process, the

output of the tank pressure transducer was about 45 psig (3 atm) at the start of the data acquisition.

The last type of experiments was conducted at low initial tank temperatures. The initial tank pressure was equal to ambient pressure. The difference in temperature of the purging gas resulted in different levels of initial internal energy in the tank. In addition, a reduction in initial tank temperature led to a decrease in the temperature gradient between the purging gases and the evaporating droplets in the two-phase spray from the nozzle. Hence, heat transfer from the gases to the droplets decreased.

During all experiments, the inflator pressure, the tank pressure and the average tank temperature were recorded. Except for the experiments at low initial tank temperature, visual observations of the formation of condensate in the tank were performed. Since the inflator pressure curves were identical for all cases, it is concluded that the tank conditions (in the range that was investigated in this research) do not influence the phenomena inside the inflator. Therefore, only the tank results and the visual observations of the tank phenomena are discussed.

4.2.1.1 Effect of Different Tank Gases: Figure 4.2 contains the tank measurements corresponding to the experiments in which the tank was purged with different gases (He, CO_2, N_2). Initial conditions in the tank were ambient (about 20 °C and 1 atm) for the three cases. Assuming ideal gas behavior of the purging gases at the initial tank conditions and a constant isochoric specific heat capacity, the initial amount of tank gases (m_{tank}) and the initial internal energy in the tank (U_{tank}) were calculated. The results are shown Table 4.1. The last three columns of this table list the amount (m_{cond}) and the

average specific internal energy of the condensate (u_{cond}) that was formed during the inflation sequence.

Table 4.1 Experiments with Different Purging Gases (1 atm)

Purging gas	m_{tank} [g]	U_{tank} [J][(1)]	m_{cond} [g]	m_{cond} [%][(2)]	u_{cond} [kJ/kg]
He	1.6	365	6.5	28	183.6
N_2	11.3	615	7.1	30	185.8
CO_2	17.8	796	6.0	26	185.6

(1) With a reference temperature of 220K, and a c_v of 3119, 745 and 611 J/kg.K for He, N_2 and CO_2, respectively.

(2) The initial amounts of CO_2(l) were calculated from equilibrium measurements (approx. 24.0 g for all cases).

Figure 4.2(b) shows a small difference in the average tank temperature at the onset of the horizontal plateau in the curves (at about 25-30 ms). The minimum average temperature is highest for the case where CO_2 was used (≈ -60 °C) and lowest for the case where the tank was purged with He (≈ -71 °C). The curve corresponding to the Reference Experiment (with N_2 as purging gas) lies between the other two cases (≈ -64 °C). Also, Figure 4.2(b) shows a strong influence on the average tank temperature during the actual inflation sequence (from 2-25 ms). The temperature drop is slower for the case in which the tank was purged with CO_2 than in the other two cases. Furthermore, when He was used as purging gas, the average tank temperature during the inflation sequence dropped below the level that is reached at the onset of the horizontal plateau. It is thought that the latter is the result of a temporary non-uniformity in tank temperature. The quality of the mixing in the tank is expected to decrease with an increase in density difference between the expanding CO_2-vapor and the tank gases. This argument explains the more uniform tank temperature in the cases where CO_2 or N_2 was used as purging gas.

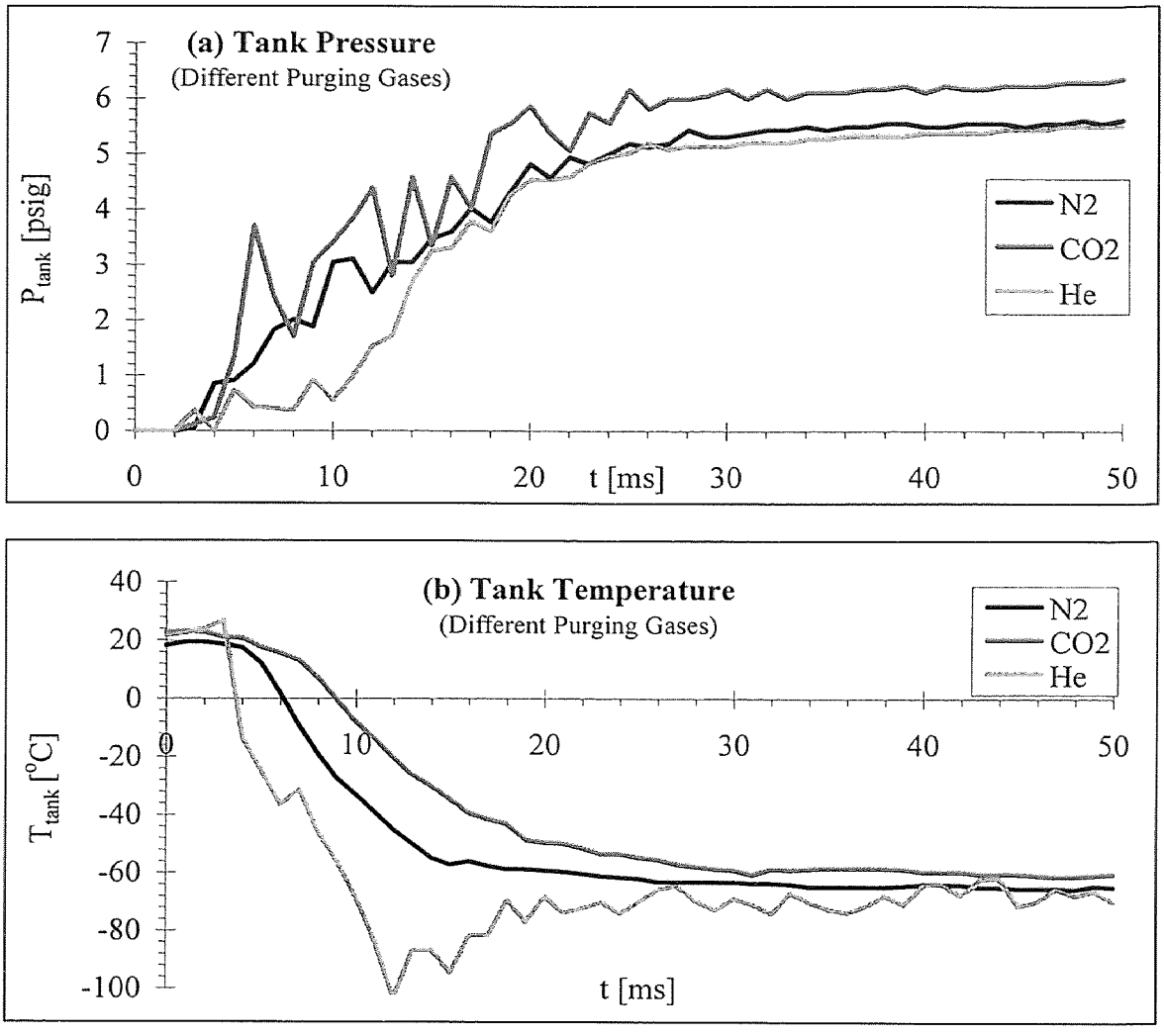

Figure 4.2 Effect of Different Tank Gases

The tank pressure curves in Figure 4.2(a) show a slightly higher pressure and a slightly longer inflation sequence when CO_2 was used to purge the tank. The lowest pressure and the shortest inflation sequence occurs in the case where the tank was purged with He. Again, the curve corresponding to the Reference Experiment (N_2 at 1 atm) lies between the other two cases. The flat part in the tank pressure curves during the first 2 ms of the experiment, is mainly the result of the finite opening time of the release mechanism.

The generated vapor mass curves, corresponding to the pressure and temperature measurements of Figure 4.2, do not show a significant difference for the three cases and are therefore omitted. This observation is confirmed by the calculated mass and average specific internal energy of the condensate that is formed during the inflation sequence (Table 4.1). In all cases, about 70% of the original amount of CO_2 was transformed into vapor by the end of the inflation process. The value of the specific internal energy of the condensate is virtually the same for the three experiments and lies within 2% of the specific internal energy of saturated solid CO_2 at the triple point (Table B.1). This indicates that the condensate is in the solid phase for the three cases. The visual observations of the formation of condensate in the tank during the inflation sequence was identical for the three experiments. In each case, similar isolated agglomerates of snow were observed.

4.2.1.2 Effect of Increased Initial Tank Pressure: The tank measurements of the experiments in which a relative initial tank pressure of 3 atm (absolute pressure of 4 atm) was used, are shown in Figure 4.3. The experiments were conducted with CO_2 and N_2 as purging gas. Table 4.2 lists the initial amount of purging gas and the initial internal energy in the receiving tank, calculated with the same assumptions as before. Similar to Table 4.1, the last three columns contain the amount and average specific internal energy of the condensate that was formed during the inflation sequence. The information about the experiments with N_2 and CO_2 at ambient initial tank pressure is included in the last two rows.

Table 4.2 Experiments at Increased Initial Tank Pressure (1 and 4 atm)

Purging gas	P_{tank} [atm]	m_{tank} [g]	U_{tank} [J][(1)]	m_{cond} [g]	m_{cond} [%][(2)]	u_{cond} [kJ/kg]
N_2	4	45.8	2496	2.4	11	--
CO_2	4	72.0	3218	5.2	21	258.1
N_2	1	11.3	615	7.1	30	185.8
CO_2	1	17.8	796	6.0	26	186.6

(1) With a reference temperature of 220K, and a c_v of 745 and 611 J/kg.K for N_2 and CO_2, respectively.
(2) The initial amounts of CO_2(l) were calculated from equilibrium measurements (approx. 24.0 g for all cases).

Both tank pressure curves of Figure 4.3(a) exhibit a different behavior compared to the experiments conducted with ambient initial tank pressure. After the delay corresponding to the opening of the release mechanism, three characteristic stages can be identified. The first stage concerns a limited, but fast increase in pressure. This is followed by a pressure drop in the second stage of the curve. The third stage in the curve shows a slow increase in pressure. While the last stage is the same for both experiments, a significant difference exists for the first two characteristic stages in the pressure curve. The pressure increase during the first stage is slightly larger when CO_2 was used as purging gas. Also, the pressure drop in the second stage of this curve is smaller than in the one corresponding to the experiment where the tank was pressurized with N_2.

Figure 4.3(b) contains the average tank temperature measurements for the experiments in Table 4.2. A clear difference between the curves is observed, both in the rate at which the temperature drops and in the value of the average tank temperature at the end of the inflation sequence (at about 30-40 ms). The experiment in which the tank was filled with CO_2 at an initial pressure of 4 atm shows the slowest and smallest decrease in average tank temperature. The largest and fastest drop in average tank temperature is observed in the curve corresponding to the experiment in which the tank contained N_2 at

1 atm. Figure 4.3(b), together with the values of U_{tank} in Table 4.2, suggests a correlation between the average tank temperature and the initial internal energy in the tank.

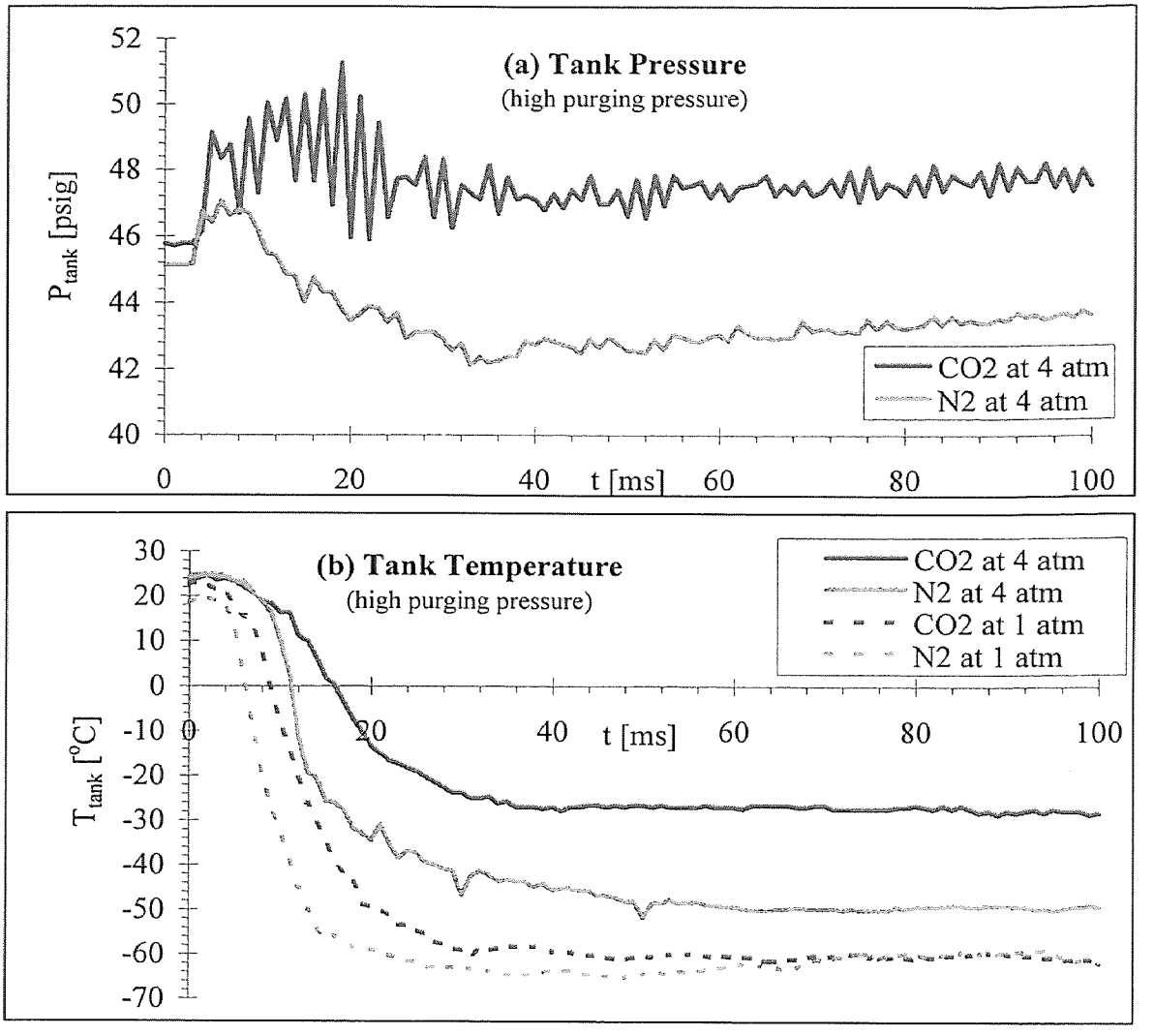

Figure 4.3 Effect of Increased Initial Tank Pressure

The generated vapor mass curves of the experiments in Table 4.2 are shown in Figure 4.4. While the difference between experiments at the same initial tank pressure is

small, a definite increase in generated vapor mass can be observed for the experiments at higher initial tank pressure.

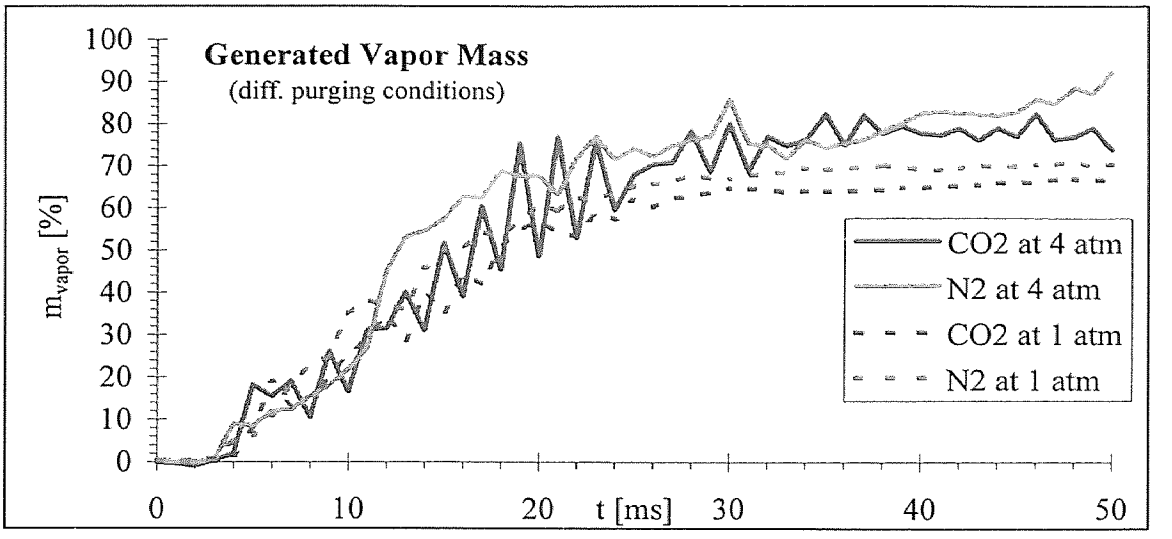

Figure 4.4 Generated Vapor Mass for Experiments with Different Purging Gases and Increased Initial Tank Pressure

For the calculation of the properties of the condensate, the end of the inflation sequence is typically taken at the end of the fast rise in the tank pressure curve (at about 30 ms). Because of the particular shape of the tank pressure curves in these experiments, the end of the inflation sequence was taken at the onset of the horizontal plateau in the average tank temperature curve. During the experiments at increased initial tank pressure, the temperature non-uniformity in the tank was considerably larger than in the experiments at ambient initial tank pressure. This was reflected by a large difference between the signal from the top and the bottom tank thermocouple. While this difference does not exceed 5-10 °C in the Reference Experiment, a prolonged difference of approximately 20 °C was observed during both experiments at increased initial tank

pressure. As a result, the uncertainty with respect to the calculation of the generated vapor mass and the formed condensate is higher than for other experiments. Furthermore, the low amount of condensate leads to additional uncertainty in the calculation of its properties. The combination of both effects is believed to be responsible for the failure of the calculation of the average specific energy of the condensate that is formed during the inflation sequence of the experiment in which the tank was purged with N_2 at 4 atm (Table 4.2). In agreement with the generated vapor mass curves of Figure 4.4, the mass of condensate for the experiments at increased initial tank pressure is lower than for the experiments at ambient initial tank pressure. In addition, the average specific internal energy for the experiment in which the tank was purged with CO_2 at 4 atm suggests that the condensate is not solid but liquid or a mixture of solid and liquid.

During the experiments at increased initial tank pressure, no snow formation was observed. Instead a dense fog settled in the tank, which lifted within 3-4 s after the activation of the release mechanism.

4.2.1.3 Effect of Decreased Initial Tank Temperature: The influence of the initial tank temperature was investigated by a series of experiments in which the purging gas was systematically cooled to lower temperatures. The initial tank temperature, together with the initial mass and the initial internal energy in the tank, is listed in Table 4.3. Also the results of the calculation of the properties of the condensate are included.

The tank measurements for the experiments in which N_2 was used as purging gas (experiments 1-4 in Table 4.3) are presented in Figure 4.5. For lower initial tank

temperatures, the rate of pressure increase during the inflation sequence (from 3-30 ms) increases.

Table 4.3 Experiments at Decreased Initial Tank Temperature (1 atm)

	Purging Gas	Initial T_{tank} [K] (°C)	m_{tank} [g]	U_{tank} [J][(1)]	m_{cond} [g]	m_{cond} [%][(2)]	u_{cond} [kJ/kg]
1	N_2	293 (20)	11.3	615	7.1	30	185.8
2	N_2	265 (-8)	12.5	420	6.6	28	180.4
3	N_2	254 (-19)	13.1	332	6.5	28	168.3
4	N_2	236 (-37)	14.1	168	6.9	30	180.9
5	CO_2	220 (-53)	23.7	0	7.4	32	176.7

(1) With a reference temperature of 220K, and a c_v of 745 and 611 J/kg.K for N_2 and CO_2, respectively.
(2) The initial amount of CO2(l) was calculated based on the initial inflator pressure and temperature (approx. 24.0 g for all cases).

At the same time, higher tank pressures are reached at the end of the inflation (at approx. 30 ms) for experiments with lower initial tank temperature. Both effects are the result of the increased initial amount of purging gas at lower initial tank temperature (Table 4.3).

The average tank temperature curves show a significant difference during the inflation sequence (3-30ms). Furthermore, at the onset of the horizontal plateau in the curves, the average tank temperature decreases slightly with the initial tank temperature.

The generated vapor mass curves corresponding to the tank measurements from Figure 4.5 were calculated, but show no significant difference between the four experiments. For the sake of brevity they were omitted.

Inspection of the tank measurements of the last experiment in Table 4.3, in which the tank was purged with cold CO_2, led to similar observations. The tank pressure curve showed a marked increase due to the additional mass of purging gas at low temperature. The average tank temperature at the onset of the horizontal plateau was the same as in

the Reference Experiment. Also the generated vapor mass at the end of the inflation sequence was about the same as in the Reference Experiment.

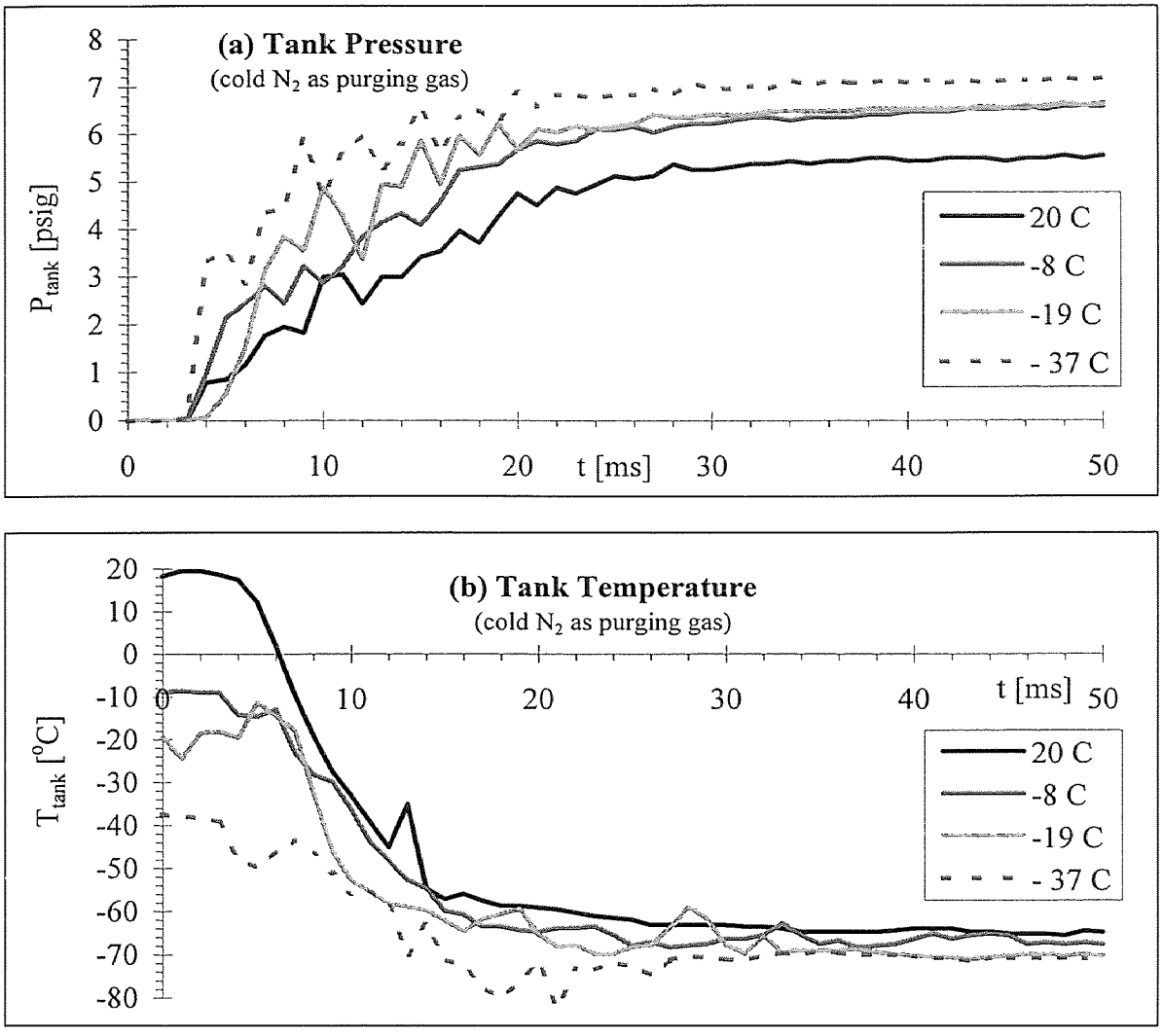

Figure 4.5 Effect of Decreased Initial Tank Temperature

The initial internal energy in the tank in the last experiment of Table 4.3 is the lowest of all experiments that were conducted in this research (obviously it is zero because of the choice of the reference temperature). In the case of an actual air bag deployment instead of a tank test, the initial internal energy in the bag is zero (strictly speaking). In this

respect, the last experiment of Table 4.3 approaches the situation of a real bag inflation more than other experiments. It is expected that the amount of generated vapor mass in this tank test is a good indication of that which would be observed in an actual bag deployment.

The last three columns in Table 4.3 indicate that virtually the same amount of condensate was formed for all experiments and that about 70% of the stored liquefied CO_2 was turned into vapor at the end of the inflation sequence. Since the specific internal energy of the condensate lies close to the value of saturated solid CO_2, it is concluded that the condensate is solid in all cases.

4.2.2 Influence of Critical Flow Section

In the standard experimental set-up, as discussed in Chapter 2, the combined area of the four nozzle exit holes is 127 mm^2. This area represents the critical section in the flow path of the expanding CO_2. An experiment was conducted in which two of the four exit holes of the nozzle were blocked. Obviously, this led to a 50% reduction of the critical flow section. The curves of the tank and the inflator measurements are presented in Figure 4.6.

For the experiment with smaller critical flow section, an increase in the duration of the rapid pressure rise in the tank is observed (Figure 4.6(a)). With respect to the Reference Experiment, the increase in this duration is about 10 ms. At the end of the rapid pressure rise, both the Reference Experiment and the experiment with smaller critical flow section reach the same tank pressure.

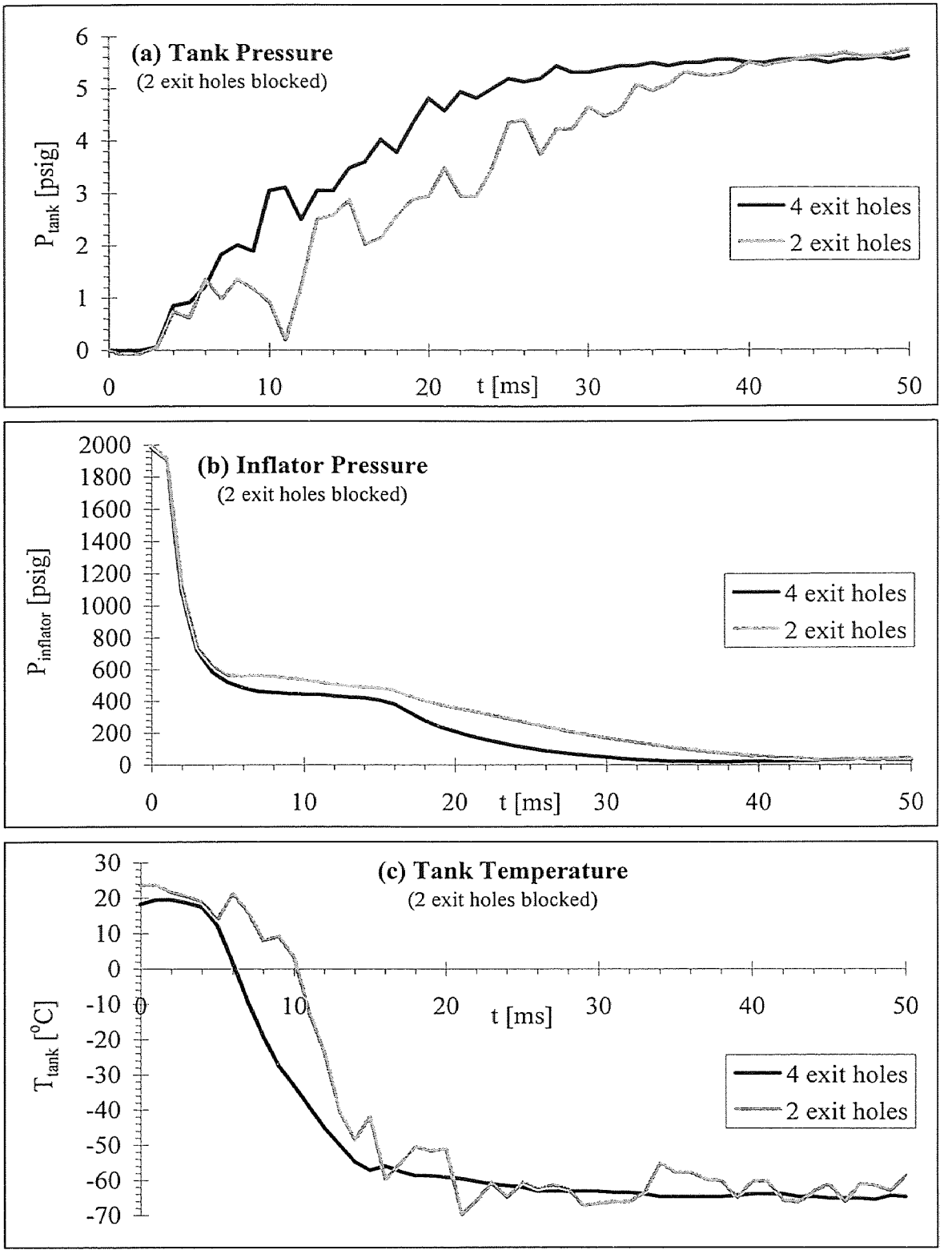

Figure 4.6 Effect of Decreased Critical Flow Section

The decrease in critical flow section leads to a slightly slower depressurization in the inflator immediately after the complete opening of the release mechanism (Figure 4.6(b)). In addition, the pressure of the horizontal plateau in the inflator pressure curve, corresponding to the experiment with smaller critical flow section, is higher. The depressurization during the last stage of the inflator pressure curve corresponding to the experiment with smaller critical flow section occurs slower than in the Reference Experiment.

Finally, the average tank temperature curve (Figure 4.6(c)), in agreement with the above, shows a slightly slower drop in temperature for the experiment with smaller critical flow section. However, after less than 20 ms, the temperature curves of both experiments are identical.

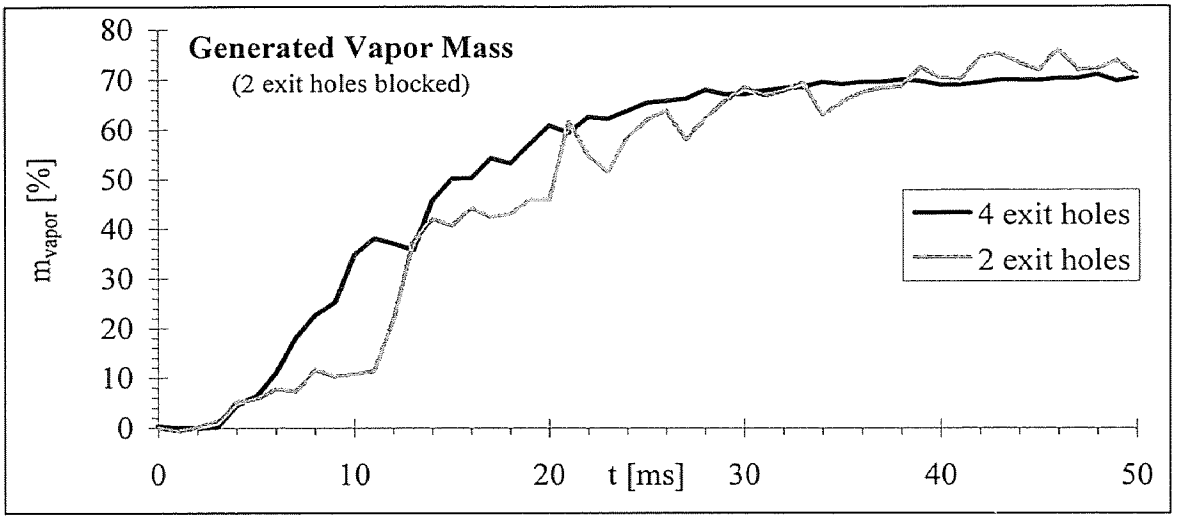

Figure 4.7 Generated Vapor Mass for Experiment with Decreased Critical Flow Section

Figure 4.7 contains the generated vapor mass curve corresponding to the experimental curves of Figure 4.6. Again, a slight decrease in the speed of the process is

observed, but the final state is identical to the one corresponding to the Reference Experiment. No difference in the formation of condensate was observed.

4.2.3 Influence of Initial Inflator Conditions

This section contains the results of the experiments in which the initial inflator conditions were varied. As indicated in Figure 4.1, the inflator conditions were changed by using:

a) different initial inflator pressures (with constant initial inflator temperature)

b) different initial inflator temperatures (with constant initial inflator pressure)

c) a different inflator volume (with nominal inflator conditions, see Table 2.3)

Nominal initial tank conditions were used for all cases (purged with N_2; ambient pressure and temperature; see Table 2.3).

4.2.3.1 Effect of Initial Inflator Pressure: The inflator conditions for the experiments at different initial inflator pressures are listed in Table 4.4.

Table 4.4 Experiments at Different Initial Inflator Pressure

	Initial $P_{inflator}$ [bar] (psig)	Initial $T_{inflator}$ [°C]	Measurements	$m_{inflator}$ (*) [g]
1	70 (1000)	24	P_{tank}, $P_{inflator}$, $T_{inflator}$	21.2
2	104 (1500)	23	P_{tank}, $P_{inflator}$, $T_{inflator}$	23.4
3	139 (2000)	24	P_{tank}, $P_{inflator}$, $T_{inflator}$	24.3
4	277 (4000)	23	P_{tank}, $T_{inflator}$	26.7
5	311 (4500)	24	P_{tank}, $T_{inflator}$	27.1

(*) Calculated using the tabulated density in [12] and the known vessel volume.

The initial amount of CO_2 in the inflator is listed in the last column. The latter indicates that the gain in stored CO_2 decreases as the initial pressure increases. For example, at

1000 psig, a 500 psi increase in pressure results in the additional storage of 2.2 g (about 10%) of CO_2. The same pressure increase (500 psi) at a storage pressure of 4000 psig, leads only to a 0.4 g (1.5%) increase in initial amount of CO_2.

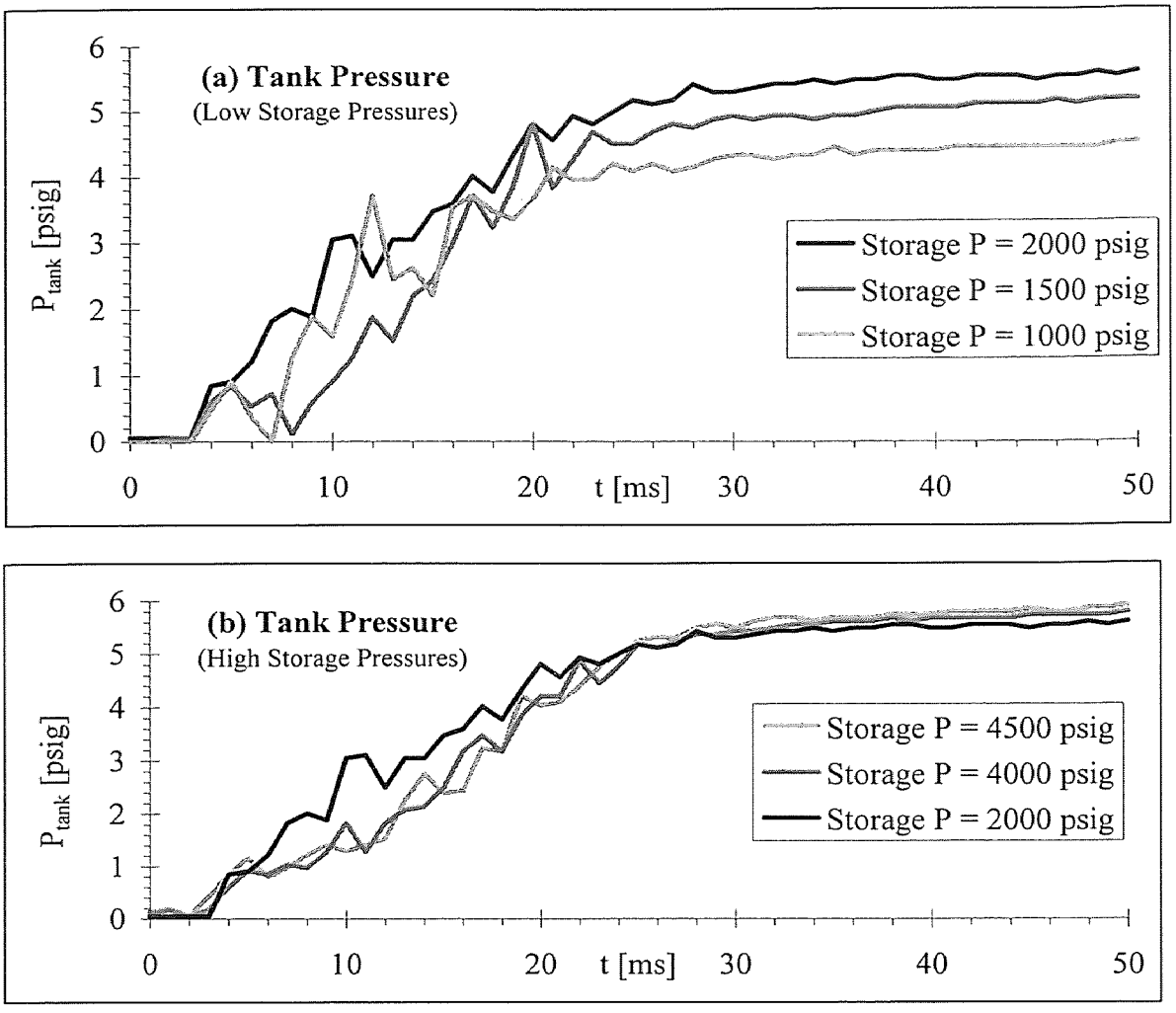

Figure 4.8 Effect of Storage Pressure

Figure 4.8(a&b) contains the results of the tank pressure measurements for experiments 1-3 and 3-5 (Table 4.4), respectively. The experiments do not indicate a significant difference in the rate at which the pressure increases during the initial rapid

rise in tank pressure. The duration of this initial rapid rise increases with the storage pressure. The most important difference between the curves in Figure 4.8 concerns the pressure that is reached at the end of the fast rise in tank pressure. An increase with the storage pressure is observed and is caused by the higher initial amount of liquefied CO_2 in the inflator (Table 4.4). As noted earlier, the increase in stored CO_2 decreases for higher storage pressures. This is reflected in Figure 4.8 by a decrease in the pressure difference at the end of the rapid rise in the curves for experiments at higher storage pressures.

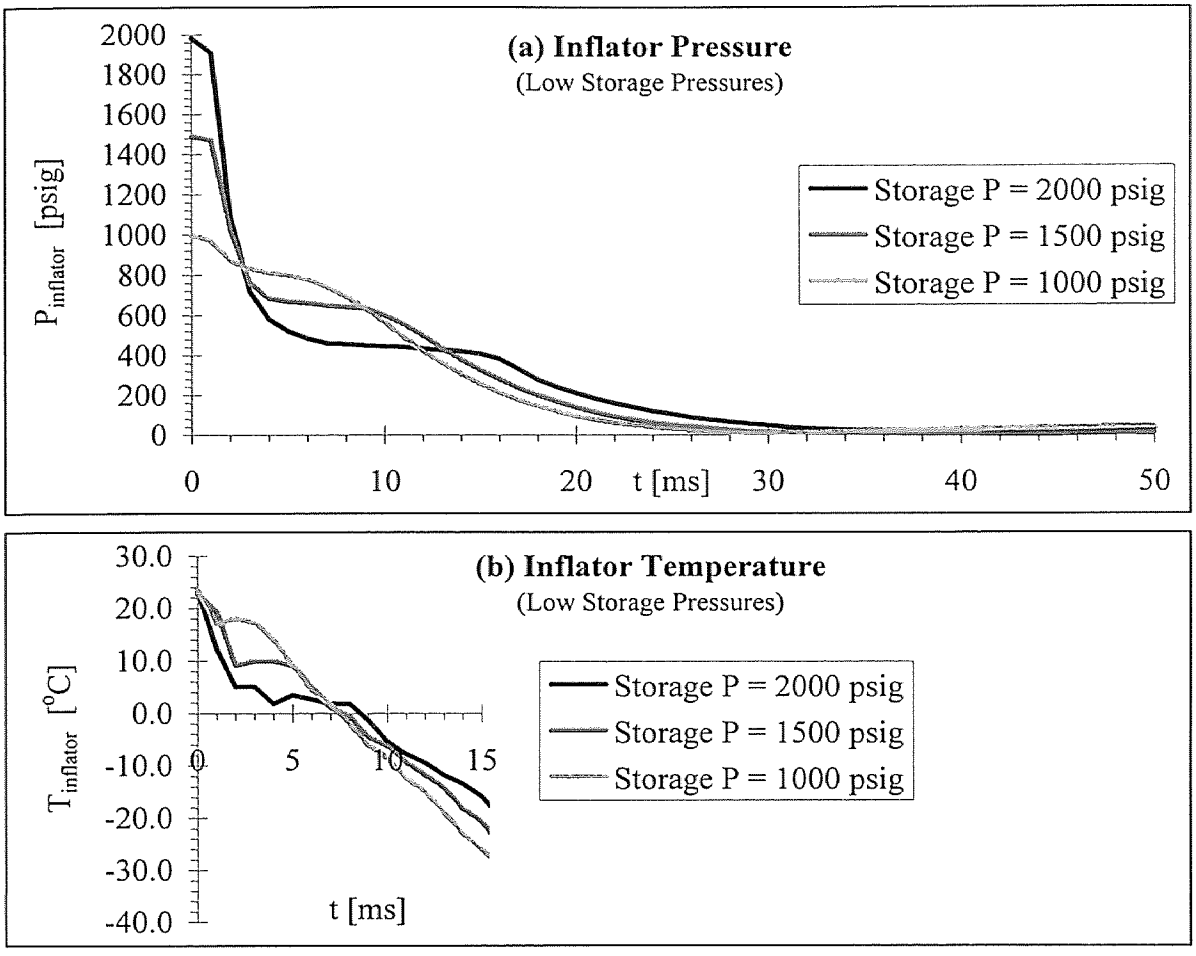

Figure 4.9 Inflator Measurements for Experiments 1-3 of Table 4.4

Figure 4.9 contains the curves corresponding to the inflator measurements for the first three experiments of Table 4.4. Since the signal from the inflator thermocouple is only reliable during the initial stages of the process (§2.2.5), the corresponding temperature curves are shown for the first 15 ms of the inflation sequence. Figure 4.9 shows that both the inflator pressure and temperature at the end of the rapid depressurization increase with a decrease in storage pressure. Furthermore, The duration of the horizontal plateau in the inflator pressure curve increases with the initial inflator pressure. Finally, the last stage in the inflator pressure curve (i.e. the relatively slow decrease to ambient pressure) lasts longer for low initial inflator pressures. These observations will be explained by means of a T-s phase diagram of the metastable region of CO_2 in section §4.3.2.1.

4.2.3.2 Effect of Initial Inflator Temperature: The results of four different experiments are presented in this section, see Table 4.5. The first three columns list the initial inflator conditions, while the last three columns contain the results of the calculation of the amount and average specific internal energy of the condensate that is formed during the inflation sequence. During all experiments, the inflator pressure, the average tank temperature and the tank pressure were recorded.

Figure 4.10(a-c) contains the measurements corresponding to the experiments in Table 4.5. With respect to the tank pressure curves, increasing the initial inflator temperature has two effects. First, the speed of the initial pressure rise in the curve increases with increasing initial inflator temperature. Second, the pressure at the end of

the first stage in the curve decreases for higher initial temperatures. The latter is the result of the lower initial amount of CO_2 in the inflator, as listed in the 4th column of Table 4.5.

Table 4.5 Experiments at Increased Initial Inflator Temperature

	Initial $P_{inflator}$ [bar] (psig)	Initial $T_{inflator}$ [°C]	$m_{inflator}$ (*) [g]	m_{cond} [g]	m_{cond} [%]	u_{cond} [kJ/kg]
1	139 (2000)	20	23.9	7.1	30	185.8
2	139 (2000)	31	22.5	5.9	26	255.6
3	139 (2000)	50	19.6	4.3	18	340.2
4	139 (2000)	70	15.7	2.9	12	471.6

(*) Calculated from equilibrium measurements.

The inflator pressure measurements (Figure 4.10b) show a gradual disappearance of the horizontal plateau in the curve with increasing initial inflator temperature. At the same time, the depressurization rate after the complete opening of the release mechanism decreases. In addition, the duration of the entire evacuation sequence decreases for higher initial inflator temperatures. The measurement of the average tank temperature (Figure 4.10c) shows little difference between the reference curve and the one corresponding to an initial inflator temperature of 31 °C. At an initial inflator temperature of 50 °C, the drop in average temperature occurs slower, but virtually the same temperature is reached after the completion of the inflation sequence as in the experiment at 30 °C initial inflator temperature. A further increase in initial inflator temperature results in an even slower drop in average temperature. Also, the temperature after the evacuation of the inflator is complete, is considerably higher, as shown for the curve corresponding to an initial inflator temperature of 70 °C.

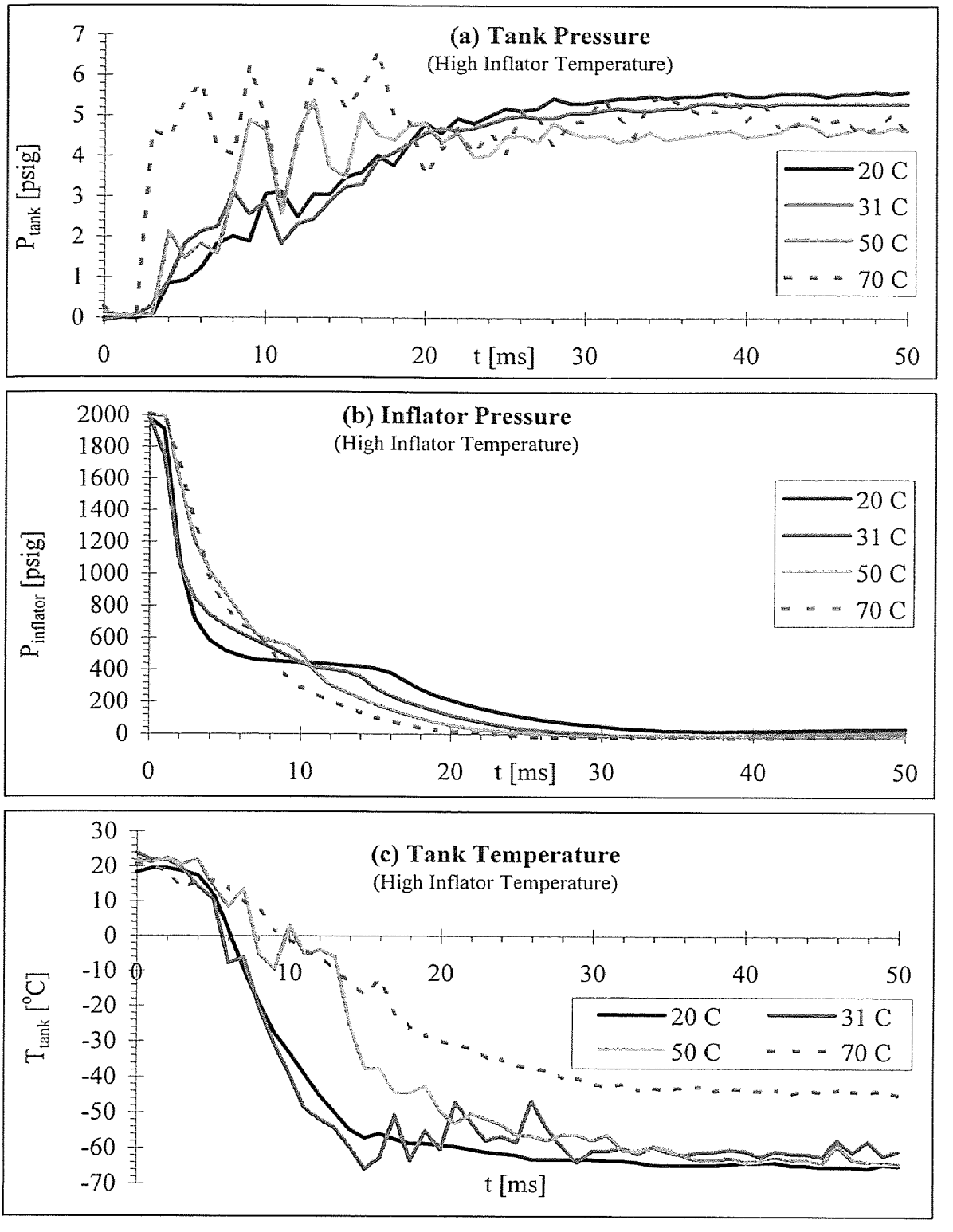

Figure 4.10 Effect of Initial Inflator Temperature

The generated vapor mass curves, calculated from the previous experimental results, are presented in Figure 4.11. While the experiments with an initial inflator temperature below 70 °C show a similar rate of vapor generation, the maximum value at the end of the inflation sequence (at about 30 ms) increases slightly with the initial temperature of the inflator. The vapor generation rate in the experiment with an initial inflator temperature of 70 °C is considerably higher and at the end of the inflation sequence, more than 80% of the initial amount of CO_2 is transformed into vapor.

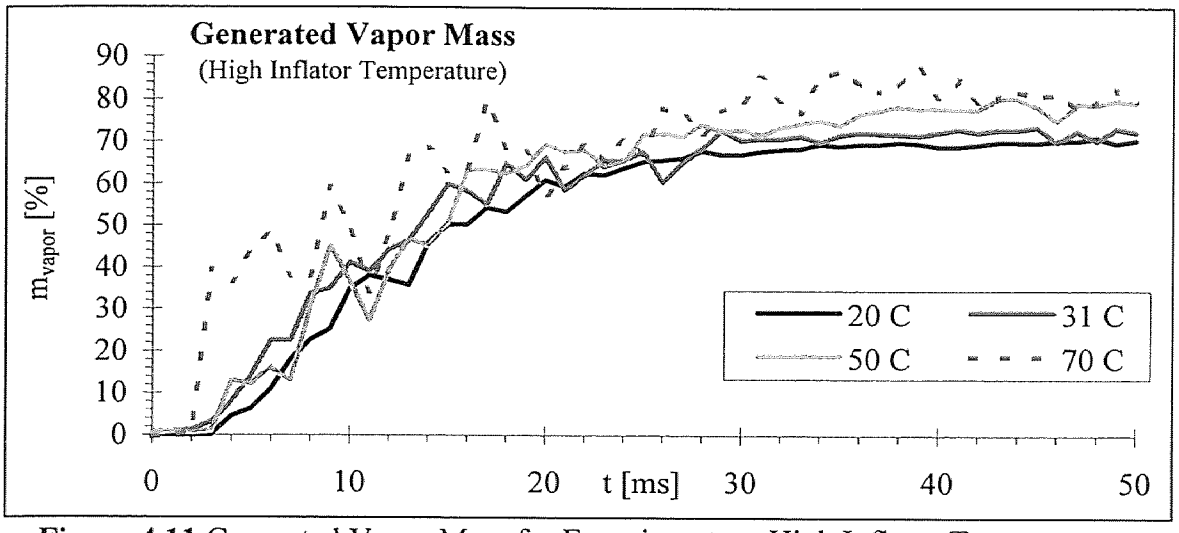

Figure 4.11 Generated Vapor Mass for Experiments at High Inflator Temperature

The visual observations of the formation of condensate in the tank were similar for the first two experiments of Table 4.5. Scattered snow deposits were formed in both cases and no difference in the amount was observed. No snow agglomerates were observed in experiment 3. Instead, the tank was temporarily filled with fog (for approx. 1.5 s). In experiment 4, hardly any fog or other form of condensate was formed. These visual observations agree with the results of the calculation of the properties of the

formed condensate, as listed in the last three columns of Table 4.5. Only in the Reference Experiment, solid condensate is produced. In all other cases, the condensate exists as a liquid or as a mixture of solid and liquid. The amount of condensate decreases with increasing initial inflator temperature and at temperatures above 70 °C, virtually no condensate is formed. The uncertainty of the calculated average specific internal energy increases with decreasing amount of condensate. Hence, the values in the last column of Table 4.5 become uncertain for higher initial inflator temperatures.

4.2.3.3 Effect of Initial Inflator Size: To study the influence of the initial volume of the inflator, experiments were conducted with the large inflator assembly (100 ml vessel and Nozzle A, §2.2.1 and §2.2.2). Table 4.6 summarizes the initial conditions of the experiments under consideration. The results are presented in Figure 4.12.

Table 4.6 Experiments with Large Inflator Vessel

	Initial $P_{inflator}$ [bar] (psig)	Initial $T_{inflator}$ [°C]	$m_{inflator}$ (*) [g]
1	70.0 (1000)	27.6	78.0
2	104.4 (1500)	27.0	91.5
3	138.9 (2000)	25.2	97.8

(*) Calculated using the tabulated density in [12] and the known vessel volume.

The opening time of the release mechanism is negligible in comparison with the duration of the inflation sequence and is not observed in the pressure curve. Similar to the experiments with the small inflator vessel, the pressure rise occurs in 2 stages with a considerably different rate of pressure increase. Both the duration of the first pressure rise

and the pressure at the onset of the slower part of the curve increase with the initial inflator pressure.

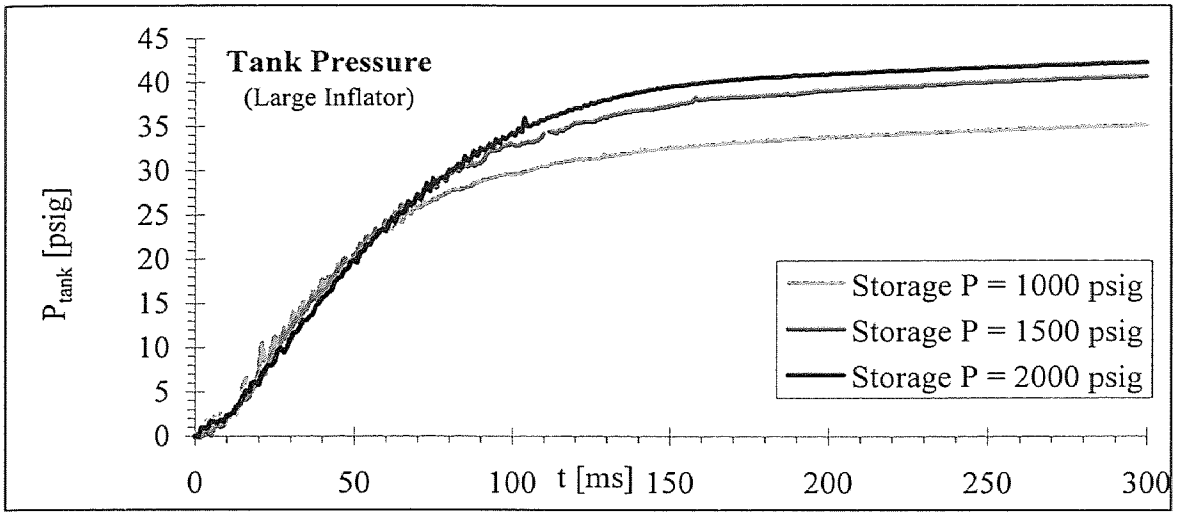

Figure 4.12 Effect of Inflator Vessel Volume

Furthermore, the results illustrate clearly that a considerably higher tank pressure can be achieved when a larger inflator is used.

4.2.4 Results of the High-Speed Cinematography

The experimental set-up and procedure of the high-speed cinematography studies were discussed in section §2.5. Three different types of recordings were made:

a) observations of the tank phenomena as they occur during the main experiments

b) observations of the two-phase spray from the nozzle, freely expanding in a stagnant N_2 atmosphere

c) observations of the flow just outside a nozzle exit hole

These three types of recordings were made for the Reference Experiment and for an experiment in which 10% (mass%) methanol was added to the system. Hence, a total of six different recordings was obtained, see Table 4.7.

Table 4.7 Summary of High-Speed Cinematographic Studies

	Recording #	Type	Duration [ms]	Imaging Rate [frames/s]
Ref. Exp.	1	Tank Phenomena	5100	1000
	2	Spray	800	250
	3	Nozzle Exit Hole	456	250
10% MeOH Exp.	4	Tank Phenomena	12040	1000
	5	Spray	720	250
	6	Nozzle Exit Hole	840	250

This section contains a brief description of the observations of the tank phenomena during the main experiments, based on recordings 1&4 of Table 4.7. The external characteristics of the spray were determined from recordings 2&5 of Table 4.7. The results about the spray penetration[1], the maximum spray width, and the spray angle are presented. At the end of this section, a description of the images concerning the nozzle exit hole is included (recordings 3&6 of Table 4.7).

4.2.4.1 Observations of the Tank Phenomena during the Main Experiments: A detailed description of each recording was made on a frame to frame basis. This section contains a summary of the descriptions of recordings 1&4 of Table 4.7.

[1] The *penetration* of a spray is defined as the maximum distance it reaches when injected into stagnant air.

Reference Experiment: The inflation sequence in the tank commences with the simultaneous appearance of the 4 jets from the nozzle. Based on the imaging rate and the length of the sprays, the penetration velocity of the jets was estimated at about 75 m/s. At this high speed, the sprays reach the side of the receiving tank in about 1 ms after their appearance. During the first millisecond, they are slightly divergent-convergent in shape, with a maximum width of about 20 mm, which is reached at about half of their length. The opacity of the jets is fairly uniform, with a denser region in the center of the sprays. After the first millisecond, the sprays hit the sides of the tank and spread both upwards and downwards along the inner wall of the tank. At the same time, a dense fog develops near the bottom plate and starts to obscure the observations. At about 6 ms after the initial appearance of the sprays, the entire tank is filled with a dense fog and intense mixing of the gases can be observed. The impact of the jets on the sides of the tank is still clearly visible. The first snow agglomerates on the sides of the tank are observed at 23 ms after the start of the experiment. At that time, the mixing of the gases in the tank continues, but it is not clear whether the jets from the nozzle still reach the side walls of the tank. In the interval from 23-33 ms, the initial snow agglomerate grows and the mixing continues. Although it is difficult to determine accurately, it is estimated that the jets from the nozzle ended shortly after the formation of the first snow agglomerates. A secondary jet[(2)] , causing a local clearing in the fog, appears about 70 ms after the start of the experiment. By that time, additional snow agglomerates have been formed and seem to have reached their maximum size. Also, the intensity of the mixing in the tank has decreased considerably. The fog in the tank lifts partially from about 120-140 ms after the start of

[(2)] The initial jet is referred to as the *primary* jet, while all jets appearing after that are called *secondary* jets.

the experiment. After that, the density of the fog remains fairly constant. A second, less powerful, secondary jet is observed around 150 ms. At that time, the snow agglomerates are still present and no significant sublimation has occurred. It is only at about 3900 ms after the start of the experiment that all condensate has sublimated. At that time, a light fog is still present in the tank.

CO_2-Methanol Experiment: Similar to the Reference Experiment, the inflation sequence starts with the simultaneous appearance of the 4 jets from the nozzle. In contrast to above, a significant difference in the size of the jets is observed. After 1 ms, the jets are barely touching the sides of the tank and the penetration velocity is estimated at about 70 m/s. With respect to the Reference Experiment, no significant difference in shape, dimension or opacity of the jets was observed. The asymmetry of the sprays is more pronounced at 2 ms after the start of the experiment, although all jets are touching the sides of the tank and spreading upwards and downwards along the tank wall. After 3 ms, the asymmetry has disappeared and a fog starts to develop a short distance above the bottom plate. During the next 3 ms, the fog fills the tank, but remains less dense than in the Reference Experiment. At the same time, an intense swirling motion of the gases in the tank is visible. At 26 ms after the start of the experiment, the primary jets lose strength and die out soon after. The fog gradually becomes denser, but no snow formation, except for an isolated agglomerate which sublimates within 50 ms, is observed. About 1 s after the first appearance of the jets, methanol can be observed on the sides of the tank, as it slowly runs down towards the bottom plate. At this time, the dense fog is still present and it obscures all inner parts of the tank. Only after about 6.5 s in the experiment, the fog slowly clears.

4.2.4.2 External Spray Characteristics: Based on recordings 2&5 of Table 4.7, measurements of the external spray characteristics were performed. These characteristics include the spray penetration (l), the maximum spray width (w) and the spray angle (θ). The results of the measurements are presented in Figure 4.13.

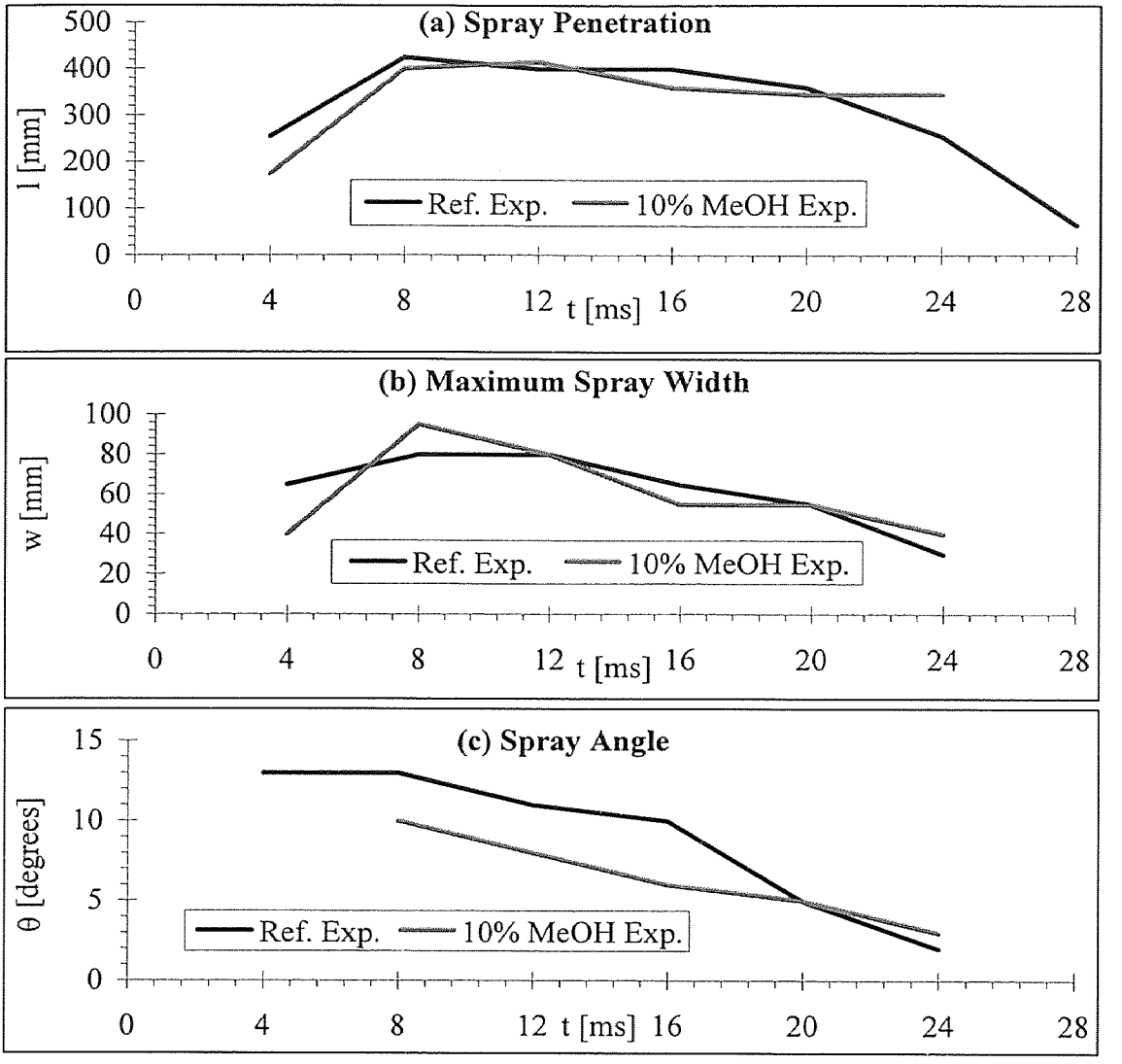

Figure 4.13 External Spray Characteristics

The spray angle was measured between the axis of the nozzle exit hole and the line that connects the point of maximum spray width with the edge of the nozzle exit hole. Since

the recordings were not synchronized with the activation of the opening mechanism, a small shift in time between the two curves of Figure 4.13 is likely to have occurred.

Figure 4.14 shows six consecutive frames of the spray images, recorded during the experiment in which methanol was added to the system (recording 5 of Table 4.7). The nozzle exit hole is located near the bottom right corner of the images and the jet expands freely in a stagnant N_2 atmosphere. The figure contains the negatives of the original recordings, and the contrast was slightly enhanced. These images are included as examples of the spray images and show the evolution of the shape and the density of the jet during the inflation sequence. The actual measurements of the external characteristics were performed on the original images, which are larger and of better quality.

As shown, the spray was symmetrical over almost its entire length. Only at the very tip, protrusions up- or downwards could be observed. In both recordings (2&5 in Table 4.7), the spray died out between 28-32 ms. During the first 8 ms, a *growth phase* was observed, in which the spray reached its maximum penetration and maximum width. While the spray penetration remained fairly constant until 20-24 ms after the start of the expansion, the density, the spray width and the spray angle slowly decreased after the end of the growth phase. Hence, the stage from 8-28 or 32 ms will be referred to as the *decay phase* of the spray. The orientation of the jet remained relatively constant during the entire sequence, although a tendency to move upwards near the end of the expansion was observed.

Both the images and the measured external spray characteristics (Figure 4.13) show no significant difference between the Reference and the methanol experiment.

Therefore, it is concluded that the addition of an organic liquid to the CO_2 prior to expansion does not influence the atomization mechanism.

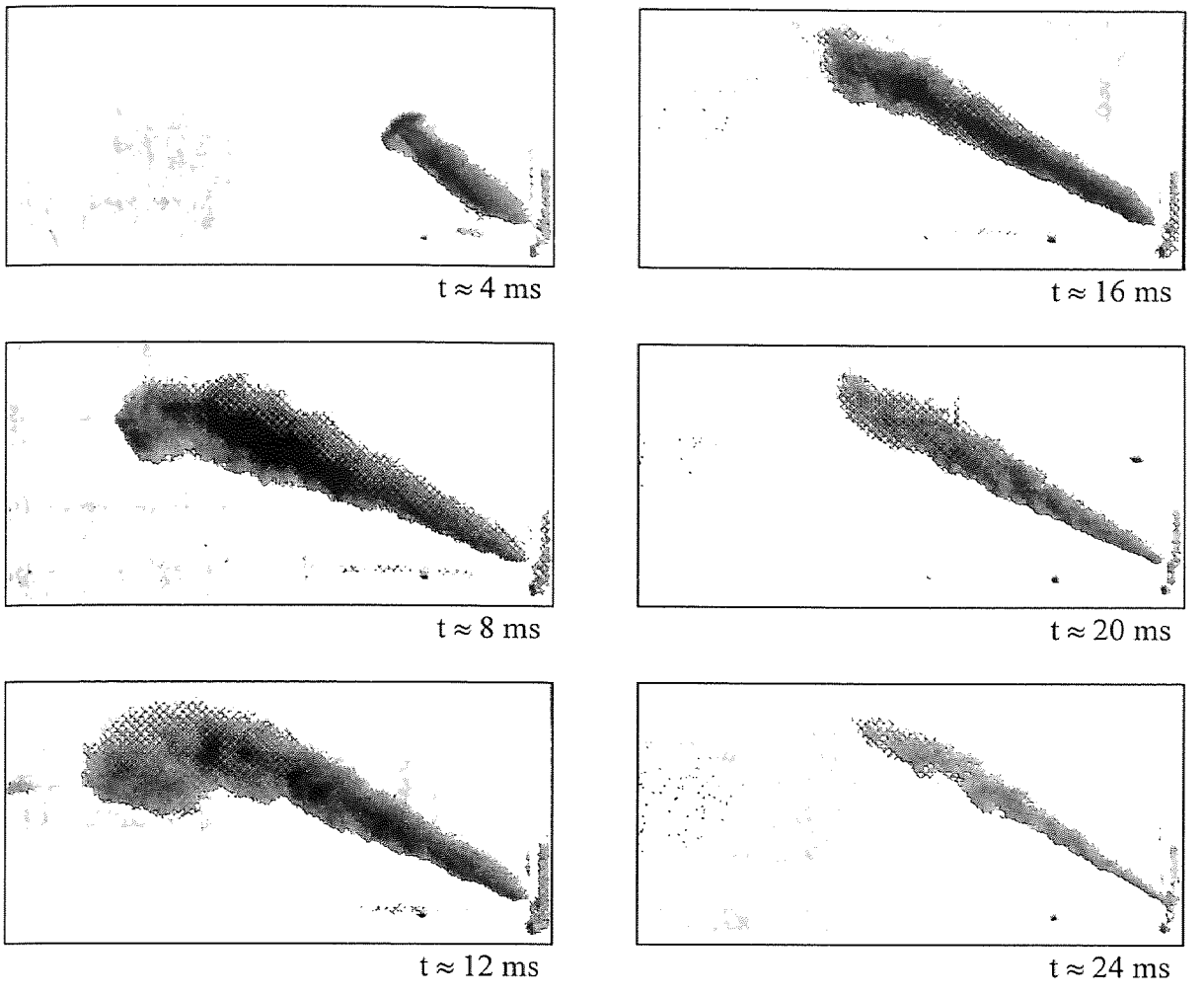

Figure 4.14 Spray Images

4.2.4.3 Nozzle Exit Recordings: In the first place, these recordings were made to accurately determine the lifetime of the primary spray from the nozzle. Furthermore, they

were expected to provide additional information on the radial expansion of the jet, which is indicative for the importance of flash atomization [62,64].

In agreement with previous observations, no significant difference could be found between the Reference Experiment and the experiment in which methanol was added to the system. In both cases, the total lifetime of the primary spray was 32-36 ms. During the last 4 ms, the intensity of the spray is very low. This explains why earlier observations failed to show the primary jet after 32 ms. During the growth phase and in the beginning of the decay phase, considerable radial expansion is observed. It occurs mainly in a region immediately downstream of the nozzle hole. In the second half of the experiment (after about 16 ms), the radial expansion decreases and the spray diameter reduces to the diameter of the exit hole. At the same time, the density of the spray decreases. After the primary spray has died out, typically a phase follows in which scattered particles exit the nozzle at low velocity. The size of the particles varies considerably but is less than 500 μm. This phase is followed by a secondary jet, or a phase in which neither a spray or particles exit the nozzle. The pattern of particle ejection, followed by a secondary spray or a phase in which no material exits the nozzle, is repeated several times and can last up to 400 ms after the activation of the release mechanism. In comparison with the primary jet, the strength and the intensity of the secondary sprays and the ejected particulate is negligible.

4.2.5 Influence of Small Amounts of Organic Liquids

A series of experiments was performed in which different organic liquids were added to the CO_2 in the inflator prior to the expansion. Different amounts and types of organic

liquids were investigated. Originally, the solvents were added in an attempt to avoid or delay the solidification of the CO_2 in the inflator at the end of the evacuation process. It was expected that an additional amount of CO_2 vapor could be produced in this manner. In the present work, it was discovered that small amounts of organic liquids have a drastic beneficial influence on the tank pressure and temperature evolution during the inflation sequence. No earlier reference to this phenomenon was found in the literature. A detailed study of the physics of this novel effect lies beyond the scope of this work. Hence, the phenomenon is introduced in this section by means of some key experiments and only a qualitative explanation is provided in the second part of this chapter.

Table 4.8 Experiments with CO_2/Organic Liquid Mixtures

	Solvent	Formula	solv. vol. [ml]	mass%(*)	mole fraction [/]
1	Methanol	CH_3OH	1.42	5	0.06
2	Methanol	CH_3OH	2.83	10	0.11
3	Acetone	CH_3COCH_3	1.52	5	0.04
4	Ethylacetate	$CH_3CO_2C_2H_5$	1.30	5	0.02

(*) With reference to the amount of CO_2, taken as 23.5 g.

Table 4.8 contains information about the organic liquids that were used in the experiments which are considered in the current section. The initial conditions of the inflator and tank were identical to those of the Reference Experiment (Table 2.3).

4.2.5.1 Effect of Different Amounts of Methanol: Figure 4.15 contains the tank measurements for experiments 1&2 of Table 4.8, and illustrates the effect of an increasing amount of methanol added to the system.

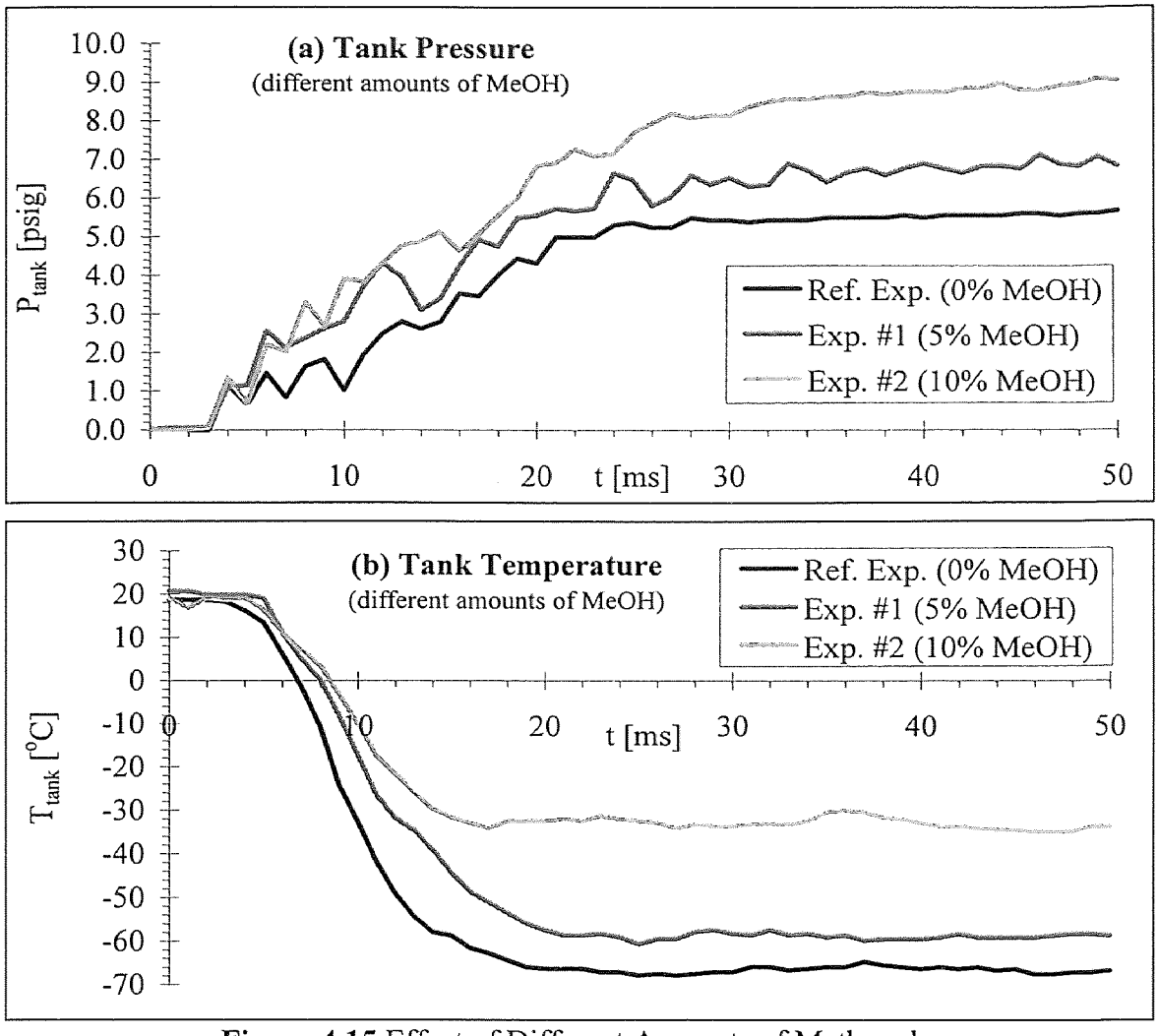

Figure 4.15 Effect of Different Amounts of Methanol

The tank pressure curves show a significant increase in pressure for the cases where methanol was added to the system. With respect to the Reference Experiment, the pressure at the end of the fast rise of the curve increased by 1.0 psig (19%) and 2.4 psig (45%) for the case of 5% and 10% methanol, respectively. A change in the slope of the slow rise in the curve can also be observed. An equally drastic change in the evolution of the average tank temperature is shown in Figure 4.15(b). Relative to the Reference

Experiment, the average temperature at the end of the actual evacuation of the vessel (at about 25-30 ms) increased by 7 °C and 31 °C in experiment 1 and 2, respectively.

For the experiments of Table 4.8, inflator pressure curves did not differ significantly from the one corresponding to the Reference Experiment. The generated vapor mass, calculated from the curves in Figure 4.15 and neglecting the vapor pressure of methanol, showed a slight increase at the end of the evacuation process, relative to the Reference Experiment. However, the main part of the increase in tank pressure is caused by the higher temperature at the end of the inflation. No snow was formed in either experiment 1 or 2. Instead a dense, white fog filled the tank after the inflation. While it never cleared completely, it started to disappear at about 6 s after the activation of the inflator.

At higher concentrations of methanol, the pressure effect is observed to decrease. It is believed that this is caused by the decreasing initial amount of CO_2 in the inflator as more methanol is added.

4.2.5.2 Effect of Different Organic Liquids: The effect of different organic liquids at a constant concentration of 5% (mass) is compared in Figure 4.16, which contains the tank curves of experiment 1,3 and 4 of Table 4.8.

At the end of the inflation sequence, the acetone experiment shows the highest tank pressure. Also in the corresponding average tank temperature curves, the effect of acetone is the largest. Similar as before, no significant difference in the inflator pressure or generated vapor mass curves could be observed. The same observations concerning the

formation of condensate as in the methanol experiments hold for the cases where other solvents were used.

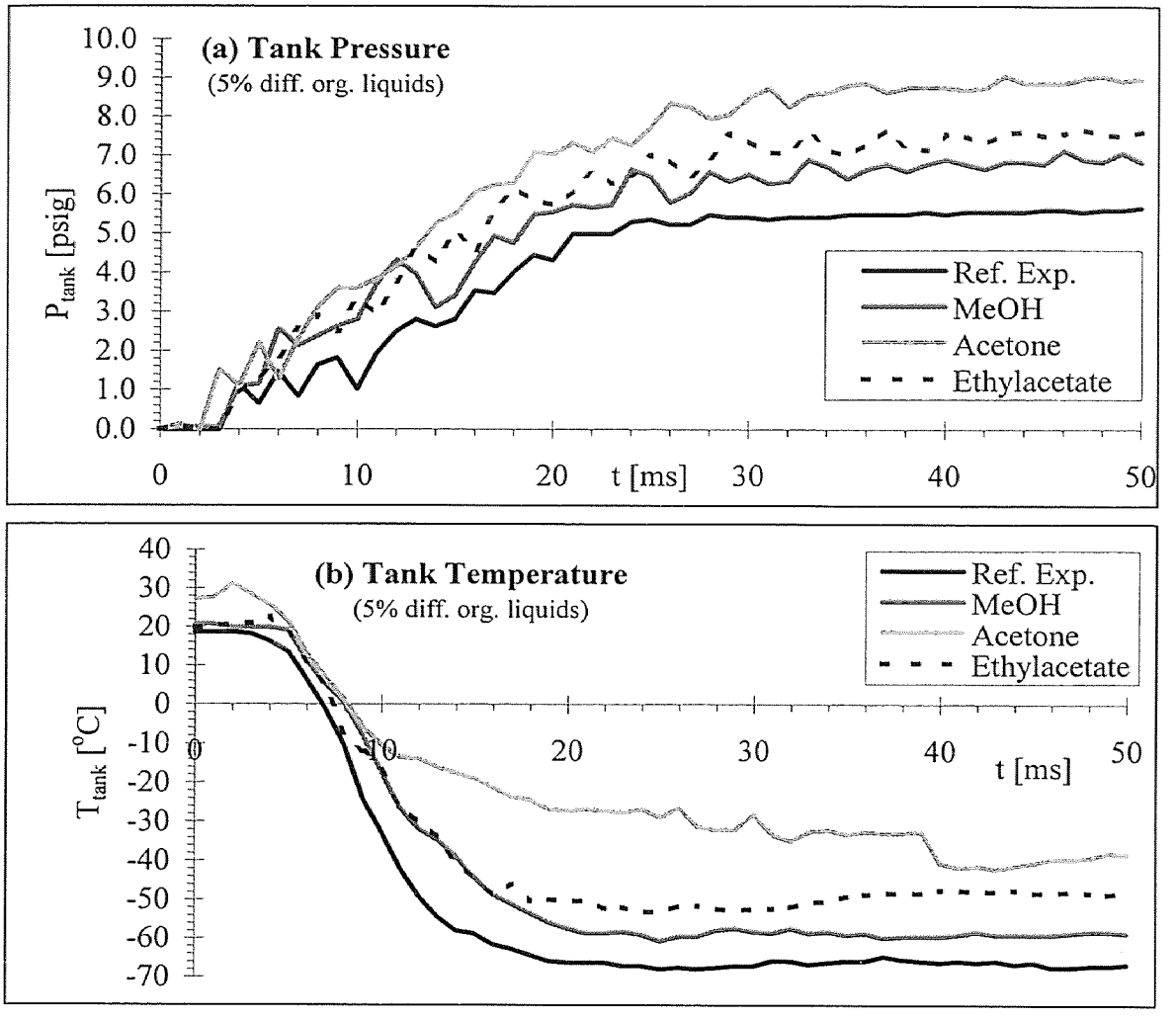

Figure 4.16 Effect of Different Organic Liquids at 5% (mass) Concentration

The complete experimental study of this phenomenon includes experiments at higher concentrations (15 and 20% mass) and using ethanol and propanol. The effect of ethanol and propanol was similar to the one described in the above. However, at higher

concentrations (20% mass), the pressure effect continued to increase, in contrast to the observations with methanol.

4.3 Discussion

The qualitative model of the SLG-Inflator is presented in this section. The model describes the interaction of the dominant physical phenomena in the various components of the system and provides a qualitative explanation of the experimental results that were presented in section §4.2.

First, the model is introduced with the aid of the curves corresponding to the tank and inflator measurements of the Reference Experiment. Four characteristic stages in the inflation sequence are identified. Second, the experimental results regarding the influence of the initial inflator conditions, the effect of a reduction in the critical flow section and the influence of the initial tank conditions are discussed based on this qualitative model.

4.3.1 Qualitative Model of the Stored Liquefied Gas Inflator

The qualitative model of the system is presented by means of Figure 4.17, which combines the measurements of the Reference Experiment with the results of the high-speed cinematographic study of the lifetime and properties of the spray. The latter is represented symbolically at the bottom of the figure and the two characteristic phases in the jet are indicated. Since a *qualitative* model is presented, no numerical values for the pressure and temperature are given. Four characteristic stages are identified. The transitions between these stages coincide with the transitions between the characteristic stages in the inflator pressure curve. The last part of the curves is colored gray since it is

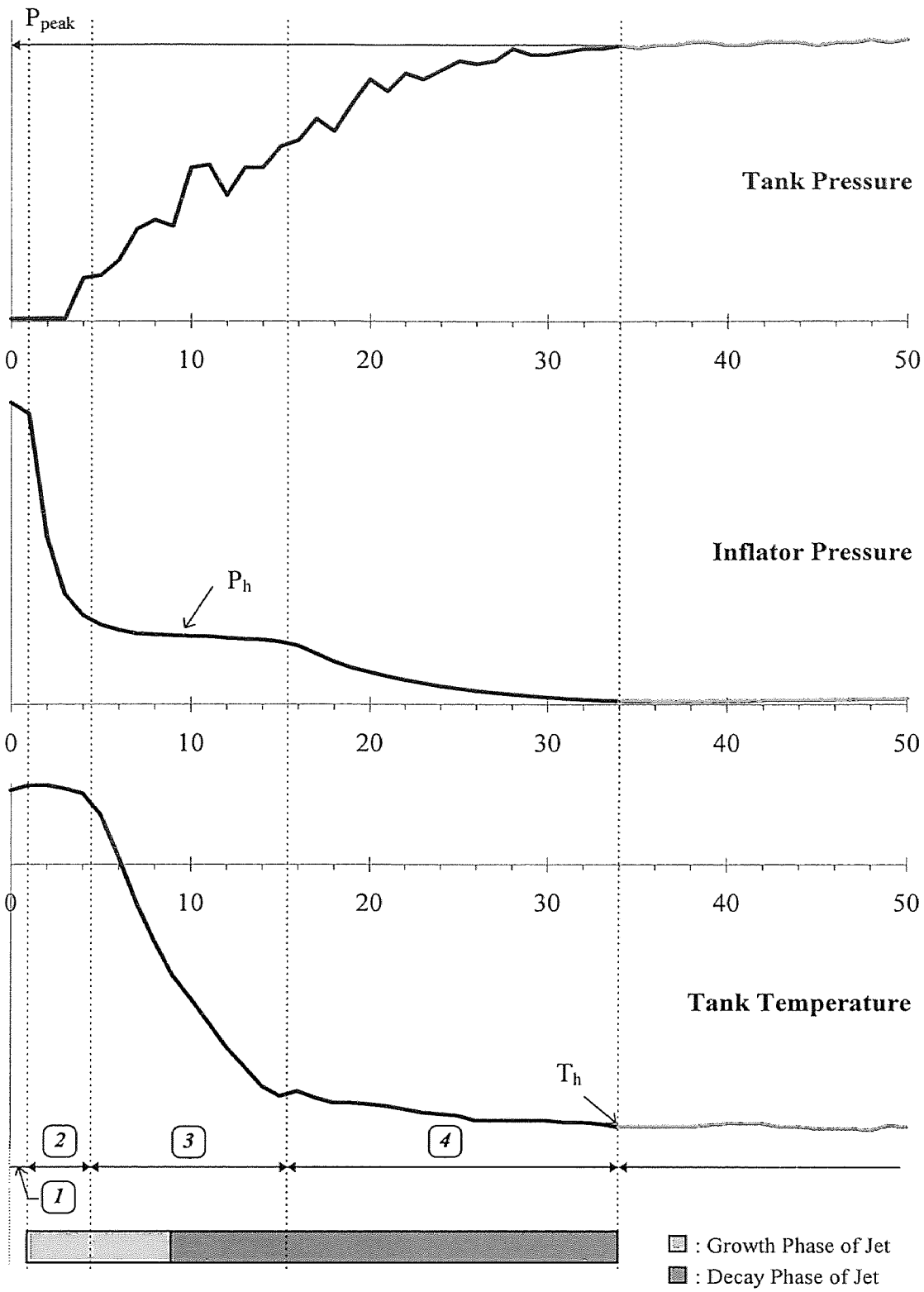

Figure 4.17 General Qualitative Model

not a part of the actual inflation sequence. After the end of the inflation sequence, heat transfer from the tank and inflator walls brings the system slowly towards equilibrium with the surroundings. The understanding of the system is introduced by describing the relevant phenomena and their interactions during each stage in the inflation sequence. Only the nominal initial conditions are considered during the description of the model (Table 2.3). The influence of different initial conditions in the inflator and tank is discussed later (sections §4.3.2-4.3.4).

4.3.1.1. Stage 1: ***Opening of the Release Mechanism and Initial Depressurization:*** The first stage in the inflation sequence corresponds to the relatively slow initial pressure drop in the inflator, which is related to the opening of the release mechanism. A cross sectional drawing of the inflator and the nozzle is shown in Figure 4.18. It represents the state of the system during this first stage. The pressure and temperature transducer are indicated by 'P' and 'T', respectively.

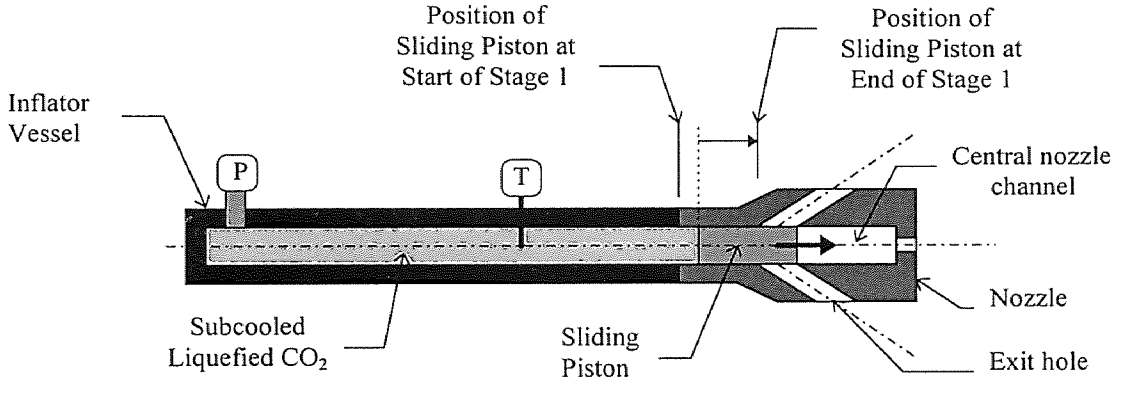

Figure 4.18 Phenomena during Stage 1 of the Inflation Sequence

The first stage is initiated when the shim in the release mechanism is ruptured, and lasts until the sliding piston reaches the lower edge of the exit holes inside the nozzle (Figure 4.18). A dynamic analysis of the motion of the sliding piston was presented in section §2.2.2.1. Based on this analysis, the duration of the first stage in the inflation sequence was calculated to be 1.3 ms for an initial inflator pressure of 2000 psig. This is in close agreement with the inflator pressure curve of Figure 4.17. During the entire first stage, the sliding piston blocks the exit holes and there is no flow from the nozzle. As a result, the tank conditions remain unchanged (Figure 4.17).

As the sliding piston moves, the liquefied CO_2 in the inflator expands isentropically and fills the growing space in the central channel of the nozzle. This isentropic expansion propagates through the inflator as a relatively flat rarefaction wave from the nozzle towards the closed end of the vessel and generates a non-uniform pressure and temperature distribution along the axis of the inflator. The pressure profile is such that the value at the location of the pressure transducer remains close to the initial pressure, while the pressure near the nozzle drops to a lower value. For the nominal initial inflator conditions (P_0=2000 psig; $T_0 \approx 22$ °C, Table 2.3), the pressure in the inflator remains above the saturation pressure at the corresponding local temperature. Therefore, at the end of the first stage, the CO_2 in the inflator remains in the subcooled liquid phase and no nucleation occurs up to this point.

4.3.1.2 Stage 2: ***Passage of the Forerunner and Initial Vapor Generation:*** The second stage of the inflation sequence is characterized by a rapid drop in the inflator pressure.

Based on Figure 4.17, a maximum depressurization rate of 55 bar/ms was estimated. This is considerably higher than most other blowdown studies [11,37,40,42].

At the start of the second stage, the sliding piston has reached the lower edge of the exit holes. According to the dynamic analysis of the release mechanism, it takes an additional 0.12 ms to reach the upper edge and clear the exit holes completely. Figure 4.19 contains a cross sectional drawing of the system, after the nozzle exit holes have been cleared completely. Note that 'e' represents the void fraction of the two-phase mixture.

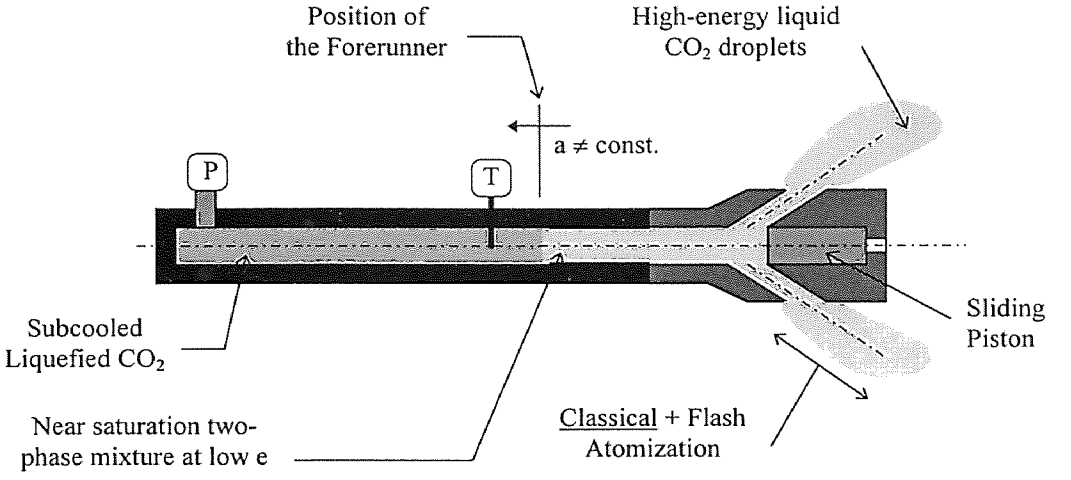

Figure 4.19 Phenomena during Stage 2 of the Inflation Sequence

The clearing of the exit holes initiates a second rarefaction wave in the inflator, traveling from the nozzle to the closed end at the local speed of sound (a). This wave corresponds to the *elastic forerunner*, as discussed in similar studies [47,63,86]. References [47,63] consider the flashing outflow of initially uniform subcooled water from a long tube which is instantaneously opened at one end at the beginning of the process. In the above studies, because of the zero opening time and the uniform initial

conditions, the forerunner consists of a steep depressurization wave which propagates at a constant velocity (equal to the local sonic velocity of liquid water, i.e. about 1000 m/s).

The passage of the forerunner in the SLG-inflator differs from that in [47,63] in two ways. First, as indicated earlier, a non-uniform pressure and temperature profile is generated during the first stage of the inflation sequence. In turn, this profile leads to a non-uniform local sonic velocity and the forerunner in the inflator is expected to gradually speed up as it propagates towards the closed end. Second, the finite opening time of the release mechanism is expected to lead to a flattened forerunner [63].

The forerunner brings about a rapid isentropic expansion of the subcooled liquid CO_2 in the inflator. Immediately downstream of the forerunner, the CO_2 exists as a metastable, superheated liquid. The amplitude of the superheat, i.e. the penetration depth in the metastable liquid region, depends on the local nucleation characteristics, as described by nucleation theories [20,29,57]. It is generally accepted that homogeneous nucleation is only possible in experiments with tightly controlled conditions (i.e. an extremely clean apparatus and working fluid) [29]. In case of homogeneous nucleation, the penetration in the metastable liquid is maximum and the liquid spinodal state is attained [20,57]. The subsequent return towards equilibrium is characterized by a very brief (approx. 1 μs [52]) and violent evaporation. In nearly all practical systems, heterogeneous nucleation initiates evaporation [14,20,29]. Studies of blowdown experiments for vessels with a small volume to internal surface ratio, have shown that nucleation predominantly occurs at the walls of the container as well as at the liquid-vapor interface [21,29]. In vessels with a large volume to internal surface ratio, heterogeneous nucleation occurs predominantly on the dissolved gases and other

impurities (particles) in the bulk of the liquid. Based on these considerations, it is expected that the nucleation in the inflator occurs mainly at the vessel walls. The nucleation rate[3] depends strongly on the local superheat and the interfacial tension [20]. In addition, it is influenced by the depressurization rate and the wall material and surface finish of the inflator vessel. In general, the delay in nucleation increases with the depressurization rate [11]. Immediately after the formation of the nuclei, intense evaporation takes place. This leads to a drastic reduction of the local superheat and causes the nucleation to cease. Therefore, nucleation occurs only at the maximum pressure undershoot near the end of the forerunner and is suppressed immediately after by intense evaporation. The latter diminishes the degree of non-equilibrium in the CO_2 liquid-vapor mixture and brings the system closer to saturation conditions. However, due to the short duration of this evaporation, only a limited void fraction is developed (Figure 4.19). This series of events is initiated at the open end of the inflator at the start of the second stage and travels at the local speed of sound towards the closed end.

Near the end of the second stage in the inflation sequence, the forerunner reaches the closed end of the inflator and is reflected towards the nozzle. This results in a local pressure drop and an enhanced evaporation which, in turn, attenuates the forerunner and causes it to die out soon after [63]. The gradual stabilization of the inflator pressure curve at the end of the second stage (Figure 4.17) is believed to be the result of two effects.

---

[3] The *nucleation rate* is defined as the volumetric rate at which evaporation nuclei are formed and is calculated by means of nucleation theories [20,29].

On the one hand, the response time of the pressure transducer exceeds the time interval in which the maximum pressure undershoot and subsequent nucleation and intense evaporation occurs. Therefore, these phenomena could not be observed in the inflator pressure curve. On the other hand, the transducer is located near the closed end of the inflator (Figure 4.19), and indicates the resulting pressure of the complex interaction between the reflection and the original forerunner. This complex interaction makes it impossible to predict the behavior of the inflator pressure without the use of sophisticated simulations.

The jets from the nozzle enter the tank shortly after the onset of the second stage in the inflation sequence (Figure 4.19). Since the ejection of the fluid occurs immediately after the nucleation and initial evaporation take place, these jets consist almost entirely of high-energy liquid. The relatively large density of the liquid phase leads to a high mass flow rate and a relatively slow acceleration of the flow. The dispersion of this high-energy liquid in the tank occurs primarily by classical atomization (i.e. driven by hydrodynamic forces between the rapidly moving liquid and the stagnant tank gas) [56]. At the same time, some degree of flash atomization occurs [6,76]. This description of the dispersion process is consistent with the high-speed cinematographic recordings of the spray during the growth phase of the jets. The radial expansion, which is observed in the recordings of the nozzle exit hole, is typical of a flashing spray and indicates flash atomization [62,64]. At the same time, the external spray characteristics (i.e. a long, narrow cigar-shaped spray), as shown in the general spray images and in the measurements of the external spray characteristics (Figure 4.13), indicate classical atomization of the liquid jets [6,56]. Because of the high temperature of the dispersed liquid, the generated droplets are

expected to evaporate quickly and generate relatively warm CO_2 vapor. The evaporation of the liquid CO_2 droplets is discussed in detail during the description of the next stage in the inflation sequence.

4.3.1.3 Stage 3: ***Passage of the Evaporation Wave and Main Discharge:*** The horizontal plateau in the inflator pressure curve (at pressure P_h), constitutes the third stage of the inflation sequence (Figure 4.17). A cross sectional drawing of the system during this stage is provided in Figure 4.20.

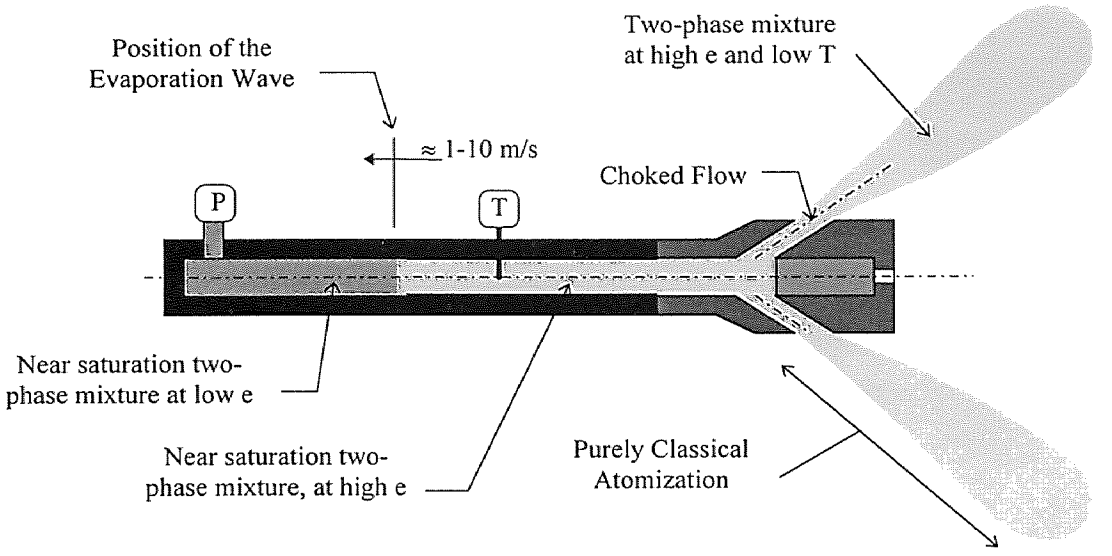

Figure 4.20 Phenomena during Stage 3 of the Inflation Sequence

At the end of the 2nd stage in the inflation sequence, the forerunner has propagated through the entire inflator and the latter is filled with a two-phase mixture at near saturation conditions. The flashing process continues in the two-phase mixture, and it is usually assumed that the rate of evaporation is limited by the thermal conductivity of the liquid [21,28]. The near saturation conditions, in combination with the relatively slow

heat conduction in the liquid, result in a slow evaporation. In turn, this leads to the horizontal part in the inflator pressure curve. This description is supported by the experimental data provided in section §4.2.3.1 (Figure 4.9). Both the inflator pressure and temperature measurements show a horizontal plateau during the third stage in the inflation sequence. Using tabulated properties of CO_2 [12], it can be verified that these horizontal plateaus correspond to conditions close to the liquid saturation line of the phase diagram. The duration and relative position of the horizontal plateaus will be explained when the influence of the initial inflator pressure is discussed (§4.3.2.1).

While evaporation proceeds slowly in the bulk of the inflator during the third stage, intense flashing occurs at the nozzle end of the vessel. The enhanced evaporation is the result of two effects. First, the outflow of the two-phase mixture causes a pressure drop near the nozzle end of the inflator and leads to increased flashing of the liquid. Second, bubble break-up occurs due to the growing bubble size and the increasing difference between the velocities of the liquid and the vapor phase in the accelerating flow. Because bubble break-up leads to a drastic increase in interfacial surface area, it enhances evaporation. The intense flashing in or near the nozzle causes a drastic increase in the local void fraction of the two-phase mixture. The lower inertia of this mixture at high void fraction leads to a swift acceleration and outflow. In turn, the latter results in a pressure drop and enhanced flashing in the inflator, at a location slightly closer towards the closed end of the vessel. The above illustrates that the interaction of the flashing process and the two-phase outflow through the phenomenon of bubble break-up creates an *evaporation wave* in the inflator [47,63]. This interfacial wave consists of a front in which intense evaporation and bubble break-up occur and propagates from the nozzle

towards the closed end of the inflator with a typical velocity of about 1-10 m/s [63]. The wave is marked by a sharp increase in the bubble number density and the void fraction.

The two-phase mixture, which is generated by the evaporation wave, has a high void fraction and a low inertia. Furthermore, because of the intense flashing in the interfacial wave, the temperature of this two-phase mixture is relatively low. In turn, this low temperature limits the flashing rate in the mixture downstream of the interfacial wave. Therefore, when this mixture is swiftly accelerated and the pressure behind the wave starts to drop, the evaporation rate is too low to sustain the pressure. Hence, a gradual pressure decrease occurs downstream of the evaporation wave. The passage of the evaporation wave at the location of the inflator pressure transducer marks the end of the third stage in the inflation sequence (Figure 4.17).

The above illustrates that the duration of the horizontal plateau in the inflator pressure curve is inversely proportional to the average propagation speed of the evaporation wave. Bearing the relevant phenomena in mind, it is clear that the speed of the evaporation wave increases with the void fraction of the upstream two-phase mixture.

During the third stage in Figure 4.17, the two-phase mixture downstream of the evaporation wave is ejected into the tank. Because of its low inertia, the mixture is accelerated swiftly and the critical flow rate is expected to be attained shortly after the onset of the third stage in the inflation sequence (i.e. the flow chokes).

Because of the low flashing rate, the dispersion of the two-phase mixture through the nozzle and in the tank occurs purely by classical atomization. This is confirmed by the high-speed cinematographic study of the spray. The latter shows little or no radial expansion of the spray, indicating the absence of flash atomization. Due to the presence

of the vapor in the spray, the dispersion is similar to that of a prefilming type airblast atomizer, where typically air is used to enhance the break-up of the liquid (i.e. the CO_2 vapor functions as the gas which assists the dispersion) [6,56,84].

Because of the low temperature downstream of the evaporation wave, the dispersed droplets will be cooler than the ones generated during the second stage of the inflation. Nevertheless, they remain fairly volatile and evaporate mainly according to the *transient* regime[(4)] [56]. As will be shown in §4.3.4, when the influence of the initial tank conditions is discussed, the interaction between the evaporating droplets and the tank gases depends primarily on the initial amount of internal energy in the tank. According to an energy analysis of the system, in experiments with low initial internal tank energy, nearly the entire amount of the latent heat of vaporization is supplied by the droplets. However, for experiments with high initial internal tank energy, a considerable fraction of the latent heat is supplied by the tank gases. In any case, the droplet temperature decreases as the evaporation progresses. When the droplet temperature attains the triple point, the liquid CO_2 freezes and turns into dry ice.

According to the above, the decrease in average tank temperature is mainly the result of two effects. On the one hand, the mixing of the generated cold CO_2 vapor and the tank gases leads to a drop in average tank temperature. On the other hand, a fraction of the internal energy of the tank gases is used to supply part of the latent heat of vaporization, and results also in a decrease of the average tank temperature.

[(4)] Droplets of low volatile liquids evaporate in a *steady state* regime, in which the internal temperature remains constant and the latent heat of vaporization is supplied entirely by the surrounding gas [56].

Additional cooling is caused by the Joule-Thomson effect when the CO_2 vapor, produced inside the inflator, expands in the tank.

4.3.1.4 Stage 4: ***Final Discharge:*** The last stage in the inflation sequence corresponds to the gradual pressure decrease in the inflator pressure curve (Figure 4.17). A cross sectional drawing of the system during the fourth stage is provided in Figure 4.21.

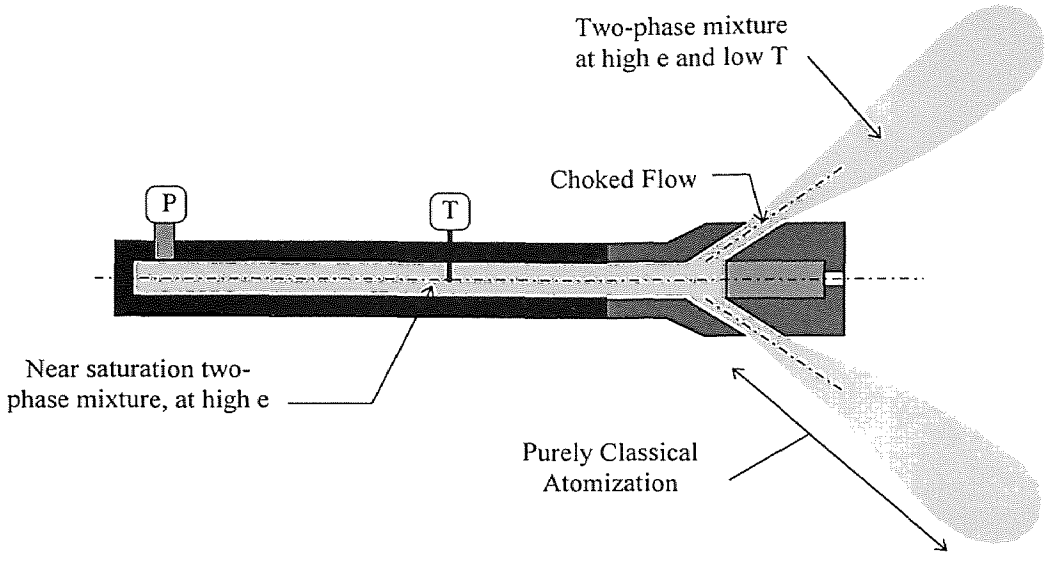

Figure 4.21 Phenomena during Stage 4 of the Inflation Sequence

As discussed in the previous section, the end of the third stage in the inflation sequence is marked by the passage of the evaporation wave at the location of the pressure transducer. Since the latter is located near the closed end of the inflator (Figure 4.21), the evaporation wave has progressed through almost the entire vessel by the time it reaches the transducer. Therefore, at the start of the last stage in the inflation sequence, the inflator is nearly completely filled with a two-phase mixture with considerable void fraction and low temperature. As discussed earlier, the latter limits the flashing process,

and the last stage consists mainly of the evacuation of the two-phase mixture from the inflator, without significant change in void fraction. The flow from the inflator is expected to remain choked during most of the fourth stage of the inflation sequence.

The pressure increase in the tank is the result of the continued evaporation of liquid CO_2 droplets, generated during this and the previous stage(s), and the expansion of the vapor from the inflator. The mixing of the generated vapor with the tank gases and the continued interaction between the evaporating drops and the tank gases causes the last part of the drop in average tank temperature. At the end of the fourth stage, 34 ms after the start of the opening of the release mechanism, the tank pressure reaches P_{peak} (Figure 4.17). This pressure corresponds to the peak pressure in tank tests, and is extensively used as an indication for the performance of the inflator. The minimal average tank temperature is T_h (Figure 4.17).

At the end of the inflation sequence, the system is mainly filled with a mixture of purging gas and generated CO_2 vapor. In addition, for nominal initial conditions (2000 psig; ± 22 °C, Table 2.3), typically about 30% of the initial amount of CO_2 is present as snow. It is likely that part of the snow was formed in the inflator, while part of it was generated by the solidification of the evaporating droplets in the tank. After the fourth stage, the snow and the CO_2 vapor in the tank are in non-equilibrium since the tank pressure and temperature differ from saturation conditions, as illustrated in Figure 4.22. The figure shows the average tank temperature and the saturation temperature corresponding to the measured tank pressure for the experiment in which the tank was purged with CO_2 at -53 °C (§4.2.1.3). As shown, the measured tank temperature remains

at least 10 °C above the saturation temperature and the actual tank conditions do not approach saturation conditions.

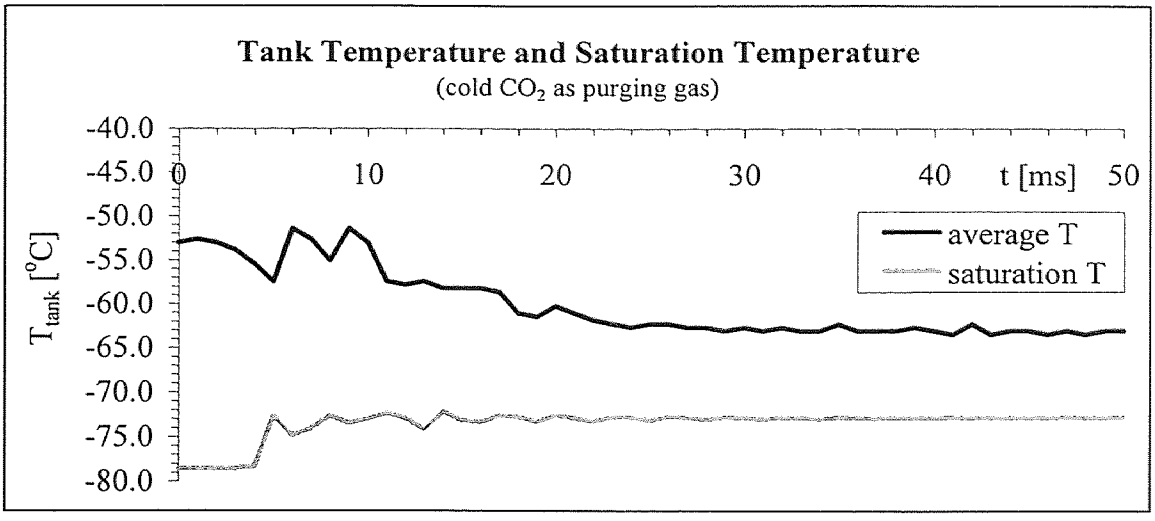

Figure 4.22 Average Tank Temperature and Corresponding Saturation Temperature

In addition, this figure indicates that condensation of the generated CO_2 vapor does not occur. This issue is discussed in detail in section §4.3.4, when the influence of the initial tank conditions is addressed. The absence of condensation implies that there are only two sources of solid CO_2 in the system (the solidification of the evaporating liquid droplets in the tank and freezing of the remaining liquid in the inflator).

4.3.1.5 Equilibration Stage: This stage corresponds to the gray parts of the curves in Figure 4.17. As discussed above, immediately after the end of the inflation sequence, the system consists of a gaseous mixture of CO_2 vapor and purging gas with about 30% of the initial amount of CO_2 present as dry ice. Since the vapor and the solid are not at saturation conditions, the system is in non-equilibrium. The limited rate of heat transfer

and sublimation results in a slow return to equilibrium with the surroundings, which typically takes about two minutes. Note that, once the inflation sequence (stages 1 through 4) has ended, the average tank temperature measurements become less reliable because of the absence of mixing in the tank and the growing thermal stratification.

4.3.2. Influence of Initial Inflator Conditions

In this section, the qualitative model is used to discuss and justify the experimental results pertaining to the study of the influence of the initial inflator conditions on the performance of the system. It is shown that the model takes all relevant phenomena into account and succeeds in explaining the experimental observations.

4.3.2.1 Effect of Initial Inflator Pressure: The corresponding experimental results are presented in section §4.2.3.1.

The tank pressure curves of Figure 4.8 indicate that an increase of the storage pressure above 2000 psig leads to a small increase in tank pressure. Therefore, 2000 psig was selected as the optimal value of the initial inflator pressure.

The observations pertaining to the inflator measurements (Figure 4.9) are explained by means of the T-s phase diagram of the metastable liquid region of CO_2 in Figure 4.23. This diagram was generated by means of the equation of state described in [46], which is also used in the quantitative model of the system (Chapter 5). Note that this diagram is an enlargement of the liquid and the superheated liquid region of Figure 1.5 and that it contains isobars in the metastable liquid region.

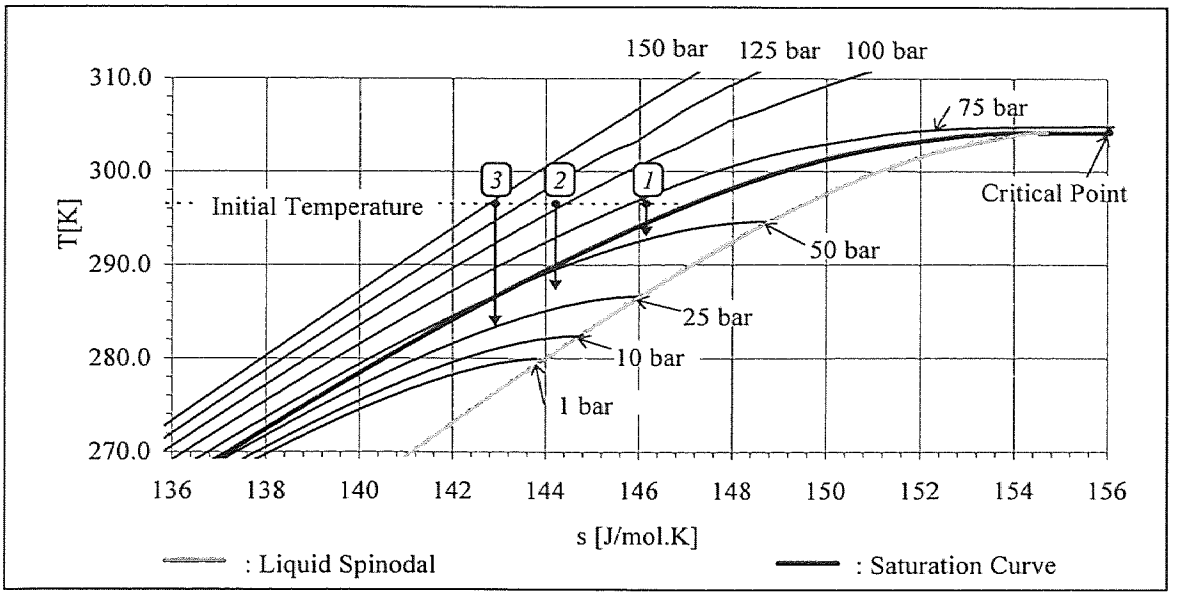

Figure 4.23 T-s Phase Diagram of the Metastable Liquid Region of CO_2

The initial states of the CO_2 in the inflator are marked by numbers, corresponding to the ones in the first column of Table 4.4. Hence, the storage pressure of initial points 1 through 3 are 1000, 1500 and 2000 psig, respectively. The total isentropic expansion of CO_2, occurring during the first and the second stage of the inflation sequence, is represented in Figure 4.23 by means of vertical arrows. The end of the expansion depends on the nucleation rate and is difficult to predict. However, the depressurization rates in the experiments are such that penetration of the metastable liquid region is certain.

Figure 4.23 clearly indicates that the expansion in experiment one, with low initial pressure, ends at a relatively high temperature and a high pressure. In experiment three, with high initial pressure, the vertical drop is longer and the end of the arrow is located at a lower pressure and temperature. This agrees well with the experimental observations concerning the lower pressure and temperature after the passage of the forerunner (Figure 4.9). Detailed inspection of the experimental results and the phase diagram indicate that

the departure from equilibrium (i.e. saturation conditions with the same entropy as the initial state) increases with increasing storage pressure. In turn, this agrees with the fact that the penetration in the metastable region is expected to increase with the depressurization rate [11]. The difference in location of the thermocouple and the pressure transducer in the inflator (Figure 2.3) explains the difference in length of the horizontal plateaus in the pressure and temperature curves of Figure 4.9. Because the thermocouple is located closer to the nozzle, the evaporation wave will reach this location earlier than that of the pressure transducer. Hence, the drop in temperature, marking the passage of the evaporation wave, occurs earlier and the horizontal plateaus in the temperature curves are shorter than in the corresponding pressure curves.

According to Figure 4.23, the two-phase mixture after the passage of the forerunner in experiment one, is at relatively high temperature. Hence, the evaporation wave proceeds swiftly through the inflator and the length of the horizontal plateau in the curve is relatively short. The low temperature of the two-phase mixture in experiment three (Figure 4.23) limits the velocity of the evaporation wave and leads to a longer horizontal plateau in the pressure curve. Again, this agrees with the experimental observations in Figure 4.9.

As stated earlier, the flow from the nozzle in the fourth stage of the inflation is choked for almost the entire duration. Previous experimental work on the critical flow rate through nozzles and orifices demonstrates a strong dependence of the mass flow rate on the quality or the void fraction of the mixture [44]. For a constant pressure drop over the nozzle or orifice, mixtures of high quality (i.e. high void fraction) have a much lower critical mass flow rate than mixtures of low quality (i.e. low void fraction). The

dependence of the evacuation rate on the void fraction explains the difference in the duration of the last stage in the inflator pressure curves. In experiment one, the two-phase mixture after the passage of the forerunner is at relatively high temperature and bubble growth proceeds at a considerable speed. Hence, the two-phase mixture is at high void fraction and the critical mass flow rate from the inflator is low. The lower temperature of the two-phase mixture in experiment three hinders bubble growth and results in a lower void fraction. In turn, this leads to a higher mass flow rate and a relatively faster evacuation of the inflator.

4.3.2.2 Effect of Initial Inflator Temperature: The corresponding experimental results are presented in section §4.2.3.2.

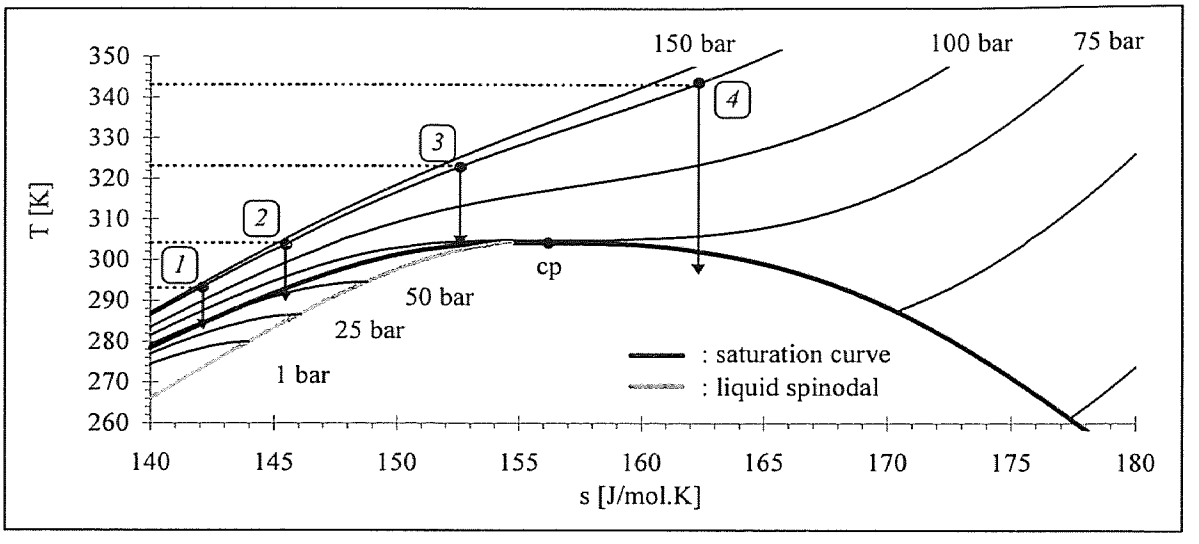

Figure 4.24 T-s Phase Diagram of the Critical Region of CO_2

Similar to the previous section, the experimental observations will be explained by means of a T-s diagram. Figure 4.24 was calculated with the equation of state which is

used in the model of the experimental system [46]. The initial states of the CO_2 in the inflator are indicated by numbers, corresponding to the first column in Table 4.5. Hence, the numbers 1 through 4 indicate the initial states at 20, 31, 50 and 70 °C, respectively.

Based on the entropy of the initial state, the experiments of Table 4.5 can be categorized in two groups (Figure 4.24). The first group contains experiments one through three, with an initial entropy below the critical value (s_c=156.58 J/mol.K). Experiment four is the sole member of the second group, with an initial entropy in excess of s_c. Note that at an initial pressure of 2000 psig (139 bar), all initial states with a temperature below 328 K (54.9 °C) belong to the first group. All initial states with a higher temperature belong to the second group.

The first group of experiments (numbers 1-3) is considered first. They are similar to the experiments that were discussed earlier, since they also penetrate the metastable liquid region upon isentropic expansion. The latter is represented in Figure 4.24 by the vertical arrows, starting in the initial points. Again, the end of the expansion is determined by the onset of nucleation and is difficult to predict theoretically. Figure 4.24 shows that the temperature and pressure at the onset of nucleation in experiment two is higher than in experiment one. As a result, the evaporation proceeds faster in experiment two and a significant void fraction develops before the arrival of the evaporation wave. This leads to a less distinct horizontal plateau in the inflator pressure curve and to a higher propagation rate of the flashing front. In turn, the higher speed of the evaporation wave results in a shorter horizontal plateau and an earlier onset of the last stage in the inflator pressure curve. These considerations explain the shape of the inflator pressure curve of experiment two (Figure 4.10(b)). In addition, because of the higher temperature

at the onset of nucleation and evaporation, the latent heat of the phase transformation is less than in experiment one. Since the internal energy of the liquid is used to compensate for the latent heat, a relatively larger amount of liquid CO_2 will transform into vapor. The latter is supported by the results of the calculation of the amount of condensate that is being formed during the inflation sequence, as listed in 6^{th} column of Table 4.5.

The initial state of experiment three is located in the supercritical region of CO_2. Because the initial entropy is close to the critical value, experiment three can be considered as a transient case between the two groups of experiments. In general, the properties of supercritical fluids lie between those of a liquid and a vapor. Hence, CO_2 at the initial conditions of experiment three, has a considerably larger compressibility than CO_2 at the initial conditions of experiment two. The increased compressibility leads to a slower depressurization during the isentropic expansion and hence, to a reduced slope in the corresponding part of the inflator pressure curve (Figure 4.10(b)). As shown in Figure 4.24, the depth of the metastable liquid region reduces to zero near the critical point. Therefore, virtually no delay in evaporation occurs in experiment three, and the phase transformation starts as soon as the saturated liquid line is crossed. The small superheated liquid region in combination with the relatively high temperature at nucleation (and therefore small latent heat of evaporation), leads to a very high evaporation rate. As a result, the evaporation wave hardly develops and the horizontal plateau is reduced to a bump in the inflator pressure curve of experiment three (Figure 4.10(b)). Consequently, the final stage of the inflator curve starts even earlier than in experiment two. Finally, because of the higher evaporation rate, less liquid will be discharged in the tank. In addition, the produced vapor is at higher temperature. Both effects lead to a slower drop

in tank temperature and a faster rise in the tank pressure, as shown in Figure 4.10(c). Furthermore, since less liquid is discharged in the tank, less condensate will be generated, as indicated by the calculation of the amount of condensate that is formed during the inflation sequence in Table 4.5. The previous explanation indicates that both wave phenomena (i.e. the forerunner and evaporation wave), which dominate the evacuation process at low initial temperature, disappear as the entropy of the initial state approaches the critical value.

Except for the average tank temperature curve, the results of experiment four are similar to those of the N_2 experiments in Chapter 3. In experiment four, the isentropic expansion of the initial amount of CO_2 does not end in the liquid phase and no phase transformation from liquid to vapor occurs. Instead, the metastable vapor region is penetrated and, depending on the initial conditions, condensation might take place. The onset of condensation is described by basically the same nucleation theories as the onset of flashing or boiling. However, as discussed in section §1.3.3.1, the limit of maximum subcooling of vapor is not located near the vapor spinodal. The bump in the inflator pressure curve at t = 8-9 ms (Figure 4.10(b)), is believed to be the result of condensation. The considerable drop in average tank temperature (Figure 4.10(c)), which was not present in the N_2 experiments, is caused by the real gas behavior of CO_2 (i.e. the Joule-Thomson Effect).

The effect of the smaller initial amount of CO_2 (column 4 in Table 4.5) was neglected in the explanation of the experimental observations. While it assists in the explanation of the faster evacuation and the slower or smaller average temperature drop, it is not sufficient because it does not account for all experimental results.

With respect to the SLG-Inflator, the above describes the changes in the system for increased ambient temperature. In terms of tank pressure and generated amount of CO_2 vapor, it is demonstrated that the system's performance improves with higher ambient temperature. At the same time, it is shown that the inflator's performance will decrease for lower ambient temperatures. The system will generate less CO_2 vapor and a lower tank pressure as the initial inflator temperature decreases.

4.3.3 Influence of Critical Flow Section

The corresponding experimental results are presented in section §4.2.2.

In agreement with intuitive expectations, the experimental results indicate an increase of the duration of the inflation sequence when reducing the critical section in the flow path. However, it can not be concluded that an increase in the critical flow section will lead to a shorter inflation process. It is expected that for some value of the exit section, the rate-limiting process will shift from the choking phenomenon in the nozzle exit holes to the actual phase transformation of CO_2. In this case, a further increase in the critical flow area will not lead to a faster pressure increase in the tank.

As discussed during the presentation of the experimental results, the inflator pressure curve of Figure 4.6(b) for the case where the nozzle holes were blocked, shows a slightly slower decrease in pressure during the second stage in the inflation sequence and a horizontal plateau at a higher pressure level during the third stage. Because of the reduced critical section, the forerunner, which is initiated at the onset of the second stage in the inflation sequence, is flattened with respect to the Reference Experiment. As a result, the depressurization rate is lower, which, in turn, leads to an earlier onset of

nucleation [11]. Therefore, the horizontal plateau in the third stage occurs at a higher level. The slower depressurization during the last stage is the result of a reduced mass flow rate through the smaller critical section. The observations pertaining to the tank measurements are easily explained. Since the mass flow rate of the two-phase jet from the inflator is smaller, the release of the liquid and vapor in the tank occurs slower and hence, leads to a slower drop in tank temperature and increase in tank pressure.

4.3.4 Influence of Initial Tank Conditions

Table 4.9 summarizes the results of the experiments in which the influence of the initial tank conditions was investigated (§4.2.1). The experiments are organized in order of increasing initial internal tank energy. For all experiments in Table 4.9, nominal initial inflator conditions were used (24 g of CO_2(l) at 2000 psig and 22 °C).

Table 4.9 Summary of Influence of Initial Tank Conditions

Tank gas	T_{tank} [°C]	P_{tank} [atm]	m_{tank} [g]	U_{tank} [J]	m_{cond} [%]	u_{cond} [kJ/kg]	%ΔH from CO_2(l)	%ΔH from tank gas
CO_2	-53	1	23.7	0	32	176.7	93	7
N_2	-37	1	14.1	168	30	180.9	84	16
N_2	-19	1	13.1	332	28	168.3	78	22
He	22	1	1.6	365	28	183.6	75	25
N_2	-8	1	12.5	420	28	180.4	76	24
N_2	18	1	11.3	615	30	185.8	72	28
CO_2	23	1	17.8	796	26	185.6	66	34
CO_2	24	4	72.0	3218	21	258.1	31	69

The first five columns characterize the initial conditions of the tank and list the tank gas, the initial tank temperature and pressure, the initial amount of tank gas and the initial internal energy. The next two columns contain the results of the calculation of the amount

and the average specific internal energy of the condensate that was formed during the inflation sequence in each experiment. All these numbers were taken from Tables 4.1-3, and additional information can be found in sections §4.2.1.1-3. In the last two columns of Table 4.9, 'ΔH' represents the enthalpy increase of the fraction of the initial amount of liquefied CO_2 that evaporated. Two effects contribute to this enthalpy increase. On the one hand, the part of the initial amount of liquefied CO_2 that is not evaporated is cooled and solidifies partially or completely (depending on the initial conditions). On the other hand, part of the consumed enthalpy (ΔH) is supplied through interaction of the tank gases and the evaporating droplets. The relative contribution of both effects was evaluated in the energy analysis of the inflation sequence, as discussed in Appendix B and is represented in the last two columns of Table 4.9. The results are also shown in Figure 4.25.

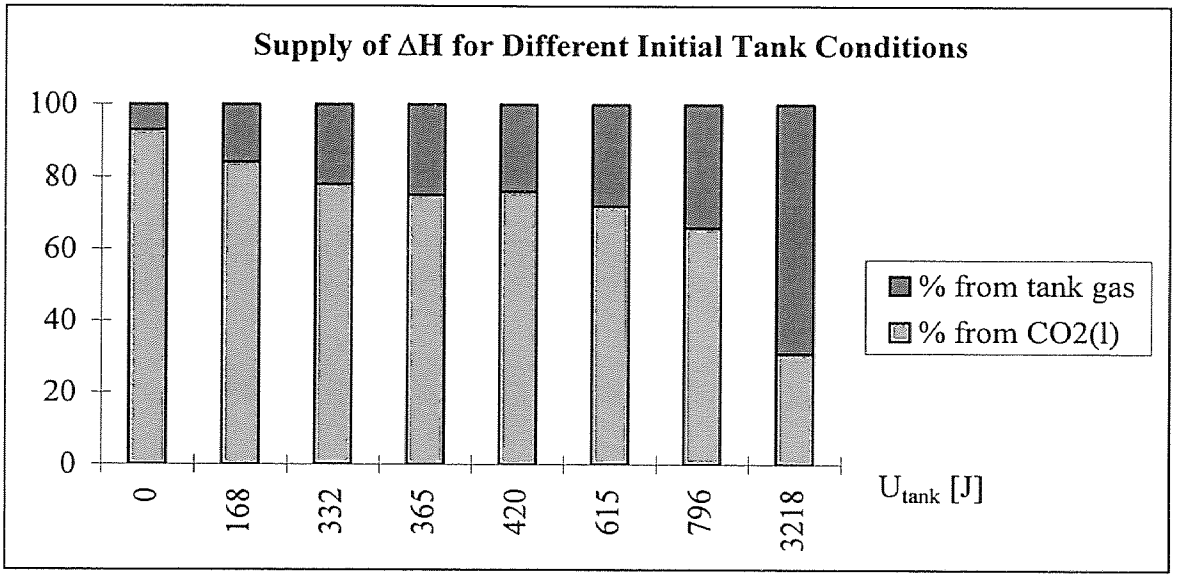

Figure 4.25 Influence of Initial Internal Tank Energy

Figure 4.25 illustrates that the fraction of ΔH that is supplied by the tank gases increases with increasing initial internal tank energy. At the same time, Table 4.9 shows that for the first seven experiments, with $U_{tank} < 800$ J, the state of the condensate is nearly constant. In these experiments, about 30% of the initial amount of liquefied CO_2 was turned into dry ice by the end of the inflation sequence. Note that for the first experiment, nearly all enthalpy is supplied by the stored liquefied CO_2. As stated earlier, this experiment reflects closely the behavior of the SLG-Inflator in case of an actual air bag deployment.

In the last experiment of Table 4.9, with considerably higher initial internal tank energy, 69% of ΔH is supplied by the tank gases, and the amount of generated condensate is lower than in the first seven experiments. In addition, the condensate is not completely solidified.

Based on the above, two conclusions can be formulated with respect to the influence of the initial tank conditions. First, the interaction between the evaporating droplets and the tank gases becomes more important as the initial internal tank energy increases. Second, there exists a threshold value of the initial internal tank energy, above which the amount of condensate decreases and only partial solidification occurs.

Due to the complex nature of the tank phenomena and their interactions, additional experiments are required to establish a detailed qualitative explanation of the above conclusions.

In section §4.3.1, Figure 4.22 was presented, which contains the measurement of the average tank temperature and the calculated saturation temperature for the experiment with cold CO_2 (-53 °C) as purging gas. Because CO_2 was used to purge the tank, the partial pressure of CO_2 is equal to the measured tank pressure. Consequently, the partial

pressure and corresponding saturation temperature of the CO_2 is considerably larger than for the experiments in which N_2 or He was used as purging gas. In addition, the low initial tank temperature will lead to a low average temperature during the inflation sequence. The combination of the high partial pressure and low average temperature during this particular experiment, creates conditions at which condensation of the generated CO_2 vapor is most likely to occur. The necessary condition for condensation requires that the measured tank temperature drops below the saturation temperature. Based on Figure 4.22, it is concluded that general condensation of the generated CO_2 vapor does not occur. However, during the experiment in which the tank was purged with ambient He (§4.2.1.1), for example, brief temperature non-uniformities in the tank were observed. During these temperature non-uniformities, the condition for condensation of the generated CO_2 vapor was fulfilled and hence, localized condensation cannot be excluded. Since these non-uniformities were only observed in a few experiments, the effect of condensation will be neglected.

The observations corresponding to the experiments at increased initial tank pressure (section §4.2.1.2) are discussed in the remainder of this section. The peculiar shape of the tank pressure curves in Figure 4.3(a) is mainly the result of the mixing of the generated CO_2 vapor with the tank gases. The tank pressure is influenced by two competing phenomena. On the one hand, the increase in the amount of gaseous mixture in the tank leads to a higher pressure. On the other hand, the mixing of the cold CO_2 vapor decreases the mixture temperature and leads to a lower pressure. Initially, the generated CO_2 vapor is relatively warm and the first phenomenon is dominant. As the inflation progresses, the temperature of the CO_2 vapor decreases and the second

phenomenon gains importance. The above explains the rise and drop of the tank pressure during the inflation sequence. The slow increase in tank pressure after the inflation sequence corresponds to the *Equilibration Stage*, as described in section §4.3.1.5.

4.3.5 Qualitative Explanation of CO_2/Organic Liquid Experiments

This section contains a concise qualitative explanation for part of the results of the experiments with CO_2/organic liquid mixtures (§4.2.5). The most important observation during the CO_2/organic liquid experiments concerns the drastic increase in average tank temperature compared to the Reference Experiment.

Consider a droplet with radius a, consisting of a CO_2/organic liquid mixture. For the sake of simplicity, it is assumed that the receiving tank was purged with CO_2 prior to the experiment. The argument can easily be extended to include an inert purging gas such as N_2 or He. With reasonable accuracy, the pressure at the droplet surface can be approximated by the measured tank pressure:

$$P(t)_{r=a} \approx P_{tank}(t) \qquad (4.1),$$

with $P(t)_{r=a}$ the pressure at the droplet surface. At the same time, the evaporating surface of the droplet is at saturation conditions. For a pure substance, the saturation pressure is function of temperature only (Gibbs Phase Rule):

$$P_{pure}^{sat}\left[T(t)_{r=a}\right] = P(t)_{r=a} \approx P_{tank}(t) \qquad (4.2),$$

with $T(t)_{r=a}$ the droplet surface temperature. For a mixture of two components, the saturation pressure is function of the temperature and the composition:

$$P_{mix}^{sat}\left[c(t)_{r=a}, T(t)_{r=a}\right] = P(t)_{r=a} \approx P_{tank}(t) \qquad (4.3),$$

with $c(t)_{r=a}$ the droplet surface concentration of one of the components of the CO_2/organic liquid mixture. Figures 4.15 and 4.16 show a higher tank pressure for the CO_2/organic liquid experiments than for the pure CO_2 experiments. These observations, in combination with (4.2 and 4.3) yield the following condition :

$$P_{mix}^{sat}\left[c(t)_{r=a}, T(t)_{r=a}\right] > P_{pure}^{sat}\left[T(t)_{r=a}\right] \qquad (4.4).$$

Meanwhile, according to *Raoult's Law*[5] [59], the saturation pressure of the CO_2/organic liquid mixture decreases for increasing concentrations (i.e. mole fraction) of the organic liquid :

$$P_{mix}^{sat}\left[c(t)_{r=a}, T(t)_{r=a}\right] = \left(1 - \eta(t)_{r=a}\right).P_{pure}^{sat}\left[T(t)_{r=a}\right] \qquad (4.5),$$

with $\eta(t)_{r=a}$ the mole fraction at the droplet surface of the organic liquid in the mixture. Taking (4.5) into account, (4.4) can only be fulfilled if the temperature of the droplet containing the mixture exceeds the temperature of the pure droplet. In other words, the decrease in saturation pressure, which occurs when adding the organic liquid to the CO_2, must be compensated by a spontaneous increase of the droplet surface temperature. In turn, the increased droplet surface temperature leads to an increase in the temperature of the generated CO_2 vapor and average tank temperature.

When it is assumed that the droplet concentration is uniform and equal to the initial concentration (Table 4.8), the predicted temperature effect by (4.5) is too small to account for the observations in section §4.2.5. However, due to the large difference in evaporation rate between CO_2 and the organic liquid, the concentration in the droplet will

---

[5] Raoult's Law holds for dilute mixtures and is used as a defining condition for 'ideal' mixtures. Although the mixture in the current application is not necessarily dilute or ideal, (4.5) indicates the correct trend in the dependence of the mixture saturation pressure (e.g. it decreases for increasing concentrations of the organic liquid).

not be uniform. Instead, the concentration of the organic liquid in the surface layer of the droplet (which determines the saturation pressure) is expected to exceed the initial concentration considerably. This phenomenon is called *Layered Evaporation* and is believed to be the explanation for the increase in the average tank temperature compared to the Reference Experiment.

The actual concentration in the surface layer can be evaluated and depends on the relative size of the evaporation rate of the CO_2 compared to the mass diffusion rate inside the droplet [36]. Using the results of [36], it has been shown that layered evaporation in the case of the CO_2-methanol experiments must occur in droplets larger than 6 μm in diameter. Although the droplet size distribution was not measured in this research, it is expected that all, or at least the majority, of the droplets in the spray from the nozzle are larger than 6 μm in diameter. Consequently, layered evaporation is believed to be the main phenomenon responsible for the drastic increase in the average tank temperature during the CO_2/organic liquid experiments.

CHAPTER 5

THEORETICAL MODELING ASPECTS

5.1 Introduction

The objective of the theoretical part of this research is to provide the foundations for the development of a comprehensive theoretical model for the simulation of the main experiments. Due to the large number of relevant physical phenomena involved, it is beyond the scope of this work to advance a complete quantitative model for this inflator. This chapter is mainly directed towards the phenomena that occur inside the inflator, rather than those which take place in the tank.

An accurate description of the behavior of CO_2 is essential for the development of the SLG-Inflator Model. The first section of this chapter addresses the issues pertaining to the modeling of the behavior of CO_2. A flexible and robust CO_2-model was developed. This model is capable of accurately predicting P-v-T information, enthalpy and entropy of a large region of the phase diagram.

The second section in this chapter contains a brief discussion of the calculation of the generated vapor mass during the inflation sequence in the main experiments. This calculation, which uses the tank pressure and temperature measurement as input, was repeatedly used in Chapter 4 to interpret the experimental data.

A quantitative model for the simulation of the main experiments is discussed in the last part of this chapter. The model consists of two main parts. The first part, *the SLG-Inflator Model*, concerns a detailed quantitative description of the phenomena inside the inflator vessel and the nozzle. The second part, the *Tank Model*, consists of a simplified

model of the main phenomena taking place in the receiving tank, i.e. the dispersion of the liquid phase, the evaporation of the produced droplets and the mixing of the CO_2 vapor with tank gases. Both models operate independently of each other and can be run separately. In addition to the simulation of the pressure, temperature, void fraction, bubble size and velocity in the inflator, the SLG-Inflator Model calculates the evolution of the characteristics of the two-phase flow exiting the nozzle. These characteristics form the input of the Tank Model. Preliminary results of the simulation of the phenomena in the inflator are presented.

5.2 Modeling the Behavior of CO_2

The generated CO_2 vapor during the inflation sequence is relatively close to saturation conditions and does not exhibit ideal gas behavior. Furthermore, the CO_2 in this inflator system does not only exist in the vapor phase, but also as a compressible liquid, a metastable liquid, a supercritical fluid and as a solid. In summary, nearly all possible fluid states and their corresponding transitions are encountered during the inflation sequence. Therefore, a first and important step towards a quantitative model of the SLG-Inflator must consist of developing a general, robust and flexible model for the behavior of CO_2.

The requirements of the CO_2-model are defined first. Next, a concise overview of the alternatives to model the behavior of a real fluid is included. Based on this overview, and keeping the requirements of the model in mind, it is opted to use a complex equation of state in the CO_2-model. A number of properties, such as the enthalpy and entropy in the low pressure limit, the saturation pressure and the latent heat, are evaluated without the use of the equation of state. This part of the model is discussed next. The equation of

state itself was selected by comparing the results of various equations with tabulated CO_2 data for a large region in the phase diagram.

5.2.1 Requirements of the CO_2-Model

The following list contains the requirements of the CO_2-model:

1. ***Easy to implement in a computer:*** Since the theoretical model consists of a numerical simulation of the phenomena in the system, the CO_2-model should be such that it can easily be incorporated in a computer code.
2. ***Maximum deviation from tabulated values of less than 3%:*** To assess the agreement of the experimental observations and the simulations, the accuracy of the model must be at least of the same order as that of the measurements. The uncertainty of the measurements was estimated in §3.4 to be approximately 3-5%.
3. ***Generate P-v-T information, but also enthalpy and entropy values:*** Besides the behavior of CO_2 in terms of the pressure-volume-temperature relation, the enthalpy and entropy of the fluid need to be calculated.
4. ***Flexible:*** Two properties suffice to determine the thermodynamic state of a pure, single phase fluid (Gibbs Phase Rule [16]). The model should be flexible in the sense that any two properties can be used as input to generate all others.

5.2.2 Alternative Models for the Non-Ideal Behavior of a Fluid

The literature contains a considerable number of methods to model the non-ideal behavior of a fluid. An overview is provided in Figure 5.1 ('eos' is used as an abbreviation of equation of state).

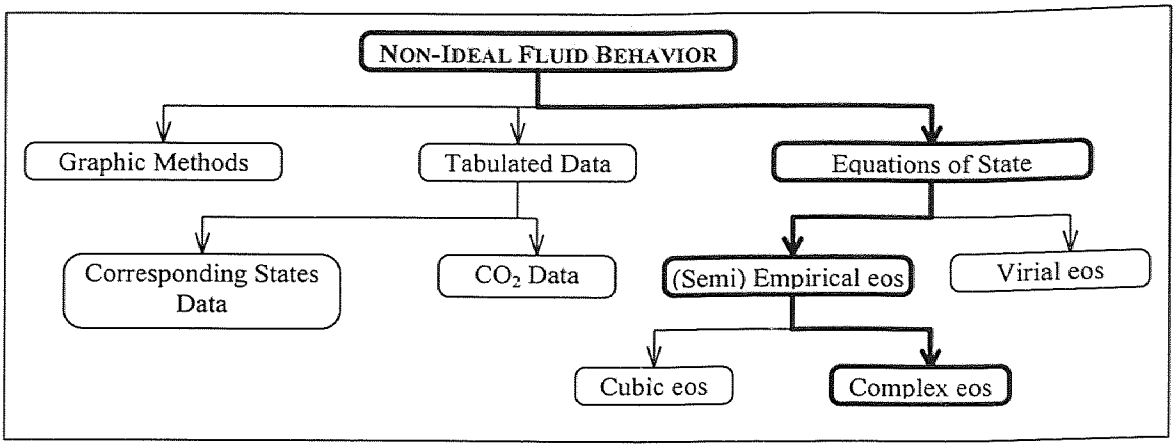

Figure 5.1 Overview of Non-Ideal Fluid Behavior Models

Keeping the first requirement of the previous section in mind, it is obvious that graphic methods, such as the 'Nelson-Obert Compressibility Charts' [16], are not suitable for application in this research. A second way of modeling the non-ideal behavior of a fluid consists of storing tabulated data in a computer and equipping it with an interpolation algorithm. This method requires a large amount of computer memory, but leads to a fast and very accurate model. By choosing tabulated data that is based on the corresponding states principle, such as the Lee & Kesler's Tables [16], the model will not be limited to one particular fluid. Typically, this method produces P-v-T information with an average accuracy of about 0.5% [66]. Tables that are specific for one fluid, for example [12,30] in the case of CO_2, will lead to even more accurate predictions. Using [12], the maximum error of the prediction of the specific volume (for a given value of the pressure and temperature) is located near the critical point and is less than 0.5%. The error of the enthalpy and entropy predictions is less than 0.2%. Accuracies of these orders of magnitude are not required for the current model. Taking this into account, together with the required computer memory and the work involved to enter the tabulated data in

the computer, the last alternative was selected, i.e. to use an equations of state. According to [79], more than 100 different eos have been developed in the past. The virial equation of state, commonly written as a power series expansion of the compressibility in the reciprocal volume, is the only one which is free of empiricism. The coefficients of the power series, which for pure substances depend on temperature only, can be derived from the intermolecular potential using statistical mechanics. Although this equation is important from theoretical point of view, it has little value for the use in this research. The most compact semi-empirical equations contain two parameters and lead to a cubic expression in the compressibility (Z), hence the name *cubic eos*. They are widely used to represent limited regions of the phase diagram and offer a good compromise between simplicity and accuracy. The Soave-Redlich-Kwong eos (1972) [83] and the Peng-Robinson eos (1976) [65] are popular examples of cubic eos [73]. For simplicity, all other empirical eos are classified in this text as *complex* eos. The latter category comprises not only classical equations such as the Beattie-Bridgeman eos (1928) and the Benedict-Webb-Rubin eos (1942), described in general thermodynamic handbooks [16], but also more recent developments such as the quartic eos (1994) [73] and the equation developed by F.H. Huang & F.M. Li et al. (1985) [46].

It is common to refer to an eos by the first letters of the last names of the authors. For example the Peng-Robinson eos is referred to as the 'PR eos' and the Soave-Redlich-Kwong eos becomes the 'SRK eos'. This notation is also used in this text.

5.2.3 General Aspects of the CO_2-Model

The following discusses the part of the CO_2-model that is independent of the choice of the eos.

5.2.3.1 Isobaric Specific Heat Capacity, Ideal Gas Enthalpy, Ideal Gas Entropy: All thermodynamic properties can be calculated from P-v-T information in combination with the knowledge of the temperature dependence of one specific heat capacity in the ideal gas limit ($P \rightarrow 0$). The thermodynamic property is determined by choosing a path between the reference state and the actual state that consists of an isobaric part at low pressure and an isothermic part [67]. The same approach is used in this research to calculate the enthalpy, the internal energy and the entropy. The first part of the thermodynamic path (i.e. the ideal gas part) is considered here. The second part, the so called *enthalpy* or *entropy departure* depends on the choice of the eos and is discussed in §5.2.4.

The temperature dependence of the isobaric specific heat capacity of CO_2 at low pressure was modeled by means of a polynomial curve fit of the 2nd order. Values of the ideal gas tables of [12] from 220-350 K served as input. Within this interval, the curve fit does not deviate from the input values by more than 0.03% (T [K] ; c_P [J/kg.K]):

$$c_p[T] = -0.00082T^2 + 1.53071T + 460.38735 \qquad (5.1)$$

Integration of (5.1) over temperature yields an expression for the enthalpy in the ideal gas limit (T [K] ; h^* [J/kg]):

$$h^*[T] = \frac{1}{3}(-0.00082)(T^3 - T_{ref}^3) + \frac{1}{2}(1.53071)(T^2 - T_{ref}^2) + (460.38735)(T - T_{ref}) + h_{ref} \qquad (5.2)$$

The reference state (h_{ref}) is chosen from the ideal gas tables of [12]:

$$h_{ref} = 32859 \frac{J}{mol} = 746575 \frac{J}{kg} \qquad (T_{ref} = 220\ K) \tag{5.3}$$

This choice ensures that the enthalpies, calculated from (5.2-3) correspond to the values listed in [12]. Using (5.2-3), the ideal gas enthalpy was calculated in the temperature interval 220-500 K and compared with the ideal gas table in [12]. This produced an *A*verage *R*elative *D*eviation (ARD)[(1)] of 0.01%.

The entropy variation in the ideal gas limit for an isobaric change of state is given by:

$$s^* - s_{ref} = \int_{T_{ref}}^{T} \frac{c_P[T]}{T} dT \tag{5.4}$$

Substitution of (5.1) in (5.4) and integration yields an expression for the entropy, corresponding to a given temperature, in the low pressure limit (T [K] ; s^* [J/kg.K]):

$$s^* = \frac{1}{2}(-0.0082).(T^2 - T_{ref}^2) + (1.53071).(T - T_{ref}) + 460.38735 \ln(\frac{T}{T_{ref}}) + s_{ref} \tag{5.5}$$

Also the entropy of the reference state (s_{ref}) is taken from the ideal gas tables in [12]:

$$s_{ref} = 202.99 \frac{J}{mol.K} = 4612.5 \frac{J}{kg.K} \qquad (T_{ref} = 220\ K) \tag{5.6}$$

Using (5.5-6), the ideal gas entropy was calculated in the temperature interval 220-500 K and compared with the ideal gas table in [12]. This produced an ARD of 0.02%.

---

(1) Per definition: $ARD = \sum_{i=1}^{N} |r_i| / N$ (with r_i: relative deviation ; N: number of datapoints)

5.2.3.2 Saturation Pressure: The condition of phase equilibrium for a one component, two-phase system, requires that the fugacities of both phases are equal [67]. By combining this condition with pressure and temperature equilibrium and the eos, the saturated vapor curve can be obtained. However, especially for complex eos, this procedure is time consuming and it is advantageous to use a correlation for the saturated vapor pressure instead [46].

Liquid-Vapor System: Two correlations were found [4,46]. Both were compared to values from [12], ranging from the triple point to the critical point. The correlation from [4] gave the best results, with an ARD of 0.3% (P_r, T_r [/]):

$$\log_{10}(P_r^{sat}) = 4.2397 - \frac{4.4229}{T_r} - 5.3795\log_{10}(T_r) + 0.1832\frac{P_r^{sat}}{T_r^2} \tag{5.7}$$

Note that this expression is implicit in pressure and needs to be solved iteratively.

Solid-Vapor System: One correlation was found for the solid-vapor system [39]: (T [K] ; P^{sat} [cmHg]):

$$\log_{10}(P^{sat}) = -\frac{1354.21}{T} + 8.69903 + 0.001588T - 4.5107.10^{-6}.T^2 \tag{5.8}$$

The correlation (5.8) is valid in the interval 154 - 195 K. It was complemented with a 4^{th} order polynomial fit for the range 195 - 216 K. Tabulated values from [30,39] were used to develop this curve fit (T[K] ; P^{sat} [Pa]):

$$P^{sat} = 0.47047T^4 - 373.01144T^3 + 111267.95312T^2 - 14788326T + 738440640 \tag{5.9}$$

By combining (5.8) and (5.9), the saturation pressure of the solid-vapor system can be predicted in the interval 154 - 216 K. These predictions were compared with tabulated

data from [30,39] and produced an ARD of 0.3%. The derivatives of (5.8) and (5.9), with respect to T, will be used later to compute the entropy of the saturated solid state.

5.2.3.3 Latent Heat of Vaporization: Similar to the saturation pressure, the latent heat can be calculated from the eos. Since this would lead to lengthy cycles of iterations, a correlation was used to predict the latent heat corresponding to a given temperature.

Liquid-Vapor Transition: Two correlations were found for the latent heat of evaporation [16]. However, both deviated more from the tabulated values in [12] than the following 4th order polynomial fit (T [K] ; L [J/kg]):

$$L = -0.01117T^4 + 11.18704T^3 - 4203.44023T^2 + 700373.52917T - 43238399.98428 \quad (5.10)$$

In the temperature range from 216-300 K, (5.10) generated an ARD of 0.9% when compared to the tables in [12].

Solid-Vapor Transition: No correlation was found in the literature for the latent heat of sublimation. Using tabulated data from [30], ranging from -130 °C to -56.6 °C, the following polynomial curve fit was developed (T [K] ; L [J/kg]):

$$L = -0.09231T^3 + 44.59902T^2 - 7687.33374T + 1058607.32266 \quad (5.11)$$

This expression reproduces the tabulated data of [30] within the specified temperature range with an ARD of 0.04%.

5.2.3.4 Internal Energy: Based on the enthalpy and the P-v-T information, the internal energy can be obtained from the enthalpy definition:

$$h[P,T] = u[P,T] + Pv \tag{5.12}$$

5.2.4 Selection of the eos

For the selection of the eos for the CO_2-model, the performance of 3 different eos was investigated by comparing their P-v-T, enthalpy and entropy predictions with tabulated values in [12] and [30].

As stated before (§5.2.2), the tables of [12] deviate very little from experimental observations and can therefore be considered as exact for the current purpose. Tables [30] do not contain any information about their accuracy, but since they compare well to [12] in the overlapping regions, they are also considered exact.

The objective of the selection procedure is to determine the simplest eos (in computational terms) that meets the requirements in §5.2.1. Therefore, the eos that were investigated were organized according to increasing complexity and the first one that met the requirements was selected.

5.2.4.1 Peng-Robinson eos: The PR eos [63] is a cubic, semi-empirical eos, with the same repulsion term as the van der Waals eos, but a different attraction term:

$$P = \frac{RT}{v-b} - \frac{a[T]}{v(v+b)+b(v-b)} \tag{5.13}$$

Parameter b is a function of the critical properties only and therefore constant. Parameter a is not constant and depends on temperature, the critical properties and the Pitzer acentric factor (ω). The complete expressions corresponding to the PR eos are listed in

Appendix C.1. When (5.13) is expressed as a function of the compressibility factor, a cubic relation is obtained:

$$Z^3 - (1-B)Z^2 + (A - 3B^2 - 2B)Z - (AB - B^2 - B^3) = 0 \qquad (5.14)$$

Both A and B are functions of P, T and a, b respectively (see Appendix C.1).

In the two-phase region, (5.14) has three positive real roots. The smallest corresponds to the compressibility of the liquid, while the largest corresponds to the compressibility of the vapor. Outside the two-phase region, (5.14) has only one real root. The enthalpy departure for the PR eos is also included in Appendix C.1.

Reference [55] contains tabulated values of the compressibility factor, predicted at different conditions and by different eos. The output of the computer code, which was generated to estimate the accuracy of the PR eos in this research, compared well with these values.

Table 5.1 Performance Checks of the PR eos

	Input			**Output**
#	Prop.	Structure	Range	
1	v, T	isochores	v : 2.3 ... 0.0009 m^3/kg T: 220 ... 420 K	P
2	P,T	isobars	P : 0.5 ... 500 bar T : 190 ... 420 K	v
3	T	saturation curve	T : -110 ... 30 °C	v
4	T, P	isotherms	T : 230 ... 330 K P : 10 ... 150 bar	h

Table 5.1 contains an overview of the performance checks that were carried out for the PR eos. Columns 2, 3 and 4 characterize the input properties. The input data was organized along characteristic lines in the phase diagram, listed in the 3rd column. The 5th

column contains the predicted property. For all data points the difference between the prediction and the tabulated value [12,30] was determined. This difference was represented with the aid of contour plots, such that the regions in the phase diagram could be identified where the eos fails to meet the 3%-accuracy requirement.

For the PR eos, it was observed that it generates acceptable values in the saturated and superheated vapor region, but it fails to meet the requirements in the saturated solid, the saturated liquid, the compressed liquid, metastable liquid and the supercritical region. Therefore, the accuracy of a more complex eos, the Beattie-Bridgeman eos [16], was investigated next.

5.2.4.2 Beattie-Bridgeman eos: The BB eos is a semi-empirical eos with five empirical constants [16]:

$$P = \frac{RT}{v^2}(1-\varepsilon)(v+B) - \frac{A}{v^2} \tag{5.15}$$

A complete list of expressions and constants for CO_2 are included in Appendix C.2. Table 5.2 (similar to Table 5.1) provides an overview of the performance checks which were performed with the BB eos.

Table 5.2 : Performance Checks of the BB eos

	Input			**Output**
#	Prop.	Structure	Range	
1	v, T	isochores	v : 2.3 ... 0.0009 m^3/kg T : 220 ... 420 K	P
2	P,T	isobars	P : 0.5 ... 500 bar T : 190 ... 420 K	v
3	T	saturation curve	T : -110 ... 30 °C	v

The only region where the BB eos produced better predictions than the PR eos is the superheated vapor region. In all other areas, it produced the same accuracy or worse than the PR eos. Next, the eos proposed in [46] was investigated.

5.2.4.3 Huang-Li eos: This empirical eos with 27 constants has the following standard form [46]:

$$Z = 1 + b_2\rho' + b_3\rho'^2 + b_4\rho'^3 + b_5\rho'^4 + b_6\rho'^5 + b_7\rho'^2.\exp\left[-c_{21}\rho'^2\right] + b_8\rho'^4.\exp\left[-c_{21}\rho'^2\right]$$
$$+ c_{22}\rho'.\exp\left[-c_{27}(\Delta T)^2\right] + c_{23}\frac{\Delta\rho}{\rho'}.\exp\left[-c_{25}(\Delta\rho)^2 - c_{27}(\Delta T)^2\right]$$
$$+ c_{24}\frac{\Delta\rho}{\rho'}.\exp\left[-c_{26}(\Delta\rho)^2 - c_{27}(\Delta T)^2\right] \qquad (5.16)$$

The coefficients b_i are temperature dependent, while the coefficients c_i are constant. A complete list of expressions and the 27 constants, together with the enthalpy and entropy departure is included in Appendix C.3. The expression of the enthalpy departure in this appendix differs from the one published in [46] with one factor: ρ' was omitted in the 8th term. This correction proved necessary to obtain a satisfactory prediction of the enthalpy. Similarly, a correction to the expression of the entropy departure proved necessary: the sign of the coefficient c_7 was reversed.

According to [46], (5.16) predicts densities over a wide range of temperatures (216 - 423K) and pressures (0-310 MPa), with an accuracy of within 1% near the critical point, and 0.1-0.2% elsewhere. Table 5.3 provides an overview of the performance checks which were performed with (5.16). The contour plots of the absolute relative error of the first four performance checks are presented in Figures 5.2-5 respectively. The white

regions represent the parts of the investigated range in which no tabulated data was available.

Table 5.3 : Performance Checks of the HL eos

	Input			# Data-points	Output
#	Prop.	Structure	Range		
1	v, T	isochores	v : 2.3 ... 0.0009 m^3/kg T : 220 ... 420 K	277	P
2	P,T	isobars	P : 0.5 ... 500 bar T : 190 ... 420 K	235	v
3	P,T	isobars	P : 1 ... 500 bar T : 220 ... 400 K	224	h
4	P, T	isobars	P : 1 ... 500 bar T : 220 ... 400 K	224	s
5	T	saturation curve	T : -110 ... 30 °C	29	v
6	T	saturation curve	T : 160 ... 304 K	22	h
7	T	saturation curve	T : 160 ... 304 K	22	s

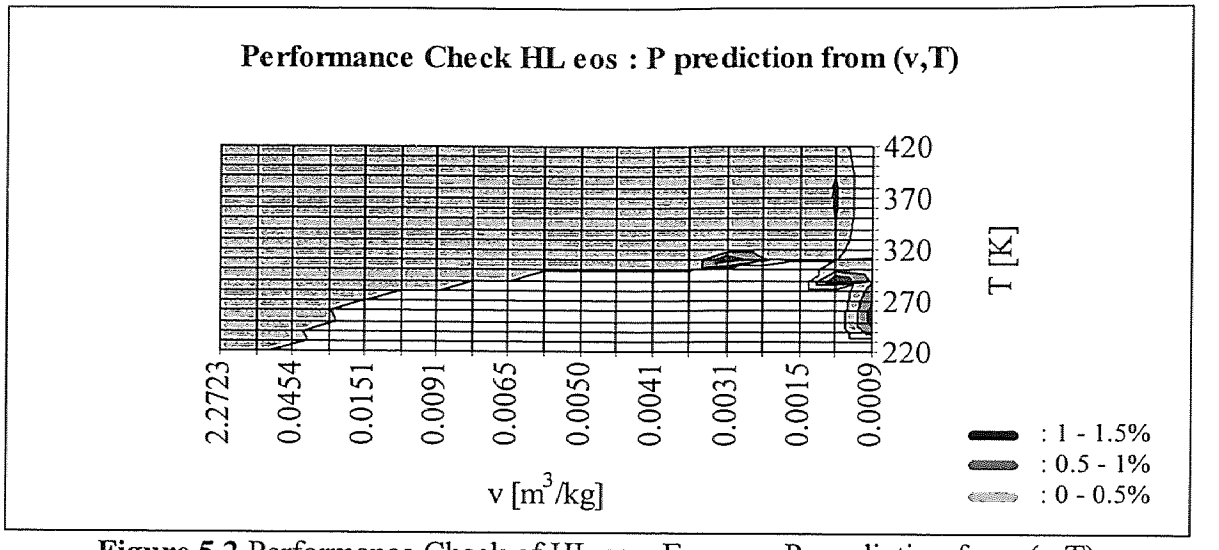

Figure 5.2 Performance Check of HL eos: Error on P-prediction from (v,T)

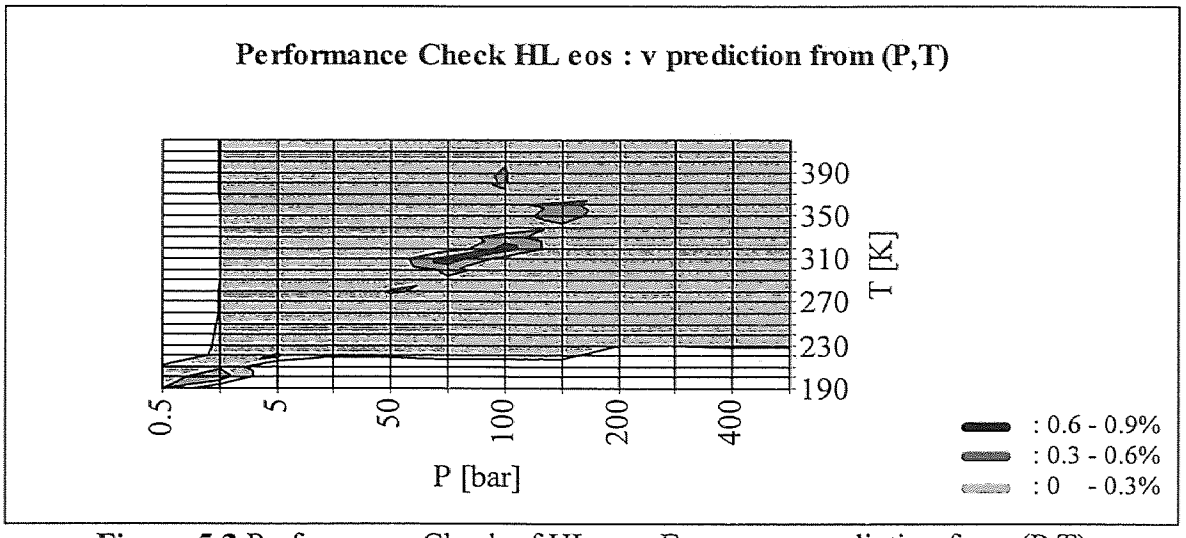

Figure 5.3 Performance Check of HL eos: Error on v-prediction from (P,T)

According to these figures, the predictions of the P-v-T information and enthalpy by (5.16) fall well within the required accuracy for the entire region of investigation. At high pressure and relatively low temperature, the entropy prediction exhibits an error in excess of 3%. Since this region will generally not be encountered during the current experiments, this effect was not further investigated.

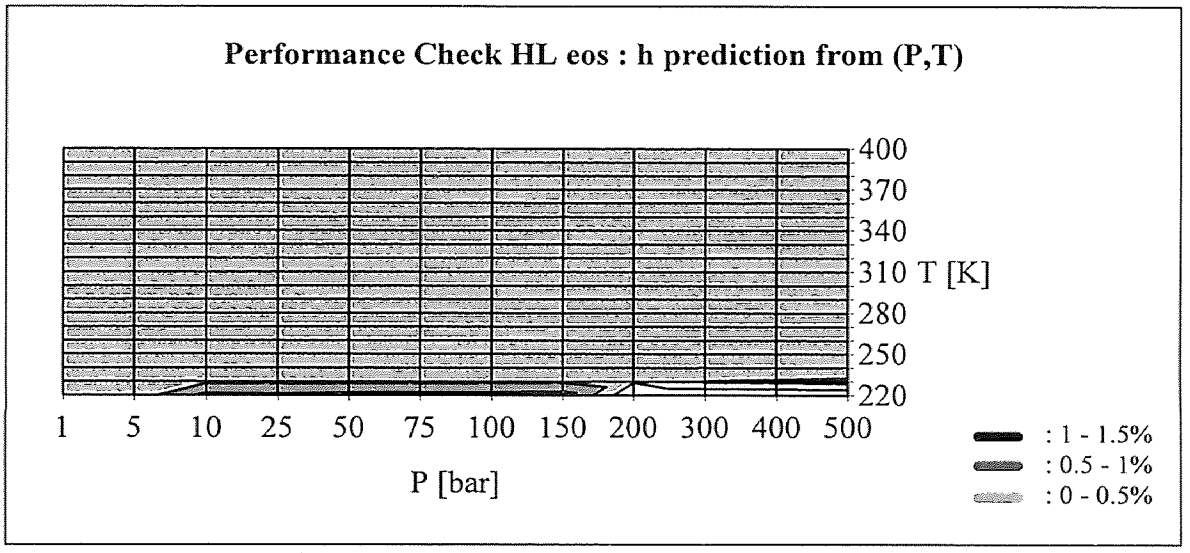

Figure 5.4 Performance Check of HL eos: Error on h-prediction from (P,T)

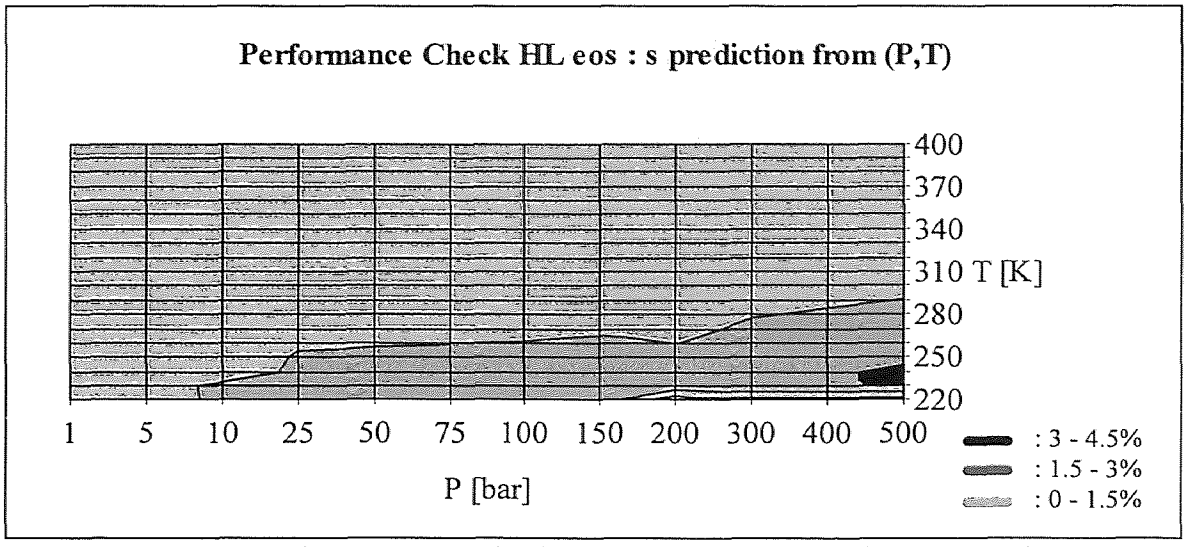

Figure 5.5 Performance Check of HL eos: Error on s prediction from (P,T)

Performance check 5 of Table 5.3 indicated that the specific volume of both the saturated vapor and the saturated liquid can be predicted with sufficient accuracy. The predicted value of the specific volume of the solid phase was not accurate. This was expected since the lower limit for which (5.16) was developed, coincides with the triple point. Bearing this in mind, the predicted volume at temperatures below T_t by (5.16) is an extrapolation of the saturated liquid line, rather than an estimate of the solid phase. For the current purpose, an estimate of the specific volume of solid CO_2 is not needed.

The 6th performance check of Table 5.3 showed that the enthalpy predictions of saturated vapor and saturated liquid are acceptable. Using the enthalpy of saturated vapor and the correlation for the latent heat of sublimation (5.11), the enthalpy of the saturated solid could be calculated:

$$h_s^{sat}[T] = h_v^{sat}[T] - L[T] \tag{5.17}$$

These values deviated by less than 3% from the tabulated values in [12].

The entropy predictions for both the saturated vapor and saturated liquid, differed by less than 3% from the tabulated values. The entropy of the saturated solid CO_2 could not be calculated directly. The following thermodynamic identity, based on the fundamental equation of phase equilibrium for a one component, two phase system, was used:

$$s_s^{sat} = s_v^{sat} - \Delta v_{vs}\left(\frac{dP}{dT}\right)_{sat} \tag{5.18}$$

The first term was generated using the eos (5.16). The change in volume during sublimation, Δv_{vs}, was calculated for the interval -110 °C to -56.6 °C, using values from [12]. It was observed that the change in volume deviates by less than 1% from the volume of saturated vapor at the same temperature. Therefore, Δv_{vs} was approximated by the saturated vapor volume, as predicted by (5.16), with an error of less than 1%. The last term of (5.18) was calculated by differentiating (5.8) and (5.9). The resulting entropy predictions of the saturated solid state in the interval -110 °C to -56.6 °C deviated from the tabulated values in [12] with an ARD of 1.1% and were therefore acceptable.

5.2.4.4 Conclusions: Based on the above results, two different eos were chosen for two different purposes.

On the one hand, the PR eos was selected for the calculation of the generated vapor mass in the tank. For this calculation, only saturated or superheated CO_2 vapor properties are needed. The performance checks in this section indicate that the PR eos

provides sufficient accuracy in this region of the phase diagram. A detailed description of the generated vapor mass calculation is given in §5.3.

On the other hand, the HL eos was selected to be used in the CO_2-model. The HL eos predicts P-v-T information, enthalpy (and therefore also internal energy according to (5.12)) and entropy with sufficient accuracy. Since the specific volume of solid CO_2 is not needed to simulate the behavior of the SLG-Inflator, the fact that the HL eos does not predict these values does not pose a problem. Using this eos, a set of subroutines was developed, which allows the calculation of P-v-T information, enthalpy, internal energy and entropy of CO_2 in subcooled and saturated liquid states, supercritical states and saturated or superheated vapor states. Only the enthalpy and the entropy of the solid state were modeled. The properties of CO_2 in the superheated liquid state are determined by the extrapolation of the HL eos in the metastable liquid region [58]. The prediction of the pressure along three isochores in the metastable liquid region was compared with the measurements in [72]. A maximum relative deviation of 2.7% was observed.

A brief description of the main subroutines of the general CO_2 model are given in Appendix D.

5.3 Generated Vapor Mass Calculations

For the calculation of the generated vapor mass, the volume of the liquid and/or solid condensate in the tank is neglected. Hence, the pressure in the system is the result of the gaseous mixture of the generated CO_2 vapor and the initial tank gases, which fills the entire volume of the system (tank and inflator).

Depending on the purging gas, two different situations need to be considered. If CO_2 was used, the tank contains only one component (CO_2), and the PR eos can be applied directly to model the real gas behavior. In case the tank was purged with N_2 or He, a mixture of two components is present in the system (either a CO_2/N_2- or a CO_2/He-mixture). The behavior of this mixture is modeled in two steps. First, a *pseudo*-fluid is created by combining the properties of the mixture components by means of a *mixing rule*. Next, the PR eos is applied to model the behavior of the pseudo-fluid. In this research, the classical van der Waals-mixing rule is used to determine the properties of the pseudo-fluid [65]:

$$a = \sum_i \sum_j x_i x_j a_{ij} \;\; ; \; b = \sum_i \eta_i \cdot b_i \qquad \text{,with} \quad a_{ij} = (1 - \delta_{ij}).\sqrt{a_i . a_j} \tag{5.19}$$

The parameters a and b characterize the pseudo-fluid and are used in the PR eos in the same way as for a pure fluid. The coefficient δ_{ij} is an empirically determined interaction coefficient, characterizing the binary interaction between the components i and j of the mixture. In [93], the PR eos and the same mixing rule was used to predict the behavior of a N_2-CO_2 mixture over the temperature range 220 - 270 K and for pressures up to 100 bar. This region does not coinicide entirely with that of the current study, but due to the lack of a better value, the same interaction coefficient for the N_2-CO_2 mixture was used:

$$\delta_{N_2\text{-}CO_2} = -0.017 \tag{5.20}$$

The small value of the coefficient indicates that there is little interaction between the two components. No value could be found for the mixture of He and CO_2. Similar to the N_2 - CO_2 case, a very weak interaction is expected. Therefore, the interaction coefficient in the case of He - CO_2 was taken to be zero.

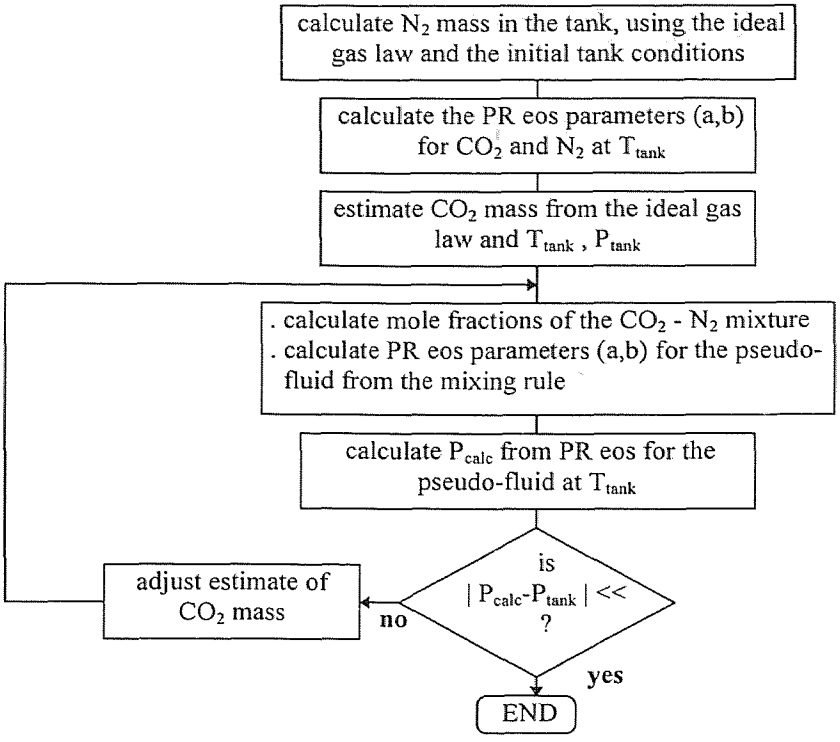

Figure 5.6 Generated Vapor Mass Calculation

The calculation of the generated vapor mass is performed in an iteration loop which contains the PR eos for the gaseous mixture. The flow chart of the calculation is included in Figure 5.6. By repeating the iteration for each measured set of tank pressure and tank temperature (P_{tank} and T_{tank}), a curve for the generated vapor mass is produced. The cases of pure CO_2 and a He-CO_2 mixture were treated similarly.

For several purposes, the partial pressures in the system were calculated. In case a mixture was filling the system, the partial pressure of CO_2 was determined by means of the expression for the fugacity for each component, as listed in Appendix C.1 [65]. Since this expression requires the specification of the mole fraction of the components of the mixture, it is advantageous to incorporate it in the calculation of the generated vapor mass.

5.4 Model of the Main Experiments

The theoretical model of the main experiments is presented in this section and consists of two parts. The first part describes the phenomena inside the inflator and the nozzle and will be referred to as the *SLG-Inflator Model*. The second part is driven by the output of the SLG-Inflator Model and describes the phenomena in the tank. These phenomena include the dispersion, evaporation and solidification of the liquid phase of the spray and the mixing of the vapor phase and the tank gases. This part will be referred to as the *Tank Model*. An overview of the complete model of the main experiments is provided in Figure 5.7. During this research, the main effort was directed towards the SLG-Inflator Model, in keeping with the original objective of the work.

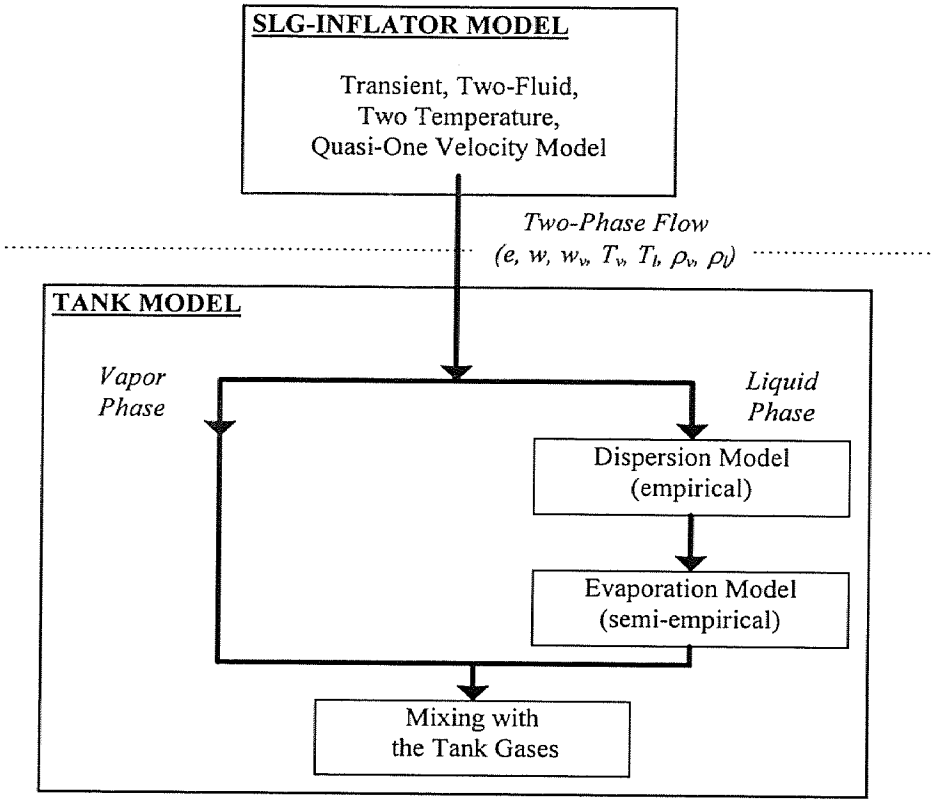

Figure 5.7 Overview of the Theoretical Model of the Main Experiments

The SLG-Inflator Model was primarily based on [47,63], in which a similar problem is considered, i.e. the outflow of flashing water of a tube with one closed end. Since the model is based on the conservation laws, supplemented with constitutive equations to obtain closure, it belongs to the category of the *Two-Fluid Models* [89], similar to [21,28,31,34,69].

As indicated in Figure 5.7, the tank model consists of three steps. The first step concerns the dispersion of the liquid phase in the spray from the nozzle and is described by an empirical correlation [6,56,84]. The evaporation of the generated CO_2 droplets is described in the second step of the tank model. This step also describes the solidification of the droplets. In the last step of the tank model, the generated CO_2 vapor, coming either directly from the nozzle spray or from the evaporation of the droplets, mixes instantaneously with the tank gases.

Both parts of the model (i.e. the SLG-Inflator Model and the Tank Model) run separately from each other. The input of the Tank Model consists of the characteristics of the two-phase spray exiting from the nozzle and this is provided by the SLG-Inflator Model.

5.4.1 Stored Liquefied Gas Inflator Model

As stated, the SLG-Inflator Model was mainly based on [47,63], in which a similar problem is discussed. However, the SLG-Inflator Model differs in several ways from [47,63]:

1. ***CO_2 is the working fluid instead of water:*** For typical initial inflator conditions (Table 2.3), liquid CO_2 is more compressible than water. This leads to smaller

gradients in the system than in [47,63]. In addition, CO_2 is more volatile than water and will evaporate faster. The latter is expected to speed up phenomena such as the outflow and the evaporation wave.

2. ***Different geometry:*** The geometry of the inflator has a similar length over diameter ratio as the tube in [47,63], but differs by about 1 order of magnitude in size. Therefore, it is expected that wall nucleation will be important instead of bulk nucleation, such as assumed in [47,63]. As a result, the parameters of the model, which correspond to the initial bubble size and concentration after nucleation, will differ from the values in [47,63].
3. ***Finite opening time of the release mechanism:*** In [47,63] an instantaneous opening of the tube end is modeled. The finite opening time of the release mechanism in the inflator is taken into account in the current model. This flattens the rarefaction waves and leads to smaller gradients in the system [63]. The smaller gradients are expected to facilitate the numerical simulations, since they allow the limits on the number of space and time steps to be relaxed.

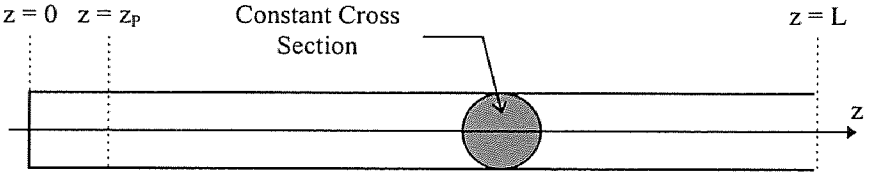

Figure 5.8 Inflator System in the SLG-Inflator Model

The system under consideration is shown in Figure 5.8 and consists of a tube with one closed, and one open end. Since a one-dimensional approach is used, only one space

coordinate is assigned (z). The cross section and the length of the tube are the same as for the inflator vessel. Since the inflator has a constant diameter, the model is developed for a constant cross section. The position of the pressure transducer is marked by z_P, near the closed end at z=0. The nozzle and opening mechanism of the inflator are located at z=L.

5.4.1.1 Main Assumptions: The following assumptions were made when developing the SLG-Inflator model :

1. ***One-dimensional model:*** As suggested by the geometry of the inflator vessel, i.e. a large length over diameter ratio, a one-dimensional approach is adapted and all properties are assumed constant within each cross section of the system. For inflators with a smaller length over diameter ratio or for geometries with drastic changes in the diameter of the vessel, it is expected that two-dimensional effects in the flow will become important.
2. ***Transient model:*** Since the model concerns the start-up of the flow and the evaporation, transient effects are essential for the explanation of the experimental observations.
3. ***Equal pressure for both phases:*** Because of the relatively large size of the bubbles and the high initial pressure, the effect of the capillary pressure[(2)] inside the bubbles is negligible. Hence, the pressure for both phases is equal and constant in every cross section.

[(2)] The *capillary* pressure refers to the pressure increase inside a bubble or droplet, due to the effect of surface tension. It is described by the Laplace (or Laplace-Kelvin) equation [20].

4. ***Vapor phase is saturated corresponding to the local pressure:*** It is assumed that the vapor in the system is saturated with respect to the local pressure. Therefore, when the latter is known, all other vapor properties, such as the temperature (T_v), density (ρ_v) and enthalpy (h_v), can be determined. The combination of assumptions 3 and 4 implies uniform bubble properties. The characteristic time to reach a uniform temperature within a bubble is calculated by means of the Fourier Number [41], which is commonly used to non-dimensionalize time in transient heat conduction problems within bodies:

$$\tau = \frac{a^2}{\alpha_v} \qquad (5.21).$$

For CO_2, at the conditions under consideration, and for the expected bubble sizes, τ was calculated in the order of 10 μs. Since this is 2 orders of magnitude smaller than the characteristic time of the inflation sequence (taken as 1 ms), it is justified to assume uniform properties inside the bubbles.

5. ***Constant pressure outside the inflator:*** The increase in tank pressure is negligible compared to the pressure drop in the inflator. Hence, when expressing the boundary condition on the open end of the inflator (z=L), the pressure is assumed constant and equal to ambient pressure (after the complete opening of the release mechanism). Note that this corresponds to assuming that both parts of the main model (Figure 5.3) operate separately.

6. ***Nucleation can be modeled by specifying the initial bubble size and concentration:*** As discussed during the description of the qualitative model (§4.3.1), predominantly wall nucleation is expected to occur in the current system. In principle, the nucleation

rate can be calculated with the aid of heterogeneous nucleation theories [14,77,97]. However, since this requires the specification of the characteristics of the nucleation cavities and accurate knowledge of the surface tension, which is strongly influenced by impurities, considerable uncertainty is involved. To avoid this uncertainty and to facilitate the numerical simulation, a simplified nucleation model is used. The latter consists of artificially introducing bubbles of known size and concentration in the flow when the pressure drops below the local saturation pressure. It is customary to consider the initial bubble characteristics (size and concentration) as parameters of the simulation and to use them to fit the predictions to the experimental observations [31,34,69]. Typically, a bubble number density of 10^{11}-10^{13} $1/m^3$ and a radius between 0.5 - 20 μm is specified [31,63,69]. This approach is also used in the current model. A few studies have been found where actual wall nucleation models or correlations were used [21,28,92].

7. ***Two-phase flow exists in the 'bubbly-flow' regime:*** The bubbly flow regime, in which isolated, near-spherical bubbles coexist in a continuous liquid phase, is typically established after the onset of flashing. As the bubbles grow, due to evaporation at the interface with the liquid, they are expected to touch each other and coalesce. The latter leads to the formation of slugs and the transition to slug or churn flow. The limit of the bubbly regime, in terms of the void fraction of the flow, depends strongly on the rate of void development. For flows with a limited evaporation rate, the transition is generally taken at $e \approx 0.2$, however, for rapidly evaporating flows (such as the current system), the transition to slug flow may be delayed until $e > 0.7$ [21,28,31,34,69]. The specification of the flow regime is

important because it influences the form of the constitutive relations, which describe the transport processes between the phases (§5.4.1.3).

8. ***Wall friction and heat transfer from the inflator walls are negligible:*** Based on the short duration of the inflation sequence, heat transfer from the inflator walls is neglected. In addition, because of the short length of the inflator vessel, also the effect of wall friction is neglected.
9. ***Viscosity and longitudinal heat transfer in the liquid is negligible:*** Customary to these kind of problems, it is assumed that the influence of the viscosity and heat transfer within the liquid phase is negligible [31,28,31,34,69]. However, viscosity is taken into account, when expressing the drag force from the liquid on the bubbles.
10. ***CO_2(v) behaves like a real gas:*** Since the vapor phase is assumed to exist at saturation conditions, its behavior deviates from ideal gas behavior and it must be modeled as a real gas.
11. ***CO_2(l) is a compressible liquid:*** The compressibility of the liquid phase of CO_2 is essential for the existence of the forerunner, and hence, for the explanation of the inflator phenomena.
12. ***Velocity difference between both phases remains small:*** The velocity difference between the phases is assumed to remain so small that it only affects the break-up process of the bubbles. It is assumed not to affect the mixture velocity. Typically, the velocity difference between the phases will be about 0.1-1.0 m/s.
13. ***Effect of gravity is negligible:*** The forces on the flow, resulting from the pressure gradient in the system, are much larger than the effect of gravity. Therefore, it is not taken into account in the SLG-Inflator model.

5.4.1.2 Governing Equations: The state of the system is defined by seven parameters: P, ρ_v, ρ_l, n, e, w, w_v, i.e. the pressure, the vapor phase density, the liquid phase density, the bubble number concentration, the void fraction, the mixture velocity and the vapor phase velocity, respectively. The following seven field equations, consistent with the above assumptions, are used to solve for the system parameters:

1. ***Conservation of mixture mass (mixture continuity)***

$$\frac{\partial \rho}{\partial t} + \frac{\partial}{\partial z}(\rho . w) = 0 \tag{5.22}$$

2. ***Conservation of vapor mass (vapor continuity)***

$$\frac{\partial}{\partial t}(\rho_v . e) + \frac{\partial}{\partial z}(\rho_v . e . w) = j . n \tag{5.23}$$

3. ***Conservation of mixture momentum (mixture impulse equation)***

$$\frac{\partial}{\partial t}(\rho . w) + \frac{\partial}{\partial z}(\rho . w^2 + P) = 0 \tag{5.24}$$

4. ***Conservation of mixture energy (1^{st} Law of Thermodynamics for the mixture)***

$$\frac{\partial}{\partial t}\left(\rho . \left(h + \frac{w^2}{2}\right) - P\right) + \frac{\partial}{\partial z}\left(\rho . w . \left(h + \frac{w^2}{2}\right)\right) = 0 \tag{5.25}$$

5. ***Conservation of the bubble concentration***

$$\frac{\partial n}{\partial t} + \frac{\partial}{\partial z}(n . w) = \psi \tag{5.26}$$

6. ***Conservation of momentum for a bubble (2^{nd} Law of Newton)***

$$\rho_v . \frac{4}{3} . \pi . a^3 . \left(\frac{\partial w_v}{\partial t} + w . \frac{\partial w_v}{\partial z}\right) = f_A + f_m + f_\mu \tag{5.27}$$

7. ***Equation of state:*** As discussed in detail in §5.2, the HL-eos [46] was used to model the behavior of CO_2.

In addition, the following definitions hold for the mixture density, the mixture enthalpy and the void fraction:

$$\rho = \rho_l.(1-e) + \rho_v.e \qquad \text{for the mixture density,} \tag{5.28}$$

$$h = \frac{\rho_l.(1-e)}{\rho}.h_l + \frac{\rho_v.e}{\rho}.h_v \qquad \text{for the mixture enthalpy and} \tag{5.29}$$

$$e = \frac{4}{3}.\pi.a^3.n \qquad \text{for the void fraction.} \tag{5.30}$$

The source terms in (5.22-27) (j, ψ, f_A, f_m, f_μ , i.e. the evaporation rate, the bubble break-up rate, the buoyancy force, the virtual mass force and the drag force, respectively) will be related to the system parameters by the constitutive expressions in §5.4.3.1.

According to assumption 12 in §5.4.1.1, the velocity difference between the phases does not affect the mixture flow. As a result, the conservation of momentum for a bubble (5.27) can be integrated separately from the other field equations. Equations (5.22-26) are rewritten in the generalized transport equation form:

$$\frac{\partial \vec{U}}{\partial t} + \frac{\partial \vec{F}[\vec{U}]}{\partial z} = \vec{J}[\vec{U}], \qquad \text{with} \tag{5.31}$$

$$\vec{U} = \begin{Bmatrix} \rho \\ \rho_v.e \\ \rho.w \\ \rho.\left(h + \frac{w^2}{2}\right) - P \\ n \end{Bmatrix}, \quad \vec{F}[\vec{U}] = \begin{Bmatrix} \rho.w \\ \rho_v.e.w \\ \rho.w^2 + P \\ \rho.w.\left(h + \frac{w^2}{2}\right) \\ n.w \end{Bmatrix}, \quad \vec{J}[\vec{U}] = \begin{Bmatrix} 0 \\ j.n \\ 0 \\ 0 \\ \psi \end{Bmatrix}. \tag{5.32}$$

The system (5.31-32) is a 1st order hyperbolic system of partial differential equations, with $\vec{U}$ the vector of the transport quantities, $\vec{F}$ the vector of the fluxes and $\vec{J}$ the vector of the sources.

5.4.1.3 Constitutive Equations: To obtain closure for (5.31-32), the source terms need to be specified. They concern the evaporation rate, the bubble break-up rate and the forces on the bubbles. This is done with the aid of the constitutive equations.

For the liquid properties, i.e. the thermal diffusivity, the surface tension and the viscosity, only data corresponding to the saturated liquid state was found. However, since these properties are used to calculate the source terms in (5.31-32), i.e. after nucleation has occurred, the condition of the liquid will be relatively close to saturation. Consequently, it is expected that the use of saturated liquid properties will not lead to significant errors .

Evaporation Rate (j): It is assumed that the evaporation process is thermally controlled and that the latent heat of evaporation is entirely supplied by the superheated liquid. The heat transfer coefficient from the liquid to the bubble-liquid interface is determined by means of a correlation, involving the Nusselt (Nu) and the Jakob number (Ja). Additional information on the bubble evaporation model can be found in [21,47,63].

The evaporation rate is calculated from:

$$j = 2.\pi.a.\alpha_l.\rho_v.Ja.Nu \qquad (5.33),$$

in which: $$Ja = \frac{c_l.\rho_l.\left(T_l - T^{sat}[P]\right)}{\rho_v.L} \quad (5.34),$$

$$Nu = \frac{12}{\pi}.Ja.\left[1 + \frac{1}{2}.\left(\frac{\pi}{6.Ja}\right)^{2/3} + \frac{\pi}{6.Ja}\right] \quad (5.35).$$

A 4th-order polynomial curve fit for the dependence of the thermal diffusivity of the liquid (α_l) on temperature was developed. Data from three sources was combined for this purpose, ranging from the triple point to 300 K [12,17,87]. The resulting expression is:

$$\alpha_l = -3.2577.10^{-11}.T_l^4 + 3.2737.10^{-8}.T_l^3 - 1.2307.10^{-5}.T_l^2 + 2.0435.10^{-3}.T_l - 0.1253 \quad (5.36).$$

The units of the calculated α_l are [cm^2/s]. This curve fit generated an ARD of 3.0% over the temperature range. The spread of the values from the three sources is partially responsible for the size of the deviation.

Another 4th order polynomial curve fit was developed for the isobaric specific heat of saturated liquid CO_2 (c_l), based on tabulated data in [12,17]. Data was used for a temperature interval from the triple point to 295 K. The following polynomial generated an ARD of 2.2% over this interval:

$$c_l = 4.3351.10^{-4}.T_l^4 - 0.4249.T_l^3 + 155.8902.T_l^2 - 25366.5537.T_l + 1545867.3729 \quad (5.37)$$

Bubble Break-up Rate (ψ): Bubble break-up is the result of surface instabilities, which grow under influence of the velocity difference between the liquid and the vapor phase, i.e. so called Kelvin-Helmholtz instabilities [19]. A flat interface model is used and break-up is assumed to occur when the wavelength of the instability equals the droplet diameter. This leads to a critical value of the Weber number of 2π: $We^{cr} = 2\pi$. When the

local Weber number exceeds the critical value, the bubbles are assumed to break into two equal smaller bubbles. Reference [47] contains a detailed description of the break-up model.

The bubble break-up rate is evaluated from:

$$\psi = \begin{cases} 0 & We < We^{cr} \\ \dfrac{n}{t^{cr}} & We \geq We^{cr} \end{cases} \tag{5.38},$$

with the local Weber number given by:

$$We = \frac{2.a.(w_v - w_l)^2}{\sigma} . \frac{\rho_l . \rho_v}{\rho_l + \rho_v} \tag{5.39}.$$

The critical time (t^{cr}) represents the time which it takes for the amplitude of the disturbance to reach a value comparable to the bubble radius and can be expressed as:

$$t^{cr} = \left[\frac{\rho_l . a^3}{\sigma} . \left(\frac{2.\pi}{We} \right)^3 \right]^{1/2} \tag{5.40}$$

The temperature dependence of the surface tension was described by an expression from [32]. It concerns the flat film value (the influence of the curvature is neglected) and the expression holds downto 160 K:

$$\sigma_\infty = 75. \left(1 - \frac{T}{T_c} \right)^{1.25} \tag{5.41}$$

The units of σ_∞ are [dynes/cm]. The results of (5.41) were verified with tabulated values in [3] and were in good agreement.

Bubble Forces (f_A, f_m, f_μ): Three forces (in addition to its own inertia) are considered in the bubble momentum balance of (5.27). They are the buoyancy force, the virtual mass force and the drag force, as given by (5.42), (5.43) and (5.44), respectively:

$$f_A = \rho_l . \frac{4}{3} . \pi . a^3 . \left(\frac{\partial w}{\partial t} + w . \frac{\partial w}{\partial z} \right) \tag{5.42}$$

$$f_m = \frac{1}{2} . \rho_l . \frac{4}{3} . \pi . a^3 . \left[\left(\frac{\partial w}{\partial t} + w . \frac{\partial w}{\partial z} \right) - \left(\frac{\partial w_v}{\partial t} + w_v . \frac{\partial w_v}{\partial z} \right) \right] \tag{5.43}$$

$$f_\mu = \frac{C}{2} \rho_l . \pi . a^2 . (w - w_v) |w - w_v| \tag{5.44}$$

The buoyancy force (f_A) is equal to the force of the displaced liquid (Principle of Archimedes). The virtual (or *apparent*) mass force (f_m) accounts for the liquid flow around the bubble, which is created when it accelerates relative to the liquid. According to [69], this effect needs to be included in the bubbly flow regime only. Although correlations were developed to determine the virtual mass coefficient (i.e. the first factor in 5.43) in terms of the local flow characteristics [31,69], a value of 0.5 is often used [28,47,63]. Many different forms for the drag force (f_μ) have been published [21,28,31,34,47,63,69]. Most expressions are similar and the relation from [47] was used in the SLG-Inflator Model:

$$C = \begin{cases} \dfrac{16}{\mathrm{Re}} & \mathrm{Re}_l \le 10.9 \\ \dfrac{48}{\mathrm{Re}} . \left(1 - \dfrac{2.2}{\sqrt{\mathrm{Re}}} \right) & \mathrm{Re}_l > 10.9 \end{cases} \tag{5.45},$$

with the bubble Reynolds number:

$$\mathrm{Re} = \frac{2 a \rho_l |w - w_v|}{\mu_l} \tag{5.46}.$$

The temperature dependence of the dynamic viscosity of the liquid phase (μ_l), was expressed through a 2nd order curve fit based on data from [17] in the range from the triple point to the critical point.

$$\mu_l = 1.0493.10^{-8}.T_l^2 - 7.0236.10^{-6}.T_l + 1.2305.10^{-3} \qquad (5.47)$$

The shape of the constitutive equations strongly depends on the flow regime of the two-phase flow. For example, when bubbly flow turns to churn or slug flow, the effect of the virtual mass force becomes negligible. The transition between flow regimes is based on the value and the rate of change of the void fraction. The above set of constitutive equations are expected to adequately model the interfacial transport processes for void fractions below 0.7.

5.4.1.4 Numerical Algorithm: Both the main system (5.31-32) and the momentum conservation for the bubbles (5.27) are solved by a *Two-step Lax-Wendroff Scheme* (LW scheme) [68], a popular algorithm for transient solutions of hyperbolic systems of PDEs. A *splitting method* [68] was used to include the source terms in the LW scheme. The set of difference equations of the numerical scheme, both for the main system and for the bubble momentum conservation law are included in Appendix E. A flow chart of the main integration loop, which demonstrates the sequence of operations, is also included in Appendix E.

The LW scheme is 2^{nd} order accurate in space and time[(3)]. The space and time step (Δz and Δt, respectively) are connected by the *CFL condition*, which is a necessary condition for the numerical stability of the algorithm (a is the local sonic velocity):

[(3)] The *order* of the numerical algorithm reflects the number of terms that was taken into account in the Taylor expansion of the solution. For example, a 2^{nd} order scheme in space has a local truncation error of the order of $(\Delta z)^3$, which is the order of the first term in the Taylor series which was not taken into account due to truncation [68].

$$\frac{a.\Delta t}{\Delta z} \leq 1 \tag{5.48}$$

Physically, (5.48) can be interpreted as a condition which ascertains that the speed at which the information travels in the numerical algorithm is higher than the rate at which the actual system changes.

During each step of the algorithm, the system properties corresponding to the local vector of transport quantities need to be determined. This involves solving a non-linear system of algebraic equations, which was done numerically by means of the *Modified Newton Method* [10]. Additional information is included in Appendix E.

5.4.1.5 Initial and Boundary Conditions: For nominal initial conditions (Table 2.3), the inflator is initially filled with uniform subcooled liquid. The initial pressure exceeds the critical value and no bubbles are present in the system. Furthermore, the fluid is at rest and the velocity is uniformly 0. These considerations allow the evaluation of the initial values of the system parameters. Similarly, for other initial inflator conditions, the system parameters are known at the onset of the process.

During the integration, the same two boundary conditions as in [47,63] were applied. At the closed end of the tube (z=0, Figure 5.4), the velocity of both phases is zero (no slip condition). This condition is readily incorporated into the numerical algorithm. The boundary condition at the open end (z=L, Figure 5.4) is commonly referred to as the *outflow* boundary condition [77,91]. After the release mechanism has opened completely, and in agreement with the 5th assumption in §5.4.1.1, the outflow boundary condition requires that the pressure outside the inflator is constant and equal to ambient pressure.

For single phase or equilibrium two-phase flow, such a condition is commonly implemented with the aid of the method of characteristics [77,91]. In the current model, the outflow boundary condition was incorporated into the solution algorithm by developing the field equations and the bubble momentum conservation law in a *1st Order Upwind Differencing Scheme* [68]. The corresponding difference equations and additional information are included in Appendix E.

The finite opening time of the release mechanism is modeled through the outflow boundary condition in two steps. The first step corresponds to the first stage of the inflation sequence (§4.3.1.1) in which there is no flow from the nozzle. The second step concerns the clearing of the exit holes by the sliding piston during the initial moments of the second stage in the inflation sequence (§4.3.1.2).

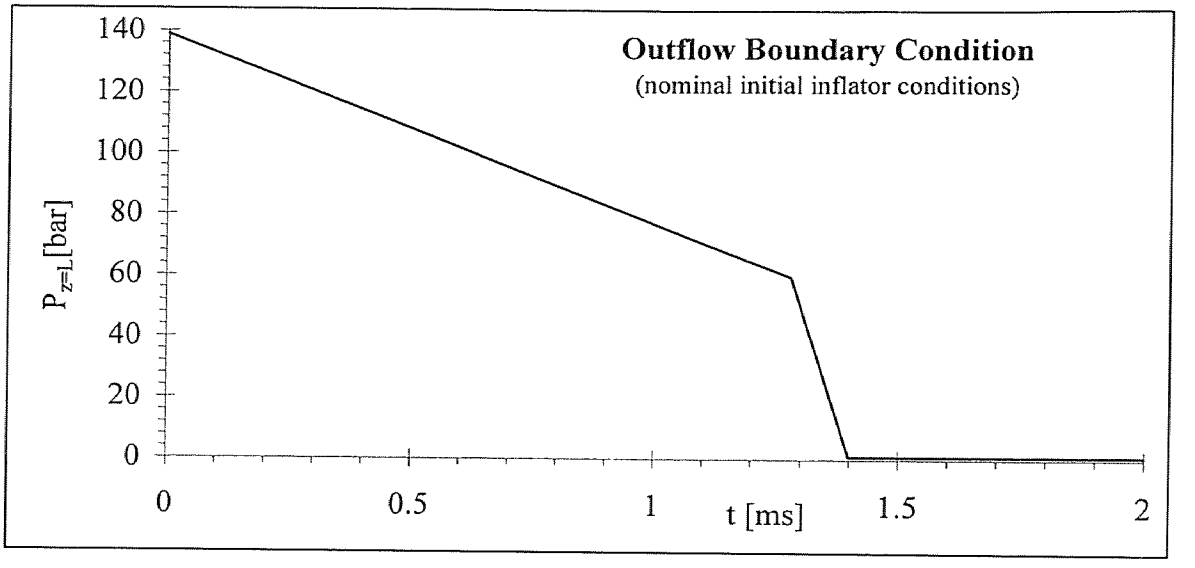

Figure 5.9 Outflow Boundary Condition

The implementation of these two steps for the case of nominal initial inflator conditions is shown in Figure 5.9. During the first step, the pressure drops linearly from its initial value (139 bar) to 60 bar in 1.28 ms. The latter corresponds to the calculated duration of the first stage of the inflation sequence, based on the dynamic analysis of the motion of the sliding piston in the mechanism. The value at the end of the first stage (60 bar) was calculated by assuming an isentropic expansion of the subcooled CO_2 in the central channel of the nozzle. The second step lasts 0.12 ms and concerns a rapid linear pressure drop to ambient pressure (1 bar). Again, this duration is evaluated in the dynamic analysis of the sliding piston.

Finally, because the implementation of the outflow boundary condition is 1^{st} order in time and space, it is expected to reduce the accuracy of the entire solution. While it is difficult to estimate the loss of accuracy, according to [35] it should be located between that of a 2^{nd} and 1^{st} order scheme. This loss of accuracy can be avoided by developing the outflow boundary condition in a 2^{nd} Order Upwind Differencing Scheme. However, since this scheme uses two 'previous' points, it leads to difficulties when starting the integration loop.

5.4.1.6 Validation of the SLG-Inflator Model: References [47,63] contain the results of the simulation of flashing outflow of water from a tubular vessel (P_0=69 bar, T_0=515). The authors did not provide information on the outflow boundary condition, the equation of state or the number of time and space steps that were used.

In order to validate the developed SLG-Inflator Model, several attempts were made to simulate the same outflow processes as discussed in [47,63]. By comparing the

output of the SLG-Inflator Model to the results in [47,63], the accuracy of the developed inflator model could be verified. For this purpose, a second version of the model was developed, in which water was used as the working fluid. The water behavior was modeled by means of the eos which was used to generate the classical steam tables of Keenan and Keyes [50]. Other properties such as viscosity, surface tension, latent heat, specific heat capacity and thermal diffusivity are readily available in the literature [95] and were approximated by polynomial curve fits. For the water model, a different boundary condition was applied than described in §5.4.1.5. It was assumed that the flow in the last space step of the tube could be approximated as uniform, i.e. properties such as velocity, void fraction and temperature were assumed to be constant. In addition, an instantaneous pressure drop to ambient pressure was applied in the outflow section at the start of the process.

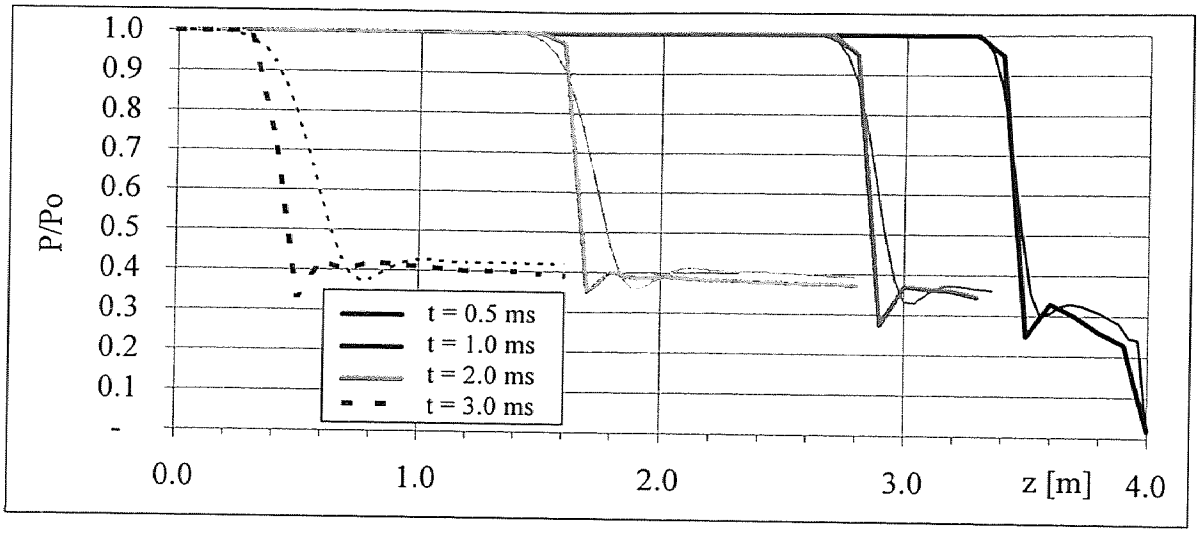

Figure 5.10 Propagation of Forerunner in the Water Model
(thin lines correspond to the current model, while the bold curves represent the published results in [47,63])

The output of the current model is compared with published results [47,63] in Figure 5.10. The number of space steps and the magnitude of the timestep for these calculations were 100 and 25 μs, respectively. Figure 5.10 represents the pressure distribution along the axis of the tubular vessel (normalized with the initial pressure) and illustrates the formation and propagation of the forerunner in the tubular vessel (length 4.0 m). Reasonable agreement between the output of the current model and the results of [47,63] is observed. It is believed that the approximated outflow boundary condition (i.e. neglecting the changes in the system in the space step before the open end of the tube), is responsible for the observed deviation between the pressure curves in Figure 5.10.

To obtain better agreement between the output of the current model and the results in [47,63], the outflow boundary condition should be applied as described in §5.4.1.5, but with an instantaneous drop to ambient pressure at the onset of the process. This should be accompanied with the use of a larger number of space and time steps to resolve the steep gradients in the system. This approach was tried during this research, but the required computation time on the computer that was available (Sun Workstation SPARC 20, shared with on average 5 other users) became unacceptable (more than a week). Therefore, further attempts to validate the SLG-Inflator Model in this manner were abandoned.

5.4.1.7 Preliminary Results and Discussion: The output of the SLG-Inflator Model consists of the axial distribution of the properties inside the inflator at different times in the inflation sequence.

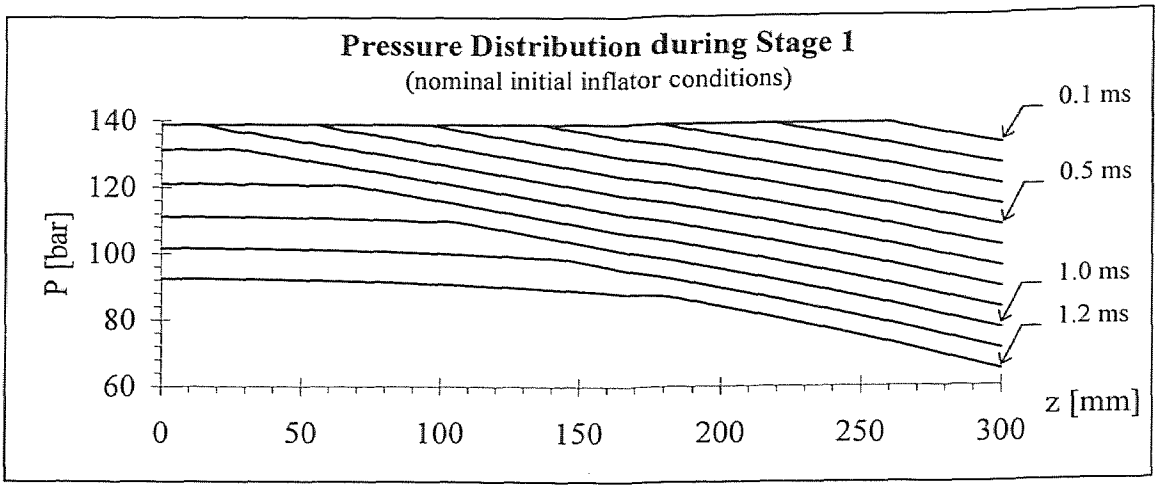

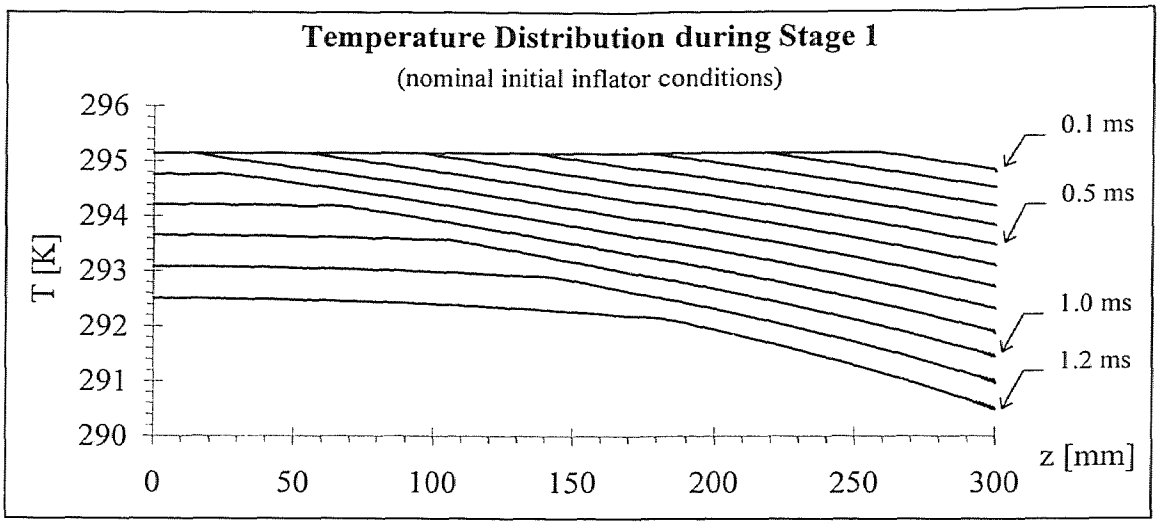

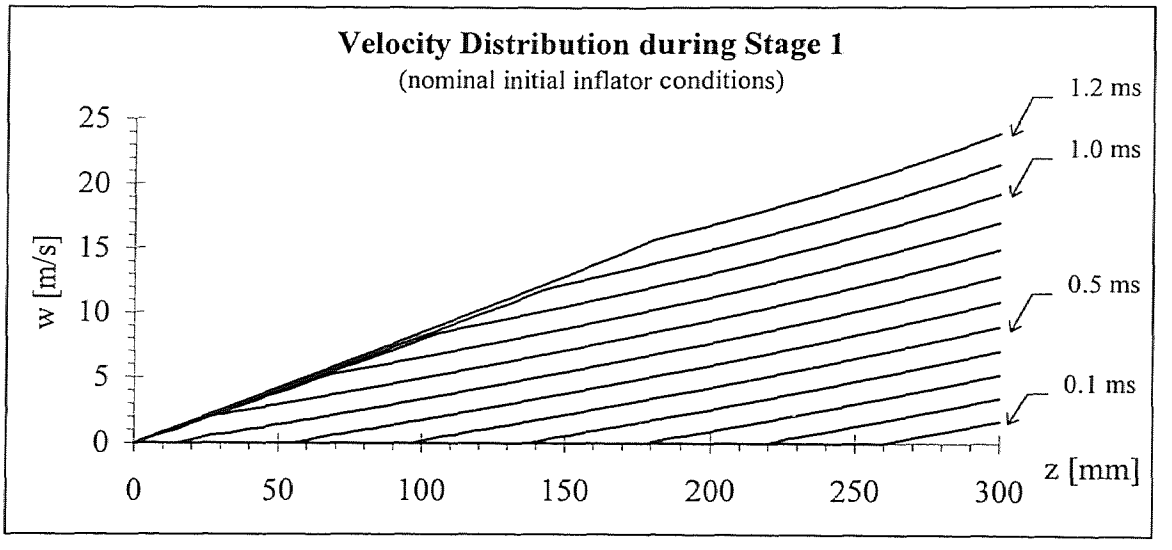

Figure 5.11 Inflator Properties during Stage 1 of the Inflation Sequence

These properties include the temperature and velocity of both phases, the void fraction, the pressure, the bubble size and the bubble concentration. Commonly, the output is represented in property profile curves, taken at a particular point in time. To assess the agreement between experiments and simulations, a series of pressure and temperature profile curves needs to be considered. The evolution of the pressure and temperature given by the series of profile curves at the locations corresponding to the positions of the pressure transducer and the thermocouple must be compared with the measurements.

At present, only preliminary results from the SLG-Inflator model are available. The simulation was performed for initial conditions corresponding to the Reference Experiment: 2000 psig (139 bar) and 22 °C (295 K). Results were obtained for the first stage and part of the second stage of the inflation sequence (up to t=1.35 ms).

The results for the first stage of the inflation sequence, with a duration of 1.28 ms, are presented in Figure 5.11. As discussed in §4.3.1, this stage corresponds to the isentropic expansion of the subcooled CO_2 in the central channel of the nozzle, and no nucleation takes place. The boundary condition (Figure 5.9) applies a linearly decreasing pressure during this stage to a value of 60 bar. Profile curves for the pressure, temperature and velocity are presented. Figure 5.11 clearly illustrates the non-uniform pressure and temperature distribution at the end of the first stage, which influences the propagation speed of the forerunner during the second stage (§4.3.1). It can be verified that the saturation pressure, corresponding to the temperature profile curves in Figure 5.11, is lower than the local pressure at all times and that no nucleation takes place. The velocity curves illustrate the no-slip boundary condition at the closed end of the tube and the gradual acceleration of the outflow.

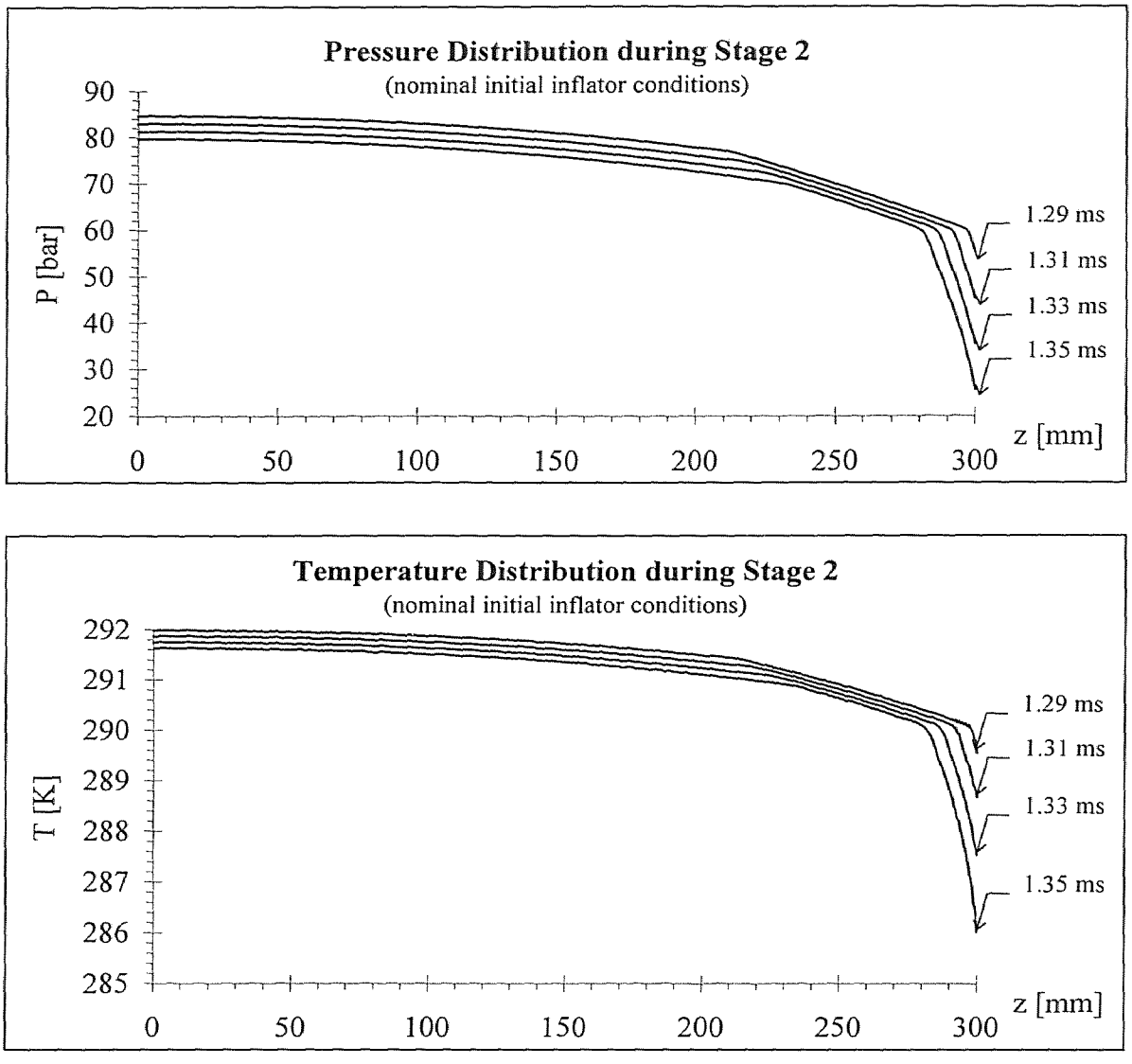

Figure 5.12 Inflator Pressure and Temperature during Stage 2 of the Inflation Sequence

Partial results for the second stage of the inflation sequence are presented in Figures 5.12 and 5.13. The pressure and temperature profiles are shown in Figure 5.12, while the development of the void fraction and the velocity distribution are illustrated in Figure 5.13. During the first 0.12 ms of the second stage, the nozzle exit holes are completely opened, and the pressure at the open end of the inflator drops from 60 bar to

ambient. This results in the forerunner, which propagates through the inflator at the local speed of sound. Due to the pressure and temperature profile in the inflator at the onset of the second stage, the forerunner is expected to speed up as it approaches the closed end of the vessel. The start of the formation of the forerunner is shown in Figure 5.12 as a rapid pressure drop near the open end of the inflator.

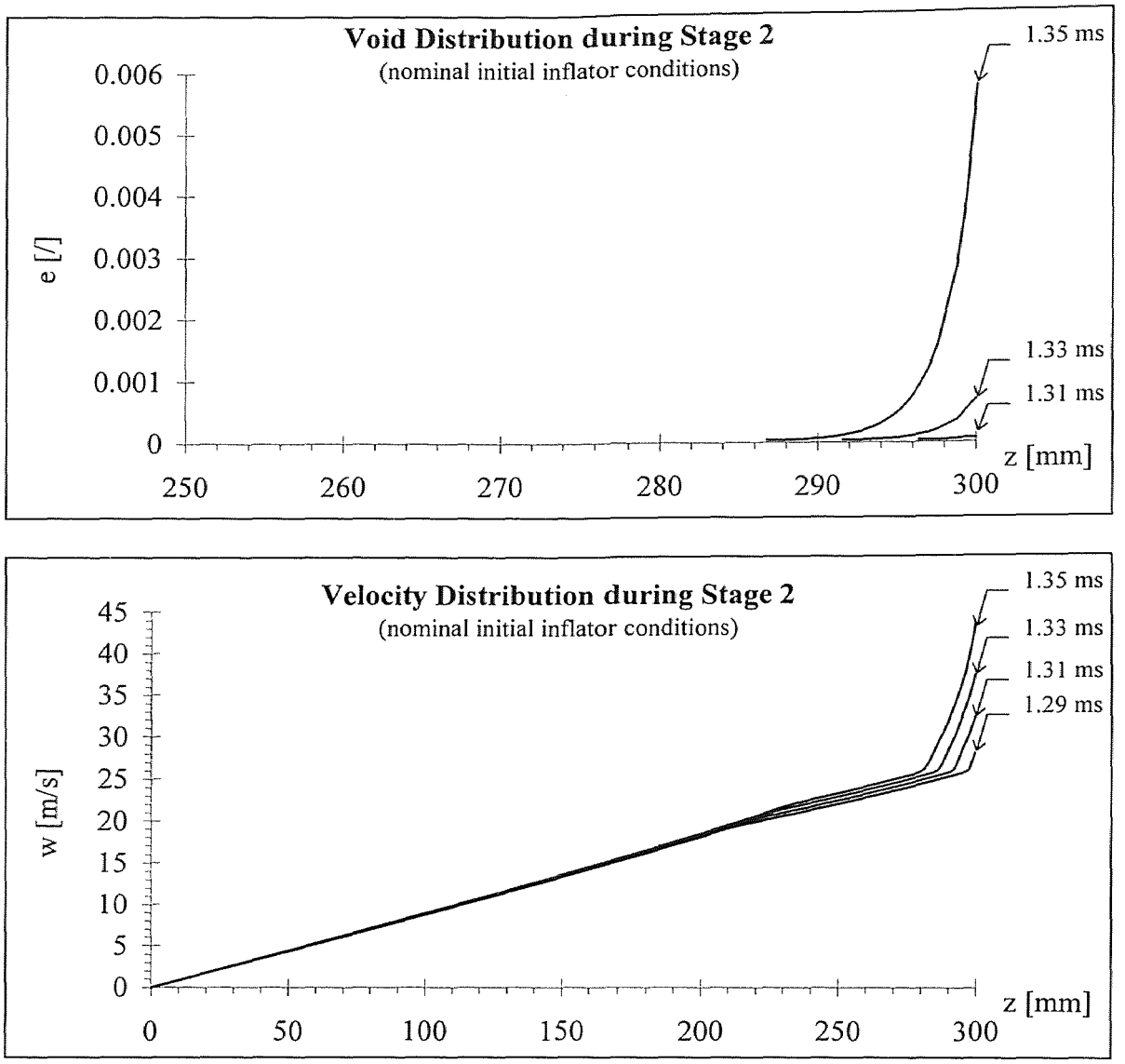

Figure 5.13 Void Fraction and Velocity in the Inflator during Stage 2 of the Inflation Sequence

Figure 5.13 shows that nucleation and evaporation commence shortly after the start of the 2nd stage in the inflation sequence. An initial bubble size of 1 μm and an initial bubble concentration of 10^{13} $1/m^3$ were used. Note that in the figure which contains the void fraction curve, only the last 50 mm of the inflator is shown.

For the above simulation, the space domain was discretized in 500 steps, while a time step of 0.5 μs was used. It is clear that the results of the simulations in Figures 5.11-13, i.e. for the first 1.35 ms of the inflation sequence, do not allow a meaningful comparison with the experimental observations.

The SLG-Inflator model was run for different values of the initial bubble size and initial bubble number concentration, ranging from 0.1-20 μm and 10^9-10^{16}, respectively. For very small initial bubble sizes (below 0.5 μm), the velocity of the vapor phase immediately after the introduction of the bubbles oscillated around the liquid velocity with growing amplitude. Within a few timesteps, the velocity difference between the phases became unacceptable. This phenomenon was not observed for larger initial bubble sizes (above 0.5 μm), in which case the term corresponding to the drag force in the bubble momentum balance is less dominant. For low initial bubble number concentrations (below 10^{11}-10^{12}), the evolution of the liquid phase during the inflation sequence was such that the spinodal line was reached. In reality, this situation corresponds to very clean operating conditions (liquid and equipment) and would lead to homogeneous nucleation.

When the above phenomena were avoided, by choosing initial bubble sizes in excess of 0.5 μm and initial concentrations above 10^{12}, another problem occurred. Independent of the values of the parameters, the temperature and void fraction in the

section prior to the open end of the inflator, were observed to grow to unacceptable values. While it is not proven at present, it is believed that this is a result of a numerical instability. In an attempt to avoid the instability, the calculation is being repeated with a larger number of space steps (1000) and a smaller time step (0.2 μs).

5.4.2 Tank Model

Three different processes are taken into account in the Tank Model (Figure 5.7):

1. the dispersion of the liquid phase of the spray (Dispersion Model)
2. the evaporation and solidification of the CO_2 droplets (Evaporation Model)
3. mixing of the CO_2 vapor with the tank gases (Mixing Model)

The CO_2 vapor in the third process is partially produced by flashing inside the inflator and partially by the evaporation of the dispersed droplets in the tank.

Both the dispersion of the liquid phase and the evaporation of the spray are highly complicated processes, with a large number of interrelated parameters. Only in the case of a low-velocity, single phase, liquid jet from a nozzle with a simple geometry, the atomization process can be described without the aid of correlations [6,56]. Similarly, all current models for the evaporation of sprays rely on empirical correlations [6,80]. Both for the dispersion of the liquid and for the evaporation of the droplets, correlations are used in the Tank Model. A large part of the research in the dispersion of liquid and the evaporation of sprays is driven by the strong interest of the automobile industry in improving the performance of injectors for internal combustion engines. The correlation

in the Dispersion Model, as well as the one in the Evaporation Model (Figure 5.7) were taken from an investigation concerning fuel injectors.

It is assumed that the generated CO_2 vapor mixes instantaneously with the tank gases. The evaluation of the resulting tank properties is similar to the calculation of the generated vapor mass (§5.3).

The input of the Tank Model consists of the characteristics of the two-phase flow in the nozzle exit plane, as calculated by the SLG-Inflator Model (Figure 5.7). These characteristics include the void fraction, the temperature, density and velocity of both phases. Since the flow from the inflator is not steady, the characteristics of the two-phase flow from the nozzle will change during the inflation sequence. It is assumed that all processes in the tank are quasi-steady, such that correlations for steady conditions apply.

To take the time dependence of the outflow characteristics into account, the tank processes are modeled by a sequence of small time steps. At the beginning of each step, the characteristics of the two-phase flow in the nozzle exit plane are considered (as calculated by the SLG-Inflator Model) and the Dispersion Model is used to predict the average diameter, the number and the temperature of the generated droplets. Before the Evaporation Model is applied, the properties of the freshly formed droplets is combined with the properties of the droplets that were already in the tank. In this manner, the average properties (i.e. size, number and temperature) of the total amount of droplets in the tank are updated. Based on these average properties, the Evaporation model predicts the change in average droplet diameter and temperature as well as the amount of generated vapor during the time step under consideration. Finally, before repeating the above in the next time step, and based on the total amount of generated vapor, the Mixing

Model is used to calculate the new conditions of the gaseous mixture in the tank. This sequence of operations is repeated until the end of the inflation process. Figure 5.14 contains a flow-chart of the Tank Model.

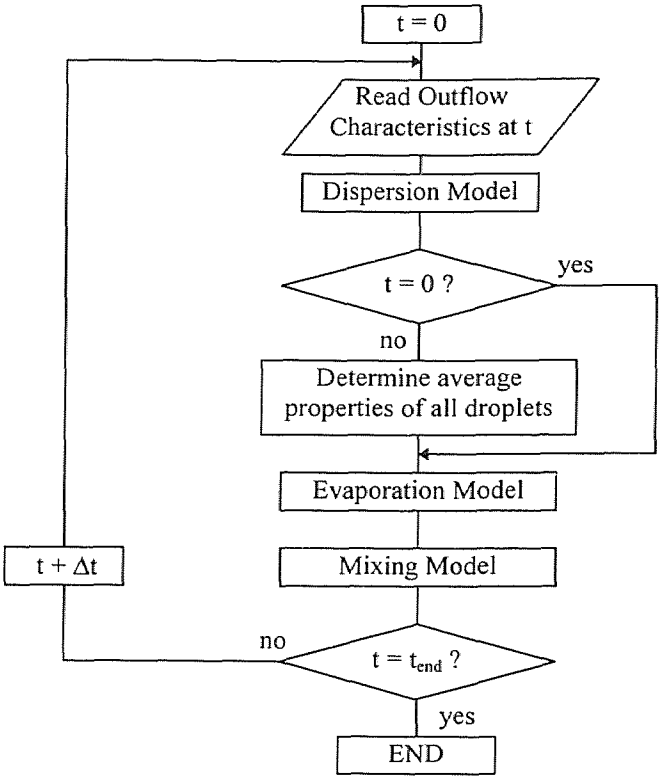

Figure 5.14 Flow-chart of the Tank Model

5.4.2.1 Dispersion Model: The dispersion model describes the break-up of the liquid phase in the two-phase outflow from the inflator. The main output of the dispersion model is the size distribution of the generated droplets. While it is impossible to characterize a size distribution by a single parameter, it is common practice to base calculations on the average diameter only [56]. Different definitions of the average diameter of a size distribution are used for different purposes [56]. For processes

involving mass transfer, it is common to use the *Sauter Mean Diameter*(SMD), which is defined as:

$$SMD = D_{32} = \frac{\sum N_i D_i^3}{\sum N_i D_i^2} \qquad (5.49),$$

with N_i the number of droplets in the size range with middle diameter D_i. Droplets with a diameter equal to the SMD have the same volume to surface ratio as the entire spray.

As discussed in detail in Chapter 4, the high-speed cinematographic observations of the shape of the spray indicate that classical atomization predominates during the entire inflation sequence. If the influence of the flashing and the presence of the vapor phase in the jet is neglected, a correlation for a Plain Pressure Orifice Atomizer can be used [56]. Numerous correlations of the SMD for liquid jets from a constant diameter orifice have been reported. The Mayer-correlation (1961) [84], was developed for conditions with relatively high liquid velocities:

$$SMD = 21.4B\left[\mu_l \left(\frac{\sigma}{\rho_l}\right)^{1/2} \Big/ \rho_v w_l^2\right]^{2/3} \qquad (5.50),$$

with B an empirical parameter of order unity.

The presence of the vapor phase in the jet from the inflator nozzle creates a similar situation as in a Twin Fluid Atomizer, where air is supplied to enhance the dispersion [56]. Based on this observation, [84] successfully employed a correlation,

developed for a Prefilming Air Blast Injector[4], to predict the average droplet size in case of a flashing injector[5] . The following correlation from [56] was used:

$$\frac{\eta_n SMD}{\left(1+\frac{\dot{m}_l}{\dot{m}_v}\right)} = 0.073\left[\frac{\sigma}{\rho_v w_v^2}\right]^{0.6}\left[\frac{\rho_l}{\rho_v}\right]^{0.1} d_P^{0.4} + 0.0006\left[\frac{w_v^2 d_P}{\sigma\rho_v}\right]^{0.5} \qquad (5.51),$$

with η_n: atomization efficiency, based on the performance of the particular injector.

Depending on the influence of the flashing and the presence of the vapor phase on the dispersion process, (5.50) or (5.51) will be most suited to be used in the Dispersion Model. It is expected that by comparing the simulated tank properties with the experimental observations, a selection between (5.50) and (5.51) will be possible. Note that all parameters in both correlations are known when the characteristics of the outflow are specified.

When the average diameter of the droplets is known, the number of drops that is being injected can be evaluated from the total amount of liquid that is discharged in the tank during that time step. Furthermore, the temperature of the drops is assumed to be uniform and equal to the temperature of the liquid phase in the exit plane of the nozzle.

5.4.2.2 Evaporation Model: The evaporation of the CO_2 droplets in the tank during the inflation sequence is described by the model for drop vaporization presented by Reitz in [31], which is based on Chapter 8 in [56].

---

[4] In a *Prefilming Air Blast Injector*, the liquid is first spread out in a thin continuous sheet and then subjected to the atomizing action of high-velocity air. They are used in a wide variety of aircraft, marine and industrial gas turbines [56].

[5] A *Flashing Injector* operates on the principle that the liquid flashes as it passes through the injector.This improves the atomization properties (reduction in drop size and spray penetration and better spread) [84].

A brief summary of this model is included in this section.

The vaporization of a spherically symmetric droplet is considered and molecular diffusion is assumed to be the rate-controlling process. Starting from Fick's law of diffusion, the rate of drop radius change for steady state evaporation can be expressed as:

$$\frac{da}{dt} = -\frac{\rho D_{CO_2-N_2}}{\rho_{CO_2(l)} a} \ln(1+B) \qquad (5.52),$$

with ρ the density of the gaseous mixture surrounding the evaporating droplet and B the mass transfer number, defined as follows:

$$B = \frac{Y_{CO_2}^{sat} - Y_{CO_2}}{1 - Y_{CO_2}^{sat}} \qquad (5.53).$$

In (5.53), $Y_{CO_2}^{s}$ and Y_{CO_2} represent the mass fraction of CO_2 at the droplet surface and the average mass fraction of CO_2 in the tank, respectively. The mass fraction at the surface is determined by assuming that the partial pressure of CO_2 is equal to the saturation pressure corresponding to the droplet temperature (T_d):

$$Y_{CO_2}^{sat} = \left[1 + \left(\frac{P}{P_{CO_2}^{sat}(T_d)} - 1\right)\frac{MW_{N_2}}{MW_{CO_2}}\right]^{-1} \qquad (5.54).$$

In (5.52), the quantity $\left(\rho D_{CO_2-N_2}\right)$ is commonly replaced with $\left(k/c_P\right)$, assuming a Lewis number of unity. The thermal conductivity and the specific heat are mean values for the gases surrounding the droplet, and are calculated at a reference temperature and composition, obtained from the *one-third rule*:

$$T_{ref} = T^{sat} + \frac{1}{3}\left(T_{tank} - T^{sat}\right) \qquad (5.55)$$

$$\left[Y_{CO_2}\right]_{ref} = Y_{CO_2}^{sat} + \frac{1}{3}\left(Y_{CO_2} - Y_{CO_2}^{sat}\right) \tag{5.56}.$$

Using these references, the thermal conductivity and specific heat can be calculated by an additive mixing rule:

$$c_P = \left[Y_{N_2}\right]_{ref}\left(c_{P,N_2}\ at\ T_{ref}\right) + \left[Y_{CO_2}\right]_{ref}\left(c_{P,CO_2}\ at\ T_{ref}\right) \tag{5.57}$$

$$k = \left[Y_{N_2}\right]_{ref}\left(k_{N_2}\ at\ T_{ref}\right) + \left[Y_{CO_2}\right]_{ref}\left(k_{CO_2}\ at\ T_{ref}\right) \tag{5.58}.$$

The above holds for the evaporation of a droplet in quiescent conditions. When a relative velocity exists between the drop and the surrounding gases, convective effects enhance the evaporation and the lifetime of the droplet decreases. This effect is taken into account by multiplying the right hand side of (5.52) with a correction factor. The latter is commonly obtained with the aid of the Frossling correlation, which involves the Reynolds and the Schmidt number.

The change in droplet temperature is calculated from the energy balance for the droplet:

$$\frac{4}{3}\pi a^3 \rho_{CO_2(l)} c_{CO_2(l)} \frac{dT_d}{dt} - 4\pi a^2 \frac{da}{dt} \rho_{CO_2(l)} L = 4\pi a^2 Q_d \tag{5.59},$$

with L the latent heat corresponding the droplet temperature and Q_d the rate of heat conduction to the drop. The Ranz-Marshall correlation is used to evaluate the heat conduction. The correlation contains the Reynolds and the Prandtl number.

The involved properties in the dimensionless numbers of the Frossling and the Ranz-Marshall correlation should be evaluated at the reference temperature and composition (5.55 and 5.56). Similar mixing rules as (5.57 and 5.58) hold for the density and the viscosity.

The main difficulty with the above model concerns the relative velocity between the droplets and the tank gases, which is required for the evaluation of the droplet Reynolds number. This velocity is not known and should be estimated or considered as a parameter of the Tank Model.

It is clear that the Evaporation Model involves severe approximations, such as neglecting the influence of the surrounding droplets and assuming steady state evaporation. Therefore, it should be considered as a first attempt to describe the evaporation process and requires further research.

5.4.2.3 Mixing Model: It is assumed that the freshly generated CO_2 vapor mixes instantaneously with the gaseous mixture, already present in the tank. The updated properties of the gaseous mixture (i.e. mole fractions, temperature and pressure) are determined by using the PR eos, in combination with the van der Waals mixing rule, similar to the procedure in §5.3.

CHAPTER 6

GENERAL CONCLUSIONS AND FUTURE WORK

6.1 General Summary

A novel type of automotive air bag inflator, called the *Stored Liquefied Gas (SLG) Inflator*, has been studied and developed. The inflator is based on the rapid evaporation of liquefied CO_2 and was investigated both experimentally and theoretically.

The main part of the experimental study consisted of tests in which the air bag inflation was simulated by discharging the inflator into a receiving tank. The resulting tank pressure and temperature were recorded as functions of time and used for a detailed evaluation of the inflator's performance. An experimental set-up was developed and constructed for this purpose where measurements were performed on a millisecond timescale. In contrast to other studies, the measurement of the average tank temperature during the inflation sequence was highly accurate. A thermodynamic analysis of the experimental data provided information about the amount of generated CO_2 vapor and the influence of the tank gases on the inflator's performance. Additional experimental observations were obtained with the aid of high-speed cinematographic recordings.

Based on the experimental study of the critical parameters of the inflator, including initial temperature and pressure, size of the inflator vessel, and area of the critical section in the discharge nozzle, the dominant physical processes in the system were identified. A comprehensive qualitative model for the inflator and the tank was established. This model was shown to provide a phenomenological explanation for the main experimental observations obtained during this research.

A recent literature model describing a transient flashing outflow of water from a tubular vessel was extended and served as the basis for a detailed quantitative model of the SLG-Inflator. Simplified quantitative models for the dominant tank phenomena were also constructed. The combination of both the inflator and tank models provides a framework for the complete quantitative description of the system.

It was demonstrated that adding small amounts of organic solvents to the system leads to a significant increase in the temperature of the generated CO_2 vapor. A qualitative explanation for this effect based on a layered evaporation model was established was established.

In comparison with existing inflator technology, the SLG-Inflator is simple, safe and environmentally attractive. At this initial stage, the SLG-Inflator does not meet all design requirements for a side impact inflator. More industrial scale research and development effort is required to produce a final version of this new air bag inflator. For the vessel dimensions that was considered in this research (26 ml volume; 10 mm diameter), the tank tests indicated that the generated peak pressure is low and is not sufficiently fast (25 ms vs. 10 ms). The peak pressure can be increased by using a larger inflator vessel and by adding small amounts of organic solvents to the system. Furthermore, an increase in vessel diameter and corresponding critical flow section in the discharge nozzle is expected to accelerate the pressure build-up. Since the system's performance depends strongly on the ambient temperature. It is expected that the required pressure at low ambient temperature can only be attained by incorporating a heat source in the system.

6.2 Claims to Original Research

1. An experimental apparatus, which measures the bulk atomization and evaporation behavior of transient sprays (with a minimum lifetime of 5-10 ms), was developed and constructed. The apparatus allows the simultaneous measurement of pressure and temperature on a millisecond timescale. In the current research the set-up was used to evaluate the performance of a new type of inflator. However, the experimental apparatus is not limited to the air bag technology, and can be used to study other types of single or two-phase transient sprays.
2. A new type of air bag inflator, based on the rapid evaporation of liquefied CO_2, was studied experimentally. The influence of the main design parameters on the performance of the system was investigated. The key parameters of the system included the initial temperature and pressure, the inflator vessel volume, and the area of the critical flow section in the discharge nozzle.
3. Based on the results of the experimental study, the dominant physical phenomena which determine the performance of the SLG-Inflator were identified. A comprehensive phenomenological model of the system was established. Also, a description of the behavior of the system in terms of the phase diagram of CO_2 was developed.
4. A quantitative model of the SLG-Inflator, based on the extension of a recently established model for a transient two-phase outflow from a tubular vessel was developed. In addition, a simplified quantitative model for the tank phenomena was formulated. The combination of both models provides the framework for an integrated quantitative description of the behavior of the SLG-Inflator in tank tests.

5. With respect to the effect of organic liquids, the effect of layered evaporation on the flashing process during the blowdown of low boiling fluids was discovered and a qualitative description was advanced.

6.3 Technological Contributions

This research constitutes the first systematic and rigorous study of a novel type of air bag inflator, based on the rapid evaporation of a liquefied gas. The dominant physical phenomena involved in the system were identified and evaluated. These included heterogeneous nucleation, flash boiling, two-phase critical outflow, two-phase dispersion, transient spray evaporation, sublimation and mixing of real gases. The SLG-Inflator is simple in principle and construction, inexpensive and environmentally attractive.

6.4 Suggestions for Future Work

The suggestions for future work can be divided into two levels: the fundamental level, relating to the physical phenomena involved, and the technological level.

6.4.1 Fundamental Level

1. The presented Tank Model needs to be extended and coupled to the SLG-Inflator Model, such that an integrated model for the experimental set-up is established.
2. High accuracy optical imaging of the two-phase spray, including the evaluation of the droplet size distribution, is necessary to study the dispersion phenomenon in detail.
3. The influence of heat transfer from the tank walls to the impinging spray needs to be investigated and quantified.

4. A wall nucleation model must be incorporated in the SLG-Inflator Model.
5. A quantitative model for the phenomenon of layered evaporation needs to be developed and validated with the experimental observations.

6.4.2 Technological Level

1. The SLG-Inflator model needs to be run for cases at different initial inflator pressure and temperature and the simulations must be compared with the experimental observations.
2. Numerical tests of SLG-inflator model must be performed.
3. Experiments with a larger vessel (approx. 50 ml) and a large critical flow section need to be conducted to assess the increase in pressure and speed of the system.
4. Different methods to add heat to the system need to be studied. These methods may include an independent chemical reaction, a combustion of a portion of the CO_2, or an optimized heat transfer from the bag material to the evaporating droplets.
5. The influence of the nozzle type and the quality of atomization must be investigated.

APPENDIX A

TYPICAL OUTPUT OF THE IDEAL GAS MODEL

Nitrogen Baseline Experiment
****
R = 296.80
Cv = 743.30
Cp = 1040.10
Gamma = 1.39900

Critical pressure ratio = 0.5285

Initial conditions INFLATOR
. mass = 0.00408134 [kg]
. pressure = 2014.696 [psi]
. temperature = 298.150 [K]
. volume = 0.00002600 [m^3]
Initial conditions TANK
. mass = 0.01112972 [kg]
. pressure = 14.696 [psi]
. temperature = 298.150 [K]
. volume = 0.00972000 [m^3]

Area of the orifice = 0.00008664 [m^2]

Timestep = 0.00050000 [sec]

time [sec]	Pratio [/]	mdot kg/s]	Mv [kg]	Mc [kg]	Pv [psi]	Tv [C]	Pc [psi]	Tc [C]
0.0000	0.0073	0.000	0.0041	0.0111	2014.7	25.0	14.696	25.0
0.0005	0.0135	2.769	0.0027	0.0125	1241.3	4.9	16.765	29.3
0.0010	0.0228	1.767	0.0018	0.0134	789.0	-10.3	17.975	29.8
0.0015	0.0364	1.155	0.0012	0.0140	513.7	-22.0	18.711	29.2
0.0020	0.0563	0.769	0.0009	0.0144	340.7	-31.3	19.174	28.3
0.0025	0.0849	0.520	0.0006	0.0146	229.4	-38.6	19.471	27.6
0.0030	0.1258	0.356	0.0004	0.0148	156.3	-44.6	19.667	26.9
0.0035	0.1841	0.245	0.0003	0.0149	107.6	-49.4	19.797	26.4
0.0040	0.2666	0.171	0.0002	0.0150	74.6	-53.3	19.886	26.1
0.0045	0.3829	0.119	0.0001	0.0151	52.1	-56.6	19.946	25.8
0.0050	0.5466	0.084	0.0001	0.0151	36.6	-59.3	19.987	25.6
-- Transition from SUPERsonic to SUBsonic flow --								
0.0055	0.7760	0.059	0.0001	0.0151	25.8	-61.5	20.016	25.4
0.0060	1.0342	0.036	0.0001	0.0152	19.4	-63.0	20.033	25.3

Figure A.1 Output of a Typical Ideal Gas Simulation

The properties followed by a 'v' refer to the conditions in the inflator, while those followed by a 'c' refer to the conditions in the tank.

APPENDIX B

ENERGY ANALYSIS OF THE INFLATION SEQUENCE

Based on a static thermodynamic analysis, the following three characteristics of the inflation sequence were calculated:

1. ***the amount of generated condensate:*** Since the condensate does not assist the inflation of the air bag, it is considered as a pure loss of CO_2 for the current purpose.
2. ***the average specific internal energy of the condensate:*** The value of the average specific internal energy serves as an indication of the phase of the condensate (i.e. liquid or solid, or a mixture of both). While the condensate is formed in the course of the inflation, the value of the specific internal energy is calculated based on measurements at the end of the process. Therefore, it indicates an average value for the specific internal energy.
3. ***the enthalpy exchange between the components of the system:*** The enthalpy exchange between the components of the system provides information about the origin of the energy used to transform the stored liquefied CO_2 into vapor. It allows the assessment of the heat transfer from the tank gases to the evaporating spray.

With the current experimental set-up, it is not possible to determine the location of the condensate at the end of the inflation sequence. It is assumed that part of it remains inside the inflator, while part of it is generated by the solidification of liquid droplets in the tank.

The control volume for the analysis comprises the inflator, the nozzle and the tank in a closed thermodynamic system, as illustrated in Figure B.1. The system is shown in its initial state and an internal constraint, corresponding to the opening mechanism in the actual system, separates the liquefied CO_2 in the inflator from the purging gases in the tank. At t=0, the internal constraint is removed and the inflation sequence commences. For the current analysis, the system is considered at two points in time. The first point (indicated with superscript '0') corresponds to the initial state of the system. The second point (indicated with superscript '1') corresponds to the end of the inflation sequence.

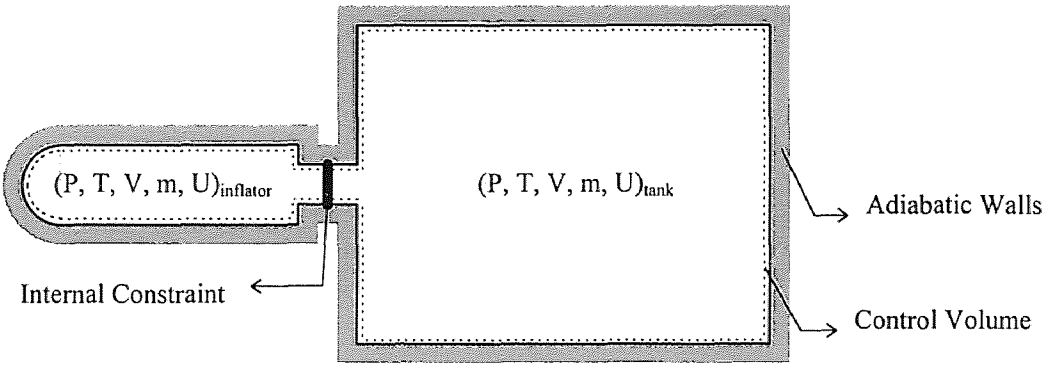

Figure B.1 Control Volume for the Energy Analysis of the Inflation Sequence

In this work, the end of the inflation sequence is taken to coincide with the end of the initial fast rise in the tank pressure curve. For a typical experiment, the time between the two points (i.e. the duration of the inflation sequence) is about 30 ms. As discussed in section §4.3.1, the end of the fast increase in tank pressure coincides with the end of the spray from the nozzle and the end of the gradual decrease of inflator pressure.

The analysis is based on a combination of the conservation of mass and the first law of thermodynamics. The latter states that, since heat transfer is negligible (because of

the short duration of the inflation sequence) and since the system produces no work (because of the rigid boundaries of the system), the total internal energy of the system is constant. In addition, taking the intense mixing during the inflation sequence into account, the temperature of the system will be assumed uniform.

$\underline{t = 0:}$

$(V, P, T)^0_{inflator} \rightarrow m^0_{CO_2(l)};\ u^0_{CO_2(l)};\ h^0_{CO_2(l)}$ *(CO_2 Tables/Real Gas Law)*

$(V, P, T)^0_{tank} \rightarrow m^0_{N_2};\ u^0_{N_2};\ h^0_{N_2}$ *(Ideal Gas Law)*

$$\Rightarrow \quad U^0_{total} = m^0_{CO_2(l)} . u^0_{CO_2(l)} + m^0_{N_2} . u^0_{N_2}$$

$\underline{t = t^1:}$

$V_{total} = V_{tank} + V_{inflator}$

$m^1_{N_2} = m^0_{N_2}$ *(Conservation of N_2 Mass)*

$(T)^1_{measured} \rightarrow u^1_{N_2};\ h^1_{N_2}$ *(Ideal Gas Law)*

$(P, T)^1_{measured},\ m^1_{N_2},\ V_{total}$ *(Real Gas Mixture Law +*

$\rightarrow m^1_{CO_2(v)};\ u^1_{CO_2(v)};\ h^1_{CO_2(v)}$ *CO_2 Tables/Real Gas Law)*

$U^1_{total} = U^0_{total}$ *(1^{st} Law of Thermodynamics)*

$$\Rightarrow \quad m^1_{CO_2(s/l)} = m^0_{CO_2(l)} - m^1_{CO_2(v)}$$ *(Conservation of CO_2 Mass)*

$$\Rightarrow \quad u^1_{CO_2(s/l)} = \frac{U^1_{total} - m^1_{CO_2(v)} . u^1_{CO_2(v)} - m^1_{N_2} . u^1_{N_2}}{m^1_{CO_2(s/l)}}$$

$h^1_{CO_2(s/l)} \approx u^1_{CO_2(s/l)}$ *(neglect condensate volume)*

$\Delta H_{l \rightarrow v} = m^1_{CO_2(v)} \left[h^1_{CO_2(v)} - h^0_{CO_2(l)} \right]$

$\Delta H_{l \rightarrow s/l} = m^1_{CO_2(s/l)} \left[h^0_{CO_2(l)} - h^1_{CO_2(s/l)} \right]$

$\Delta H_{N_2} = m^1_{N_2} \left[h^0_{N_2} - h^1_{N_2} \right]$

Figure B.2 Summary of the Energy Analysis of the Inflation Sequence

The mass of the generated CO_2 vapor at the end of the inflation is calculated based on the assumption that the volume of the condensate is negligible. The same procedure as for the

generated vapor mass curves is followed. A detailed discussion of this procedure is included in Chapter 5. The complete analysis is summarized in Figure B.2 for the case of the Reference Experiment and is easily changed for different purging gases and/or other initial conditions. Note that the properties corresponding to the condensate are indicated with a subscript '(s/l)' because it is unknown during the analysis whether it concerns liquid or solid CO_2.

The calculated average internal energy can be used as an indication for the phase of the condensate. Table B.1 lists the value of the internal energy of saturated solid CO_2 for temperatures slightly below the triple point [30]. When the value of the calculated average specific internal energy of the condensate ($u^{l}_{CO_2(s/l)}$) is close to the ones listed in the last column of Table B.1, it may be concluded that the condensate is in the solid phase. For values higher than the ones listed in Table B.1, it must be concluded that the condensate does not consist of solid CO_2, but of liquid or a mixture of liquid and solid CO_2.

Table B.1 Specific Internal Energy of Saturated Solid CO_2

T [°C]	u [kJ/kg]
-56.6(*)	181.4
-60.0	176.7
-65.0	169.8
-70.0	163.1
-75.0	156.6
-80.0	150.1

(*) Triple point

Figure B.3 contains a graphical representation of the energy redistribution in the system during the inflation sequence corresponding to the Reference Experiment.

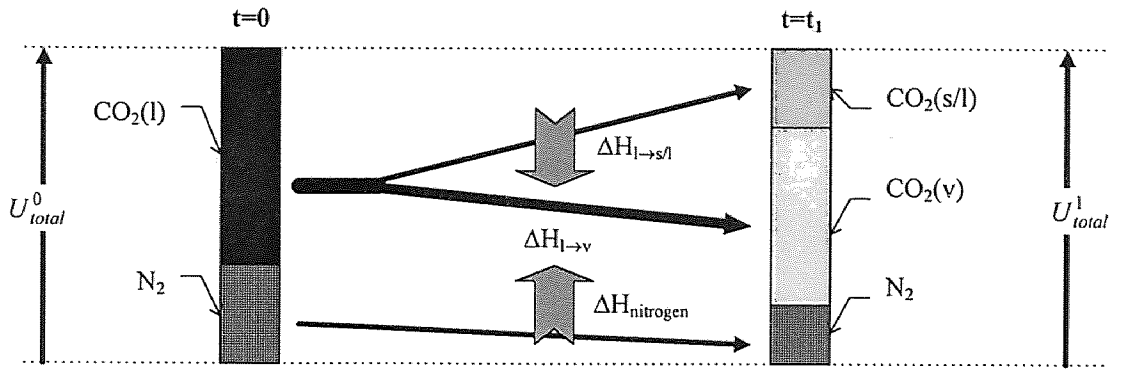

Figure B.3 Energy Redistribution during the Inflation Sequence

The size of the bars represents the amount of energy that is stored in each component. Note that the total energy of the system is constant, as indicated by the two arrows at each side of the figure. During the inflation sequence, enthalpy is used to transform the liquefied CO_2 into vapor: $\Delta H_{l\rightarrow v}$. This enthalpy is supplied by the cooling and solidification (in the case of the Reference Experiment) of part of the original amount of CO_2 ($\Delta H_{l\rightarrow s/l}$) and by interaction with the tank gases ($\Delta H_{nitrogen}$). Since these are the only enthalpy fluxes in the system, they must be balanced:

$$\Delta H_{l\rightarrow v} = \Delta H_{l\rightarrow s/l} + \Delta H_{nitrogen} \qquad \text{(B.1)}.$$

Based on these values, the origin of the energy which is used to vaporize the liquefied CO_2 can be determined and the importance of the heat transfer between the tank gases and the evaporating spray can be assessed.

APPENDIX C

EQUATIONS OF STATE FOR THE REAL GAS BEHAVIOR OF CO_2

C.1 Peng-Robinson Equation of State [65]

C.1.1 Standard From

$$P = \frac{RT}{v-b} - \frac{a[T]}{v(v+b)+b(v-b)} \qquad \text{with} \quad a[T] = a_c.\alpha\left[T_r,\kappa\right]$$

$$a_c = 0.45724\frac{R^2T_c^2}{P_c}$$

$$\alpha\left[T_r,\kappa\right] = \left(1+\kappa(1-\sqrt{T_r})\right)^2$$

$$\kappa = 0.37464 + 1.54226\omega - 0.26992\omega^2$$

$$b_c = 0.07880\frac{RT_c}{P_c}$$

C.1.2 Cubic Form

$$Z^3 - (1-B)Z^2 + (A - 3B^2 - 2B)Z - (AB - B^2 - B^3) = 0$$

$$\text{with} \quad A = \frac{aP}{R^2T^2} \quad \text{and} \quad B = \frac{bP}{RT}$$

C.1.3 Enthalpy Departure

$$H - H^* = RT(Z-1) + \frac{T\frac{da}{dT} - a}{2b\sqrt{2}}\ln\left(\frac{Z+2.44B}{Z-0.414B}\right)$$

$$\text{with} \quad \frac{da}{dT} = \frac{a_c\kappa}{T_c}\sqrt{\frac{T_c}{T}}\left(1+\kappa(1-\sqrt{\frac{T}{T_c}})\right)$$

C.1.4 Fugacity of a Mixture Component k

$$\ln\frac{f_k}{\eta_k P}=\frac{b_k}{b}(Z-1)-\ln(Z-B)-\frac{A}{2B\sqrt{2}}\left(\frac{2\sum_i \eta_i a_{ik}}{a}-\frac{b_k}{b}\right)\ln\left(\frac{Z+2.414B}{Z-0.414B}\right)$$

C.2 Beattie-Bridgeman Equation of State [16]

C.2.1 Standard From

$$P=\frac{RT}{v^2}(1-\varepsilon)(v+B)-\frac{A}{v^2}\quad\text{with}\quad A=A_o(1-\frac{a}{v})$$

$$B=B_o(1-\frac{b}{v})$$

$$\varepsilon=\frac{c}{vT^3}$$

C.2.2 Constants for CO_2

A_o	262.07	$\left[N.m^4/kg^2\right]$
a	$1.62129\ 10^{-3}$	$\left[m^3/kg\right]$
B_o	$2.3811\ 10^{-3}$	$\left[m^3/kg\right]$
b	$1.6444\ 10^{-3}$	$\left[m^3/kg\right]$
c	$14.997\ 10^{3}$	$\left[m^3.K^3/kg\right]$

C.3 Huang F.-H. & Li M.-H. Equation of State [46]

C.3.1 Standard Form

$$Z=1+b_2\rho'+b_3\rho'^2+b_4\rho'^3+b_5\rho'^4+b_6\rho'^5+b_7\rho'^2.\exp\left[-c_{21}\rho'^2\right]+b_8\rho'^4.\exp\left[-c_{21}\rho'^2\right]$$
$$+c_{22}\rho'.\exp\left[-c_{27}(\Delta T)^2\right]+c_{23}\frac{\Delta\rho}{\rho'}.\exp\left[-c_{25}(\Delta\rho)^2-c_{27}(\Delta T)^2\right]$$
$$+c_{24}\frac{\Delta\rho}{\rho'}.\exp\left[-c_{26}(\Delta\rho)^2-c_{27}(\Delta T)^2\right]$$

with $T' = \frac{T}{T_c}$; $\Delta T = 1 - T'$; $\rho' = \frac{\rho}{\rho_c}$; $\Delta\rho = 1 - \frac{1}{\rho'}$

$$b_2 = \left(c_1 + \frac{c_2}{T'} + \frac{c_3}{T'^2} + \frac{c_4}{T'^3} + \frac{c_5}{T'^4} + \frac{c_6}{T'^5} \right)$$

$$b_3 = \left(c_7 + \frac{c_8}{T'} + \frac{c_9}{T'^2} \right) \quad ; \quad b_4 = \left(c_{10} + \frac{c_{11}}{T'} \right)$$

$$b_5 = \left(c_{12} + \frac{c_{13}}{T'} \right) \quad ; \quad b_6 = \left(\frac{c_{14}}{T'} \right)$$

$$b_7 = \left(\frac{c_{15}}{T'^3} + \frac{c_{16}}{T'^4} + \frac{c_{17}}{T'^5} \right) \quad ; \quad b_8 = \left(\frac{c_{18}}{T'^3} + \frac{c_{19}}{T'^4} + \frac{c_{20}}{T'^5} \right)$$

C.3.2 Constants

c_1	0.376194
c_2	0.118836
c_3	-3.04379
c_4	2.27453
c_5	-1.23863
c_6	0.250442
c_7	-0.115350
c_8	0.675104
c_9	0.198861
c_{10}	0.216124
c_{11}	-0.583148
c_{12}	0.119747E-1
c_{13}	0.537278E-1
c_{14}	0.265216E-1
c_{15}	-2.79498
c_{16}	5.62393
c_{17}	-2.93831
c_{18}	0.988759
c_{19}	-3.04711
c_{20}	2.32316
c_{21}	1.07379
c_{22}	-0.599724E-4
c_{23}	0.885339E-4
c_{24}	0.316418E-2
c_{25}	10
c_{26}	50
c_{27}	80000

C.3.4 Enthalpy Departure

$$\frac{H-H^*}{RT} = (Z-1) + \left(\frac{c_2}{T'} + 2\frac{c_3}{T'^2} + 3\frac{c_4}{T'^3} + 4\frac{c_5}{T'^4} + 5\frac{c_6}{T'^5}\right)\rho' + \frac{1}{2}\left(\frac{c_8}{T'} + 2\frac{c_9}{T'^2}\right)\rho'^2$$
$$+ \frac{1}{3}\left(\frac{c_{11}}{T'}\right)\rho'^3 + \frac{1}{4}\left(\frac{c_{13}}{T'}\right)\rho'^4 + \frac{1}{5}\left(\frac{c_{14}}{T'}\right)\rho'^5$$
$$+ \frac{1}{2c_{21}^2}\left(3\frac{c_{18}}{T'^3} + 4\frac{c_{19}}{T'^4} + 5\frac{c_{20}}{T'^5}\right)\left\{1 - (1 + c_{21}\rho'^2).\exp(-c_{21}\rho'^2)\right\}$$
$$- 2c_{22}c_{27}T'(\Delta T).\exp\left\{-c_{27}(\Delta T)^2\right\} + \frac{c_{23}c_{27}}{c_{25}}T'(\Delta T).\exp\left\{-c_{25}(\Delta\rho)^2 - c_{27}(\Delta T)^2\right\}$$
$$+ \frac{1}{2c_{21}}\left(3\frac{c_{15}}{T'^3} + 4\frac{c_{16}}{T'^4} + 5\frac{c_{17}}{T'^5}\right)\left\{1 - \exp(-c_{21}\rho'^2)\right\}$$
$$+ \frac{c_{23}c_{27}}{c_{26}}T'(\Delta T).\exp\left\{-c_{26}(\Delta\rho)^2 - c_{27}(\Delta T)^2\right\}$$

C.3.5 Entropy Departure

$$\frac{S-S^*}{R} = -\ln(\rho RT) - \left(c_1 - \frac{c_3}{T'^2} - 2\frac{c_4}{T'^3} - 3\frac{c_5}{T'^4} - 4\frac{c_6}{T'^5}\right)\rho' - \frac{1}{2}\left(-c_7 - \frac{c_9}{T'^2}\right)\rho'^2 - \frac{1}{3}c_{10}\rho'^3$$
$$- \frac{1}{4}c_{12}\rho'^4 + \frac{1}{2c_{21}}\left(2\frac{c_{15}}{T'^3} + 3\frac{c_{16}}{T'^4} + 4\frac{c_{17}}{T'^5}\right)\left\{1 - \exp\left(-c_{21}\rho'^2\right)\right\}$$
$$+ \frac{1}{2c_{21}^2}\left(2\frac{c_{18}}{T'^3} + 3\frac{c_{19}}{T'^4} + 4\frac{c_{20}}{T'^5}\right)\left\{1 - \left(1 + c_{21}\rho'^2\right)\exp(-c_{21}\rho'^2\right\}$$
$$- c_{22}\left(1 + 2c_{27}T'\Delta T\right)\rho'\exp\left\{-c_{27}(\Delta T)^2\right\}$$
$$+ \frac{c_{23}}{2c_{25}}\left(1 + 2c_{27}T'\Delta T\right)\exp\left\{-c_{25}\left(\Delta\rho\right)^2 - c_{27}(\Delta T)^2\right\}$$
$$+ \frac{c_{24}}{2c_{26}}\left(1 + 2c_{27}T'\Delta T\right)\exp\left\{-c_{26}\left(\Delta\rho\right)^2 - c_{27}(\Delta T)^2\right\}$$

Note that the argument of the logarithmic term (ρRT) is expressed in [atm].

APPENDIX D

DESCRIPTION OF THE CO_2-MODEL

The CO_2-model is intended to be used in a temperature range of 154-420 K and for pressures up to 500 bar. It provides predictions of P-v-T information, enthalpy and entropy in the liquid (including the metastable state), supercritical and vapor region of the phase diagram. In addition, the enthalpy and the entropy of the saturated solid state can be calculated.

Several iteration loops are implemented in the CO_2-model. The *bisection*-method was used in all cases [10]. The computation time of the SLG-Inflator Model depends strongly on the speed of the general CO_2-model. Therefore, considerable time was spent to minimize the number of iteration steps in the CO_2-model. The main strategy consisted of reducing the number of steps by providing the best possible initial value for each iteration. All subroutines allow the specification of the optimal initial value, based on earlier calculations.

The CO_2-model consists of the following subroutines:

- ***Psat(T):*** This function calculates the saturation pressure corresponding to a given temperature. Depending on the latter, different correlations are used :

  $T_t < T < T_c$: expression (5.7)

  $195 < T < T_t$: expression (5.9)

  $154\ K < T < 195\ K$: expression (5.8)

- ***Tsat(P):*** This subroutine determines the saturation temperature corresponding to a given pressure by iteration on *Psat(T)*. Hence, the same expressions as in the previous subroutine are used.
- ***P_Tv(T,v):*** Expression (5.16), together with the constants and the additional equations from Appendix C.3, are used to predict the pressure when both the temperature and the specific volume are given.
- ***v_PT(P,T) and T_Pv(P,v):*** Both functions use the previous subroutine in an iteration loop to predict the specific volume and the temperature, respectively.
- ***LatHeat(T):*** This subroutine calculates the latent heat corresponding to a given temperature. Depending on the latter, different expressions are used:

  $T_t < T < T_c$: expression (5.10)

  $140\ K < T < T_t$: expression (5.11)

- ***H_PT(P,T):*** Using the pressure and the temperature as input, the specific enthalpy is calculated. The ideal gas enthalpy is determined using (5.2) and the reference state (5.3). For temperatures above the triple point, the enthalpy departure of (5.16), which is listed in Appendix C.3, is used. The enthalpy of the vapor phase below T_t is obtained in the same manner. For the solid phase, the enthalpy along the saturation curve is calculated by means of (5.17).
- ***U_PT(P,T):*** Using the previous subroutine and (5.12), the internal energy is calculated when the pressure and the temperature are given.
- ***S_PT(P,T):*** First, the entropy corresponding to the specified temperature, but in the low pressure limit, is calculated by means of (5.5-6). Next, the entropy departure of (5.16), as listed in Appendix C.3 is used to obtain the specific entropy for liquid or

gaseous CO_2. An additional subroutine (*dPsatdT(T)*) was developed to determine the derivative of expressions (5.8) and (5.9) with respect to temperature. This allows the calculation of the specific entropy of saturated solid CO_2 by means of (5.18).

The above list contains the main subroutines of the general CO_2 model. Additional subroutines were developed to determine the liquid spinodal.

Note that the CO_2-model can be considered as not flexible, since it is not possible to generate all properties starting from any two arbitrary properties. However, additional subroutines, consisting of an iteration loop containing one of the existing subroutines are easily developed and lead to a flexible model.

APPENDIX E

NUMERICAL ASPECTS OF THE SLG-INFLATOR MODEL

E.1 Main Two-Step Lax-Wendroff Scheme [68]

In the following, $\vec{U}$, $\vec{F}[...]$ and $\vec{J}[...]$correspond to the vectors in (5.31-32), but the arrows were omitted.

$$(U')_{j+1/2}^{n+1/2} = \frac{1}{2}\left(U_{j+1}^{n} + U_{j}^{n}\right) - \frac{\Delta t}{2\Delta z}\left\{F\left[U_{j+1}^{n}\right] - F\left[U_{j}^{n}\right]\right\} \tag{E.1}$$

$$U_{j+1/2}^{n+1/2} = (U')_{j+1/2}^{n+1/2} + \frac{\Delta t}{2} J\left[(U')_{j+1/2}^{n+1/2}\right] \tag{E.2}$$

$$(U')_{j}^{n+1} = U_{j}^{n} - \frac{\Delta t}{\Delta z}\left\{F\left[U_{j+1/2}^{n+1/2}\right] - F\left[U_{j-1/2}^{n+1/2}\right]\right\} \tag{E.3}$$

$$U_{j}^{n+1} = (U')_{j}^{n+1} + \Delta t . J\left[(U')_{j}^{n+1}\right] \tag{E.4}$$

E.2 Bubble Momentum Conservation

The conservation of momentum for the bubbles (5.27) was rewritten, using the assumption that $\rho_l \gg \rho_v$, as:

$$\frac{\partial(\rho w_v)}{\partial t} + \frac{\partial(\rho w_v^2)}{\partial z} = \frac{\partial(3\rho w)}{\partial t} + \frac{\partial(3\rho w^2)}{\partial z} + I \tag{E.5},$$

with $$I = \frac{9\mu_l(w_l - w_v)C_\mu}{a^2}(1-e) \tag{E.6}.$$

In (E.5), I can be considered as the source term and the expression can be developed in the following two-step Lax-Wendroff scheme:

$$\left[(\rho w_v)'\right]_{j+1/2}^{n+1/2} = \frac{1}{2}\left\{(\rho w_v)_{j+1}^{n} + (\rho w_v)_{j}^{n}\right\} - \frac{\Delta t}{2\Delta z}\left\{(\rho w w_v)_{j+1}^{n} - (\rho w w_v)_{j}^{n}\right\}$$
$$+\left[(3\rho w)'\right]_{j+1/2}^{n+1/2} - \frac{1}{2}\left\{(3\rho w)_{j+1}^{n} + (3\rho w)_{j}^{n}\right\} \qquad \text{(E.7)}$$
$$+\frac{\Delta t}{2\Delta z}\left\{(3\rho w^2)_{j+1}^{n} - (3\rho w^2)_{j}^{n}\right\}$$

$$(\rho w_v)_{j+1/2}^{n+1/2} = \left[(\rho w_v)'\right]_{j+1/2}^{n+1/2} + \frac{\Delta t}{2}[I']_{j+1/2}^{n+1/2} \qquad \text{(E.8)}$$

$$\left[(\rho w_v)'\right]_{j}^{n+1} = (\rho w_v)_{j}^{n} - \frac{\Delta t}{\Delta z}\left\{(\rho w w_v)_{j+1/2}^{n+1/2} - (\rho w w_v)_{j-1/2}^{n+1/2}\right\}$$
$$+\left[(3\rho w)'\right]_{j}^{n+1} - (3\rho w)_{j}^{n} \qquad \text{(E.9)}$$
$$+\frac{\Delta t}{\Delta z}\left\{(3\rho w^2)_{j+1/2}^{n+1/2} - (3\rho w^2)_{j-1/2}^{n+1/2}\right\}$$

$$(\rho w_v)_{j}^{n+1} = \left[(\rho w_v)'\right]_{j}^{n+1} + \Delta t.[I']_{j}^{n+1} \qquad \text{(E.10).}$$

In (E.8), $[I']_{j+1/2}^{n+1/2}$ represents I from (E.6), calculated using the values from $(U')_{j+1/2}^{n+1/2}$ and $\left[(\rho w)'\right]_{j+1/2}^{n+1/2}$. Similarly, in (E.10), $[I']_{j}^{n+1}$ represents I from (E.6), calculated using the values from $(U')_{j}^{n+1}$ and $\left[(\rho w)'\right]_{j}^{n+1}$.

E.3 Main Integration Loop

The sequence of the operations in the main integration loop is shown in the flow chart of Figure E.1. In this figure, j and n are the counters for the space and time step, respectively. The total number of space steps is L, while the integration is performed over a total of N timesteps.

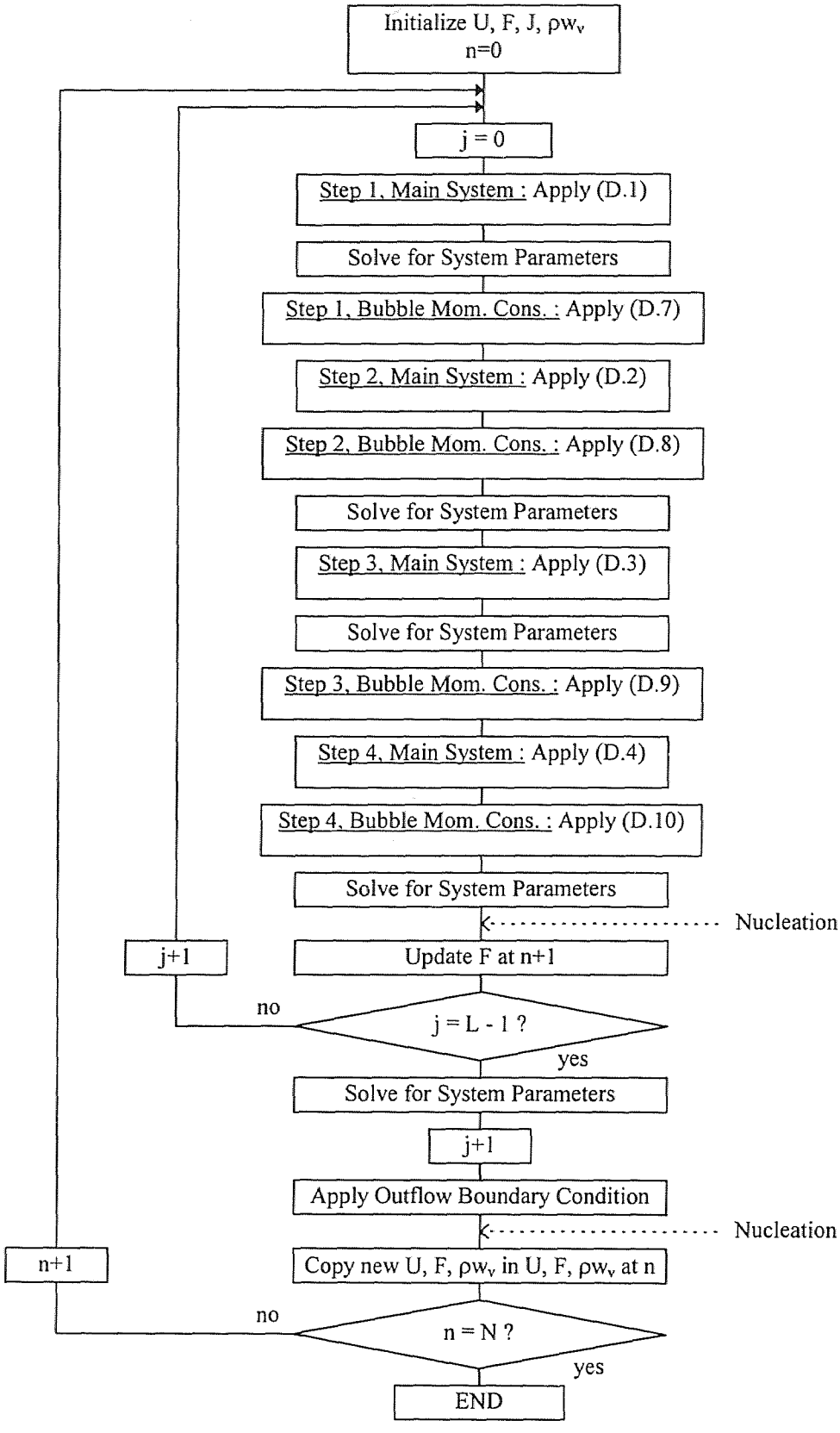

Figure E.1 Flow-chart of the Main Integration Loop

The subroutine *Solve for System Parameters* is used repeatedly in the main integration loop and concerns the calculation of the system parameters from a given $\vec{U}$. It involves solving a system of non-linear algebraic equations and is discussed in §E.4. The outflow boundary condition is applied in the last space step. Issues pertaining to the outflow boundary condition are addressed in §E.5.

As discussed, the nucleation in the system was modeled by injecting a known concentration of bubbles of certain size into the system when the local pressure dropped below the saturation pressure. The nucleation in the model can occur at two locations, as indicated by the dotted arrows in Figure E.1. At these locations, the local pressure is compared with the saturation pressure corresponding to the local liquid temperature. If the saturation pressure is larger than the local pressure, and nucleation has not occurred before, the bubbles are injected into the system. The vapor in the bubbles is saturated with respect to the local pressure, in agreement with the 4^{th} assumption in §5.4.1.1. When the bubbles are introduced, the enthalpy and density of the system is adjusted such that the conservation laws are respected.

E.4 Solving for the System Parameters

Depending on whether nucleation has occurred, a different subroutine was used to solve for the system parameters. Both subroutines are based on the *Modified Newton Method* [10]. Since the case for pure liquid, i.e. nucleation has not yet occurred, is simpler and very similar to the case of a two-phase mixture, only the latter is discussed.

The problem at hand is to solve for the 7 system parameters (P, ρ_v, ρ_l, n, e, w, w_v) when $\vec{U}$ is given. $\vec{U}$ was introduced in (5.32) as:

$$\vec{U} = \begin{Bmatrix} u_1 \\ u_2 \\ u_3 \\ u_4 \\ u_5 \end{Bmatrix} = \begin{Bmatrix} \rho \\ \rho_v . e \\ \rho . w \\ \rho . \left(h + \dfrac{w^2}{2} \right) - P \\ n \end{Bmatrix} \qquad \text{(E.11).}$$

Clearly, the mixture velocity (w) and the bubble number density (n) can be solved for immediately. Using the definitions of the mixture density and enthalpy (5.28-29), (E.11) was transformed into the following system of 3 algebraic non-linear equations in P, e and T_l:

$$\begin{cases} u_1 - (1-e)\rho_l[P,T_l] - e\rho_v^{sat}[P] = 0 \\ (u_1 - u_2)h_l[P,T_l] + u_2 h_v^{sat}[P] + \dfrac{u_3^2}{2u_1} - P - u_4 = 0 \\ u_2 - e\rho_v^{sat}[P] = 0 \end{cases} \qquad \text{(E.12)}$$

This system was solved by the Modified Newton Method, which consists of solving each equation by the Newton Method for one unknown, while considering all other quantities as known. The derivatives with respect to P and T_l were calculated through numerical differentiation. With respect to the classical Newton Method for systems, the current method avoids the solution of a linear system in each iteration step, but it will require more iterations. Once the solution of (E.12) is known, the remaining parameters are easily calculated by means of the equation of state and the definition of the void fraction.

E.5 Outflow Boundary Condition

The outflow boundary condition consists of applying a given pressure at the open end of the inflator. To incorporate this condition in the main numerical scheme, the field equations and the conservation of momentum for a bubble were developed in a *1st order*

Upwind Differencing Scheme [68]. Two different procedures are implemented, depending on whether nucleation has occurred or not. Since the pure liquid case is simpler and easily derived from the two-phase case, only the latter is discussed.

Because the pressure is specified at the inflator end, and the vapor is assumed to be saturated, all vapor properties are known. When writing the field equations and the bubble conservation of momentum in a 1st order upwind difference scheme, the remaining system parameters on the boundary can be determined directly:

$$\rho_L^{n+1} = \rho_L^n - \frac{\Delta t}{\Delta z}\left\{(\rho w)_L^n - (\rho w)_{L-1}^n\right\} \tag{E.13}$$

$$w_L^{n+1} = \frac{1}{\rho_L^{n+1}}\left\{(\rho w)_L^n - \frac{\Delta t}{\Delta z}\left[(\rho w^2 + P)_L^n - (\rho w^2 + P)_{L-1}^n\right]\right\} \tag{E.14}$$

$$e_L^{n+1} = \frac{1}{(\rho_v)_L^{n+1}}\left\{(\rho_v e)_L^n + \Delta t(jn)_L^t - \frac{\Delta t}{\Delta z}\left[(\rho_v ew)_L^n - (\rho_v ew)_{L-1}^n\right]\right\} \tag{E.15}$$

$$n_L^{n+1} = n_L^n + \Delta t.\psi_L^n - \frac{\Delta t}{\Delta z}\left\{(nw)_L^n - (nw)_{L-1}^n\right\} \tag{E.16}$$

$$\begin{aligned}(\rho w_v)_L^{n+1} = (\rho w_v)_L^n + \Delta t.I_L^n + (3rw)_L^{n+1} - (3rw)_L^n + \frac{\Delta t}{\Delta z}\left\{(3rw^2)_L^n - (3rw)_{L-1}^n\right\} \\ - \frac{\Delta t}{\Delta z}\left\{(rww_v)_L^n - (rww_v)_{L-1}^n\right\}\end{aligned} \tag{E.17}.$$

The index L indicates the boundary of the space domain (z=L) and n is the counter corresponding to time, i.e. n is the current timestep and n+1 is the next timestep.

REFERENCES

1. Air bag information web-page, The Insurance Institute for Highway Safety, February 2, 1998 (http://www.nhtsa.dot.gov/airbags/)

2. Air Bag On-Off Switches: Questions and Answers, NHTSA, November 17, 1997

3. *CRC: Handbook of Chemistry and Physics*, 49th Edition, The Chemical Rubber Company Co., Cleveland, OH, 1968

4. *Encyclopedia of Chemical Technology*, 4th Ed., Wiley, New York, NY, 1991

5. 1995 Ford Taurus Air Bag Specification Sheet, Breed Technologies Inc., Boonton, NJ

6. Lecture notes for the *'Short Course on Spray Technology'*, N.A. Chigier, R.D. Reitz, W. Bachalo et al., Carnegie Mellon University, Pittsburgh, PA, Spring 1997

7. *The Temperature Handbook*, Vol. 29, Omega Engineering Inc., Stamford, CT, 1995

8. *Temperature Measurement Handbook*, Vol. III, Nanmac Corporation, Framingham, MA, 1996

9. Side-Impact Air Bags on Safety Marquee, Insurance Institute for Highway Safety Status Report, Vol. 31, No. 4, May 1996

10. Akai T., *Applied Numerical Methods for Engineers*, J. Wiley, New York, NY, 1994

11. Alamgir Md., Lienhard J.H., Correlation of Pressure Undershoot During Hot-Water Depressurization, Journal of Heat Transfer, Transactions of the ASME, Vol. 103, pp. 52-55, 1981

12. Angus S., Armstrong B., de Reuck K. M., *International Thermodynamic Tables of the Fluid State. Volume 3 : Carbon Dioxide*, IUPAC, Pergamon Press, Oxford, 1976

13. Atkinson K.E., *An Introduction to Numerical Analysis*, John Wiley & Sons, New York, NY, 1989

14. Avedisian C.T., Homogeneous Bubble Nucleation within Liquids : A Review, HTD-Vol. 197, Two-Phase Flow and Heat Transfer, ASME 1992

15. Bayley G.S., Development of a test device for air bag gas generants, Automotive Engineering, v 100, n 6, p. 32-34, 1992

16. Bejan A., *Advanced Engineering Thermodynamics*, John Wiley & Sons, New York, NY, 1988

17. Bejan A., *Convection Heat Transfer*, John Wiley & Sons Inc., New York, NY, 1995

18. Bettis R.J., Jagger S.F., Some Experimental Aspects of Transient Releases of Pressurized Liquefied Gases, Institution of Chemical Engineers Symposium Series, No. 130, pp. 211-227, 1992

19. Birkhoff G., *Hydrodynamics*, Princeton Univ. Press, Princeton, NJ, 1960

20. Blander M., Katz J.L., Bubble Nucleation in Liquids, AIChE Journal, Vol. 21, No. 5, pp. 833-848, 1975

21. Blinkov V.N., Jones O.C. and Nigmatulin B. I., Nucleation and Flashing in Nozzles (part 2): Comparison with experiments using a five-equation model for vapor void development, Int. J. Multiphase Flow, Vol. 19, No. 6, pp. 965-986, 1993

22. Boley J., TRW takes lead in airbag technology, Automotive Engineer (London), v 22, n 8, pp. 49-50, Oct 1997

23. Bouré J. A., Fritte A. A., Giot M.M. et al., Highlights of Two-Phase Critical Flow : on the links between maximum flow rates, sonic velocities, propagation and transfer phenomena in single and two-phase flow, Int. J. Multiphase Flow, Vol. 3, pp. 1-22, 1976

24. Butler P.B., Kang J., Krier H., Modeling and Numerical Simulation of the Internal Thermochemistry of Automotive Airbag Inflators, Prog. Energy Combust. Sci., Vol. 19, pp. 365-382, 1993

25. Cha Y.S., Henry R.E., Bubble Growth During Decompression of a Liquid, Journal of Heat Transfer, Transactions of the ASME, Vol. 103, pp. 56-60, 1981

26. Chan T. L., White D. M. and Damian S. A., Exposure Characterization of Aerosols and Carbon Monoxide from supplemental Inflatable (Automotive Air Bag) Systems, J. Aerosol Sci., Vol. 20, No. 6, pp.657-665, 1989

27. Corti D.S., Debenedetti P.G., A Computational Study of Metastability In vapor-liquid Equilibrium, Chemical Engineering Science, Vol. 49, No. 17, pp. 2717-2734, 1994

28. Dagan R., Elias E., Wacholder E. et al., A Two-Fluid Model for Critical Flashing Flows in Pipes, Int. J. Multiphase Flow, Vol. 19, No. 1, pp. 15-25, 1993

29. Deligiannis P. & Cleaver J.W., Determination of the Heterogeneous Nucleation Factor during a Transient Liquid Expansion, Int. J. Multiphase Flow, Vol. 18, No. 2, pp. 273-278, 1992

30. Din F., *Thermodynamic functions of Gases vol. 1*, Butterworths Scientific Publications, London, 1956

31. Dobran F., Nonequilibrium Modeling of Two-Phase Critical Flows in Tubes, Journal of Heat Transfer, Vol. 109, pp. 731-738, August 1987

32. Duff K.M., Non-equilibrium Condensation of Carbon Dioxide in Supersonic Nozzles, Gas Turbine Laboratory Report No. 84, Ph.D. Thesis, MIT, Cambridge, MA, January 1966

33. Elkotb M.M., Fuel Atomization for Spray Modeling, Prog. Energy Combust. Sci., Vol. 8, pp. 61-91, 1982

34. Ewan B.C.R., Moodie K., Evaluation of a Numerical Critical Pipe Flow Model with Wall Nucleation, Int. J. Multiphase Flow, Vol. 16, No. 5, pp. 751-759, 1990

35. Ferziger J.H., *Numerical Methods for Engineering Application*, John Wiley & Sons, New York, NY, 1981

36. Gardner G.C., Asymptotic Concentration Distribution of an Involatile Solute in an Evaporating Drop, Int. J. Heat Mass Transfer, Vol. 8, pp. 667-668, 1965

37. Gebbeken B., Eggers R., Blowdown of carbon dioxide from initially supercritical conditions, J. Loss Pre. Process Ind., Vol. 9, No. 4, pp. 285-293, 1996

38. Giot M., Experiments and Modeling of Choked Flow, Proceedings of the First World Conference on Experimental Heat Transfer, Fluid Mechanics and Thermodynamics, 1988

39. Giauque W.F., Egan C.J., Carbon Dioxide. The Heat Capacity and Vapor Pressure of the Solid. The Heat of Sublimation. Thermodynamic and Spectroscopic Values of the Entropy, Journal of Chemical Physics, Volume 5, pp. 45-54, 1937

40. Gühler M., Hannemann R.J., Sallet D.W., Unsteady Two-Phase Blowdown of a Flashing Liquid from a Finite Reservoir, in Two-Phase Momentum, Heat and Mass Transfer in Chemical, Process, and Energy Engineering Systems, Volume 2, Hemisphere Publishing Corporation, Washington, 1979

41. Gyarmathy G., The Spherical Droplet in Gaseous Carriers Streams: Review and Synthesis, in *Multiphase Science and Technology*, vol. 3, p. 99 - 279, Hemisphere Pub. Corp., Washington, DC, 1982

42. Hanaoka Y., Maeno K., Zhao L. et al., A Study of Liquid Flashing Phenomenon Under Rapid Depressurization, JSME International Journal, Series II, Vol. 33, No. 2, pp. 276-282, 1990

43. Henry R.E., Fauske H.K., The Two-Phase Critical Flow of One-Component Mixtures in Nozzles, Orifices, and Short Tubes, Journal of Heat Transfer, Transactions of the ASME, pp. 179-187, May 1971

44. Hesson J.C., Peck R.E., Flow of Two-Phase Carbon Dioxide Through Orifices, AIChE, Vol. 4, No. 2, pp. 207-210, June 1958

45. Houberechts A., *La Thermodynamique technique. Tables et Diagrammes Thermodynamiques*, Vander, Brussels, Belgium, 1975

46. Huang F.-H., Li M.-H, Lee L.L. et al., An Accurate Equation of State for Carbon Dioxide, Journal of Chemical Engineering Japan, Vol. 18, No. 6, pp. 490-496, 1985

47. Ivashniov O.E., Soplenkov K.I., A model involving break-up to explain peculiarities of the boiling liquid efflux process, Int. J. Multiphase Flow, Vol. 18, No. 5, pp. 727-738, 1992

48. Jones O.C. Jr., Zuber N., Bubble Growth in Variable Pressure Fields (1), Journal of Heat Transfer, Transactions of the ASME, Vol. 100, pp. 453-459, Aug. 1978

49. Jost K., Air-bag inflator alternatives, Automotive Eng., pp. 66-67, May 1995

50. Keenan J.H., Keyes F.G., Hill P.G. et al., *Steam Tables : Thermodynamic Properties of Water. Including Vapor, Liquid, and Solid Phases*, J. Wiley & Sons Inc., New York, NY, 1969

51. Kim Y., O'Neal D. L., A Semi-Empirical Model of Two-Phase Flow of Refrigerant-134a through Short Tube Orifices, Experimental Thermal and Fluid Science, Vol. 9, No. 4, pp. 426-435, 1994

52. Kim-E., M.E., Reid R.C.,The Rapid Depressurization of hot, high Pressure Liquids or Supercritical Fluids, Chem. Engin. Supercrit. Fluid. Cond., pp. 81-100, 1983

53. Kwauk X., Debenedetti P. G., Mathematical Modeling of Aerosol Formation by Rapid Expansion of Supercritical Solutions in a Converging Nozzle, J. Aerosol Sci., Vol. 24, No. 4, pp. 445-469, 1993

54. Leblond J., Roulleau M., Kazan L., Model for inception of boiling in superheated flowing liquid, PCH PhysicoChemical Hydrodynamics, Vol. 10, No. 3, pp. 321-340, 1988

55. Lee, B-I., A Modified Redlich-Kwong Equation for Phase Equilibrium and Enthalpy Calculations, AIChE Journal, Vol. 38, No. 8, pp. 1299-1301, August 1992

56. Lefebvre A.H., Atomization and Sprays, Hemisphere Publishing Corporation, New York, NY, 1989

57. Lienhard J.H., Shamsundar N., Biney P.O., Spinodal Lines and Equations of State: A Review, Nuclear Engineering and Design, Vol. 95, pp. 297-314, 1986

58. Magalhaes J.L., Leblond J., Roulleau M., Superheating and initiation of boiling in flowing CO_2, PCH PhysicoChemical Hydrodynamics, Vol. 6, No. 4, pp. 415-434, 1985

59. Mahan B.H., *University Chemistry*, Addison-Wesley, Palo Alto, CA, 1965

60. Materna P., Temperature Compensated Stored Gas Inflator, Proceedings of the 1996 SAE International Congress & Exposition, Feb. 26-29, Detroit, MI, 1996

61. Minato A., Takamori K., Suzuki A., Numerical Study of Two-Dimensional Structure in Critical Steam-Water Two-Phase Flow, Journal of Nuclear Science and Technology, Vol. 32, No. 5, pp. 464-475, 1995

62. Nielsen K.A., Glancy C.W., Hoy K.L. et al., A New Atomization Mechanism for Airless Spraying: The Supercritical Fluid Spray Process, Proceedings ICLASS-91 (5^{th}), Gaithersburg, MD, USA, July 1991

63. Nigmatulin R.I., Soplenkov K.I., Non-stationary outflow and rarefaction waves in flashing liquid, Nuclear Engineering and Design, Vol. 151, pp. 131-144, 1994

64. Oza R.D., On the Mechanism of Flashing Injection of Initially Subcooled Fuels, Journal of Fluids Engineering, Transactions of the ASME, Vol. 106, pp. 105-109, 1984

65. Peng D.Y., Robinson D.B., A New Two-Constant Equation of State, Ind. Eng. Chem. Fundam., Vol. 15, No. 1, pp. 59-64, 1976

66. Perry R.H., Green D.W., *Perry's Chemical Engineer's Handbook* (6^{th} Ed.), McGraw-Hill Book Company, New York, NY, 1984

67. Prausnitz J.M., Molecular Thermodynamics of Fluid-Phase Equilibria, Prentice-Hall Inc., Englewood Cliffs, NJ, 1969

68. Richtmyer R.D., Morton K.W., *Difference Methods for Initial-Value Problems*, 2^{nd} Edition, Interscience Publishers, New York, NY, 1967

69. Schwellnus C.F., Shoukri M., A Two-Fluid Model for Non-Equilibrium Two-Phase Critical Discharge, The Canadian Journal of Chemical Engineering, Vol. 69, pp. 188-197, February 1991

70. Scriven L.E., On the dynamics of phase growth, Chemical Engineering Science, Vol. 10, Nos. 1/2, p. 1-13, 1959

71. Senda J., Hojyo Y., Fujimoto H., Modeling on atomization and vaporization process in flash boiling spray, JSAE Review 15, pp. 291 - 296, 1994

72. Sengers J.M.H. Levelt, Chen W.T., Vapor Pressure, Critical Isochore, and Some Metastable States of CO_2, Journal of Chemical Physics, Vol. 56, No. 1, pp. 595-608, 1972

73. Shah V.M., Bienowksi P.R., Cochran H.D., Generalized Quartic Equation of State for Pure Nonpolar Fluids, AIChE Journal, Vol. 40, No. 1, pp. 152-159, 1994

74. Shapiro A.H., *The Dynamics and Thermodynamics of Compressible Fluid Flow - volumes I and II*, The Ronald Press Company, New York, NY, 1954

75. Sheperd J.E., McCahan S., Cho J., Evaporation Wave Model for Superheated Liquids, in *Adiabatic Waves in Liquid-Vapor Systems*, pp. 3-12, IUTAM Symposium Göttingen, 8/28 - 9/1/1989, Springer-Verlag, Berlin

76. Sher E., Elata C., Spray Formation from Pressure Cans by Flashing, Ind. Eng. Chem., Process Des. Dev., Vol. 16, No. 2, pp. 237-242, 1977

77. Shin T.S. and Jones O.C., Nucleation and Flashing in Nozzles (part 1): A distributed nucleation model, Int. J. Multiphase Flow, Vol.. 19, No. 6, pp. 943-964, 1993

78. Shin Y.W., Wiedermann A.H., A Hybrid Numerical Method for Homogeneous Equilibrium Two-Phase Flows in One Space Dimension, Journal of Pressure Vessel Technology, Transactions of the ASME, vol. 103, pp. 20-26, 1981

79. Simons W.J., *Algemene en Technische Thermodynamika*, de sikkel, Kapellen, Belgium 1978

80. Sirignano W.A., Fluid Dynamics of Sprays - 1991 Freeman Scholar Lecture, Journal of Fluids Engineering, Transactions of the ASME, Vol. 115, pp. 345-378, 1993

81. Skripov V.P., Thermodynamic Stabilities of Superheated and Supercooled Liquids, Fluid Mechanics Research, Vol. 21, No. 3, pp. 43-50, 1992

82. Smith et al., Fluid Fueled Air Bag Inflator, US Patent #5,470,104, Nov. 28, 1995

83. Soave G., Equilibrium constants from a modified Redlich-Kwong equation of state, Chemical Engineering Science, Vol. 27, pp. 1197-1203, 1972

84. Solomon A.S.P., Rupprecht S.D., Chen L.-D. et al., Flow Atomization in Flashing Injectors, Atomization and Spray Technology, No. 1, pp. 53-76, 1985

85. Tabani Y., Automobile Air Bag Inflation System Based on Fast Combustion Reactions, Ph.D. Dissertation, Department of Mechanical Engineering, New Jersey Institute of Technology, Newark, NJ, October 1997

86. Thompson P.A., Liquid-Vapor Adiabatic Phase Changes and Related Phenomena, in *Nonlinear waves in real fluids*, pp.147-213, Courses and Lectures no. 315, Springer-Verlag, New York, NY, 1991

87. Touloukian Y.S., Liley P.E., Saxena S.C., *Thermal Conductivity: Nonmetallic Liquids and Gases*, IFI/Plenum, New York, NY, 1970

88. Vafai K., Holmes A. G., Photographic Evaluation of Fuel Injectors for Spark ignition Engines, Int. Comm. Heat Mass Transfer, Vol. 16, pp. 755-762, 1989

89. Wallis G. B., Critical Two-phase Flow, Int. J. Multiphase Flow, Vol. 6, pp. 97-112, 1980

90. Wang J.T., Are Tank Pressure Curves Sufficient to Discriminate Airbag Inflators ?, SAE Transactions, Vol. 100, Section 6, 1991

91. Warren M.D., Open-end Outflow Boundary Approximations for the Solution of the Equations of Unsteady One-Dimensional Gas Flow by the Lax-Wendroff Method, Int J Heat Fluid Flow, v 5, n 1, pp. 43-50, 1984

92. Watanabe T., Lee G.J., Iseki T. et al., A Mechanistic Model for the Analysis of Flashing Phenomena, Ann. Nucl. Energy, Vol. 23, No. 10, pp. 801-811, 1996

93. Weber W., Zeck S., Knapp H., Gas solubilities in liquid solvents at high pressures : apparatus and results for binary and ternary systems of N_2, CO_2 and CH_3OH, Fluid Phase Equilibria, No. 18, pp. 253-278, 1984

94. Werner J.V., Sorenson W.W., Survey of Air Bag Involved Accidents : An Analysis of Collision Characteristics, System Effectiveness and Injuries, International Congress & Exposition, Detroit 1994, SAE Technical Paper #940802

95. White F.M., *Heat and Mass Transfer*, Addison-Wesley, Reading, MA, 1991

96. White F.M., *Viscous Fluid Flow*, Mc Graw Hill, New York, NY, 1991

97. Yan F., Giot M., Mechanism of Flashing Inception and its Modeling, Heat and Technology (Calore e Tecnologia), Vol. 10, No. 3-4, pp. 145-161, 1992